

Université du Québec  
Institut National de la Recherche Scientifique  
Centre Énergie, Matériaux et Télécommunications

# **DEVELOPMENT OF MEMBRANELESS MIXED-REACTANT MICROFLUIDIC FUEL CELLS: ELECTROCATALYSIS AND EVOLUTION THROUGH NUMERICAL SIMULATION**

Par

Juan Carlos Abrego Martínez

Thèse présentée pour l'obtention du grade de  
Philosophiae Doctor (Ph.D.)  
en sciences de l'énergie et des matériaux

## **Jury d'évaluation**

Président du jury et  
examineur interne

Andreas Ruediger  
Professeur à l'INRS-ÉMT

Examineur externe

Ricardo Izquierdo  
Professeur à l'École de technologie  
supérieure (ETS)

Examineur externe

Sasha Omanovic  
Professeur à l'Université de McGill

Directeur de recherche

Mohamed Mohamedi  
Professeur à l'INRS-ÉMT

Codirecteur de recherche

Shuhui Sun  
Professeur à l'INRS-ÉMT



## ACKNOWLEDGMENTS

---

First and foremost, I would like to thank my supervisor, Prof. Mohamed Mohamedi for offering me the opportunity to undertake my PhD studies in his research group, for providing the tools and trusting me to carry out this project and for the excellent guidance and support throughout this period.

I also express my gratitude to my co-supervisor, Prof. Shuhui Sun for closely following the research progress and for his valuable contribution for accomplishing my PhD project.

I thank the Jury members, Prof. Andreas Ruediger, Prof. Ricardo Izquierdo and Prof. Sasha Omanovic for agreeing and taking the time to review and evaluate this work.

I would like to thank my group colleagues, Youling Wang, Alonso Moreno, Haixia Wang, Naser Mohammadi, Xiaoying Zheng, Khawtar Hasan and Soraya Bouachma, for sharing their knowledge and experience through discussions and experiments in the laboratory.

I thank Dr. Francisco Cuevas (CIDETEQ, Mexico) for his contribution in the early stages of this work.

I'm also grateful to the INRS technical staff members, Mr. Christophe Chabanier and Mr. Étienne Charette for their valuable and professional technical support. Likewise, to the administrative staff, Mrs. Hélène Sabourin, Hélène Tanguay and Michelle Marcotte for their help and professionalism.

I thank the UNESCO-MATECSS (Materials and Technologies for Energy Conversion, Saving and Storage) and the Excellence Scholarship program for awarding me the doctoral scholarship that allowed me to carry out my PhD studies.

I thank as well the Natural Sciences and Engineering Research Council of Canada (NSERC), Fonds de recherche du Québec – Nature et technologies (FRQNT) and the Centre Québécois sur les Matériaux Fonctionnels (CQMF) for their financial contribution to the research.

Last but not least, I'm deeply grateful to my family, especially my parents for their unconditional love, understanding and support at all moments in my life.



## ABSTRACT

---

Rising energy demands and the environmental deterioration have motivated the research for developing new, alternative and green energy conversion and storage devices with high efficiency. This also applies for consumer products such as portable electronic devices, which are essential tools in modern life. The introduction of next-generation smartphones, portable computers and a variety of gadgets is severely restricted by the autonomy, which is the fundamental issue of Li-ion batteries employed as power supply on practically all commercial portable electronic devices. It is now well known that power demand is outpacing developments in conventional battery technology. In the quest for an alternative power source capable of overcoming this situation, micro fuel cells appear as an attractive solution as they can offer the mobility and freedom sought by the consumer by offering faster recharging speed and longer service life. In addition, this technology has important environmental benefits because the fuels can be obtained from sustainable organic sources. Methanol is considered to be a potential fuel for miniaturized fuel cells due to its high energy density and relatively safe use. As a promising power source of such, methanol-fed membraneless mixed-reactants microfluidic fuel cells (MR- $\mu$ DMFCs) fabricated on polymeric substrate have recently been proposed as a technology capable of fulfill the energetic requirements for electronic portable devices. In order to improve their performance, this thesis centers on the development of a highly efficient cathode material for MR- $\mu$ DMFCs, added to an accurate understanding of a single cell operation. This is intended to be achieved by employing numerical simulations and implementing stack cell improvements established on these simulation results. Consequently, a selective cathode was synthesized in this work and subsequently used in a 4-cell MR- $\mu$ DMFC stack developed in this thesis. The stack was tested in passive conditions producing 1.1 mW of peak power in series connection, a power considered sufficient for micro-devices. The proof of concept is demonstrated by using the stack for powering a green LED during 4 h with a single charge of 234  $\mu$ L.

Keywords: Mixed-reactant fuel cell; direct methanol fuel cell; selective catalyst; oxygen reduction reaction; microfluidics; numerical simulation.



## RESUME

---

La demande croissante d'énergie et la détérioration de l'environnement ont motivé la recherche pour développer de nouveaux dispositifs de conversion et de stockage d'énergie alternative et verte à haute efficacité. Cela vaut également pour les produits de consommation tels que les appareils électroniques portables, qui sont des outils essentiels dans la vie moderne. L'introduction de smartphones, d'ordinateurs portables et de gadgets de nouvelle génération, est limitée par l'autonomie, qui est le problème fondamental des batteries Li-ion utilisées comme alimentation sur pratiquement tous les appareils électroniques portables commerciaux. Il est désormais bien connu que la demande d'énergie dépasse les développements de la technologie de batterie conventionnelle. Dans la quête d'une source d'énergie alternative capable de surmonter cette situation, les micro-piles à combustible apparaissent comme une solution intéressante car elles peuvent offrir la mobilité et la liberté recherchées par le consommateur en offrant une vitesse de recharge plus rapide et une durée de vie plus longue. De plus, cette technologie présente des avantages environnementaux importants car les carburants peuvent être obtenus à partir de sources organiques durables. Le méthanol est considéré comme un combustible potentiel pour les piles à combustible miniaturisées en raison de sa densité énergétique élevée et de son utilisation relativement sûre. Les piles à combustible microfluidiques à réactifs mixtes sans membrane alimentées au méthanol (MR- $\mu$ DMFC) ont récemment été proposées comme technologie capable de répondre aux exigences énergétiques des appareils électroniques portables. Afin d'améliorer leurs performances, cette thèse se concentre sur le développement d'un matériau de cathode très efficace pour les MR- $\mu$ DMFC, ajouté à une compréhension précise d'un fonctionnement à cellule unique. Ceci est prévu à être réalisé en utilisant des simulations numériques et en mettant en œuvre des améliorations de cellules de pile établies sur ces résultats de simulation. Par conséquent, une cathode sélective a été synthétisée dans ce travail et ensuite utilisée dans une pile MR- $\mu$ DMFC à 4 cellules développée dans cette thèse. La pile a été testée dans des conditions passives produisant 1,1 mW de puissance de crête en connexion série, une puissance jugée suffisante pour les micro-appareils. La preuve de concept est démontrée en utilisant la pile pour alimenter une LED verte pendant 4 h avec une seule charge de 234  $\mu$ L.

Mots-clés: Pile à combustible à réactifs mixtes; pile à combustible à méthanol direct; catalyseur sélectif; réaction de réduction d'oxygène; microfluidique; simulation numérique.



## SYNOPSIS

---

Cette thèse est composée de 6 chapitres:

Le chapitre 1 présente une introduction générale à la problématique et les motivations de ce travail. Les objectifs de cette thèse sont également énoncés au chapitre 1.

Le chapitre 2 comprend la revue de la littérature sur les fondamentaux des piles à combustible. Différents types de piles à combustible et leur possibilité d'être mis en œuvre sur des appareils portables sont discutés ici. Ce chapitre se concentre sur les avantages des piles à combustible à réactifs mixtes. Le chapitre deux présente également plus en détail la réaction de réduction de l'oxygène et du méthanol et leurs mécanismes. Il se poursuit par une revue de la littérature sur certains catalyseurs tolérants au méthanol et il décrit enfin les fondamentaux des méthodes de synthèse et de caractérisation utilisées dans cette thèse.

Le chapitre 3 décrit la méthodologie suivie dans cette thèse. Tout d'abord, la synthèse de deux cathodes tolérantes au méthanol, Ag/Pt/CP et Mn<sub>2</sub>O<sub>3</sub>/Pt/CP, est présentée, suivie des méthodes employées pour caractériser lesdits matériaux et l'évaluation des cathodes dans un ML- $\mu$ DMFC. Ensuite, le développement d'un nouveau concept de MR- $\mu$ DMFC est décrit, suivi par la conception et la fabrication et le test d'une pile MR- $\mu$ DMFC à 4 cellules.

Le chapitre 4 présente les résultats concernant le catalyseur Ag/Pt/CP, une cathode tolérante au méthanol. La caractérisation électrochimique et physico-chimique est présentée ici, suivie de l'évaluation de la capacité de tolérance au méthanol en utilisant la cathode dans un ML- $\mu$ DMFC dans des conditions de réactifs mixtes.

Le chapitre 5 présente les résultats concernant le catalyseur Mn<sub>2</sub>O<sub>3</sub>/Pt/CP, la deuxième cathode tolérante au méthanol synthétisée dans ce travail. La caractérisation électrochimique et physico-chimique est présentée ici, suivie de l'évaluation de la capacité de tolérance au méthanol en utilisant la cathode dans un ML- $\mu$ DMFC dans des conditions de réactifs mixtes. Les résultats des piles à combustible ont été comparés à ceux obtenus avec la cathode Ag/Pt/CP au chapitre 4 afin de déterminer le meilleur candidat pour un MR- $\mu$ DMFC.

Le chapitre 6 présente les résultats concernant le développement d'un nouveau type de MR- $\mu$ DMFC et d'une pile MR- $\mu$ DMFC à 4 cellules à travers un modèle mathématique obtenu dans cette thèse. Ce chapitre décrit la fabrication et l'évaluation des nouveaux dispositifs de piles à combustible microfluidiques. Enfin, la capacité d'application pratique en tant que preuve de concept de la pile MR- $\mu$ DMFC à 4 cellules est démontrée ici.

## Introduction

Les sociétés technologiquement avancées ont besoin d'outils et d'équipements spécialisés pour effectuer leurs diverses activités quotidiennes. Les appareils électroniques portables tels que les ordinateurs portables, les téléphones portables, les montres intelligentes, etc. sont des instruments essentiels pour de nombreuses personnes dans leur vie quotidienne. En conséquence, un certain nombre de gadgets avec des fonctionnalités plus élevées et une taille réduite sont apparus sur le marché ces dernières années. Cela implique que la nouvelle technologie nécessite plus de puissance dans des facteurs de forme plus petits. Les sources d'énergie pour tous les types d'appareils électroniques sont soumises à une pression constante pour atteindre des niveaux d'efficacité plus élevés en augmentant la densité d'énergie et en diminuant à la fois le volume et le poids tout en réduisant le coût des sources d'alimentation portables en même temps [1-4]. À ce jour, la batterie rechargeable au lithium (Li-ion, Li-poly) est la principale source d'alimentation pour les appareils portables. Ces batteries offrent une densité d'énergie élevée, par rapport à d'autres batteries chimiques, cependant, il existe certaines inquiétudes concernant la disponibilité du lithium à l'avenir, en raison de ses sources limitées et de son coût en constante augmentation [5]. Un inconvénient majeur de l'utilisation de batteries rechargeables est qu'elles ont besoin d'une source d'alimentation électrique externe pour se recharger. En raison de la capacité limitée de la batterie, elles ne peuvent être utilisées qu'avec une source électrique existante, ce qui représente une limitation en termes de mobilité de l'appareil. Dans les zones reculées où il n'y a pas de réseau électrique, le fonctionnement d'un appareil sur des batteries portables est problématique [18,19]. Il existe également des problèmes liés à la sécurité en raison de la possibilité d'incendie ou d'explosion causée par un court-circuit à l'intérieur de la cellule, en particulier pendant la charge. De plus, les longs temps de recharge restent l'un des principaux défis pour les batteries à base de Li [5]. Cette situation a conduit de nombreux chercheurs à rechercher des sources d'alimentation alternatives pour remplacer la technologie des batteries pour les applications portables.

Une autre source d'énergie qui a été explorée ces dernières années est la technologie des piles à combustible. Une pile à combustible est un dispositif électrochimique qui convertit l'énergie chimique stockée dans un combustible et un oxydant en énergie électrique grâce à des processus électrochimiques impliquant des réactions d'oxydoréduction [5,21]. Il est possible de penser à une pile à combustible comme une «usine» qui prend le combustible en entrée et produit de l'électricité en sortie. Comme une usine, une pile à combustible générera un produit (électricité) tant que la matière première (combustible) sera fournie. Les avantages des piles à combustible

incluent la mise à l'échelle indépendante plus simple entre la puissance et la capacité, tandis que les batteries évoluent mal à de grandes tailles [22]. Dans les batteries, l'énergie est stockée dans des sources relativement lourdes et volumineuses telles que les dérivés du lithium, les oxydes métalliques et les matériaux graphitiques. Par contre, les piles à combustible ont des fonctions de stockage et de conversion d'énergie découplées et peuvent produire de l'électricité à partir de matériaux beaucoup plus légers tels que les gaz et les alcools [1,23]. Les piles à combustible ne sont pas consommées lors de la production d'électricité, elles peuvent fonctionner en mode passif ou actif et, plus important, elles peuvent être rechargées instantanément [1,5,22]. Ces caractéristiques sont les principales différences entre les piles à combustible et les batteries et pour ces raisons, ces premières représentent une technologie prometteuse pour un large éventail d'applications. Les piles à combustible sont très polyvalentes, car elles peuvent fonctionner avec une variété de combustibles, d'oxydants et d'électrolytes dans différentes plages de températures [22,27-29]. L'hydrogène et l'oxygène purs ont été largement utilisés comme combustible et oxydant, respectivement, principalement parce que l'oxydation de l'hydrogène est un processus relativement simple et qu'il produit une densité de puissance élevée avec des émissions pratiquement nulles [30]. Cependant, un inconvénient majeur des piles à combustible à hydrogène est associé au stockage et à la distribution d'hydrogène, et son utilisation est limitée aux applications de transport et résidentielles [30,31]. L'utilisation de liquides à température ambiante riches en l'hydrogène, tels que des alcools, a été proposée pour remplacer l'hydrogène dans les piles à combustible pour des applications portables [27,32,33].

Dans le cas des appareils électroniques portables, le méthanol, l'alcool le plus simple est particulièrement attractif en raison de sa haute densité énergétique (4820 Wh L<sup>-1</sup>), de son faible coût et de sa facilité de stockage et de transport par rapport à l'hydrogène gazeux (530 Wh L<sup>-1</sup> @ 20 MPa) [32,34]. D'un autre côté, l'oxygène, pur ou provenant de l'air, est généralement utilisé comme oxydant, en raison de son faible coût et de son abondance [35,36]. La réaction de réduction de l'oxygène (RRO) est un processus multiélectronique qui est d'une grande importance pour les piles à combustible. Cette réaction a été au centre de l'attention dans le développement de catalyseurs en raison de sa cinétique lente et de sa surtension élevée sur pratiquement tous les matériaux de catalyseur, et elle a été identifiée comme la réaction limitante dans les piles à combustible à base d'oxygène. À ce jour, le Pt reste le catalyseur de choix pour la RRO dans la plupart des systèmes de piles à combustible, car il présente de meilleures performances globales que la plupart des matériaux catalytiques [37], cependant, car le Pt est un métal précieux rare et cher, l'un des principaux objectifs du développement de la cathode est de réduire la teneur en Pt.

Le mécanisme de la RRO sur Pt est étudié depuis de nombreuses années, et bien que des progrès significatifs aient été accomplis dans la compréhension de son déroulement, le mécanisme de réaction exact fait encore l'objet de discussions approfondies [36]. Il est généralement admis que dans les solutions aqueuses, les molécules de  $O_2$  peut être réduit électrochimiquement directement en eau via un transfert à quatre électrons, ou réduit de deux électrons en  $H_2O_2$  (ou  $HO_2^-$ ) et ensuite réduit en eau (ou  $OH^-$ ) par un autre transfert à deux électrons [36,37]. La cinétique de la RRO dans les milieux alcalins est plus rapide et fournit un environnement moins corrosif aux catalyseurs, par rapport aux milieux acides [20]. Cela a stimulé la recherche sur les catalyseurs de la RRO dans les milieux alcalins.

Les piles à combustible qui utilisent des solutions de méthanol et de l'oxygène sont appelées piles à combustible au méthanol directes (DMFC) [38]. Le type de DMFC le plus étudié repose sur une membrane échangeuse de protons (PEM), généralement du Nafion®, pour séparer les deux demi-réactions, l'oxydation du méthanol (ROM) à l'anode et la réduction de l'oxygène à la cathode [42,43]. Ce type de pile à combustible est donc dénommé PEM-DMFC et leurs principaux composants sont représentés sur la figure 1.3. Les PEM-DMFC font l'objet d'études intensives depuis deux décennies, en raison de leurs avantages par rapport aux PEM-FC alimentés en hydrogène. Cependant, la diffusion du méthanol de l'anode à la cathode à travers la membrane est un problème récurrent qui a un impact négatif sur les performances globales des PEM-DMFC. La présence de méthanol à la cathode provoque des pertes de dépolarisation dues aux processus simultanés de réduction de l'oxygène et d'oxydation du méthanol. Ce phénomène est connu sous le nom d'effet de croisement du méthanol [41,44]. Ainsi, la concentration de solutions de méthanol est souvent limitée à pas plus de 10% en poids, et l'utilisation d'une concentration plus élevée est contre-productive [45]. D'autres problèmes liés à la membrane comprennent une faible résistance mécanique et la gestion de l'eau pour l'hydratation et des performances optimales [46,47]. En plus de plus leur coût élevé, les PEM-DMFC conventionnels sont considérés comme trop volumineux pour les applications portables [5].

L'introduction de piles à combustible microfluidiques sans membrane (ML- $\mu$ FFC) au début des années 2000, a présenté la possibilité d'intégrer des sources d'énergie plus simples et miniaturisées sur des appareils portables. Comme son nom l'indique, cette technologie ne nécessite aucune membrane pour fonctionner. Au lieu de cela, les ML- $\mu$ FFC (ML- $\mu$ DMFC si alimentés au MeOH) s'appuient sur le flux co-laminaire de carburant et d'oxydant dans un canal microfluidique pour séparer les deux demi-réactions électrochimiques (oxydation du méthanol et réduction de l'oxygène) [33,39]. Les réactifs s'écoulent sous un régime laminaire, caractérisé par

un faible nombre de Reynolds ( $Re$ ) [5]. Comme les flux de carburant et d'oxydant s'écoulent parallèlement dans un format co-laminaire, l'interface liquide-liquide sert de séparateur sans avoir besoin d'une membrane. À faible  $Re$  (inférieur à 1000), les deux flux couleront parallèlement dans un microcanal. Le dépassement du seuil entraînera une transition vers un écoulement turbulent et une déstabilisation de l'interface d'écoulement co-laminaire, conduisant à un mélange excessif et à une perte de tension de la cellule [5]. En éliminant la membrane et les plaques bipolaires, le coût d'un ML- $\mu$ DMFC est considérablement réduit. De plus, le croisement du méthanol peut être diminué dans une large mesure en réglant avec précision le débit de carburant et d'oxydant [33,39].

Pour des applications pratiques, l'intégration de plusieurs piles à combustible microfluidiques est nécessaire, cependant, le développement de piles microfluidiques sans membrane est difficile en raison du besoin de structures d'écoulement efficaces et de manifold dans des réseaux de cellules à efficacité spatiale [5,55]. Selon la stratégie d'empilement, la livraison des réactifs, l'étanchéité et l'isolation ionique entre les cellules unitaires deviennent plus compliquées avec l'augmentation du nombre de cellules. Pour ces raisons, peu de travaux sur les piles sans membrane se trouvent dans la littérature. Parmi les plus représentatifs, on trouve un réseau microfluidique plan à 5 cellules rapporté par Cohen et al. [56], une pile plane à 2 cellules avec des ports d'entrée partagés proposée par Ho et Kjeang [57], une conception en tandem qui permet la réutilisation du carburant développée par Salloum et Posner [58], une architecture basée sur un réseau hexagonal de tiges de graphite rapporté par Kjeang et al. [59] et un empilement de 6 cellules dans un arrangement circulaire proposé par Wang et Leung [60]. Malgré les architectures très différentes des cheminées susmentionnées, elles présentent toutes un flux colaminaire de combustibles et d'oxydants et l'utilisation impérative de pompes externes pour empêcher le mélange des réactifs, ce qui est finalement une perte énergétique rarement prise en compte dans l'équilibre général. Cet inconvénient n'est pas nécessairement présent dans les piles à combustible à réactifs mixtes (MRFC), où la séparation des réactions cathodiques et anodiques est traitée par des catalyseurs sélectifs [61-63] (Fig. 1.7). Par conséquent, ils ne nécessitent pas de flux laminaire de réactifs et peuvent donc fonctionner en mode passif. En d'autres termes, des pompes externes ne sont pas nécessaires, résultant en des systèmes beaucoup plus compacts avec un fonctionnement plus simple.

Les MRFCs offrent donc une solution potentielle au problème de l'empilement des piles à combustible microfluidiques, ce qui peut conduire au développement d'une pile microfluidique passive de petites dimensions et d'une production d'énergie suffisante pour une application à

faible puissance. Essentiellement, dans une MRFC, le carburant et l'oxydant sont mélangés en un seul flux et l'utilisation d'électrocatalyseurs sélectifs est nécessaire pour minimiser le potentiel mixte aux électrodes [63,64]. Ainsi, une MR- $\mu$ DMFC nécessite une anode active pour la réaction d'oxydation du méthanol, et une cathode active uniquement pour la réaction de réduction de l'oxygène. Il y a un certain nombre d'avantages associés à l'utilisation des MRFC par rapport à d'autres FCs, par exemple, pas besoin de membrane polymère solide ou d'écoulement laminaire et de pompes externes, poids et volume réduits, manifold simplifié, exigences d'étanchéité réduites et, dans l'ensemble, ils ont des conceptions plus simples. En ayant un volume plus petit, une pile MR- $\mu$ DMFC peut conduire à une densité de puissance volumétrique plus élevée [62-65]. D'un point de vue technique, cela se traduit par une fabrication moins chère et un fonctionnement plus facile que les piles à combustible conventionnelles. Calabrese-Barton et son groupe ont mis au point des MRFC à base de MEA [61,63,66], et plus récemment, un MRFC à base de borohydrure-oxygène a été signalé [65,67,68]. Néanmoins, peu de travaux sur les MRFC à base de méthanol se retrouvent dans la littérature, principalement en raison de la nécessité d'électrodes sélectives, notamment la cathode. Bien que la ROM soit à peine affectée par la présence d'oxygène, le RRO est supprimé par la présence de MeOH [69,70]. Comme mentionné ci-dessus, malgré son coût élevé, le Pt est largement utilisé pour les catalyseurs cathodiques en raison de son excellente activité catalytique, cependant, le principal inconvénient de l'utilisation du Pt comme cathode dans tout DMFC est qu'il oxyde également le méthanol [41,71]. Par conséquent, l'utilisation de Pt comme cathode pour les MR-DMFC n'est pas appropriée, car essentiellement, la cathode ne doit pas être active sur la ROM. De nombreux groupes ont travaillé sur le développement de cathodes tolérantes au méthanol, comprenant principalement des catalyseurs sans Pt, tels que Pd / Ag [72], Ru / Se [73], PdSe [74], Pd / Co [75], Fe-NC [76,77], CoSe<sub>2</sub> [78] et RuSe<sub>2</sub> [79] pour les PEM-DMFC. Cependant, le RRO sur ces matériaux a une surtension plus élevée, des taux de réaction cinétiques plus lents et une activité spécifique de faible masse, par rapport au Pt. Feng et al. [80] ont rapporté la synthèse d'un catalyseur de cathode à nanoparticules de Pt-Ru à cage-cloche (core-shell), tolérant au méthanol 1 M. L'intérêt de ce travail est que le noyau Pt sert de catalyseur pour le RRO tandis que la coque poreuse Ru agit comme une protection pour le noyau, en raison de la diffusion différentielle du méthanol et de l'oxygène. Sur la base de cette approche, dans ce travail, nous proposons le développement d'une cathode à base de Pt avec un matériau poreux ajouté comme protection pour le Pt afin d'empêcher la diffusion du méthanol mais en permettant la diffusion de l'oxygène. Ceci est destiné à être réalisé grâce à une architecture couche sur couche, où la couche de base, Pt, servira de catalyseur pour la RRO, tandis qu'une couche secondaire ou superficielle fonctionnera comme

protection (inhibiteur). Ce faisant, nous nous attendons à ce que les cathodes présentent une activité de masse élevée et des propriétés tolérantes au méthanol pour une utilisation dans MR- $\mu$ DMFC.

La technique du dépôt laser pulsé (PLD) a été précédemment utilisée dans notre groupe pour le dépôt de divers métaux et oxydes métalliques directement sur du papier carbone (CP) et des substrats de nanotubes de carbone (CNTs) en tant que catalyseurs anodiques pour l'oxydation de l'éthanol [83] et du glucose [84] avec de meilleures performances globales que les catalyseurs supportés sur du carbone Vulcan, plus couramment utilisés. Pour ces raisons, la PLD a été choisie dans ce projet pour le développement de cathodes couche sur couche à base de Pt avec des propriétés de tolérance au méthanol pour une utilisation dans un MR- $\mu$ DMFC.

Quant à la conception et à l'étude de nouveaux systèmes de piles à combustible, la modélisation par simulation est une ressource permettant de gagner du temps qui permet d'examiner une variété de phénomènes et de systèmes sans les dépenses et les difficultés d'expérimentation. Ces dernières années, la simulation numérique s'est révélée être un outil très utile pour l'analyse des phénomènes électrochimiques [85,86], la distribution des espèces chimiques [86,87] et un moyen pratique d'optimiser certains composants des piles à combustible, tels que les structures d'écoulement [88,89]. Les performances des piles à combustible peuvent être améliorées en adaptant les géométries des microcanaux et le placement stratégique des électrodes pour favoriser une meilleure utilisation du combustible [90]. Dans les MR- $\mu$ DMFC, les électrodes peuvent être inhabituellement plus proches que dans les piles à combustible co-laminaires, car le croisement du méthanol n'est pas un problème. La simulation numérique peut aider à l'optimisation de ces paramètres critiques pour développer un empilement MR- $\mu$ DMFC plus économe en carburant et plus performant.

## **Objectifs de la thèse**

1. Développer une cathode nanostructurée avec une activité catalytique élevée et une sélectivité envers la RRO pour une utilisation dans les MR- $\mu$ DMFCs.

Ce qui précède est destiné à être atteint à travers les objectifs spécifiques suivants.

a) Faire croître un film de Pt sur substrat de carbone par PLD puis en enduire le Pt d'une couche d'Ag, Fe<sub>2</sub>O<sub>3</sub> ou Mn<sub>2</sub>O<sub>3</sub> afin d'obtenir une structure bicouche. Des films de morphologies et de charges massiques différentes seront déposés.

b) Caractériser les catalyseurs par des techniques physico-chimiques et électrochimiques afin d'étudier la morphologie et la composition, ainsi que d'évaluer l'activité électrocatalytique vers le RRO et le ROM.

c) Évaluer et comparer les cathodes dans un seul ML- $\mu$ DMFC dans des conditions de réactifs mixtes et en mode passif afin d'identifier la cathode la mieux adaptée pour une utilisation dans un MR- $\mu$ DMFC.

2. Développer une pile MR- $\mu$ DMFC comme preuve de concept qui utilise la cathode sélective obtenue à partir de l'objectif 1 afin de démontrer le potentiel pour des applications pratiques.

La conception, l'optimisation et la fabrication de la pile MR- $\mu$ DMFC doivent être réalisées à travers les objectifs spécifiques suivants.

a) Obtenir un modèle mathématique par le biais d'un logiciel d'analyse par éléments finis et valider expérimentalement le modèle afin d'étudier deux arrangements électrodes-microcanaux différents pour un MR- $\mu$ DMFC.

b) Fabriquer un seul MR- $\mu$ DMFC par micro-usinage CNC avec les caractéristiques optimales selon la simulation numérique.

c) Évaluer expérimentalement la performance du seul MR- $\mu$ DMFC afin d'établir la base pour la fabrication d'un empilement MR- $\mu$ DMFC.

d) Incorporer différentes cellules dans un seul appareil pour obtenir un empilement MR- $\mu$ DMFC et le fabriquer par micro-usinage CNC.

e) Évaluer les performances de la pile en connexions série et parallèle et l'utiliser pour alimenter une LED afin de démontrer les capacités pour des applications pratiques.

## **Méthodes expérimentales**

### **Synthèse**

Des électrodes de cathode sans liant nanostructurées ont été synthétisées par PLD sur un substrat de carbone. Ces matériaux catalytiques ont été préparés en 2 étapes. En premier, une couche de Pt a été déposée sur le substrat et celle-ci a ensuite été recouverte d'une couche de métal ou d'oxyde métallique (Ag, Fe<sub>2</sub>O<sub>3</sub> ou Mn<sub>2</sub>O<sub>3</sub>), ayant ainsi une architecture couche sur couche, comme illustré sur la figure 3.1. L'objectif est d'obtenir un matériau d'électrode avec une activité catalytique élevée vers la RRO et qui ne présente aucune activité vers la ROM, c'est-à-dire une cathode sélective à la réduction d'oxygène pour une utilisation dans des piles à

combustible à méthanol direct à réactif mixte. Afin d'obtenir la performance vers la RRO et la tolérance au méthanol souhaitée, plusieurs dépôts ont été effectués en modifiant certains paramètres clés de dépôt. Trois valeurs de pression de fond ont été utilisées pour la synthèse: sous vide (UV), 0,5 Torr de He et 2 Torr de He. En changeant la pression, il est possible d'obtenir différentes morphologies de surface. La quantité de matière déposée et donc l'épaisseur du film dépend du nombre d'impulsions laser, pour cette raison des dépôts avec un nombre d'impulsions différent ont été effectués pour chaque catalyseur de morphologie différente. L'objectif était d'étudier l'effet de l'épaisseur sur la diffusion de l'oxygène et du méthanol à travers des couches poreuses. Dans le tableau 3.2 sont reportées les conditions expérimentales optimales pour la synthèse des deux cathodes les plus performantes développées dans ce travail: Ag/Pt/CP et Mn<sub>2</sub>O<sub>3</sub>/Pt/CP. Les dépôts de Pt, Ag et Mn<sub>2</sub>O<sub>3</sub> ont été réalisés par PLD utilisant CP comme substrat. Les cibles Pt (99,99%), Ag (99,99%) et Mn<sub>2</sub>O<sub>3</sub> (99,90%) utilisées pour le dépôt ont été achetées auprès de Kurt J. Lesker Co. Tous les dépôts ont été effectués à température ambiante à l'aide d'un laser excimer KrF ( $\lambda = 258 \text{ nm}$ ), largeur d'impulsion = 17 ns et taux de répétition = 40 Hz. La fluence du laser pour Pt et Ag a été fixée à 4 J cm<sup>-2</sup> et pour Mn<sub>2</sub>O<sub>3</sub>, elle a été réglée à 2,5 J cm<sup>-2</sup>. Dans tous les cas, la distance cible-substrat a été fixée à 5 cm. Avant chaque dépôt, la chambre a été évacuée à l'aide d'une turbopompe (4 × 10<sup>-5</sup> Torr). Afin d'obtenir une ablation uniforme, les cibles ont été tournées en continu et translatées pendant le dépôt.

### **Caractérisation physicochimique**

La morphologie de surface des matériaux synthétisés a été étudiée par SEM (TESCAN, LYRA3) opéré à 15 et 20 kV. La structure cristalline de tous les dépôts a été déterminée par DRX à l'aide d'un diffractomètre Bruker D8 Advance équipé d'une source Cu K $\alpha$ . Le diffractomètre a fonctionné à 40 kV et 40 mA. Tous les diffractogrammes ont été acquis en mode de balayage par diffraction d'incidence du pâturage (GID) avec un angle d'incidence de 2°, un pas angulaire de 2 $\theta$  de 0,05° et un temps d'acquisition de 5 s par pas. Des mesures XPS ont été effectuées afin de déterminer la composition chimique des éléments de surface sur les échantillons et leurs états d'oxydation. L'étude a été réalisée dans un VG Escalab 220i-XL équipé d'une source Al K $\alpha$  (1486,6 eV). L'anode a fonctionné à 10 kV et 20 mA et l'énergie de passage de l'analyseur a été fixée à 20 eV. Les échantillons ont été analysés avec une taille de spot de 150 × 800  $\mu\text{m}$  située approximativement au centre de l'échantillon. Tout d'abord, des spectres d'enquête dans la gamme 0 – 1350 eV ont été acquis, suivis par des spectres de balayage multiplex à plus haute résolution (niveaux de base Ag 3d, Mn 3s, Mn 2p, Pt 4f, O 1s et C 1s). L'analyse des éléments a été réalisée avec le logiciel CasaXPS (Casa Software Ltd.) en ajustant les spectres de niveau de

cœur après une suppression du fond de Shirley. Le pic du niveau de base en C 1s à 284,6 eV, résultant des contaminants d'hydrocarbures à la surface a été utilisé comme référence interne. Tous les spectres ont été recalibrés par rapport au pic du niveau de cœur C 1s de contamination accidentelle au carbone.

### **Caractérisation électrochimique**

Les propriétés électrochimiques des échantillons ont été étudiées en milieu alcalin (0,5 M KOH, Fisher Chemical, 85,8%) dans une cellule électrochimique à trois compartiments à température ambiante, en utilisant un potentiostat/galvanostat Autolab PGSTAT302N. Les électrodes de travail ont une surface géométrique de 0,370 cm<sup>2</sup>. Une spirale de Pt a été utilisée comme contre-électrode et une Ag/AgCl, 4 M KCl, comme électrode de référence. Tous les potentiels rapportés dans le présent travail sont référés à une électrode à hydrogène réversible (RHE). Les profils électrochimiques ont été obtenus en utilisant la voltampérométrie cyclique (CV) dans une solution sans oxygène (Ar barboté pendant 30 min avant chaque CV). La fenêtre de potentielle a été cyclée jusqu'à l'obtention d'une réponse stable et reproductible. Des techniques de voltampérométrie à balayage linéaire (LSV) et d'électrode annulaire disque rotatif (RRDE) ont été utilisées pour étudier l'activité catalytique vers la RRO dans une solution de KOH 0,5 M saturée en oxygène (O<sub>2</sub> a bullé pendant 30 min avant chaque test). Les mesures de RRDE ont été effectuées avec un bipotentiostat (Pine, modèle AFCBP1) et un rotateur d'électrodes AFMSRCE (Pine Research Instrumentation), en utilisant un RRDE avec un disque de GC (diamètre 5,5 mm) et un anneau de Pt (diamètre intérieur et extérieur 6,5 et 8,5 mm, respectivement). Les échantillons, avec une surface géométrique de 0,19 cm<sup>2</sup>, ont été attachés au disque de carbone vitreux en utilisant du ruban conducteur en carbone. Pour la détection de H<sub>2</sub>O<sub>2</sub> généré sur le disque, le potentiel de l'anneau Pt a été fixé à 1,3 V vs RHE. Le rendement en peroxyde et le nombre de transfert d'électrons (n) ont été calculés selon les équations 76 et 77, respectivement. La tolérance au méthanol a été évaluée par le LSV sous atmosphère d'oxygène en présence de différentes concentrations (1 à 5 M) de MeOH (réactif ACS, ≥99,8%).

### **Test dans une pile à combustible**

Un dispositif de pile à combustible microfluidique a été fabriqué afin d'évaluer les catalyseurs. La conception de la pile à combustible utilisée à ce stade de l'étude découle d'une pile à combustible respirant l'air avec des électrodes à écoulement, rapportée par Ortiz-Ortega et al. [149]. Quelques modifications ont été apportées aux dimensions des composants afin de miniaturiser davantage l'appareil. Cet appareil est dénommé Cellule G1 tout au long de ce travail. La pile à combustible

est constituée d'électrodes poreuses dans un canal avec une géométrie en forme de V (figure 3.3). L'ensemble d'électrodes-canaux a été pris en sandwich entre deux plaques de PMMA fabriquées par un système de micro-fraisage à commande numérique par ordinateur (CNC) et l'ensemble a été serré par des vis à métaux M1,6, ayant des dimensions totales de 38 x 38 x 8,4 mm (L × W × H) avec un volume du microcanal de 25  $\mu\text{L}$ . Une fenêtre de 0,1  $\text{cm}^2$  a été réalisée sur les plaques inférieure et supérieure comme entrées d'air pour la cathode respirant l'air. Des broches Pogo ont été utilisées comme collecteurs de courant, ce qui a permis de réduire considérablement les dimensions de l'appareil. Comme d'habitude avec les piles à combustible à électrodes à écoulement continu, les valeurs de densité de courant et de puissance rapportées ici sont normalisées à la section transversale de l'électrode (0,015  $\text{cm}^2$ ) au flux de réactifs. Dans tous les cas, l'anode était un catalyseur composite PtRu (50:50, charge massique de 4  $\text{mg cm}^{-2}$ ) acheté auprès de Fuel Cell Store. Cette conception de pile à combustible était initialement conçue pour fonctionner avec un débit à 2 flux typique [149], comme le montre la figure 3.4, cependant, pour évaluer les cathodes tolérantes au méthanol dans des conditions de réactifs mixtes, la pile à combustible a été alimentée avec une solution unique contenant MeOH dans KOH sous forme d'électrolyte, fourni simultanément à la fois à l'anode et à la cathode, comme illustré sur la figure 3.5b. Cinq concentrations différentes de méthanol (1–5 M) ont été utilisées. Des mesures de stabilité dans des conditions de réactifs mixtes ont été effectuées en utilisant la technique de chronoampérométrie en appliquant 0,35 V pendant 2 h. Toutes les mesures de performance des piles à combustible ont été effectuées à température ambiante en mode totalement passif, et les données ont été enregistrées à l'aide d'un système de test des piles à combustible Scribner (Scribner Associates modèle 890CL), contrôlé par la version du logiciel de test des piles à combustible 3.8.

## **Développement d'un nouveau MR- $\mu\text{DMFC}$**

### **Méthodologie numérique et définition de modèle**

La construction du modèle mathématique pour étudier de nouvelles conceptions de piles à combustible nécessite certaines données expérimentales afin de prédire au mieux le comportement des futurs systèmes expérimentaux. Pour cette raison, les tests de la cellule G1 dans des conditions de réactifs mixtes ont été utilisés comme base pour le développement de la simulation numérique. Afin d'obtenir le modèle, chaque composant de la cellule G1 a été construit à l'aide d'un logiciel de conception assistée par ordinateur (CAD). COMSOL Multiphysics® a été utilisé pour résoudre les réactions électrochimiques couplées et les phénomènes de transport

dans le microcanal du  $\mu$ FFC. La définition du modèle comprenait des électrodes poreuses et une cathode respirant l'air. Les propriétés de chaque composant, telles que les caractéristiques des électrodes, la densité et la viscosité des fluides et les paramètres électrochimiques, fournies dans les tableaux 3.3 et 3.4 ont été annexées à la base de données dans le logiciel. La concentration initiale du carburant a été fixée à 4 M à l'anode et à zéro à la cathode. Pour la simulation de la cathode respirant l'air, une section de l'électrode est exposée à la température ambiante avec une concentration d'entrée égale à la concentration d'oxygène dans l'atmosphère ( $9,35 \text{ mol m}^{-3}$ ). Afin de faciliter la simulation numérique, une opération à débit constant avec une vitesse d'entrée unique de  $0,083 \text{ } \mu\text{L min}^{-1}$  a été établie au lieu d'utiliser un comportement transitoire.

### **Fabrication et évaluation de la cellule G2**

Deux configurations d'électrodes-microcanaux différentes ont été étudiées dans ce travail à travers le modèle obtenu. Les dispositions des électrodes sont représentées sur la Fig. 3.7 et décrites en détail dans la section 6.2. Par la suite, un nouveau MR- $\mu$ DMFC a été développé avec les caractéristiques optimales en fonction de la simulation numérique. Le dispositif microfluidique résultant est dénommé cellule G2 tout au long de ce travail. L'entrée de flux unique est positionnée à gauche de l'anode et le canal s'ouvre en forme de V jusqu'à rencontrer la longueur des électrodes (10 mm). Le volume résultant du microcanal est de  $56 \text{ } \mu\text{L}$  et les dimensions totales du dispositif sont indiquées sur la figure 3.8. Les pièces des plaques supérieure et inférieure ont ensuite été usinées sur du poly (méthacrylate de méthyle) de 2,5 mm (PMMA) par micro-usinage à commande numérique par ordinateur (CNC). Une coupe de 10 mm à 1,5 mm a été usinée sur la plaque inférieure comme fenêtre pour la cathode respirant l'air. Un séparateur (feuille de polyéthylène téréphtalate,  $200 \text{ } \mu\text{m}$  d'épaisseur) a été utilisé entre l'anode et la plaque inférieure, tandis que la couche d'étanchéité supérieure façonne le profil du microcanal. Les composants d'étanchéité étaient faits de couches Silastic™, d'une épaisseur de  $200 \text{ } \mu\text{m}$ . Un traceur de découpe a été utilisé pour obtenir le profil du microcanal, du séparateur et des joints. Les dimensions des électrodes sont de  $10 \text{ mm} \times 1,5 \text{ mm} \times 0,15 \text{ mm}$ . Les contacts électriques ont été réalisés avec des bandes de ruban de cuivre (SPI Supplies®). L'ensemble électrodes-microcanaux a été pris en sandwich entre les deux plaques en PMMA et l'ensemble a été serré par des vis mécaniques M1.6. La cellule G2 a été testée en utilisant  $56 \text{ } \mu\text{L}$  de MeOH 4 M dans une solution de KOH 0,5 M à température ambiante et en fonctionnement passif. La durabilité et la stabilité ont été évaluées en utilisant la technique de chronoampérométrie en appliquant 0,3 V pendant 6 h.

## **Développement d'une pile MR- $\mu$ DMFC à 4 cellules – Conception, fabrication et évaluation**

Une nouvelle pile MR- $\mu$ DMFC à 4 cellules a été développée à partir de la cellule unique G2. Les appareils se composent essentiellement de 4 cellules G2 unifiées dans un seul bloc. La description détaillée de la cheminée est présentée à la section 6.4. Les matériaux et les méthodes de fabrication de la pile à combustible sont les mêmes que ceux décrits à la section 3.5.2. Dans une première étape de test, 4 M de MeOH dans une solution de 0,5 M de KOH ont été fournis à la pile et chaque cellule a été évaluée individuellement en utilisant les mêmes conditions décrites pour la cellule G2 dans la section 3.5.3. Ensuite, les quatre cellules ont été connectées en série et en parallèle et les performances de l'appareil ont été testées. La stabilité des quatre cellules connectées en série a été évaluée en appliquant 1,2 V pendant 120 min.

### **Résultats et discussion**

#### **Caractérisation physicochimique de la cathode $Mn_2O_3/Pt/CP$**

La figure 5.1 montre des images SEM de matériaux Pt,  $Mn_2O_3$  et  $Mn_2O_3/Pt$  synthétisés par PLD sur CP. L'image de Pt/CP (Fig. 5.1a) montre les caractéristiques de la couche de Pt déposée sur le substrat. Ce film présente une surface rugueuse et une morphologie poreuse, typique des matériaux synthétisés à une pression de fond élevée en raison de l'interaction entre les espèces énergétiques dans le panache de plasma et le gaz inerte [81,170]. Ces observations sont cohérentes avec les films de Pt précédemment rapportés [171]. D'un autre côté, le film  $Mn_2O_3$  (Fig. 5.1b) présente une surface rugueuse, mais moins poreuse en raison de la pression de fond inférieure réglée pendant le dépôt. Une morphologie assez similaire est observée pour le matériau  $Mn_2O_3/Pt/CP$  (Fig. 5.1c), ce qui signifie que le film  $Mn_2O_3$  recouvre de manière homogène la couche de Pt en dessous. Une image SEM en coupe transversale du matériau bicouche (Fig. 5.1d) montre clairement les deux couches déposées sur une fibre CP, avec une épaisseur estimée à 25 nm pour chaque couche.

Les diffractogrammes XRD des dépôts Pt,  $Mn_2O_3$  et  $Mn_2O_3/Pt$  sont présentés à la Fig. 5.3. Le profil de l'échantillon Pt présente une structure cubique à faces centrées typique. La taille moyenne des cristallites, calculée par l'équation de Scherrer, était de 19 nm et le paramètre de réseau estimé à partir du pic Pt (111) était de 3,92 Å, ce qui est conforme à la norme Pt (JCPDS 04-0208). Des signaux du support carbone (marqués d'un (\*)) ont également été détectés. En revanche, dans le diffractogramme de l'échantillon  $Mn_2O_3$ , seuls les pics du support C ont été observés, ce qui suggère que le  $Mn_2O_3$  synthétisé par PLD est très probablement amorphe. En

ce qui concerne le matériau binaire  $\text{Mn}_2\text{O}_3/\text{Pt}$ , les plans cristallographiques (111), (200), (220) et (311) de Pt ont été observés mais avec une intensité considérablement inférieure à celle de l'échantillon de Pt, probablement en raison de la couche de  $\text{Mn}_2\text{O}_3$  sur le Pt. Tous les pics sont situés dans les mêmes positions précédemment décrites pour Pt/CP, suggérant qu'il n'y a pas d'interaction entre les couches Pt et  $\text{Mn}_2\text{O}_3$ .

Les spectres de balayage de l'inspection par XPS, présentés sur la figure 5.4, ont révélé que [Pt, C, O] et [Mn, C, O] sont les seuls éléments existant à la surface des matériaux Pt/CP et  $\text{Mn}_2\text{O}_3/\text{CP}$ , respectivement. Cependant, lors de l'analyse par sondage de l'échantillon binaire  $\text{Mn}_2\text{O}_3/\text{Pt/CP}$ , seuls les éléments Mn, C et O ont été facilement identifiés, tandis que les signaux de Pt ont été à peine observés, indiquant que le film de Pt est recouvert de manière homogène par la couche de  $\text{Mn}_2\text{O}_3$ . Le spectre XPS Pt 4f à haute résolution de base de Pt/CP est affiché sur la figure 5.5a. Le spectre présente un doublet composé d'une bande de basse énergie (Pt 4f7/2) et d'une bande de haute énergie (Pt 4f5/2) situées à 70,92 et 74,25, respectivement. Un ajustement satisfaisant a été obtenu en utilisant un seul composant avec un profil asymétrique. La position des pics Pt 4f7/2 et Pt 4f5/2 et la différence d'énergie de liaison (BE) de 3,33 eV entre eux sont cohérentes avec le platine à l'état métallique [164]. Sur la figure 5.5b, le spectre XPS de niveau de base Mn 3s haute résolution obtenu à partir de l'échantillon  $\text{Mn}_2\text{O}_3/\text{CP}$  est montré, car il a été signalé que l'analyse de la division par multiplets du pic Mn 3s est une méthode utile et fiable pour déterminer l'état d'oxydation de Mn [172,173]. Le fractionnement multiplet du pic Mn 3s se compose d'un pic d'énergie de liaison plus faible et d'un pic d'énergie de liaison plus élevé, situés à 83,40 et 88,90 eV, respectivement. La différence de 5,50 eV BE entre les 2 pics est cohérente avec Mn (III) dans  $\text{Mn}_2\text{O}_3$  [173,174]. Des résultats similaires ont été obtenus pour le matériau binaire  $\text{Mn}_2\text{O}_3/\text{Pt/CP}$ . L'analyse du pic de Mn 3s, représentée sur la figure 5.5c, a révélé que Mn se trouve sous la forme de  $\text{Mn}_2\text{O}_3$ , car la différence BE du fractionnement multiplet est de 5,5 eV. Après plusieurs balayages à haute résolution de la région Pt 4f, le doublet a été suffisamment enregistré pour être étudié (Fig. 5.5d). Les pics Pt 4f7/2 et Pt 4f5/2 étaient situés à 70,95 et 74,28 eV respectivement, et l'ajustement a été obtenu avec une seule composante asymétrique. La différence de 3,33 eV BE entre les pics indique que Pt se trouve à l'état métallique. Cette étude a confirmé que les films de Pt et de  $\text{Mn}_2\text{O}_3$  n'interagissent pas l'un avec l'autre, car l'état de valence du Pt et du Mn reste inchangé dans le matériau bicouche.

### **Caractérisation électrochimique de la cathode $\text{Mn}_2\text{O}_3/\text{Pt/CP}$**

Les figures 5.7a, b et c montrent les profils électrochimiques des catalyseurs Pt,  $\text{Mn}_2\text{O}_3$  et  $\text{Mn}_2\text{O}_3/\text{Pt}$ , respectivement, enregistrés à un taux de balayage de  $20 \text{ mV s}^{-1}$  dans une solution

KOH 0,5 M sans oxygène. Le voltammogramme cyclique obtenu à partir de Pt/CP (Fig. 5.7a) présente des caractéristiques bien définies d'une électrode Pt typique [176]. La figure 5.7b montre le profil électrochimique de  $\text{Mn}_2\text{O}_3/\text{CP}$ , qui, dans ces conditions, est caractérisé par l'apparition de plusieurs pics voltampérométriques associés à différents processus redox se produisant lors de la formation électrochimique de divers oxydes de manganèse [177,178]. Dans ce CV, différentes régions ont été identifiées selon des rapports similaires dans la littérature [177-180]. Les mêmes caractéristiques sont observées dans le profil électrochimique du catalyseur  $\text{Mn}_2\text{O}_3/\text{Pt}/\text{CP}$  (Fig. 5.7c) mais avec une densité de courant globalement plus élevée pour tous les processus redox. Notez que les caractéristiques de Pt sont masquées par celles du  $\text{Mn}_2\text{O}_3$ . Le pic de réduction de PtOx apparaît à un potentiel très proche de la formation de  $\text{Mn}_2\text{O}_3$  et  $\text{Mn}_3\text{O}_4$ , donc les caractéristiques plus larges dans la région entre 0,8 et 0,7 V. La région hydrogène est également légèrement observée dans le voltammogramme de l'électrode bicouche entre 0,2 et 0,4 V dans les analyses cathodiques et anodiques. Ces résultats indiquent que la couche de Pt est recouverte par la couche de  $\text{Mn}_2\text{O}_3$ , ce qui est en accord avec les analyses XRD et XPS.

#### **Performance de la cathode $\text{Mn}_2\text{O}_3/\text{Pt}/\text{CP}$ vers la RRO**

La figure 5.8a montre les voltammogrammes RRDE typiques obtenus à 400 rpm dans une solution de 0,5 M KOH saturée en  $\text{O}_2$  à une vitesse de balayage de  $10 \text{ mV s}^{-1}$ . On peut voir que la densité de courant à 0,9 V pour  $\text{Mn}_2\text{O}_3$  est de  $-0,17 \text{ mA cm}^{-2}$ , tandis que pour  $\text{Mn}_2\text{O}_3/\text{Pt}/\text{CP}$  elle est de  $-1,11 \text{ mA cm}^{-2}$ . Ce dernier est nettement similaire à la densité de courant pour Pt/CP, qui est de  $-1,15 \text{ mA cm}^{-2}$ . La quantité de peroxyde d'hydrogène produite aux catalyseurs Pt/CP et  $\text{Mn}_2\text{O}_3/\text{Pt}/\text{CP}$  est inférieure à 4% à tout moment, contrairement à  $\text{Mn}_2\text{O}_3/\text{CP}$ , où elle augmente de 22 à 28% lorsque le potentiel est balayé vers la direction cathodique. Comme le montre la figure 5.8b. Ces observations indiquent que le RRO sur Pt et les cathodes bicouches se déroule presque entièrement par la voie des quatre électrons. Cela a été confirmé par le calcul de  $n$  pour les trois catalyseurs. Comme le montre la figure 5.8c, la valeur moyenne  $n$  dans la plage de potentiel de 0,9 à 0,45 V est de 3,94 et 3,91 pour Pt/CP et  $\text{Mn}_2\text{O}_3/\text{Pt}/\text{CP}$ , respectivement. Il y a une légère diminution de  $n$  à des potentiels moins positifs, en raison de la réduction de l' $\text{O}_2$  sur le carbone, qui se produit à des surtensions plus élevées. Ces résultats révèlent que le revêtement  $\text{Mn}_2\text{O}_3$  n'affecte pas l'activité catalytique de la couche inférieure de Pt, car le nombre d'électrons transférés est pratiquement le même que celui obtenu pour le catalyseur Pt ( $3,9 \text{ e}^-$ ), qui est proche de la valeur théorique de 4 électrons. Ce qui précède suggère que la RRO sur le catalyseur bicouche est effectivement réalisée sur la couche interne de Pt, alors que la couche externe de  $\text{Mn}_2\text{O}_3$  ne participe pas ou a un effet négligeable sur les performances RRO du Pt dans ces

conditions. Une explication possible est que les molécules d'oxygène sont capables de diffuser à travers la couche poreuse de  $\text{Mn}_2\text{O}_3$  et de réagir au Pt, un phénomène précédemment étudié dans une coquille de Ru poreuse avec un noyau en Pt [80].

### **Sélectivité de la cathode $\text{Mn}_2\text{O}_3/\text{Pt}/\text{CP}$ vers la RRO et tolérance au méthanol**

En premier, l'activité catalytique des électrodes Pt,  $\text{Mn}_2\text{O}_3$  et  $\text{Mn}_2\text{O}_3/\text{Pt}$  vers la ROM a été étudiée. La figure 5.9a montre les CV enregistrés dans une solution sans oxygène 1 M MeOH + 0,5 M KOH. Dans le cas du Pt, le pic typique de l'oxydation du méthanol [181], à partir de 0,44 V est observé, confirmant l'activité du Pt/CP vers la ROM. Cependant, pour les électrodes  $\text{Mn}_2\text{O}_3/\text{CP}$  et  $\text{Mn}_2\text{O}_3/\text{Pt}/\text{CP}$ , les profils CV obtenus sont pratiquement les mêmes que ceux acquis dans une solution sans méthanol (voir Fig. 5.7b et 5.7c). Ce résultat démontre que  $\text{Mn}_2\text{O}_3$  n'est pas actif vis-à-vis de la ROM et indique en outre qu'après le revêtement de Pt avec la couche de  $\text{Mn}_2\text{O}_3$ , l'adsorption de méthanol sur Pt est bloquée. Ensuite, l'électroactivité des trois catalyseurs vers la RRO en absence et en présence de MeOH a été étudiée par LSV à  $5 \text{ mV s}^{-1}$ . À partir des voltammogrammes obtenus dans une solution de KOH 0,5 M saturée en oxygène (Fig. 5.9b), il est observé que le potentiel de début de la RRO sur Pt/CP est situé à 0,97 V. Par contre, un potentiel de début moins positif de la RRO (0,89 V) ainsi qu'une plus faible densité de courant de crête ont été observées pour l'électrode  $\text{Mn}_2\text{O}_3/\text{CP}$  en raison d'une surtension plus élevée, en comparaison avec Pt/CP. En accord avec la figure 5.8, le catalyseur bicouche  $\text{Mn}_2\text{O}_3/\text{Pt}/\text{CP}$  présente une activité très similaire à celle de Pt/CP, car les courbes se chevauchent pratiquement. On observe que le potentiel d'apparition de la RRO est identique dans les deux systèmes et, en outre, la vitesse de réaction est apparemment la même. Afin de comparer ces résultats avec l'activité vers la RRO en présence de MeOH, la figure 5.9c montre les voltammogrammes linéaires obtenus dans une solution de 0,5 M KOH saturée en oxygène contenant 1 M de MeOH. D'après les courbes, il est évident que la RRO sur Pt/CP est complètement inhibé en raison de la ROM dans un événement compétitif, qui est le comportement attendu d'une électrode Pt. D'autre part, les catalyseurs  $\text{Mn}_2\text{O}_3/\text{CP}$  et  $\text{Mn}_2\text{O}_3/\text{Pt}/\text{CP}$  effectuent clairement la RRO, et les caractéristiques des courbes indiquent une activité similaire à celle des systèmes sans méthanol, c'est-à-dire pratiquement le même potentiel de démarrage du RRO et la même densité de courant que ceux illustrés dans Fig. 5.9b. Une hypothèse expliquant ces observations pourrait être proposée sur la base du volume moléculaire des molécules d'oxygène et de méthanol. Le volume d' $\text{O}_2$  est de  $26,8 \text{ \AA}^3$  tandis que pour MeOH est de  $41,6 \text{ \AA}^3$ . Ainsi, les molécules d'oxygène diffuseraient plus facilement à travers la couche poreuse de  $\text{Mn}_2\text{O}_3$  et réagiraient à la surface du Pt, car comme indiqué, la RRO est plus favorable

sur Pt que sur  $\text{Mn}_2\text{O}_3$ . D'un autre côté, les molécules de méthanol de plus grande taille moléculaire sont gênées sur la couche superficielle de  $\text{Mn}_2\text{O}_3$ , ce qui explique pourquoi l'oxydation du méthanol n'est pas effectuée au niveau du catalyseur bicouche. Par conséquent, l'inhibition de la ROM sur  $\text{Mn}_2\text{O}_3/\text{Pt}/\text{CP}$  est attribuée à  $\text{Mn}_2\text{O}_3$  et en conséquence, le processus entre la ROM et la RRO devient un événement non compétitif. Remarquablement, même à une concentration de méthanol aussi élevée que 5 M, la cathode  $\text{Mn}_2\text{O}_3/\text{Pt}/\text{CP}$  est restée tolérante à l'oxydation du méthanol, car le décalage négatif sur le potentiel d'apparition du RRO n'était que de 19 mV, tandis que la densité de courant n'a diminué que de 15% en comparaison avec 0 M MeOH, comme le montre la figure 5.9d.

### **Performance de la cathode $\text{Mn}_2\text{O}_3/\text{Pt}/\text{CP}$ dans une pile à combustible**

Les figures 5.10a et 5.10b montrent les performances du ML- $\mu$ DMFC obtenu avec un fonctionnement à 2 flux et des conditions de réactifs mixtes, respectivement. On observe que dans tous les cas, les piles à combustible fonctionnant avec 2 flux (réactifs séparés) présentaient une OCV légèrement plus élevée, 20 mV en moyenne pour chaque concentration, par rapport à l'opération de réactifs mixtes. De même, la densité de courant maximale atteinte par la pile à combustible avec des réactifs séparés est légèrement plus élevée ( $6 \text{ mA cm}^{-2}$ ) à toutes les concentrations de méthanol par rapport à l'opération de réactifs mixtes. Fait intéressant, la densité de puissance maximale obtenue avec la pile à combustible dans des conditions de réactifs mixtes était supérieure à celle générée par la pile à combustible à 2 flux. Cela a été observé pour des concentrations de méthanol dans la plage de 1 à 4 M, tandis qu'avec 5 M, la valeur de densité de puissance de crête est assez similaire dans les deux cas. De la courbe de polarisation des piles à combustible, il est possible de déduire que ce comportement est clairement dû à la région ohmique de la courbe. Dans tous les cas, on observe que la pile à combustible à réactifs mixtes présente des pertes ohmiques plus faibles que la pile à combustible fonctionnant avec 2 flux. La différence est peut-être due au manque d'interface anolyte-catholyte dans la pile à combustible à réactifs mixtes, ce qui contribue à une résistance globale à l'électrolyte plus faible, résultant en une pile à combustible plus performante. Par conséquent, le concept MR- $\mu$ DMFC est une alternative viable à la pile à combustible microfluidique typique. La stabilité de la pile à combustible dans des conditions de réactifs mixtes a été évaluée par chronoampérométrie à 0,35 V pendant 2 h en utilisant une solution de 4 MeOH dans 0,5 M de KOH. La courbe  $i-t$  est représentée sur la figure 5.11, où un comportement stable est observé. En moyenne, la pile à combustible a produit  $15 \text{ mA cm}^{-2}$ , démontrant une stabilité à court terme dans des conditions de réactifs mixtes.

## **Développement d'un empilement de piles à combustible microfluidique à réactifs mixtes**

### **Validation du modèle**

Après avoir obtenu le modèle mathématique, les données ont été validées en comparant une courbe de polarisation simulée avec une courbe expérimentale. La figure 6.2 montre les courbes de polarisation et de puissance obtenues avec la cellule G1 et à partir de la simulation numérique, dans les deux cas avec 4 M MeOH. Il est clair que le modèle est en accord avec l'expérience, car les performances observées dans les deux cas sont pratiquement les mêmes. La différence de densité de puissance de crête entre les deux courbes n'est que de  $0,57 \text{ mW cm}^{-2}$ . Cela indique que le modèle est précis et qu'il peut être utilisé pour étudier de nouveaux systèmes de piles à combustible ayant des caractéristiques similaires, telles que les dimensions des électrodes et la charge des catalyseurs. Par conséquent, le modèle a été appliqué pour développer l'évolution de la cellule G1, dénommée systématiquement cellule G2.

### **Développement de la cellule G2**

Deux configurations d'électrodes-microcanaux différentes ont été étudiées dans ce travail, où la principale différence entre elles est notablement la position des électrodes. Dans la première configuration (Fig. 6.3a), les électrodes sont dans le même plan, comparable à une géométrie en bande-cellule [61] d'une manière similaire à la cellule G1 et d'autres travaux dans la littérature [149,184,185]. D'autre part, la deuxième configuration introduit une nouvelle architecture avec un séparateur qui permet de placer la cathode dans un plan parallèle sous le plan anodique (Fig. 6.3b), modifiant ainsi la disposition des microcanaux. Les deux différents arrangements électrodes-microcanaux ont été analysés par le modèle nouvellement obtenu. Les courbes de polarisation et de puissance simulées pour les deux systèmes sont représentées sur la figure 6.4a. On observe que la conception des piles à combustible avec des électrodes dans des plans parallèles présente une performance supérieure théorique. Selon la simulation, avec cette configuration, il est possible d'obtenir 50% de densité de courant en plus et 20% de densité de puissance en plus, par rapport à la configuration avec des électrodes dans le même plan. De plus, l'utilisation du combustible a été calculée pour les deux conceptions à différentes valeurs de tension de cellule. Les résultats indiquent qu'une utilisation du carburant considérablement plus élevée peut être obtenue avec des électrodes dans des plans parallèles, atteignant jusqu'à 74%, contrairement à 55% obtenus avec des électrodes dans le même plan.

L'explication de la différence de performance peut être trouvée à travers de la simulation de flux. La figure 6.5 montre le courant de carburant et d'électrolyte à l'intérieur du microcanal des deux

conceptions de piles à combustible. La simulation a révélé que, dans le cas de la cellule avec des électrodes dans le même plan (Fig.6.5, en haut), une région turbulente est générée autour de la cathode, en raison de la porosité de l'électrode en conjonction avec les fenêtres de respiration d'air. On observe qu'après avoir mouillé la cathode, le fluide a tendance à sortir du microcanal à travers les fenêtres créant une zone d'inondation qui entrave le flux d'air de l'atmosphère vers la cathode. En revanche, la conception avec des électrodes dans des plans parallèles (Fig. 6.5, en bas) ne présente pas ce problème. Étant donné que le flux peut s'écouler sans turbulence sur la cathode, la fenêtre unique pour respirer l'air au fond reste non obstruée et l'air peut circuler librement et réagir à la cathode. Sur la base de ces résultats, la proposition d'électrodes dans différents plans est le choix évident vers le développement d'une pile à combustible microfluidique à réactifs mixtes plus efficace.

Afin d'augmenter encore les performances des piles à combustible, l'effet de la séparation anode-cathode a été analysé. Trois valeurs de distance ont été considérées (3 mm, 1,5 mm et 0,3 mm). La figure 6.6b montre les courbes de polarisation et de densité de puissance simulées. Une augmentation constante des performances est observée lorsque la distance entre les électrodes se raccourcit. À 3 mm, la densité de courant maximale est de  $130 \text{ mA cm}^{-2}$ . Cela augmente à  $142 \text{ mA cm}^{-2}$  à 1,5 mm et monte jusqu'à  $154 \text{ mA cm}^{-2}$  à 0,3 mm, ce qui est expérimentalement la limite inférieure pour la séparation des électrodes. De même, la densité de puissance maximale passe de  $20 \text{ mW cm}^{-2}$  à  $24 \text{ mW cm}^{-2}$  pour 3 mm et 0,3 mm, respectivement, ce qui est en accord avec l'équation (94). De plus, l'utilisation du combustible a été calculée en fonction de la tension de cellule appliquée. La figure 6.6c montre que l'utilisation maximale du combustible est atteinte sur la pile à combustible avec la distance la plus courte entre les électrodes. Selon la simulation, l'utilisation de carburant la plus élevée possible pour l'arrangement initial est de 74%, et elle augmente jusqu'à 81% à une séparation d'électrode de 0,3 mm. La figure 6.5d montre les profils de combustible à l'anode calculés en fonction du potentiel appliqué, obtenus pour une cellule avec une distance entre les électrodes de 0,3 mm. Comme on peut le constater sur les profils, le carburant n'est pas réapprovisionné par le flux, du fait de son très faible débit (fonctionnement passif dans une vraie pile à combustible). Par conséquent, une consommation de carburant plus élevée est favorisée au niveau de l'électrode poreuse, étant plus visible à gauche de l'anode où la baisse de concentration est plus prononcée à des valeurs de potentiel plus faibles. Les résultats rapportés sur la figure 6.6 ont été pris en compte pour l'optimisation de la cellule G2 et donc la séparation des électrodes dans la conception finale est de 0,3 mm. Le dispositif résultant est illustré à la Fig. 6.7a.

## **Performance de la cellule G2**

La figure 6.8a montre la courbe de polarisation expérimentale obtenue à partir de la cellule G2 nouvellement développée et la comparaison des performances avec la cellule G1, toutes deux employant 4 M MeOH dans 0,5 M KOH en fonctionnement passif. Bien que la couche de catalyseur à la cathode soit absolument exposée au carburant dans l'électrolyte, la cellule G2 génère un OCV de 0,8 V, qui est une valeur représentative des DMFC [100, 189, 190]. Cela indique que le croisement de méthanol n'affecte pas les performances des électrodes et que la ROM et la RRO se produisent uniquement à l'anode et à la cathode, respectivement. Ce système a atteint une densité de courant maximale de  $150 \text{ mA cm}^{-2}$  et une densité de puissance de pointe de  $28 \text{ mW cm}^{-2}$ . Le profil de tension de la cellule présente une chute brutale de tension au début de la courbe, en raison de la perte d'activation de l'anode et de la cathode, typique des DMFC [22,191]. En se concentrant sur la région ohmique de la courbe de polarisation, il convient de souligner que la perte ohmique est sensiblement plus petite par rapport à la cellule G1. Étant donné que la résistance ionique a tendance à dominer la résistance électronique, l'amélioration marquée résulte de la réduction de la distance entre les électrodes, diminuant ainsi la résistance globale de la pile à combustible. En comparaison avec la courbe de polarisation théorique de la cellule G2 (figure 6.8b), l'expérience a donné une performance légèrement supérieure, avec une densité de puissance de pointe de  $28 \text{ mW cm}^{-2}$  contre  $24 \text{ mW cm}^{-2}$  pour la simulation. L'OCV et la densité de courant maximale sont pratiquement les mêmes dans les deux cas, donc le modèle peut être considéré comme précis. En ce qui concerne la zone de transfert de masse, aucune perte significative n'a été observée en raison de l'utilisation d'une concentration élevée de MeOH et de la régénération constante d' $\text{O}_2$  de l'air à la cathode [149]. Le test de stabilité de la pile à combustible est illustré sur la figure 6.8c. Une mesure chronoampérométrique a été réalisée à 300 mV pendant 6 h. La valeur moyenne de la densité de courant obtenue à partir du dispositif était de  $15 \text{ mA cm}^{-2}$ , confirmant ainsi la stabilité de la cellule G2 dans cette période. Une comparaison des performances de différents DMFC microfluidiques est présentée dans le tableau 6.2. A partir de cette comparaison, on peut observer que dans des conditions similaires (électrolyte, concentration en carburant, température), la cellule G2 présente les performances les plus fortes.

## **Développement et performances d'une pile MR- $\mu$ DMFC à 4 cellules**

Une pile à combustible microfluidique a été développée à partir de la pile à combustible à réactifs mixtes G2. Tous les composants, l'assemblage et une photographie du dispositif fabriqué sont illustrés à la Fig. 6.9. La pile se compose de 4 cellules G2 incorporées dans un seul appareil

intégré. Les piles à combustible sont disposées de façon série, c'est-à-dire qu'il n'y a qu'une seule entrée au début du chemin pour la cellule 1. La sortie de la cellule 1 devient alors l'entrée de la cellule 2, qui à son tour conduit à la cellule 3 jusqu'à atteindre par la suite cellule 4. Cette conception simplifie la livraison du réactif aux cellules individuelles et les connexions électriques entre elles. De plus, il permet d'optimiser les dimensions du dispositif en réduisant la quantité de composants typiquement nécessaires dans une pile à combustible. Le volume total du microcanal dans la pile à 4 cellules est de 234  $\mu\text{L}$ . Puisqu'aucun système de pompes n'est nécessaire, l'appareil résultant a une empreinte de pas de 22,5  $\text{cm}^2$  et il occupe un volume total de 12,6  $\text{cm}^3$ . Étant une pile à combustible très compacte, il est théoriquement possible d'obtenir une puissance plus élevée par unité de volume total [65,66], ce qui est souhaitable pour tout type de système de conversion d'énergie. Afin d'équilibrer la pression entre les cellules et de minimiser le courant de dérivation, un champ d'écoulement en serpentin (20,75 mm de longueur  $\times$  500  $\mu\text{m}$  de largeur) a été conçu. La serpentine, placée entre la sortie et l'entrée des cellules adjacentes, génère une résistance ionique suffisamment élevée et empêche un court-circuit dans l'appareil provoqué par la conductivité de l'électrolyte.

Pour étudier les performances de la pile MR- $\mu\text{DMFC}$ , les quatre cellules ont d'abord été testées individuellement. La figure 6.10a montre les courbes de polarisation et de puissance obtenues à partir de chaque cellule en utilisant 4 M de MeOH dans 0,5 M de KOH. Dans tous les cas, l'OCV se situe entre 0,77 et 0,80 V, ce qui est dans les valeurs observées dans la cellule G2 unique. Cependant, une tendance émerge lorsque l'on regarde la densité de courant maximale et la densité de puissance de crête de chaque cellule. Ces deux valeurs diminuent au fur et à mesure que nous passons de la cellule 1 à 4. Afin d'expliquer ce phénomène, les profils de combustible de toutes les cellules de la cheminée ont été étudiés à une tension de cellule proche de l'OCV. La simulation a révélé une relation dépendante entre la concentration de carburant et la longueur du trajet de carburant. Sur la figure 6.10b, on peut observer qu'une légère quantité, moins de 1 M de carburant est consommée lors de son écoulement de la cellule 1 à 4. Par conséquent, chaque cellule a moins de combustible réactif que la cellule précédente, ce qui entraîne une densité de courant et de puissance inférieure. Sur la base de ce résultat, il est possible de déduire que bien qu'il semble intuitif d'ajouter plus de cellules dans le chemin série, ce serait une mesure contre-productive pour obtenir une performance de pile stable. Ensuite, nous avons évalué l'empilement avec les quatre cellules connectées électriquement en série et en parallèle (schéma de circuit sur la figure 6.11) et l'efficacité de la connexion a été calculée selon l'équation (95) [203].

Les performances de la pile sans normalisation de courant et de puissance sont affichées sur la figure 6.12, ainsi que les performances de la cellule 1 à des fins de comparaison. La figure 6.12a montre la courbe de polarisation obtenue en connexion parallèle, qui présente un OCV de 0,78 V et une sortie de courant maximale de 5,8 mA, tandis qu'une puissance de crête de 1,3 mW a été atteinte. Ces valeurs représentent une efficacité de 73,80%. Les pertes d'efficacité sont, dans une plus large mesure, la conséquence des différences de performances des cellules [22]. De plus, les interconnexions microfluidiques fournissent probablement des connexions électriques indésirables entre les cellules unitaires, entraînant des courants parasites. La serpentine entre les cellules est censée diminuer cet effet, cependant, les gradients de potentiel inter-cellules générés par les processus d'électrodes sont capables de conduire les courants ioniques à travers le fluide, provoquant des pertes d'énergie [163,203,204]. Il en va de même pour la courbe de polarisation obtenue en connexion en série, illustrée sur la figure 6.12b, qui présente une OCV de 2,46 V et une sortie de courant maximale de 2,7 mA, tandis qu'une puissance de crête de 1,1 mW a été obtenue avec une connexion d'efficacité de 64,23%. La stabilité de la pile MR- $\mu$ DMFC a été évaluée en connexion série à 1,2 V pendant 2 h. La courbe chronoampérométrique, représentée sur la figure 6.12c, présente un comportement stable pendant cette fenêtre temporelle avec une densité de courant moyenne de 0,23 mA.

Enfin, afin de démontrer les capacités potentielles de cette pile MR- $\mu$ DMFC vers des applications pratiques, l'appareil a été utilisé comme alimentation pour une LED (Fig. 6.13). Les quatre cellules de la pile ont été connectées en série pour répondre aux exigences de tension et l'ensemble a été directement connecté à la LED. Comme on peut l'observer sur la photo, l'appareil est capable de fonctionner dans des conditions proches de l'application réelle, c'est-à-dire à température ambiante et en mode passif dans un emballage compact. Ce test a démontré que la pile MR- $\mu$ DMFC est non seulement capable d'alimenter la LED, mais elle maintient également un fonctionnement constant pendant au moins 4 h (Fig. 6.14) avec une seule charge de 234  $\mu$ L de solution de réactif. Il est à noter que l'utilisation d'une cathode sélective et le concept de pile à combustible à réactifs mixtes ont permis de développer un système très compact et performant avec moins de composants et un fonctionnement plus simple que la plupart des piles à combustible. Ce qui précède est un exploit remarquable et un pas en avant vers le développement de piles à combustible plus efficaces. Nous reconnaissons que les performances du dispositif pourraient être encore améliorées en effectuant une séparation plus efficace entre les cellules unitaires pour minimiser les pertes dues aux courants parasites. Il peut également être nécessaire de mettre en œuvre une méthode d'assemblage garantissant que toutes les cellules de la pile se

comportent de manière équivalente. En outre, la simulation numérique peut être utilisée pour optimiser la fenêtre de respiration de l'air, un élément crucial de ce type de pile à combustible, car la structure du flux d'air joue un rôle clé dans l'efficacité de la cathode [88,205,206] et donc dans les performances globales de la pile à combustible. En cas de succès, ces augmentations de performances positionneraient les piles à combustible microfluidiques à réactifs mixtes comme un candidat viable et rentable pour la prochaine génération d'appareils portables.



# TABLE OF CONTENTS

---

ACKNOWLEDGMENTS.....	iii
ABSTRACT.....	v
RESUME .....	vii
SYNOPSIS .....	ix
TABLE OF CONTENTS .....	xxxiii
LIST OF FIGURES .....	xxxvii
LIST OF TABLES.....	xlili
LIST OF ABBREVIATIONS.....	xliv
CHAPTER 1 INTRODUCTION.....	1
1.1 General introduction.....	1
1.2 Justification.....	13
1.3 Objectives.....	14
CHAPTER 2 LITERATURE REVIEW.....	15
2.1 Fuel cell fundamentals .....	15
2.1.1 Thermodynamics .....	20
2.1.2 Kinetics.....	23
2.1.3 Charge transport.....	29
2.1.4 Mass transport.....	33
2.2 Types of fuel cells .....	37
2.2.1 Proton-exchange membrane fuel cell (PEM-FC).....	38
2.2.2 Membraneless microfluidic fuel cell (ML- $\mu$ FFC) .....	39
2.2.3 Mixed-Reactant fuel cell (MRFC) .....	42
2.2.4 Direct methanol fuel cell (DMFC) .....	45
2.2.5 MR- $\mu$ DMFC .....	46
2.3 Oxygen Reduction Reaction (ORR) .....	46
2.3.1 ORR in Alkaline media.....	47
2.4 Methanol Oxidation Reaction (MOR) .....	49
2.4.1 MOR in acidic and alkaline media.....	50
2.5 Methanol-tolerant catalysts for ORR .....	52
2.6 Synthesis methods.....	54
2.6.1 Pulsed Laser Deposition (PLD).....	55

2.7	Material characterization: Physicochemical techniques.....	57
2.7.1	Scanning Electron Microscopy (SEM).....	57
2.7.2	X-Ray Diffraction (XRD).....	59
2.7.3	X-Ray Photoelectron Spectroscopy (XPS).....	60
2.7.4	Neutron Activation Analysis (NAA).....	61
2.8	Material characterization: Electrochemical techniques.....	62
2.8.1	Cyclic Voltammetry (CV).....	62
2.8.2	Linear Scan Voltammetry (LSV).....	64
2.8.3	Chronoamperometry (CA).....	64
2.8.4	Rotating Ring Disk Electrode (RRDE).....	65
CHAPTER 3 METHODOLOGY.....		69
3.1	Synthesis.....	69
3.1.1	Substrate.....	69
3.1.2	Catalytic materials.....	70
3.1.5	Experimental conditions.....	70
3.2	Physicochemical characterization.....	72
3.3	Electrochemical characterization.....	73
3.4	Fuel cell testing.....	74
3.5	Development of a new MR- $\mu$ DMFC.....	76
3.5.1	Numerical methodology and model definition.....	76
3.5.2	Fabrication of Cell G2.....	82
3.5.3	Test of the single cell.....	84
3.6	Development of a 4-cell MR- $\mu$ DMFC stack.....	84
3.6.1	Test of the stack.....	84
CHAPTER 4 RESULTS: Ag/Pt/CP CATHODE.....		87
4.1	Physicochemical characterization.....	87
4.2	Electrochemical characterization.....	90
4.3	ORR performance.....	92
4.4	Selectivity of the Ag/Pt/CP cathode towards the ORR and methanol tolerance.....	93
4.5	Fuel cell performance.....	95
CHAPTER 5 RESULTS: Mn <sub>2</sub> O <sub>3</sub> /Pt/CP CATHODE.....		99
5.1	Physicochemical characterization.....	99
5.2	Electrochemical characterization.....	105
5.3	ORR performance.....	106

5.4	Selectivity of the Mn <sub>2</sub> O <sub>3</sub> /Pt/CP cathode towards the ORR and methanol tolerance ...	108
5.5	Fuel cell performance .....	110
CHAPTER 6 RESULTS: DEVELOPMENT OF A MIXED-REACTANT MICROFLUIDIC FUEL CELL STACK.....		113
6.1	Validation of the model .....	113
6.2	Development of Cell G2.....	115
6.3	Performance of cell G2 .....	120
6.4	Development and performance of a 4-cell MR- $\mu$ DMFC stack.....	123
CONCLUSIONS.....		129
PERSPECTIVES .....		131
REFERENCES .....		133
APPENDIX I.....		151
APPENDIX II.....		157



## LIST OF FIGURES

---

Figure 1.1	Ragone plot showing performance comparison of different types of batteries [20].	2
Figure 1.2	Ragone plot showing performance comparison of various energy storage devices [24].	3
Figure 1.3	Types of fuel cells.	4
Figure 1.4	Main components of a PEM-FC	7
Figure 1.5	Principle of membraneless fuel cell	9
Figure 1.6	Main microfluidic fuel cells architectures developed to date: a) monolithic flow-by cell with electrodes on floor, monolithic cell with electrodes on walls, c) air-breathing flow-by cell, d) monolithic flow-through cell and d) monolithic dual-pass flow through cell [5].	9
Figure 1.7	Representation of a simple channel layout and components of a MRFC.	11
Figure 2.1	Schematic comparison of electrical energy generation of fuel cells, batteries and combustion engines.	15
Figure 2.2	a) Schematic comparison of fuel cells and batteries systems and b) relation between power and capacity in batteries and fuel cells (Adapted from [22]).	16
Figure 2.3	Illustration of the main components of fuel cells and the major steps for electrochemical generation of electricity: (1) reactant transport, (2) electrochemical reaction, (3) ionic and electronic conduction and (4) product removal (Adapted from [22]).	18
Figure 2.4	A typical fuel cell i-V curve	19
Figure 2.5	A typical fuel cell power density curve	20
Figure 2.6	Activation barrier ( $\Delta G^\ddagger$ ) impedes the conversion of products to reactants.	24
Figure 2.7	Effect of reducing the Galvani potential on the size of the forward and reverse activation barriers (Adapted from [22]).	27
Figure 2.8	Effect of activation overpotential on fuel cell performance.	28
Figure 2.9	Effect of ohmic loss on fuel cell performance.	31
Figure 2.10	The total ohmic resistance of a fuel cell is the sum of all the components resistances in series.	32
Figure 2.11	Schematic of diffusion layer that develops at the anode of a fuel cell. $C^0$ and $C^*$ represent concentration at the bulk and at the catalyst layer, respectively (Adapted from [22]).	34
Figure 2.12	Time dependence of reactant and product concentration profiles at fuel cell electrode (Adapted from [22]).	35
Figure 2.13	Effect of concentration loss on fuel cell performance.	37
Figure 2.14	Schematic of PEM-FC main components [95].	38

Figure 2.15	Schematic of the co-laminar flow based fuel cell presented by Choban et al. [33]. .....	40
Figure 2.16	Primary co-laminar flow fuel cells developments: a) monolithic with electrodes on floor, b) monolithic with electrodes on walls, c) F-channel with air-breathing cathode and d) monolithic with flow-through electrodes [97]. .....	42
Figure 2.17	Mixed-reactant strip cell concept [61]. .....	44
Figure 2.18	Cross-section of construction of the 2-cell Swiss-roll MRFC [65]. .....	44
Figure 2.19	Illustration of double-layer structure during ORR in alkaline media. Insets (a, b) illustrate the inner and outer sphere electro transfer processes [109]. .....	48
Figure 2.20	Simplified pathway for methanol oxidation [113]. .....	50
Figure 2.21	Illustration of differential diffusion of oxygen and methanol in cage-bell structure Pt-Ru nanoparticles [80]. .....	53
Figure 2.22	Left panel: Schematic illustration of single beam PLD setup. Right panel: Description of the PLD process. .....	57
Figure 2.23	Signals generated form the interaction between electron beam and specimen under study in SEM. ....	58
Figure 2.24	Diffraction of X-ray by parallel planes of atoms in a crystalline material [139].	59
Figure 2.25	Schematic diagram of the working principle of XPS [141,142]. .....	61
Figure 2.26	Schematic diagram of the process of neutron capture, followed by radioactive decay and gamma radiation [144]. .....	62
Figure 2.27	a) Potential-time wave applied for CV, and b) resulting current-potential curve (cyclic voltammogram). .....	63
Figure 2.28	a) Typical waveform of CA, and b) current-time response. ....	64
Figure 2.29	a) Typical waveform of a voltammogram in RRDE, and b) resulting current-potential curve. ....	65
Figure 2.30	a) RRDE cross-section and top view, and b) streamlines during operation. ....	66
Figure 2.31	Typical curves obtained from the ferricyanide/ferrocyanide system at a RRDE. .. .....	67
Figure 3.1	Illustration of the bilayer structure of the catalyst synthesized on this work. ....	69
Figure 3.2	SEM image of the carbon paper substrate. ....	70
Figure 3.3	Schematic representation of the components and assembly of the microfluidic fuel cell G1 (1-Pogo pin, 2-Screw, 3-Top PMMA plate, 4-Porous electrodes, 5-Microchannel and 6-Bottom PMMA plate) and b) flow of reactants in the microchannel.....	74

Figure 3.4	a) Flow simulation of cell G1 in a typical 2 stream configuration and b) reactant profiles. ....	75
Figure 3.5	Cell G1 in a) 2 stream configuration and b) mixed-reactant configuration .....	76
Figure 3.6	Impedance spectra recorded for cell G1 at OCV.....	80
Figure 3.7	Representation of the two different electrode arrangements. The components are not to scale. ....	82
Figure 3.8	Representation of components and assembly of cell G2, developed after numerical simulation. ....	83
Figure 3.9	CNC machine used for the fabrication of the devices.....	83
Figure 4.1	SEM images of a) Pt/CP, b) Ag/CP and c) Ag/Pt/CP. (a' b', c') corresponding higher magnifications, and (a'', b'', c'') corresponding cross-section images. ....	87
Figure 4.2	XRD patterns of Pt/CP, Ag/CP and Ag/Pt/CP. (*) Carbon.....	88
Figure 4.3	XPS survey scans of Pt/CP, Ag/CP and Ag/Pt/CP. ....	89
Figure 4.4	High-resolution XPS core-level spectra of Pt 4f in Pt/CP, Ag 3d in Ag/CP and Ag 3d in Ag/Pt/CP. ....	90
Figure 4.5	Electrochemical profiles of a) Pt/CP, b) Ag/CP and c) Ag/Pt/CP catalysts recorded by CV at 20 mV s <sup>-1</sup> scan rate in 0.5 M KOH oxygen free solution.....	91
Figure 4.6	RRDE voltammograms of Pt/CP, Ag/CP and Ag/Pt/CP acquired in O <sub>2</sub> saturated 0.5 M KOH solution at 400 rpm, b) H <sub>2</sub> O <sub>2</sub> yield, c) electron transfer number (n) and d) Tafel plots. ..	93
Figure 4.7	Electroactivity towards a) MOR in oxygen-free 1 M MeOH in 0.5 M KOH solution, b) ORR in oxygen-saturated 0.5 M KOH solution, c) ORR in oxygen-saturated 0.5 M KOH + 1 M MeOH, and d) ORR at Ag/Pt/CP cathode in oxygen-saturated 0.5 M KOH containing 0–5 M MeOH. ....	95
Figure 4.8	Polarization curves (full symbols) and power density curves (open symbols) obtained during the operation of the passive ML- $\mu$ DMFC in a) typical 2-stream configuration and b) under mixed-reactant operation using different concentrations of MeOH, c) OCV, current density and power density values extracted from Fig. 4.8 a and b.....	96
Figure 4.9	Chronoamperometric curve obtained at 0.35 V for the study of the stability of the ML- $\mu$ DMFC using 3 M MeOH.....	97
Figure 5.1	SEM images of a) Pt/CP, b) Mn <sub>2</sub> O <sub>3</sub> /CP, c) Mn <sub>2</sub> O <sub>3</sub> /Pt/CP and d) Cross-section of Mn <sub>2</sub> O <sub>3</sub> /Pt/CP. ....	99
Figure 5.2	EDS elemental mapping of Mn <sub>2</sub> O <sub>3</sub> /Pt/CP. ....	100
Figure 5.3	XRD patterns of Pt/CP, Mn <sub>2</sub> O <sub>3</sub> /CP and Mn <sub>2</sub> O <sub>3</sub> /Pt/CP.....	101

Figure 5.4	XPS survey scans of Pt/CP, Mn <sub>2</sub> O <sub>3</sub> /CP and Mn <sub>2</sub> O <sub>3</sub> /Pt/CP. ....	102
Figure 5.5	High-resolution XPS core-level spectra of a) Pt 4f in Pt/CP, b) Mn 3s in Mn <sub>2</sub> O <sub>3</sub> /CP, c) Mn 3s in Mn <sub>2</sub> O <sub>3</sub> /Pt/CP and d) Pt 4f in Mn <sub>2</sub> O <sub>3</sub> /Pt/CP.....	104
Figure 5.6	High-resolution XPS core-level spectra of Mn 2p in Mn <sub>2</sub> O <sub>3</sub> /CP(left) and Mn 2p in Mn <sub>2</sub> O <sub>3</sub> /Pt/CP (right). ....	105
Figure 5.7	Electrochemical profiles of a) Pt/CP, b) Mn <sub>2</sub> O <sub>3</sub> /CP and c) Mn <sub>2</sub> O <sub>3</sub> /Pt/CP, obtained in 0.5 KOH oxygen-free solution at 20 mV s <sup>-1</sup> scan rate.....	106
Figure 5.8	RRDE voltammograms of Pt/CP, Mn <sub>2</sub> O <sub>3</sub> /CP and Mn <sub>2</sub> O <sub>3</sub> /Pt/CP acquired in O <sub>2</sub> saturated 0.5 M KOH solution at 400 rpm, b) H <sub>2</sub> O <sub>2</sub> yield, c) electron transfer number (n) and d) Tafel plots. ....	108
Figure 5.9	Electroactivity towards a) MOR in oxygen-free 1 M MeOH in 0.5 M KOH solution, b) ORR in oxygen-saturated 0.5 M KOH solution, c) ORR in oxygen-saturated 0.5 M KOH + 1 M MeOH, and d) ORR at Mn <sub>2</sub> O <sub>3</sub> /Pt/CP cathode in oxygen-saturated 0.5 M KOH containing 0–5 M MeOH. ....	110
Figure 5.10	Polarization curves (full symbols) and power density curves (open symbols) obtained during the operation of the passive ML- $\mu$ DMFC in a) typical 2-stream configuration and b) under mixed-reactant operation using different concentrations of MeOH, c) OCV, current density and power density values extracted from Fig. 5.10 a and b.....	111
Figure 5.11	Chronoamperometric curve obtained at 0.35 V for the study of the stability of the ML- $\mu$ DMFC using 4 M MeOH.....	112
Figure 6.1	Comparison of polarization curves obtained at 0.083 $\mu$ L min <sup>-1</sup> flowrate and at passive operation.....	114
Figure 6.2	Comparison of experimental and simulated polarization curves for validation of the model obtained with cell G1 using 4 M MeOH.....	115
Figure 6.3	Representation of the two different electrode arrangements studied with the mathematical model. The components are not to scale.....	115
Figure 6.4	Comparison of a) polarization and power density curves and b) fuel utilization, calculated for the 2 different electrode configurations. The distance between electrodes in both cases is 3 mm. ....	116
Figure 6.5	Flow simulation study of the 2 different electrode configuration. ....	117
Figure 6.6	a) CAD-created models used for the computational study, b) effect of electrode separation on fuel cell voltage profile c) fuel utilization for the three distances between electrodes, and d) fuel profiles at the anode under different potentials operation (0.3 mm electrode separation). ....	119

Figure 6.7	Representation of components and assembly of cell G2 developed after numerical simulation. ....	120
Figure 6.8	a) Performance comparison between cells G1 and G2, b) comparison between model and cell G2 and c) chronoamperometry of cell G2 obtained with 4 M MeOH at 0.3 V. ...	121
Figure 6.9	Representation of components, assembly and photograph of the 4-cell MR- $\mu$ DMFC stack. ....	124
Figure 6.10	a) Polarization and power density curves and b) fuel profiles of individual cells in the MR- $\mu$ DMFC stack. ....	125
Figure 6.11	Circuit diagram of connections performed for the study of the 4-cell MR- $\mu$ DMFC stack ....	126
Figure 6.12	Polarization and power density curves of the 4-cell stack in a) parallel connection, b) series connection, and d) chronoamperometric curve of the stack in series connection. In all cases 4 M MeOH in 0.5 M KOH was used. ....	127
Figure 6.13	Photograph of fuel cell powering a green LED.....	128
Figure 6.14	Voltage profile of the MR- $\mu$ DMFC stack during operation of the green LED. ...	128



## LIST OF TABLES

---

Table 1.1	Power requirement of some common electronic portable devices.....	1
Table 1.2	Liquid fuels for fuel cells [32].....	5
Table 3.1	Materials synthesized by PLD.....	71
Table 3.2	Optimum synthesis conditions of the bilayer cathodes developed in this work. ....	72
Table 3.3	Input values for the generation of the model. ....	81
Table 3.4	Boundary conditions. ....	82
Table 6.1	Calculated resistance for different values of distance between electrodes. ....	118
Table 6.2	Literature survey of recent microfluidic DMFCs.....	122



## LIST OF ABBREVIATIONS

---

AFC	Alkaline fuel cell
ASR	Area-specific resistance
BE	Binding energy
CAD	Computer-aided design
CBS	Cage-bell structure
CP	Carbon paper
CE	Counter electrode
CNC	Computer numerical control
DC	Direct current
DMFC	Direct methanol fuel cell
EMF	Electromotive force
ESA	Electroactive surface area
FCC	Face-centered cubic
FC	Fuel cell
FMO	Functional metal oxides
FWHM	Full width at half maximum
GDL	Gas diffusion layer
IHP	Inner Helmholtz plane
JCPDS	Joint committee for powder diffraction standards
KE	Kinetic energy
LED	Light-emitting diode
LCD	Liquid-crystal display
LSV	Linear scan voltammetry
MCFC	Molten carbonate fuel cell
MEA	Membrane-electrode assembly
ML	Membraneless
MOR	Methanol oxidation reaction

MR	Mixed-reactant
NAA	Neutron activation analysis
NHE	Normal hydrogen electrode
OHP	Outer Helmholtz plane
ORR	Oxygen reduction reaction
OCP	Open circuit potential
OCV	Open circuit voltage
PAFC	Phosphoric acid fuel cell
PDF	Powder diffraction file
PEMFC	Polymer electrolyte membrane or Proton-exchange membrane fuel cell
PMMA	Poly(methyl methacrylate)
PLD	Pulsed laser deposition
PVD	Physical vapor deposition
RDE	Rotating disk electrode
RDS	Rate-determining step
RE	Reference electrode
RHE	Reversible hydrogen electrode
RRDE	Rotating ring-disk electrode
RF	Roughness factor
SEM	Scanning electron microscope
SHE	Standard hydrogen electrode
SOFC	Solid oxide fuel cell
TOF	Time of flight
UV	Under vacuum
WE	Working electrode
XPS	X-ray photoelectron spectroscopy
XRD	X-ray diffraction
$\mu$ FFC	Microfluidic fuel cell

# CHAPTER 1 INTRODUCTION

## 1.1 General introduction

Technologically advanced societies require specialized tools and equipment to perform their diverse day-to-day activities. Electronic portable devices such as laptops, cellphones, smart watches, etc. are now essential instruments for many people in their daily lives. As a consequence, a number of gadgets with higher functionality and reduced size have shown up in the market in recent years. This implies that the new technology requires more power in smaller form-factors. Energy sources for all kind of electronic devices are under constant pressure to achieve higher efficiency levels by increasing the energy density and decreasing both volume and weigh while reducing the cost of portable power sources at the same time [1-4]. The average power for such devices can range from microwatts to a few watts, depending on function and duty cycle [1,5]. Table 1.1 reports some common electronic devices and their power requirements for operation.

**Table 1.1 Power requirement of some common electronic portable devices.**

Type	Description	Voltage (V)	Current (mA)	Power (mW)	Ref.
Accelerometer	KXTJ3-1057	1.7	0.10	0.17	[6]
Pressure sensor	SparkFun Flex Glove Controller	2	0.150	0.3	[7]
LCD Display	MIKROE-55	0.8	1.2	0.96	[8]
LED	Green LED LG L29K	1.7	2	3.4	[9]
LED	Red LED SLR-56 Series	2	10	20	[10]
DC motor	N20 DC 1.5 V	1.5	20	30	[11]
Microcontroller	Arduino Micro	5	10	50	[12]
LCD Touchscreen	Adafruit PiTFT 3.5"	5	75	375	[13]
Image sensor	CMOS camera module CM-32	12	50	600	[14]
Cell phone	Samsung Galaxy S2 HD LTE (standby)	-	-	283	[15]
Cell phone	Samsung Galaxy S2 HD LTE (Call)	-	-	2200	[15]
Laptop	IBM ThinkPad R40 (Idle system)	-	-	8230	[16]
Laptop	Apple MacBook 2017 (Idle system)	-	-	2690	[17]

To date, the lithium-based (Li-ion, Li-poly) rechargeable battery is the major power source for portable devices. These batteries offer a high energy density, in comparison with other chemical batteries (Fig. 1.1), however, there are some concerns regarding the availability of lithium in the future, due to its limited sources and constantly rising cost [5]. A major disadvantage of using rechargeable batteries is that they need an external electrical power source to charge. Due to the limited battery capacity, they can only be used with an existing electrical source and this represents a limitation in terms of device mobility. In remote areas where there is no electric power grid, running a device on portable batteries is problematic [18,19]. There also exist safety related concerns due to the possibility of fire or explosion caused by short-circuit within the cell, especially during charging. Additionally, the long recharge times remain as one of the main challenges for Li-based batteries [5]. This situation has led many researchers to seek alternative power sources to replace battery technology for portable applications.

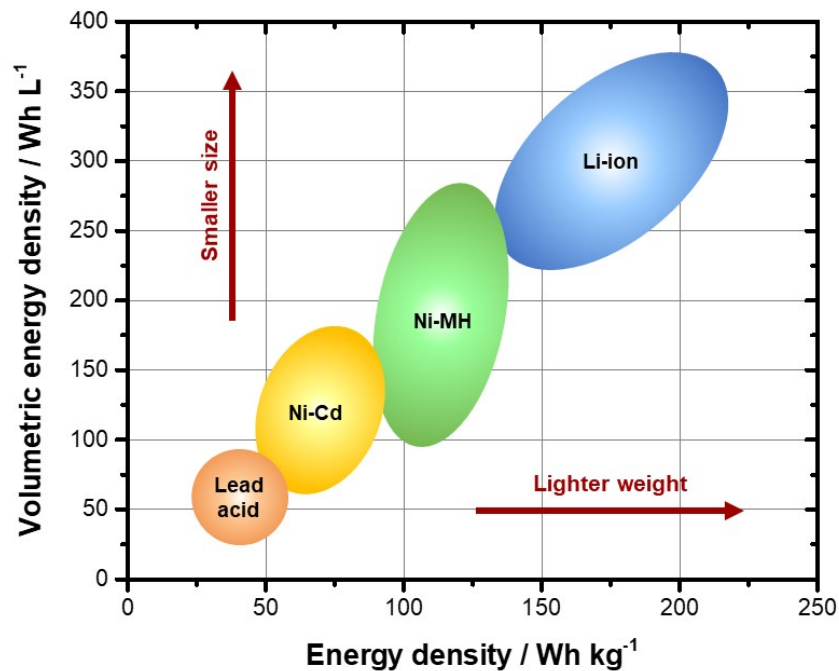


Figure 1.1 Ragone plot showing performance comparison of different types of batteries [20].

An alternative power source that has been explored in recent years is the fuel cell technology. A fuel cell is an electrochemical device that converts chemical energy stored in a fuel and oxidant into electrical energy through electrochemical processes involving oxidation-reduction reactions [5,21]. It is possible to think of a fuel cell as a “factory” that takes fuel as input and produces

electricity as output. Like a factory, a fuel cell will generate a product (electricity) as long as raw material (fuel) is supplied. Advantages of fuel cells include the simpler independent scaling between power and capacity, whereas batteries scale poorly at large sizes [22]. In batteries, energy is stored in relatively heavy and voluminous sources such as lithium derivatives, metal oxides and graphitic materials. On the other hand, fuel cells have decoupled energy storage and energy conversion functions and can produce electricity from much lighter materials such as gases and alcohols [1,23]. A fuel cell is not consumed when it produces electricity, they can operate either in passive or active mode and more importantly, they can be instantly recharged [1,5,22]. These features are the key differences between fuel cells and batteries and for these reasons, fuel cells represent a promising technology for a wide range of applications. A performance comparison between fuel cells and other energy storage and conversion devices is shown in Fig. 1.2.

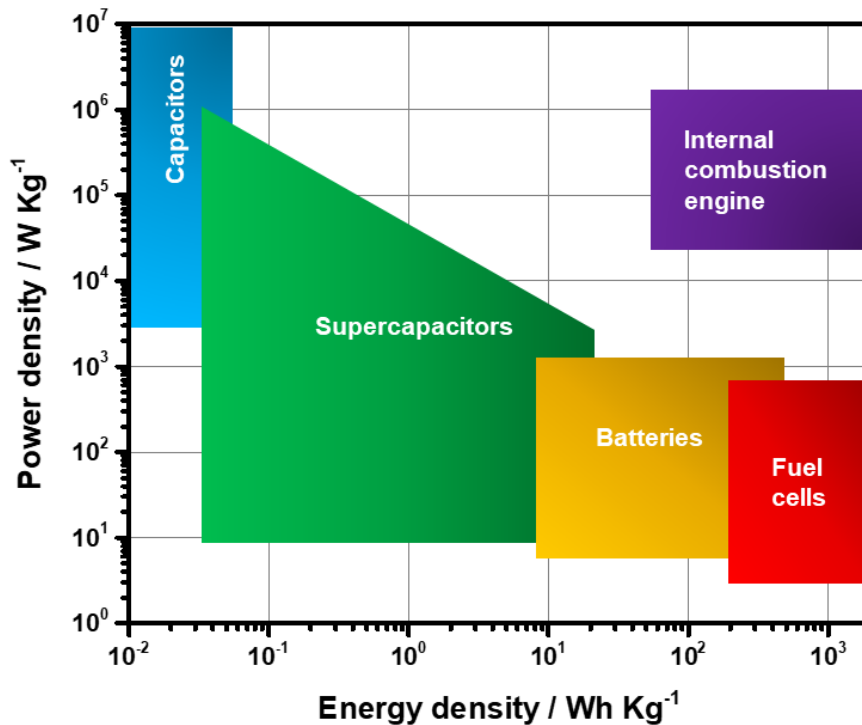


Figure 1.2 Ragone plot showing performance comparison of various energy storage devices [24].

The fuel cell market can be divided into different segments based on power level and end use. These areas are: (i) mini or micro power ( $10 \mu\text{W}$  to  $1 \text{ W}$ ), (ii) small portable power ( $1$  to  $100 \text{ W}$ ), (iii) traction power (portable supplies at  $10$  to  $100 \text{ kW}$ ), (iv) back-up power (tens to hundreds of

kilowatts) and (v) stationary plug power (hundreds of megawatts) [1,4]. Fuel cells have the potential to provide clean, efficient, sustainable power in all market segments, although they become more convenient at the lower end of the power requirement scale. Heat engines (Rankine & Brayton cycles of stationary power and Otto & Diesel cycles for traction) are highly competitive in high power-density applications where device size and fuel infrastructure are not primary concerns. However, at smaller sizes, electrochemical devices become more competitive because they are simpler than heat engines, requiring no moving parts, while providing higher energy densities since they scale as a function of their electroactive surface area, not device volume [1,25,26].

Fuel cells are greatly versatile, as they are able to operate using a variety of fuels, oxidants and electrolytes in different ranges of temperatures (Figure 1.3) [22,27-29]. Pure hydrogen and oxygen have been largely used as fuel and oxidant, respectively, mainly because hydrogen oxidation is a relatively simple process and it produces high power density with practically zero emissions [30]. However, a major drawback of hydrogen fuel cells is associated with the storage and distribution of hydrogen, and its use is restricted to transportation and residential applications [30,31]. The use of hydrogen-containing room-temperatures liquids (Table 1.2), such as alcohols, has been proposed to replace hydrogen in fuel cells for portable applications [27,32,33].

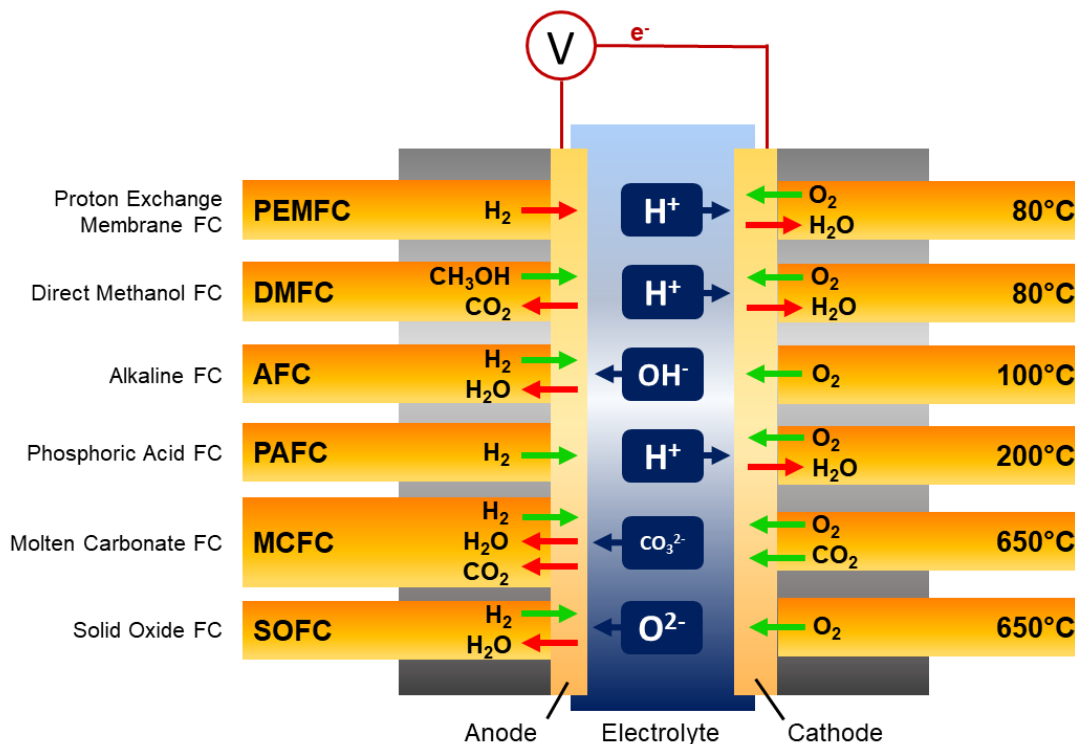


Figure 1.3 Types of fuel cells.

**Table 1.2 Liquid fuels for fuel cells [32].**

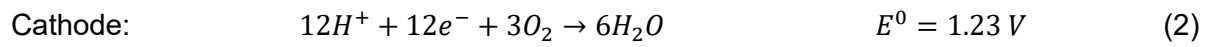
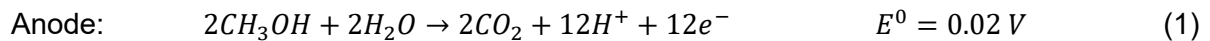
Fuel	Reaction	Standard theoretical potential, $E^0$ (V)	Energy density (Wh L <sup>-1</sup> )
Methanol	Anode	$CH_3OH + H_2O \rightarrow CO_2 + 6H^+ + 6e^-$	4820
	Cathode	$6H^+ + 6e^- + (3/2)O_2 \rightarrow 3H_2O$	
	Overall	$CH_3OH + (3/2)O_2 \rightarrow CO_2 + 2H_2O$	
Ethanol	Anode	$C_2H_5OH + 3H_2O \rightarrow 2CO_2 + 12H^+ + 12e^-$	6280
	Cathode	$12H^+ + 12e^- + 3O_2 \rightarrow 6H_2O$	
	Overall	$C_2H_5OH + 3O_2 \rightarrow 2CO_2 + 4H_2O$	
Propanol	Anode	$C_3H_7OH + 5H_2O \rightarrow 3CO_2 + 18H^+ + 18e^-$	7080
	Cathode	$18H^+ + 18e^- + (9/2)O_2 \rightarrow 9H_2O$	
	Overall	$C_3H_7OH + (9/2)O_2 \rightarrow 3CO_2 + 5H_2O$	
Ethylene glycol	Anode	$C_2H_6O_2 + 2H_2O \rightarrow 2CO_2 + 10H^+ + 10e^-$	5800
	Cathode	$10H^+ + 10e^- + (5/2)O_2 \rightarrow 5H_2O$	
	Overall	$C_2H_6O_2 + (5/2)O_2 \rightarrow 2CO_2 + 3H_2O$	
Glycerol	Anode	$C_3H_8O_3 + 3H_2O \rightarrow 3CO_2 + 14H^+ + 14e^-$	6400
	Cathode	$14H^+ + 14e^- + (7/2)O_2 \rightarrow 7H_2O$	
	Overall	$C_3H_8O_3 + (7/2)O_2 \rightarrow 3CO_2 + 7H_2O$	
Formic acid	Anode	$HCOOH \rightarrow CO_2 + 2H^+ + 2e^-$	1750
	Cathode	$2H^+ + 2e^- + (1/2)O_2 \rightarrow H_2O$	
	Overall	$HCOOH + (1/2)O_2 \rightarrow CO_2 + H_2O$	

In the case of portable, electronic devices, methanol, the simplest alcohol is particularly attractive due to its high energy density (4820 Wh L<sup>-1</sup>), low cost and ease of storage and transportation compared to hydrogen gas (530 Wh L<sup>-1</sup> @20MPa) [32,34]. On the other hand, oxygen, either pure or from the air, is generally used as oxidant, due to its low cost and abundance [35,36]. The oxygen reduction reaction (ORR) is a multi-electron process that is of great importance for fuel cells. This reaction has been on the spotlight of catalysts development due to its sluggish kinetics and high overpotential at practically all catalyst materials, and it has been identified as the limiting reaction in oxygen-based fuel cells. To date, Pt remains as the catalyst of choice for the ORR in most fuel cell systems, since it exhibits better overall performance than most catalytic materials [37], however, since Pt is a scarce, expensive precious metal, one of the main targets of cathode development is to reduce the content of Pt. The mechanism of the ORR on Pt has been studied for many years, and though significant progress has been made in understanding how it occurs, the exact reaction mechanism is still the subject of extensive discussions [36]. It is generally

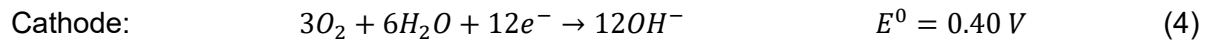
accepted that in aqueous solutions,  $O_2$  can be electrochemically reduced directly to water via a four-electron transfer, or reduced by two electrons to  $H_2O_2$  (or  $HO_2^-$ ) and subsequently reduced to water (or  $OH^-$ ) through another two electrons transfer [36,37]. The ORR kinetics in alkaline media is more rapid and provides a less corrosive environment to the catalysts, in comparison with acidic media [20]. This has stimulated the research on catalysts for ORR in alkaline media.

Fuel cells that use methanol solutions and oxygen are called direct methanol fuel cells (DMFC) [38].

The occurring reactions in a DMFC in acidic media are [33]:



And in alkaline media are [33]:



With an overall reaction in acidic or alkaline:



In a real DMFC, the cell voltage is always lower than the thermodynamic value due to different losses, such as anodic and cathodic activation overpotential, crossover effect, ohmic overpotential and mass transport losses [22]. Depending on the pH, the catalysts employed, cell configuration and tests conditions, a DMFC can generate an open-circuit voltage (OCV) between 0.6 and 0.8 V [32,39-41].

The most studied type of DMFC relies on a proton exchange membrane (PEM), usually Nafion®, to separate the two half reactions, methanol oxidation (MOR) at the anode and oxygen reduction at the cathode (ORR) [42,43]. This type of fuel cell are therefore denominated PEM-DMFCs, and their main components are shown in Fig. 1.4.

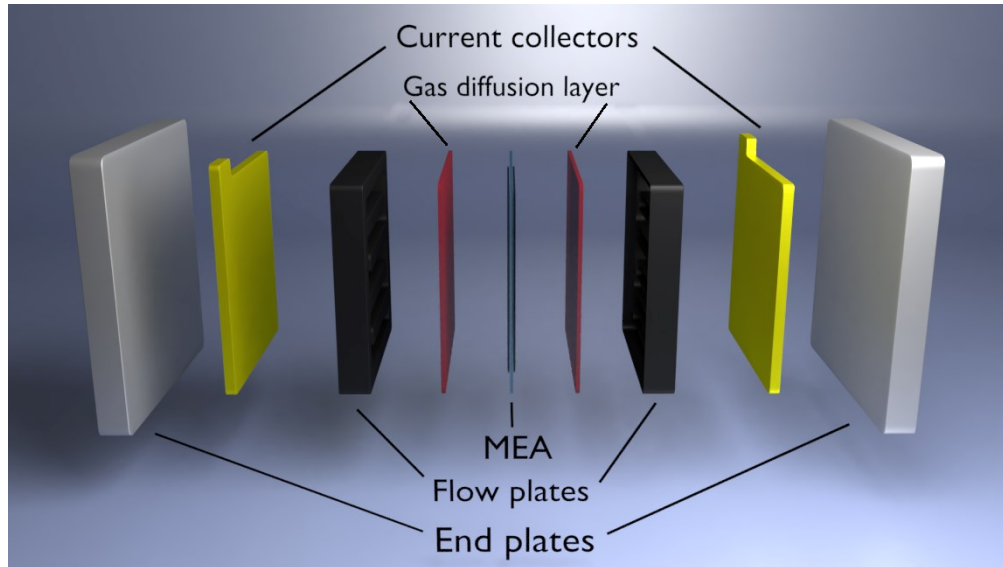


**Figure 1.4 Main components of a PEM-FC**

PEM-DMFCs concept and operation derive from the hydrogen fuel cell, which is considered to be the pioneer of this type of fuel cells and that performs well in vehicle and stationary applications [22,43]. PEM-DMFCs have been under intense study for the last couple of decades, due to their advantages over hydrogen-fed PEM-FCs. However, methanol diffusion from the anode to the cathode through the membrane is a recurrent issue that impacts negatively on the overall performance of PEM-DMFCs. The presence of methanol at the cathode causes depolarization losses due to simultaneous oxygen reduction and methanol oxidation processes. This phenomenon is known as methanol crossover effect [41,44]. Thus, the concentration of methanol solutions is often limited to no more than 10 wt%, and the use of higher concentration is counterproductive [45]. Other issues related to the membrane include low mechanical strength and water management for hydration and optimal performance [46,47]. From Equation 5, we can deduce that for a practical application, it is necessary to design and fabricate stacks to increase the voltage and current of DMFCs. It is at this point where the development and commercialization of PEM-DMFCs meets a setback. Due to the number of components in a stack (catalysts, membrane, gas diffusion layers, bipolar plates, clamping plates, current collectors, gaskets, hardware etc.), the fabrication cost escalates rapidly. As recently shown by Sgroi et al. [48] in their cost analysis of PEM-DMFC stacks, the fabrication expenses of a lab-made 10-cell stack prototype can reach almost €3000, of which only 12% is due to the catalysts, 20% to the membrane-electrode assembly (MEA) and 60% is related to bipolar plates, clamping plates and

current collectors. Furthermore, conventional PEM-DMFCs are considered to be too bulky for portable applications [5].

There exist two main research axes for the miniaturization of fuel cell technology. The first one is simply a reduction in size of existing PEM-DMFCs, whereas the second one is the development of new concepts, materials and structures that allow the fabrication of smaller fuel cell devices [1]. Although the former seems to be the most straightforward approach, it becomes problematic when miniaturizing the membrane and adapting the flow structures, which necessitates the use of expensive microfabrication techniques, such as micro- and nano-electromechanical systems (MEMS/NEMS) [1,49-52]. Alluding to the second approach, the concepts of membraneless microfluidic fuel cell (ML- $\mu$ FFC) and mixed-reactant fuel cell (MRFC) put forward a different strategy for developing compact energy sources.

The introduction of ML- $\mu$ FFCs in the early 2000s [33,53], presented the possibility of integrating simpler, media-flexible and miniaturized power sources on portable devices. As the name itself suggests, this technology does not require any membrane to operate. Instead, ML- $\mu$ FFCs (ML- $\mu$ DMFC if fueled by MeOH) rely on the co-laminar flow of fuel and oxidant in a microfluidic channel to separate the two half-reactions [33,39]. As illustrated in Fig. 1.5, all the components related to the electrochemical reactions are located in a single microchannel (1–1000  $\mu$ m in either L, W or H). The schematic shows a Y-shape microfluidic channel that is used to merge two liquid streams, fuel and oxidant solutions. The reactants flow under laminar regime, characterized by low Reynold's number ( $Re$ ) [5]. As the fuel and oxidant streams flow parallel in a co-laminar format, the liquid-liquid interface serves as a separator without need for a membrane. At low  $Re$  (under 1000), the two streams will flow parallel down a microchannel. Exceeding the threshold will result in transition to turbulent flow and destabilization of the co-laminar flow interface, leading to excessive mixing and loss of cell voltage [5]. In ML- $\mu$ FFCs, diffusive mixing is restricted to a thin interfacial width at the center of the channel, which exhibits an hourglass shape with maximum width at the channel walls. The position of the electrodes is thus constrained by the width of the co-laminar interdiffusion zone. Additionally, the fuel and oxidant are depleted near the electrodes, which limits the dimensions of the electrodes. Consequently, the diffusion and depletions zones set a maximum effective length for the fuel cell, typically micrometers to millimeters [5,22].

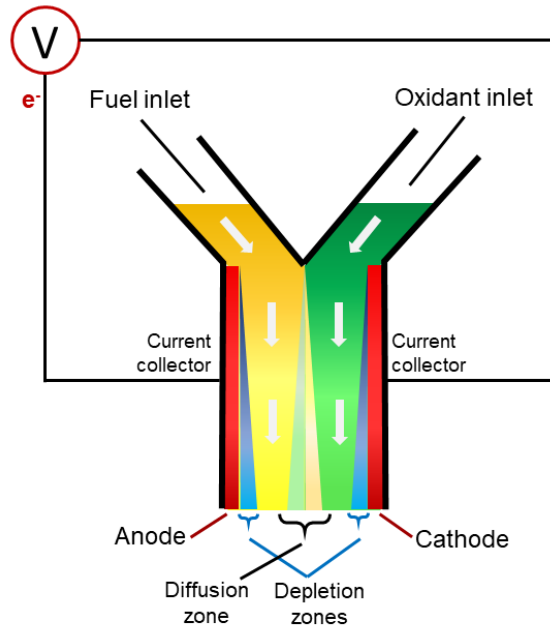


**Figure 1.5 Principle of membraneless fuel cell.**

By eliminating the MEA and the bipolar plates, the cost of a ML- $\mu$ DMFC is drastically lowered. An interesting feature of this type of fuel cells, is that the mixing of streams can be kept at minimum and thus, the methanol crossover can be diminished to a great extent by fine tuning the flow rate of fuel and oxidant [33,39]. Since then, many membraneless fuel cells architectures have been reported (Fig. 1.6), but most of them as proof-of concept single cells with insufficient power output for real applications [5,54].

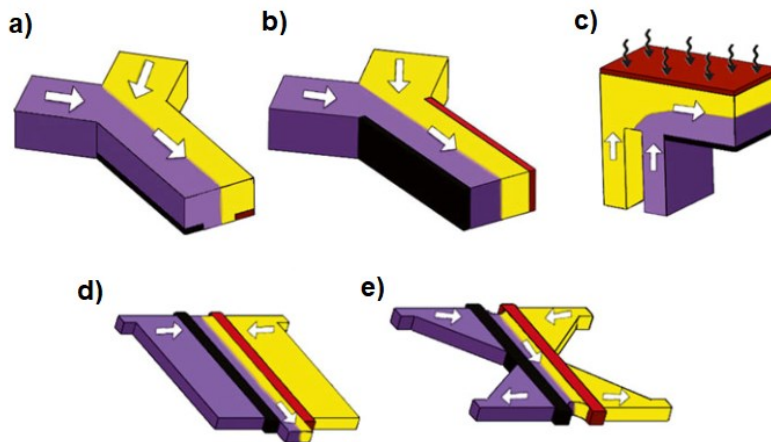


**Figure 1.6 Main microfluidic fuel cells architectures developed to date: a) monolithic flow-by cell with electrodes on floor, monolithic cell with electrodes on walls, c) air-breathing flow-by cell, d) monolithic flow-through cell and d) monolithic dual-pass flow through cell [5].**

For practical applications, the integration of multiple microfluidic fuel cells is necessary, nevertheless, the development of membraneless microfluidic stacks is challenging due to the need for efficient flow structures and manifolding in spatial-efficient cells arrays [5,55]. Depending on the stacking strategy, reactant delivery, sealing and ionic insulation between unitary cells become more complicated with increasing number of cells. For these reasons, not many works on membraneless stacks are found in the literature. Among the most representative, are a planar 5-cell microfluidic array reported by Cohen et al. [56], a planar 2-cell stack with shared fluidic inlet ports proposed by Ho and Kjeang [57], a tandem design that allows fuel reutilization developed by Salloum and Posner [58], an architecture based on a hexagonal array of graphite rods reported by Kjeang et al. [59] and a 6-cell stack in a circular arrangement proposed by Wang and Leung [60]. Despite the widely different architectures of the above-mentioned stacks, they all feature the co-laminar flow of fuel and oxidant streams and the imperative use of external pumps for preventing reactant mixing, which is ultimately an energetic loss rarely taken into account in the general balance. This downside is not necessarily present in mixed-reactant fuel cells, where the separation of the cathodic and anodic reactions is dealt by selective catalysts [61-63] (Fig. 1.7). Consequently, they don't require co-laminar flow of reactants and therefore, can operate in passive mode. In other words, external pumps are not necessary, resulting in much more compact systems with simpler operation.

Mixed-reactant fuel cells offer a potential solution to the problem of stacking microfluidic fuel cells and this can lead to the development of a passive microfluidic stack with small dimensions and sufficient energy output for a low power application. Essentially, in a MRFC, the fuel and oxidant are mixed in a single stream and the use of selective electrocatalysts is necessary to minimize mixed-potential at the electrodes [63,64]. Thus, a MR- $\mu$ DMFC requires an anode active to the methanol oxidation reaction (MOR), and a cathode active to only oxygen reduction reaction (ORR).

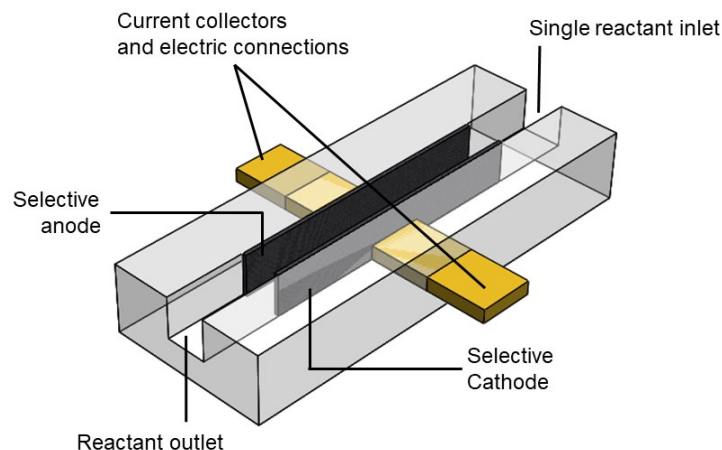


**Figure 1.7 Representation of a simple channel layout and components of a MRFC.**

There are a number of advantages associated to the use of MRFCs compared with other FCs, e.g., no need for solid polymer membrane or laminar flow and external pumps, reduced weight and volume, simplified manifolding, reduced sealing requirements and, overall they have simpler designs. By having smaller volume, a MR- $\mu$ DMFC stack can lead to higher volumetric power density [62-65]. From an engineering point of view, this translates into cheaper fabrication and easier operation than conventional fuel cells. Calabrese-Barton and his group have developed some MEAs-based MRFCs [61,63,66], and more recently a borohydride-oxygen Swiss-roll MRFC was reported [65,67,68]. Nevertheless, not many works on methanol MRFCs are found in the literature, due mainly to the requirement of selective electrodes, particularly the cathode. Though the MOR is hardly affected by the presence of oxygen, the ORR is suppressed by the presence of MeOH [69,70]. As mentioned above, despite its high cost, Pt is widely employed for cathode catalysts due to its excellent catalytic activity, however, the main disadvantage of using Pt as cathode in any DMFC is that it is also oxidizes methanol [41,71]. Therefore, the use of Pt as cathode for MR-DMFCs is unsuitable, since essentially, the cathode should not be active to the MOR. Numerous groups have worked on developing methanol tolerant cathodes, mainly featuring Pt-free catalysts, such as Pd/Ag [72], Ru/Se [73], PdSe [74], Pd/Co [75], Fe-N-C [76,77], CoSe<sub>2</sub> [78] and RuSe<sub>2</sub> [79] for PEM-DMFCs. However, the ORR on those materials have higher overpotential, slower kinetics reaction rates and low mass specific activity, in comparison with Pt. Feng et al. [80] reported the synthesis of a cage-bell structured Pt-Ru nanoparticles cathode catalyst tolerant to 1 M methanol. The interesting of this work is that the Pt core serves as the catalyst for the ORR while the porous Ru shell acts a protection for the core, due to the differential diffusion of methanol and oxygen.

Based on this approach, in this work we propose the development of Pt-based cathode with an added porous material as a protection for Pt in order to prevent the diffusion of methanol but allowing the diffusion of oxygen. This is intended to be achieved through a layer-onto-layer architecture, where the base layer, Pt, will serve as the catalysts for ORR, while a secondary or superficial layer will function as protection. By doing so, we expect the cathodes to exhibit high mass activity and methanol tolerant properties for use in MR- $\mu$ DMFC.

The preparation of catalysts generally involves long, multi-step synthesis methods, such as impregnation, ionic exchange, colloidal methods or microemulsions. Nonetheless, physical methods, such as the pulsed laser deposition (PLD), offer a faster, more controllable alternative for material synthesis. The PLD technique is a physical vapor deposition process that has emerged in the last decade as a viable means of producing high quality thin films of a wide variety of materials, including insulators, semiconductors, high temperature superconductors, metals, and metal oxides [81]. It is a rapid, simple, and contaminant-free alternative synthesis method that allows good control on the deposition parameters [82]. In conventional PLD, a high power pulsed laser is focused onto a target of the material to be deposited. The laser pulse vaporizes or ablates a small amount of the material creating a forward directed plasma plume. The ablation plume provides the material flux for film growth. This process can be carried out in ultra-high vacuum or in the presence of a background gas, such as oxygen, helium or argon. The PLD has a number of practical advantages for laboratory development of new materials, and it delivers a much higher deposition rate than sputtering. Furthermore, the size, morphology and composition of deposited materials could be well controlled by modifying deposition conditions (background atmosphere and pressure, target-to-substrate distance, and incident energy) [81,82]. The PLD technique has been previously used in our group for the deposition of various metals and metal oxides directly on carbon paper (CP) and carbon nanotubes (CNTs) substrates as binderless anodic catalysts for ethanol [83] and glucose [84] oxidation with overall better performance than the more commonly used Vulcan carbon-supported catalysts. For these reasons, the PLD technique was chosen in this project for the development of Pt-based layer-onto-layer cathodes with high methanol tolerance properties for use in a MR- $\mu$ DMFC.

As for the design and study of new fuel cells systems, simulation modeling is a time saving resource that allows to examine a variety of phenomena and systems without the expenses and difficulty of experimentation. In recent years, numerical simulation has proven to be a very useful tool for the analysis of electrochemical phenomena [85,86], distribution of chemical species [86,87] and a convenient way for optimizing certain fuel cell components, such as flow structures

[88,89]. Fuel cell performance can be improved by tailoring microchannel geometries and strategic electrode placement for promoting better fuel utilization [90]. Another way to increase efficiency is by reducing the overall cell resistance. The ohmic losses in fuel cells result from the ionic and electronic resistance, but generally, the contribution from ion transport is more significant, as it is far more difficult than electron transport [22]. In MR- $\mu$ DMFCs, the electrodes can be unusually closer than in co-laminar fuel cells because methanol crossover is not a concern. In addition, it is also possible to study electrode configurations different from the traditional opposing walls arrangement. Numerical simulation can assist on the optimization of these critical parameters for developing a more fuel-efficient and better performing MR- $\mu$ DMFC stack.

Thus, the present thesis focuses on two main objectives, the synthesis of a selective cathode for ORR in MR- $\mu$ DMFCs, and the development through numerical simulation of a proof of concept MR- $\mu$ DMFC stack to demonstrate the capabilities for low power applications.

## 1.2 Justification

The growing market demand for portable electronic devices has encouraged the quest for new compact energy sources that allow longer operation periods without need for recharging. Direct methanol fuel cell (DMFC) technology represents an attractive alternative to the ongoing Li-ion batteries, due to the possibility of being instantly recharged and the relatively safe storage and transportation of methanol. Mixed-reactant  $\mu$ DMFCs are a feasible solution to the elaborate operation and stacking design of other types of DMFCs, such as PEM-based DMFCs and membraneless  $\mu$ DMFCs. MR- $\mu$ DMFCs operate with a mix of fuel and oxidant in a single solution and can work in passive mode, therefore there is no need for membrane as in PEM-DMFCs or external pumps for guaranteeing laminar flow as in ML- $\mu$ DMFCs. MR- $\mu$ DMFCs are the most compact type of fuel cell, having the lowest fabrication costs as well as the simplest designs and operation. Despite these advantages, MR- $\mu$ DMFCs have not widely been regarded as alternative power sources for portable applications, mainly due to the need for selective catalysts, particularly the cathode. For these reasons, we consider that the synthesis of an outstanding cathode, i.e. high catalytic activity and selectivity towards the ORR, is crucial for the development of a more compact and better performing MR- $\mu$ DMFC. Additionally, an efficient MR- $\mu$ DMFC design is essential to simplify the fabrication and operation of a MR- $\mu$ DMFC stack, which is necessary for achieving any practical application. Therefore, in this work we propose the synthesis and implementation of a selective cathode for the development of a proof of concept MR- $\mu$ DMFC stack in order to demonstrate the potential for practical applications.

### 1.3 Objectives

1. To develop a nanostructured cathode with high catalytic activity and selectivity towards the ORR for use in MR- $\mu$ DMFCs.

The aforementioned is intended to be achieved through the following specific objectives.

- a) To grow a Pt film on carbon substrate by PLD and subsequently coating the Pt with a layer of Ag, Fe<sub>2</sub>O<sub>3</sub> or Mn<sub>2</sub>O<sub>3</sub> in order to obtain a bilayer structure. Films with different morphologies and mass loadings will be deposited.
  - b) To characterize the catalysts by physicochemical and electrochemical techniques in order to study morphology and composition, as well as to evaluate the electrocatalytic activity towards ORR and MOR.
  - c) To evaluate and compare the cathodes in a single ML- $\mu$ DMFC under mixed reactant conditions and passive mode in order to identify the best-suited cathode for use in a MR-  $\mu$ DMFC.
2. To develop a proof of concept MR- $\mu$ DMFC stack that employs the selective cathode obtained from objective 1 in order to demonstrate the potential for practical applications.

The design, optimization and fabrication of the MR- $\mu$ DMFC stack is intended to be achieved through the following specific objectives.

- a) To obtain a mathematical model through finite element analysis software and to experimentally validate the model in order to study two different electrode-microchannel arrangements for a MR- $\mu$ DMFC.
- b) To fabricate a single MR- $\mu$ DMFC by CNC micromachining with the optimal features according to numerical simulation.
- c) To evaluate experimentally the performance of the single MR- $\mu$ DMFC in order to establish the base for the fabrication of a MR- $\mu$ DMFC stack.
- d) To incorporate various cells in a single device to obtain a MR- $\mu$ DMFC stack and to fabricate it by CNC micromachining.
- e) To evaluate the performance of the stack in series and parallel connections and to employ it for powering an LED in order to demonstrate the capabilities for practical applications.

## CHAPTER 2 LITERATURE REVIEW

### 2.1 Fuel cell fundamentals

A fuel cell is an electrochemical device capable of converting the chemical energy stored in a fuel directly into electrical energy. Such process is carried out through electrochemical reactions. Fuel cells can be considered as “factories” where a product (electricity) will be constantly produced as long as raw material (fuel and oxidant) is supplied. In this sense, combustion engines could also be viewed as “chemical factories”, as they convert the energy stored in a fuel into useful mechanical or electrical energy (Fig. 2.1). However, in combustion engines, the chemical energy is first converted into heat, then mechanical energy and finally electricity, while fuel cells produce electricity directly from chemical energy. For this reason, fuel cells are far more efficient than combustion engines. Additionally, fuel cells have no moving parts, which makes their operation silent and long-lasting [22].

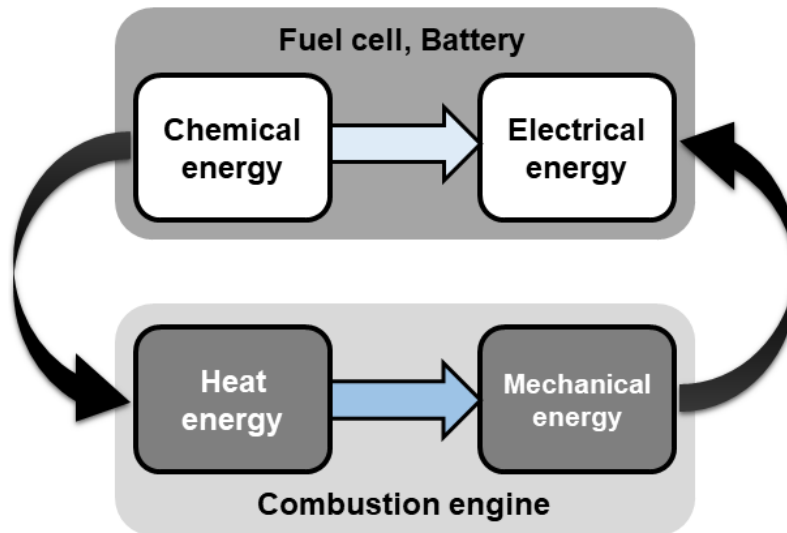


**Figure 2.1** Schematic comparison of electrical energy generation of fuel cells, batteries and combustion engines.

Similarly, batteries also produce electrical power directly from chemical energy, however, they differ in the way electrical power output and current density are delivered over time. This is illustrated in Fig. 2.2a with an analogy of buckets filled with water. In both cases, the power output is determined by the operating voltage (height of water in the bucket) and current density (the amount of water flowing through the tap at the lower part of the bucket). A fuel cell is portrayed as an open system, capable of being continually replenished with fuel, resulting in constant operating

voltage in time. In contrast, batteries are represented as closed systems with an internal and finite amount of reactants. The reactants cannot be replenished and they deplete over time, resulting in decreasing water level (operating voltage). Besides, the battery voltage does not decrease linearly, represented by the shape of the bucket. As a consequence, in fuel cells, power and capacity (determined by fuel cells size and fuel reservoirs size respectively) can be independently designed and operated, while in batteries, power and capacity are heavily dependent (Fig. 2.2b) [22]. Therefore, fuel cells can potentially operate for much longer periods of time than batteries.

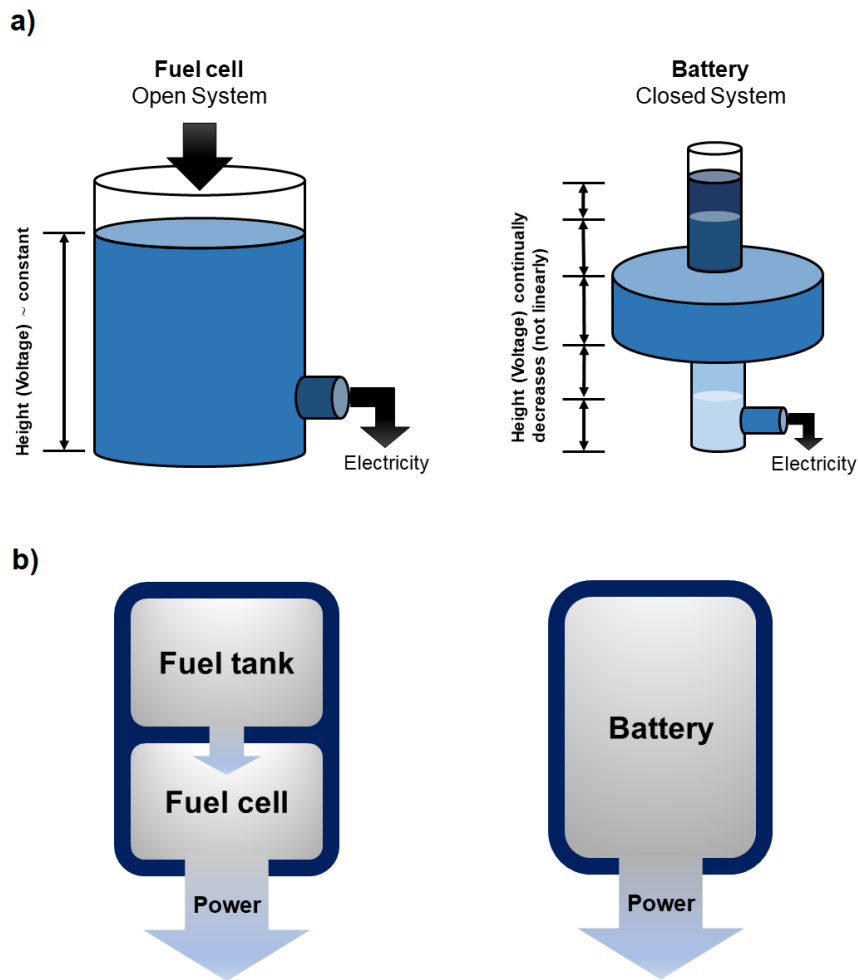


**Figure 2.2** a) Schematic comparison of fuel cells and batteries systems and b) relation between power and capacity in batteries and fuel cells (Adapted from [22]).

Fuel cells produce electricity through electrochemical reactions when it is fed with a fuel and an oxidant. The fuel oxidation and oxidant reduction reactions take place at the anode and cathode, respectively. The electrodes are spatially separated but ionically connected by a thin material,

called electrolyte, which conducts ionic charge carriers such as protons or hydroxide ions while blocking undesired transport of reactants and electrons. The electrodes are electrically connected through an external circuit, which ensures the electrons transport from the anode to the cathode [5,31]. Fig. 2.3 illustrates the main components of a fuel cell and the steps for energy conversion. The production of electricity is carried out through four major steps [22]:

- 1) **Reactant delivery into the fuel cell:** As mentioned above, a fuel cell must be continually supplied with fuel and oxidant. When operated at high current, the fuel cell demands for great amount of reactants. If those are not supplied quickly enough, the device will “starve”. Efficient delivery of reactants is commonly accomplished by using flow field plates in combination with porous electrode structures. Size, shape and pattern of flow channels, as well as porous electrode geometry can significantly affect the fuel cell performance. The study of the influence of these parameters is related to mass transport, diffusion and fluid mechanics.
- 2) **Electrochemical reaction:** Once the reactants reach the electrodes, electrochemical reactions take place. The current generated by the fuel cell is associated to the kinetics of the oxidation and reduction reactions. Fast reactions result in high current output while sluggish reactions produce low current output. Therefore, catalysts are used to increase the speed and efficiency of the electrochemical reactions.
- 3) **Ionic conduction through the electrolyte and electronic conduction through external circuit:** The ions produced at one electrode in step 2 must be transported to the other electrode where they will be consumed. The same applies for electrons. As long as an electrically conductive path, e.g., a wire, exists between the electrodes, electrons will easily flow from one electrode to the other. However, the transport process for ions tends to be more difficult, mainly because ions are much larger and massive than electrons. Ions are transported through an electrolyte that has to be as thin as possible to minimize resistance loss.
- 4) **Product removal from fuel cell:** Products generated by the electrochemical reactions must be removed from the fuel cell in order to avoid accumulation of water and other species at the electrodes. The same principles of mass transport and fluid mechanics applied in step 1 can assist in the product removal.

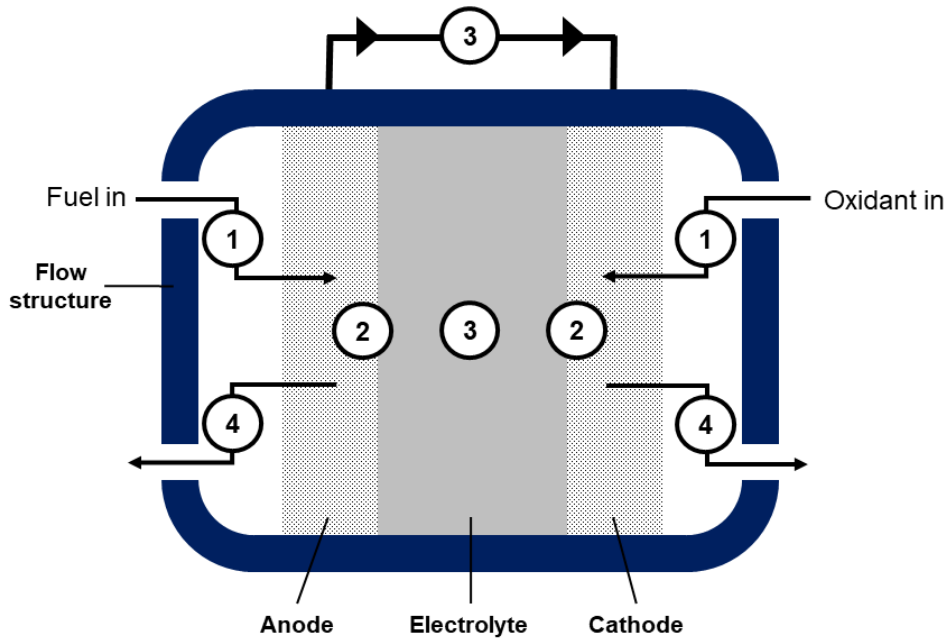


**Figure 2.3** Illustration of the main components of fuel cells and the major steps for electrochemical generation of electricity: (1) reactant transport, (2) electrochemical reaction, (3) ionic and electronic conduction and (4) product removal (Adapted from [22]).

In general terms, the performance of a fuel cell can be evaluated through a graph that displays the fuel cell voltage output for a given current output. Fig. 2.4 shows a typical current–voltage ( $i$ – $V$ ) curve of a fuel cell, where the current is displayed in the X axis and the cell voltage is located in the Y axis. Since the current produced by a fuel cell scales with size of reaction area,  $i$  is normalized by the fuel cell area, thus obtaining current density to make results comparable. Ideally, a fuel cell would supply a steady amount of current while maintaining a constant voltage, determined by thermodynamics. However, in a real fuel cell, the maximum voltage is lower than the thermodynamically predicted value and, furthermore, due to irreversible losses, the voltage decreases as current is drawn from the fuel cell. There are three major losses experienced by fuel cells, which give a fuel cell  $i$ – $V$  curve its characteristic shape, as indicated in Fig. 2.4 [22]:

1. Activation losses: Due to electrochemical reactions
2. Ohmic losses: Due to ionic and electronic conduction
3. Concentration losses: Due to mass transport

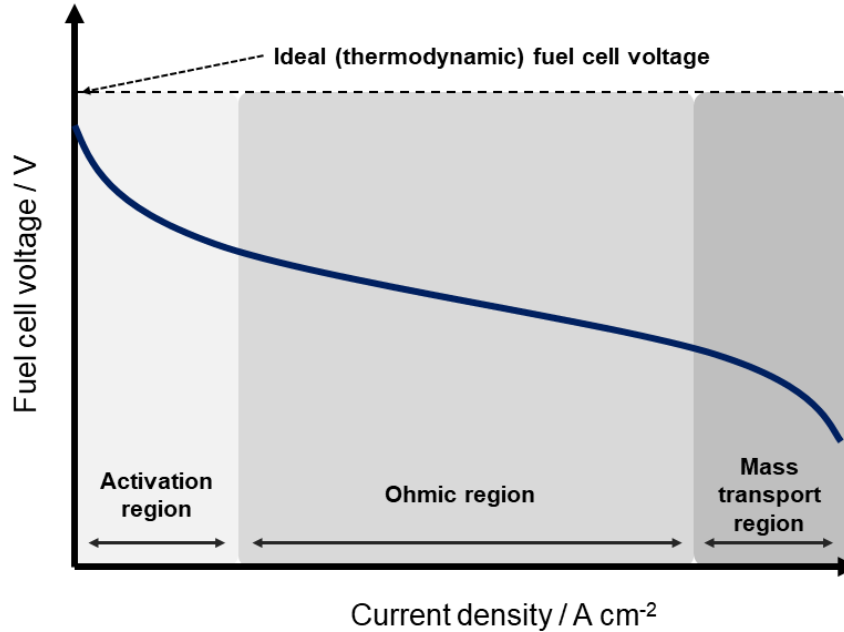


Figure 2.4 A typical fuel cell i-V curve.

The real voltage output of a fuel cell can be described by starting from the thermodynamically predicted voltage output and then subtracting the voltage drops due to the various losses:

$$V = E_{thermo} - \eta_{act} - \eta_{ohmic} - \eta_{conc} \quad (6)$$

where  $V$  is the real voltage output,  $E_{thermo}$  is the thermodynamically predicted voltage output,  $\eta_{act}$  are the activation losses due to reaction kinetics,  $\eta_{ohmic}$  are the ohmic losses from ionic and electronic conduction and  $\eta_{conc}$  are the concentration losses due to mass transport. It is observed that the activation losses affect the initial part of the curve, the ohmic losses become more significant in the middle section of the curve and the concentration losses have greater impact at the tail of the curve. Each of these issues are addressed individually in sections 2.1.1 to 2.1.4.

From the shape of the  $i$ - $V$  curve, it is clear that the more current is drawn from the fuel cell, the lower the cell voltage, thus limiting the total power that can be delivered. The power ( $P$ ) delivered by a fuel cell is given by the product of current and voltage [22]:

$$P = iV \quad (7)$$

From the information given in a fuel cell  $i$ - $V$  curve, a power density curve can be constructed by plotting the product of the voltage and its corresponding current density as a function of the current

density. Fig 2.5 shows the typical profile of a power density curve, which exhibits increasing power density that reaches a maximum and then falls at higher current densities. Fuel cells are designed to operate at or below maximum power density [22].

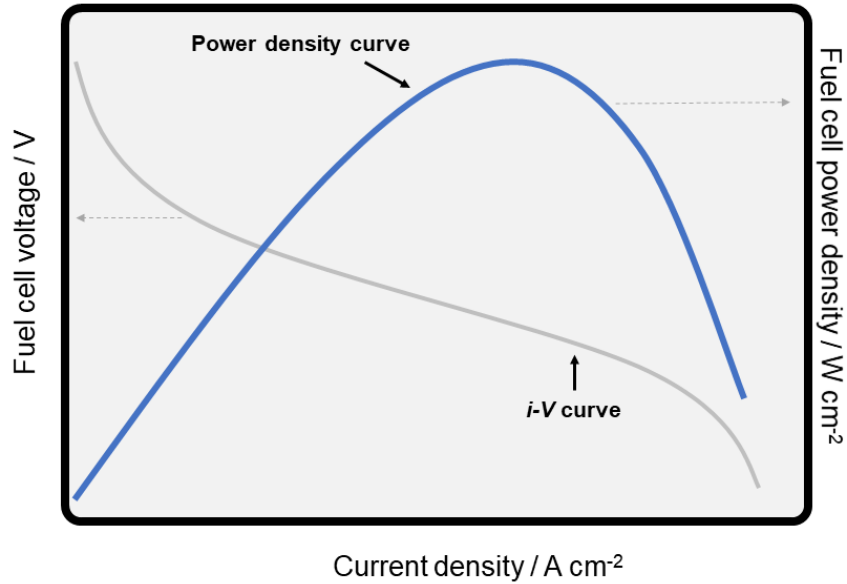


Figure 2.5 A typical fuel cell power density curve.

### 2.1.1 Thermodynamics

Fuel cells are energy conversion devices, therefore it is of key importance to study fuel cell thermodynamics to understand the conversion of chemical energy into electrical energy. Thermodynamics can predict whether a candidate fuel cell reaction is energetically favorable and it also indicates the maximum electrical potential that can be generated in that reaction. In other words, thermodynamics sets the theoretical limits or the ideal case for fuel cells. A fuel cell converts energy stored within a fuel into other forms of energy. The intrinsic energy of a fuel is quantified by a property known as internal energy ( $U$ ), however, a fuel cell cannot convert all the internal energy into electrical energy. The limits of conversion are set by the first and second laws of thermodynamics (Equations 8 and 9, respectively).

$$dU = dQ - dW \quad (8)$$

$$S = k \log \Omega \quad (9)$$

The first law of thermodynamics expresses that the change in the internal energy of a closed system ( $dU$ ) must be equal to the heat transferred to the system ( $dQ$ ) minus the work done by

the system ( $dW$ ), while the second law introduces the concept of entropy, where  $S$  is the total entropy of the system,  $k$  is the Boltzmann's constant ( $1.38064852 \times 10^{-23} \text{ m}^2 \text{ kg s}^{-2} \text{ K}^{-1}$ ) and  $\Omega$  denotes the number of possible microstates accessible to the system. Unfortunately,  $S$  is not easily measurable experimentally, for this reason it is necessary to introduce a thermodynamic description of a system that depends on temperature ( $T$ ) and pressure ( $p$ ), called the Gibbs free energy ( $G$ )

$$dG = -S dT + V dp \quad (10)$$

The Gibbs free energy is the energy needed to create a system minus the energy provided by the environment due to heat transfer.

The Gibbs free energy can be used to calculate the maximum amount of electrical work that can be extracted from a fuel cell reaction. The maximum electrical work that a system can perform at constant  $T$  and  $p$  conditions is given by the negative of the Gibbs free-energy difference for the process (reaction):

$$W_{elec} = -\Delta G_{rxn} \quad (11)$$

Additionally, the Gibbs free energy can be used to determine the spontaneity of a reaction. If  $\Delta G = 0$ , no electrical work can be extracted from the reaction, if  $\Delta G > 0$ , work must be input for a reaction to occur, and if  $\Delta G < 0$ , indicates a energetically favorable reaction.

When studying electrochemical systems, such as fuel cells, it is quite frequent to find the quantity  $nF$ , where  $n$  is the number of moles of electrons transferred and  $F$  is Faraday's constant ( $96,485 \text{ C mol}^{-1}$ ). This is because in any electrochemical reaction, there is an integer correspondence between the moles of a reacting chemical species and the moles of electrons transferred. Thus,  $nF$  expresses the quantized transfer of electrons, in the form of electrical current, between reacting chemical species. To convert molar quantities of electrons to quantities of charge, it is necessary to multiply  $n$  by Avogadro's number ( $N_A = 6.022 \times 10^{23} \text{ electrons mol}^{-1}$ ) to obtain the number of electrons and then multiply it by the charge of electron ( $q = 1.60 \times 10^{-19} \text{ C electron}^{-1}$ ) to get the total charge:

$$Q = nN_A q = nF \quad (12)$$

Thus, Faraday's constant is actually  $N_A \times q$ .

The potential of a system to perform electrical work is measured by voltage, thus, the electrical work necessary to move a charge through an electrical potential difference  $E$  is

$$W_{elec} = EQ \quad (13)$$

If the charge is assumed to be carried by electrons, then combining Equations (11), (12) and (13) yields

$$\Delta G = -nFE \quad (14)$$

Thus, the Gibbs free energy sets the reversible voltage for an electrochemical reaction.

A reversible fuel cell voltage is the voltage produced by a fuel cell at thermodynamic equilibrium, however, standard-state reversible fuel voltages ( $E^0$ ) are only useful under standard-state conditions (room temperature, atmospheric pressure, unit activities of all species). Since fuel cells frequently operated under a variety of conditions, it is necessary to calculate the reversible voltage of a fuel cell under non-standard-state conditions. The most important variation for fuel cells occurs with reactant concentration.

In order to understand how the reactant concentration affects the reversible voltage, it is necessary to introduce the concept of chemical potential, which measures the Gibbs free energy change with the chemistry of the system.

$$\mu_i^\alpha = \left( \frac{\partial G}{\partial n_i} \right)_{T,p,n_{j \neq i}} \quad (15)$$

where  $\mu_i^\alpha$  is the chemical potential of a species  $i$  in a phase  $\alpha$  and  $\left( \frac{\partial G}{\partial n_i} \right)_{T,p,n_{j \neq i}}$  expresses the change of Gibbs free energy for infinitesimal changes of quantity of the species  $i$ . In other words, the Gibbs free energy changes by modifying the concentration of chemical species in a fuel cell. Chemical potential is related to concentration through *activity*  $a$ :

$$\mu_i = \mu_i^0 + RT \ln a_i \quad (16)$$

where  $\mu_i^0$  is the reference chemical potential of species  $i$  at standard-state conditions and  $a_i$  is the activity of the species  $i$ . For a dilute or ideal solution,  $a_i = c_i/c^0$  where  $c_i$  is the molar concentration of the species and  $c^0$  is the standard-state concentration. For non-ideal solutions,  $a_i = \gamma(c_i/c^0)$  where  $\gamma$  is a coefficient that describes departure from ideality with a value between

0 and 1. The activity of liquid water is usually taken as 1. The change in Gibbs free energy caused by changes in concentration of species  $i$  can be calculated by combining Equations (15) and (16):

$$dG = \sum_i \mu_i dn_i = \sum_i (\mu_i^0 + RT \ln a_i) dn_i \quad (17)$$

For an arbitrary reaction:



where A and B are the reactants, M and N are the products and 1, b, m and n are the number of moles of A, B, M and N respectively,  $\Delta G$  can be calculated from the chemical potentials of the various participating species:

$$\Delta G = \Delta G^0 + RT \ln \frac{a_M^m a_N^n}{a_A^1 a_B^b} \quad (19)$$

and by combining (14) and (19):

$$E = E^0 + \frac{RT}{nF} \ln \frac{a_M^m a_N^n}{a_A^1 a_B^b} \quad (20)$$

Thus, the general form of Equation (20) for a reaction with any number of products and reactants species is:

$$E = E^0 + \frac{RT}{nF} \ln \frac{\prod a_{Products}^v}{\prod a_{Reactants}^v} \quad (21)$$

where  $v$  is the stoichiometric coefficient. This is known as the Nernst equation and it describes the reversible electrochemical cell voltage as a function of the species concentration.

### 2.1.2 Kinetics

All electrochemical reactions involve the transfer of electrons between an electrode and a chemical species, therefore, the number of electrons per time (current) produced by a fuel cell, depends on the rate of the electrochemical reaction. Since electrons are either generated or consumed, the current resulting from the reaction is a direct measure of the reaction rate. In other words, current (in ampere) expresses the rate of charge transfer, according to Eq. (22) [22,91]

$$i = \frac{dQ}{dt} \quad (22)$$

where  $Q$  is the charge (C) and  $t$  is time.

Even if an electrochemical reaction is thermodynamically and energetically favorable, the reaction rate is finite because of an energetic barrier, called activation energy hinders the conversion of reactants to products. As illustrated in Fig. 2.6, the reactants must overcome the energetic barrier in order to be converted into products. The ease with which reactants overcome the barrier, determines the rate at which the reaction occurs. Even the most elementary reactions consist of a series of simpler steps, and each of these steps may occur at a different rate, thus the overall reaction rate will be limited by the slowest step in the series [22,91].

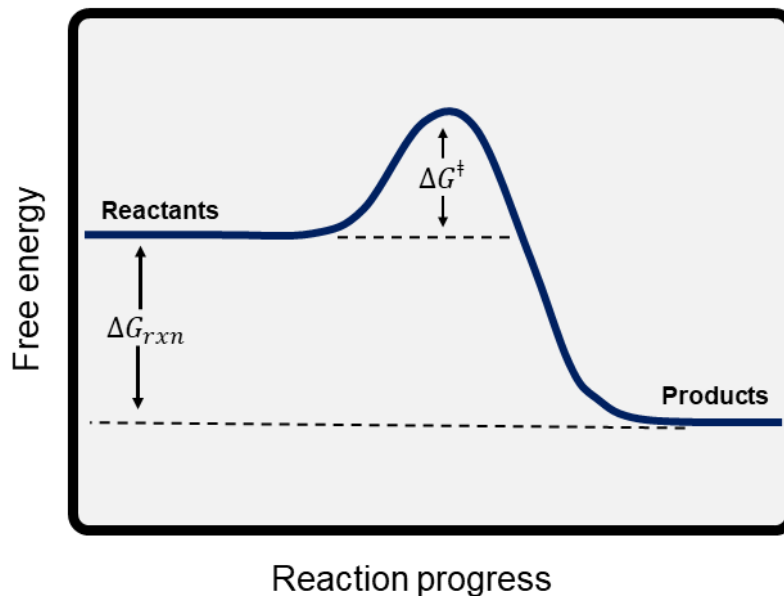


**Figure 2.6** Activation barrier ( $\Delta G^\ddagger$ ) impedes the conversion of products to reactants.

Only species in the activated state can undergo the transition from reactants to products, therefore, the reaction rate depends on the probability of find reactant species in the activated state ( $P_{act}$ ) [22]:

$$P_{act} = e^{-\Delta G_1^\ddagger/(RT)} \quad (23)$$

where  $\Delta G_1^\ddagger$  is the energy barrier between the activated state and reactant,  $R$  is the gas constant and  $T$  is the temperature in K. Determining the reaction rate is then a statistical process that

involves the number of reactants available for participating in the reaction, the probability of finding those species in the activated state and the frequency at which the activated species form products [22]:

$$J_1 = C_R^* \times f_1 \times P_{act} = C_R^* f_1 e^{-\Delta G_1^\ddagger / (RT)} \quad (24)$$

where  $J_1$  is the reaction rate in forward direction,  $C_R^*$  is the reactant surface concentration (mol cm<sup>-2</sup>) and  $f_1$  is the decay from activated species to products.

In order to evaluate the overall rate of a reaction ( $J$ ), the rates of both forward and reverse reactions must be considered. The net rate is given by the difference in these two rates [22]:

$$J = J_1 - J_2 \quad (25)$$

In general,  $J_1$  and  $J_2$  tend to not be equal, which means activation barriers of different magnitudes for the forward and reverse reactions, resulting in a greater reaction rate for one direction. Using Eq. 24, the reaction rate  $J$  can be expressed as

$$J_1 = C_R^* f_1 e^{-\Delta G_1^\ddagger / (RT)} - C_P^* f_2 e^{-\Delta G_2^\ddagger / (RT)} \quad (26)$$

where  $C_P^*$  is the product surface concentration and  $\Delta G_2^\ddagger$  is the activation barrier for the reverse reaction.  $\Delta G$  quantities are always calculated as *final state* – *initial state*. For both  $\Delta G_1^\ddagger$  and  $\Delta G_2^\ddagger$ , the final state is the activated state, which is always positive, thus Eq. 26 can be expressed in terms of only the forward activation barrier [22]:

$$J_1 = C_R^* f_1 e^{-\Delta G_1^\ddagger / (RT)} - C_P^* f_2 e^{-(\Delta G_1^\ddagger - \Delta G_{rxn}) / (RT)} \quad (27)$$

Eq. 27 expresses that the net reaction rate is given by the difference between the forward and reverse reaction rates, which are exponentially dependent on the activation barrier  $\Delta G_1^\ddagger$ .

Since electrochemical reactions occur at interfaces, the current produced is typically directly proportional to the reaction area, therefore it results convenient to measure the current per unit of area (current density), as it allows the comparison of reactivity of different surfaces. Current density  $j$  is typically expressed in amperes per square centimeter (A cm<sup>-2</sup>) [22,91].

$$j = \frac{i}{A} \quad (28)$$

where  $A$  is the area. Area-normalized reaction rates are usually expressed in units of moles per square cm per time ( $\text{mol cm}^{-2} \text{s}^{-1}$ ) (Farady's constant is necessary to convert a mole of electrons to charge in coulombs) [92]:

$$J = \frac{1}{A} \frac{dN}{dt} = \frac{i}{nFA} = \frac{j}{nF} \quad (29)$$

Therefore, the forward current density can be expressed as [22]:

$$j_1 = nFC_R^* f_1 e^{-\Delta G_1^\ddagger / (RT)} \quad (30)$$

and the reverse current as:

$$j_2 = nFC_P^* f_2 e^{-(\Delta G_1^\ddagger - \Delta G_{rxn}) / (RT)} \quad (31)$$

At the thermodynamic equilibrium, both reactions must balance, resulting in no net current density ( $j = 0$ )

$$j_1 = j_2 = j_0 \quad (\text{at equilibrium}) \quad (32)$$

$j_0$  is called exchange current density, and it indicates that at equilibrium, the net reaction rate is zero. This means that both forward and reverse reactions are taking place at a rate which is the value of  $j_0$  [22].

The free energy of charged species is sensitive to voltage, therefore, by varying the cell potential, it is possible to manipulate the size of the activation barrier. This concept is illustrated in Fig. 2.7, which depicts the phenomenon at the anode-electrolyte interface. It is shown that decreasing the Galvani potential by  $\eta$  reduces the forward activation barrier ( $\Delta G_1^\ddagger < \Delta G^\ddagger$ ) and increases the reverse activation barrier ( $\Delta G_2^\ddagger > \Delta G^\ddagger$ ). Note that the forward activation barrier is decreased by  $\alpha nF\eta$ , while the reverse activation barrier is increased by  $(1-\alpha)nF\eta$ , where  $\eta$  represents the voltage sacrificed to overcome the activation barrier. The value of  $\alpha$ , called transfer coefficient, depends on the symmetry of the activation barrier and it expresses how the change in electrical potential affects the size of the forward and reverse activation barriers. The value of  $\alpha$  is always between 0 and 1. For "symmetric" reactions,  $\alpha = 0.5$ , while for most electrochemical reactions, the value of  $\alpha$  ranges from 0.2 to 0.5 [22].

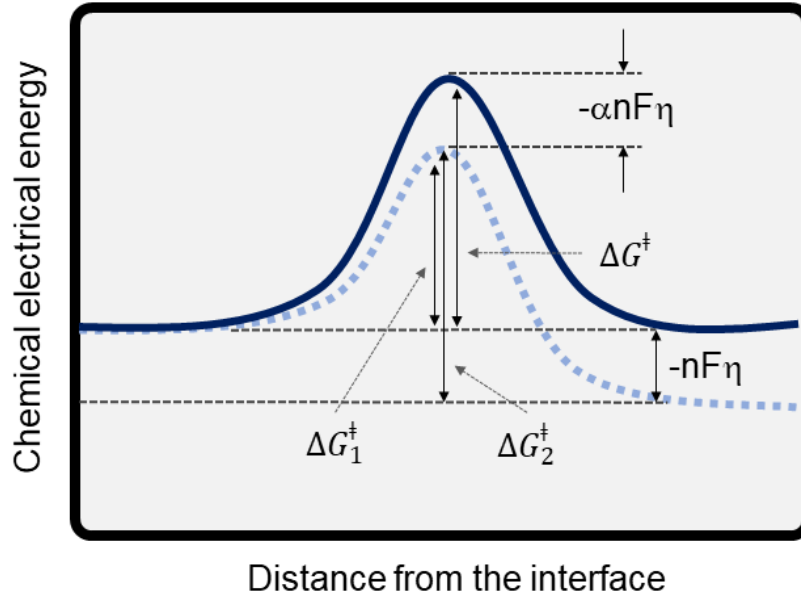


Figure 2.7 Effect of reducing the Galvani potential on the size of the forward and reverse activation barriers (Adapted from [22]).

Away from equilibrium, the forward and reverse reactions can be written by starting from  $j_0$  and taking into account the changes in the activation barrier of both reactions as follows [22,91]:

$$j_1 = j_0 e^{(anF\eta)/(RT)} \quad (33)$$

$$j_2 = j_0 e^{-(1-\alpha)nF\eta/(RT)} \quad (34)$$

And the net current ( $j_1 - j_2$ ) is

$$j = j_0 e^{(anF\eta)/(RT)} - e^{-(1-\alpha)nF\eta/(RT)} \quad (35)$$

Eq. (35) is known as the Butler-Volmer equation and it is considered as one of the foundations of the electrochemical kinetics [22], and it states that the current produced by an electrochemical reaction increases exponentially with activation overvoltage  $\eta$ . In a fuel cell, this means that obtaining more current will be achieved at the cost of voltage loss. This is known as the activation losses  $\eta_{act}$ , which is one of the losses that fuel cells undergoes, as mentioned in section 2.1.

In fuel cells, reaction kinetics inflict an exponential voltage loss, described by the Butler-Volmer equation and that is reflected on the  $j$ - $V$  curve of a fuel cell. Fig. 2.8 shows the effect of activation overvoltage on fuel cell performance. The curve starts from theoretical thermodynamic cell

voltage and the subsequent curves illustrate the subtraction of  $\eta_{act}$ , in other words, different values of  $j_0$ . It is observed that the voltage loss depends on the magnitude of  $j_0$ , therefore, having a high  $j_0$  is crucial for good fuel cell performance [22].

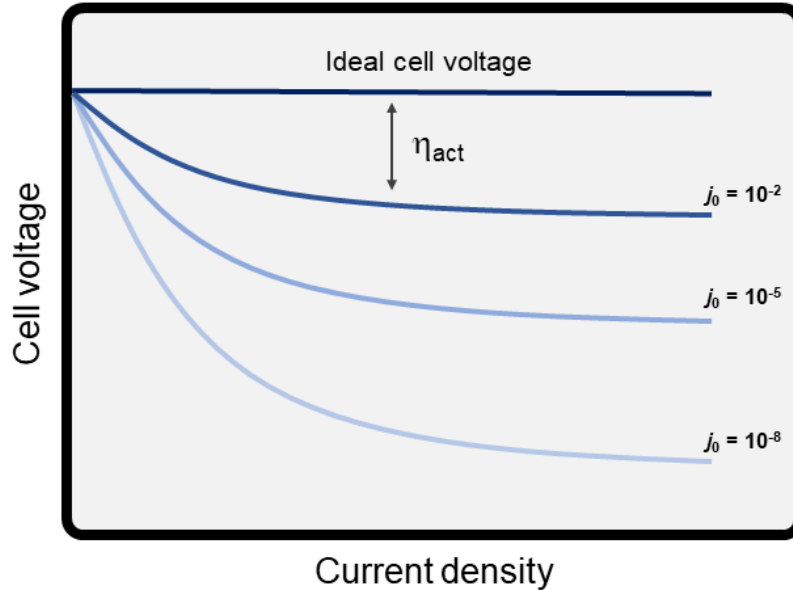


**Figure 2.8** Effect of activation overpotential on fuel cell performance.

In order to improve kinetic performance, it is necessary to increase  $j_0$ , which can be achieved through 4 major ways [22]:

1. *Increase the reactant concentration.*

The kinetic benefits of increasing the reactant concentration are significant, due to a linear impact, in contrast with the logarithmic form of the Nernst equation, in which an increase of concentration produces a minor thermodynamic benefit. However, decreasing the concentration also means significant unfavorable kinetic effect. This represents a challenge for the development of real fuel cells, for example, using air instead of pure oxygen causes 5x reduction of oxygen kinetics. Additionally, local decrease of reactant concentration caused by the reactions at the electrodes, results in further kinetic penalties.

2. *Decrease the activation barrier.*

A significant decrease of the activation barrier is achieved with a catalytic electrode, and since  $\Delta G_1^\ddagger$  appears as exponent, even small decreases cause large effects. A catalytic electrode lowers

the activation barrier by changing the free-energy surface of reaction, thus, the free-energy and activation barriers for given reactions depend on the nature of the electrode metal.

3. *Increase the temperature.*

A raise in the reaction temperature will increase the thermal energy available in the system. Higher thermal activity results in more energy for reactants and higher probability to reach the activated state, thus increasing the reaction rate. Modifying the temperature also has an exponential effect on  $j_0$ .

4. *Increase the number of possible reaction sites.*

Current densities are generally based on a plane or projected area, thus, if an electrode surface is extremely rough, the true electrode area may be significantly larger than the geometric area and potentially provide much more active sites for reaction. Since  $j_0$  represents reaction current per unit area, the effective  $j_0$  of a rough electrode will be greater than the  $j_0$  of a smooth electrode simply because of larger surface area.

### 2.1.3 Charge transport

There are two types of charged species involved in electrochemical reactions: ions and electrons. The transport of ions and electrons is essentially different due to the large difference in mass between the two of them. In fuel cells, ion transport is typically more difficult than electron transport [22,93,94], therefore, this section focuses on understanding ionic conductivity and how it affects fuel cell performance.

The rate at which certain species moves through a material is described in terms of *flux* ( $J$ ), which basically measures how much of a given quantity flows per unit area per unit time. In other words, flux is the normalization of flowrate by a cross-sectional area. One common type of flux is molar flux ( $\text{mol cm}^{-2} \text{ s}^{-1}$ ). Similarly, charge flux measures the amount of charge that flows through a material per unit time ( $\text{C cm}^{-2} \text{ s}^{-1} = \text{A cm}^{-2}$ ). Thus, charge flux is the same as current density [22]:

$$j = z_i F J \quad (36)$$

However, the quantity  $z_i F$  is necessary to convert molar flux  $J$  to charge flux  $j$ , where  $z_i$  is the charge number for the charge-carrying species and  $F$  is the Faraday's constant.

In all materials, an acting force is required for a charge transport to occur. In fuel cells, there are three major driving forces that induce charge transport: electrical driving forces (electrical potential

gradient  $dV/dx$ ), chemical driving forces (chemical potential gradient  $d\mu/dx$ ) and mechanical driving forces (gradient of pressure  $dP/dx$ ). In most fuel cells, the electrical driving force dominates the ion transport, thus, the governing equation for transport can be written as [22]

$$j = \sigma \frac{dV}{dx} \quad (37)$$

where  $j$  is charge flux (not molar flux),  $dV/dx$  is the electric field that provides the driving force and  $\sigma$  is the conductivity of the material.

Unfortunately, the charge transport in fuel cells is achieved at the cost of voltage loss due to the intrinsic resistance to charge flow of fuel cell materials. Consider a conductor material with cross-sectional area  $A$  and length  $L$ . Applying Eq. (37):

$$j = \sigma \frac{V}{L} \quad (38)$$

Solving for  $V$ :

$$V = j \left( \frac{L}{\sigma} \right) \quad (39)$$

An equation similar to Ohm's law ( $V = iR$ ) is obtained, and since charge flux and current are related by  $i = jA$ , Eq. 39 is rewritten as

$$V = i \left( \frac{L}{A\sigma} \right) = iR \quad (40)$$

$L/A\sigma$  is the resistance of the conductor and  $V$  is the voltage that must be applied in order to transport charge at a rate given by  $i$ . Therefore, this is the voltage that is lost in order to accomplish charge transfer. Since this voltage obeys Ohm's law, it is called "Ohmic loss", and it is denoted by  $\eta_{ohmic}$ . Both ionic and electronic transport are considered in the Ohmic loss:

$$\eta_{ohmic} = iR_{ohmic} = i(R_{elec} + R_{ionic}) \quad (41)$$

Ionic transport is generally more difficult than electron transfer, thus the ionic contribution to  $R_{ohmic}$  tends to dominate. From Eq. 40 it is noted that the operating voltage decreases linearly with resistance as current increases, which is illustrated in Fig. 2.9.

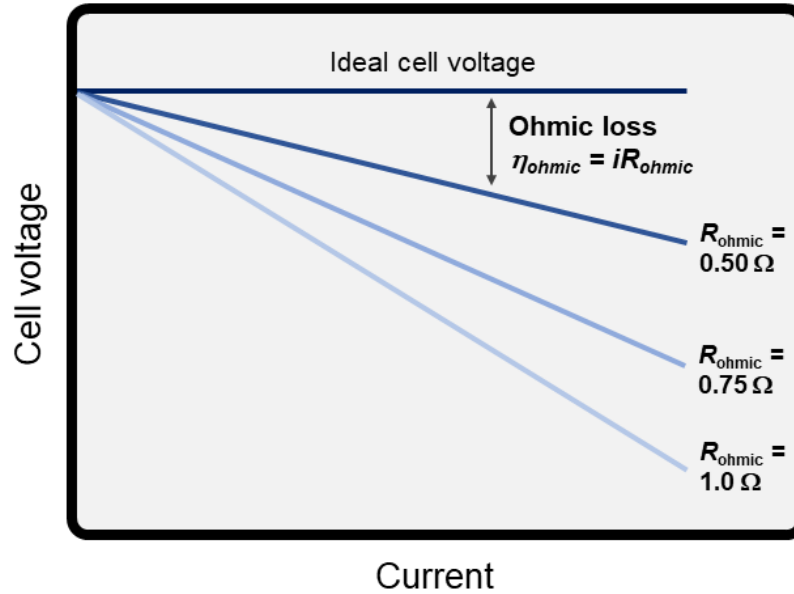


Figure 2.9 Effect of ohmic loss on fuel cell performance.

If the ionic resistance in a fuel cell is decreased, fuel cell performance will improve. In fuel cells, all the resistances are additive, consequently, the various resistances losses occurring at different points in the fuel cell will be all summed in series. However, the electrolyte resistance usually dominates, thus, bigger improvements in performance can be done by improving the electrolyte component [22,93].

Resistance scales with area, for this reason fuel cells are generally compared in per-unit-area basis using current density. By using area-specific resistance (ASR, units  $\Omega \text{ cm}^{-2}$ ), ohmic losses can be calculated from current density via [22]

$$\eta_{ohmic} = j(ASR_{ohmic}) \quad (42)$$

Resistance also scales with length (or thickness) of the ionic conductor. Ionic conductivity is orders of magnitude lower than electronic conductivity of metals, for this reason it is critical to minimize the resistance of the fuel cell electrolyte. In practical terms, that means to create the shortest path possible between the anode and the cathode in a fuel cell. There are some practical issues that restraint the thickness of the electrolyte [22]:

**Mechanical integrity:** applicable to solid electrolytes (membrane), means that if the membrane is too thin, it may be at risk of breaking, causing great damage to fuel cell operation.

**Uniformity:** Even if a membrane is mechanically sound, areas with thickness variations may become hot spots subject to deterioration and failure.

**Shorting:** Applicable to solid and liquid electrolytes, if they are extremely thin, there is the possibility of physical contact between the anode and the cathode, causing electrical shorting.

**Fuel crossover:** The reactant crossover may increase as the electrodes are closer. Fuel crossover leads to parasitic losses that considerably affect fuel cell performance.

As mentioned before, the total ohmic resistance of a fuel cell is the sum of all the resistances originated from different components of the device (Fig. 2.10), however, it is experimentally very difficult to determine the contribution of the various sources to the total resistance loss. This is basically due to variations in contact resistances, assembly processes and operation conditions [22]. Despite the experimental difficulties in pinpointing all the sources of resistance loss, it is known that the resistance of the electrolyte is the greatest contribution to the ohmic loss for most fuel cells devices [22,93].

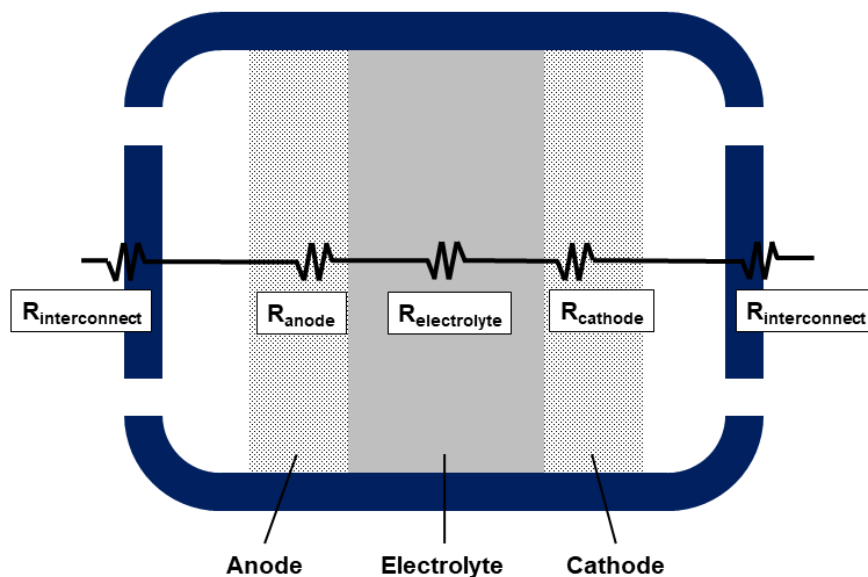


**Figure 2.10** The total ohmic resistance of a fuel cell is the sum of all the components resistances in series.

There are three major types of electrolyte materials: aqueous, polymer and ceramic electrolytes. Regardless of the class, any fuel cell electrolyte must meet the following requirements [22,93]:

- High ionic conductivity

- Low electron conductivity
- High stability in oxidizing and reducing environments
- Low fuel crossover
- Mechanical strength (if solid)
- Ease of manufacturability

This thesis addresses only ionic conduction in aqueous electrolytes, employed in membraneless fuel cells. An aqueous electrolyte is a water-based solution containing dissolved ions capable of transporting charge. In liquids, ions accelerate under the force of an electric field until frictional drag exactly counteracts the electric field force. The mobility of ions is determined by the ions size, charge and the liquid viscosity. KOH is the electrolyte of choice in alkaline fuel cells since it is extremely inexpensive and it exhibits the highest ionic conductivity of all the hydroxide compounds ( $0.03 \Omega^{-1} \text{ cm}^{-1}$  for a 0.1 M aqueous solution of KOH) [22].

#### **2.1.4 Mass transport**

Mass transport in fuel cells devices is the process of supplying reactants and removing products that result from the electrochemical reactions. Fuel cell mass transport mostly focuses on the study of the movement of uncharged species (reactants and products) within a fuel cell, rather than from an external fuel tank to the fuel cell. Unlike ion and electrons, uncharged species are unaffected by voltage gradients, therefore their transport must rely on convective and diffusive forces. Fuel cell performance is affected by reactant and product concentration within the catalyst layer, not at the fuel cell inlet, thus, reactant depletion at the catalyst results in significant fuel cell performance losses, denominated concentration loss or mass transport loss. This loss can be minimized by optimizing mass transport within the fuel cell flow structures and in the electrodes [22,93].

The difference between mass transport in fuel cell electrodes and in fuel cell flow structures is the length scale, which leads to different transport mechanisms. In flow structures, having geometrically well-defined channel arrays, dimensions are generally on the millimeter-centimeter scale, and reactant transport is dominated by fluid flow and convection. On the other hand, electrodes exhibit porosity and structures on the micrometer-nanometer scale. The tortuous geometry of electrodes insulate reactant molecules from the convective forces in flow structures, resulting in reactant transport dominated by diffusion [5,22].

The convective forces in the flow channels are imposed by the user, who feeds the fuel cell with reactants at a given rate, while concentration gradients that dominate diffusive transport in the electrodes develop due to species consumption/production within the catalyst layer. Inside flow channels, convection keeps the reactant stream well mixed and concentration gradients don't occur, however, in the absence of convective mixing (within the electrode), concentration gradients form from the stagnant reactant at the electrode, as illustrated in Fig. 2.11. The stagnant reactant region is called diffusion layer, and its thickness can vary, depending on the flow conditions, flow geometry and electrode structure. At very low reactant velocities, the diffusion layer may stretch out to middle of the flow channel or beyond. In contrast, at extremely high velocities, convective mixing may penetrate into the electrode [5].

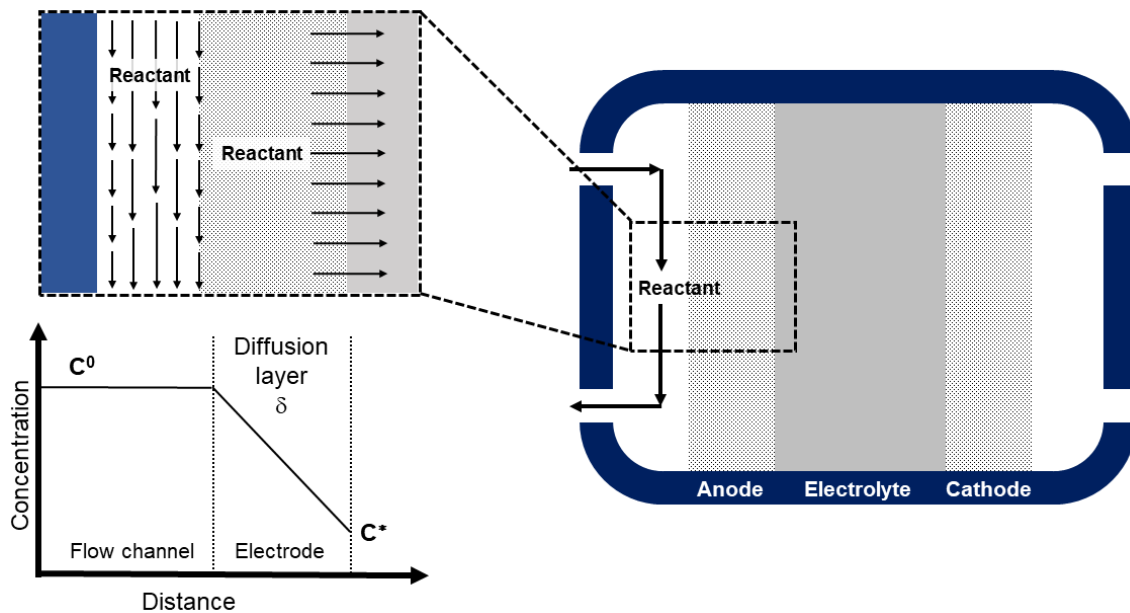


**Figure 2.11** Schematic of diffusion layer that develops at the anode of a fuel cell.  $C^0$  and  $C^*$  represent concentration at the bulk and at the catalyst layer, respectively (Adapted from [22]).

Diffusion is driven by electrochemical reactions, since the reactant depletion (and product accumulation) originates concentration gradients. The depletion of reactant causes 2 effects that contribute to the mass transport loss in fuel cells [22]:

**Nernstian Losses:** The reversible fuel cell voltage will decrease according to Nernst equation, due to the lower concentration of reactant at the catalyst layer, relative to the bulk concentration.

**Reaction Losses:** The activation losses will increase due to the lower concentration of reactant at the catalyst layer.

The resulting combination of these two effects is known as the fuel cell concentration (mass transfer) overvoltage,  $\eta_{\text{conc}}$ , which is the last of the three types of overvoltage (along with  $\eta_{\text{act}}$  and  $\eta_{\text{ohmic}}$ , mentioned in section 2.1) that contribute to the shape of  $i$ - $V$  curves for fuel cells.

In order to determine the magnitude of the concentration loss, it is fundamental to study the reactant concentration differential between the bulk and the catalyst layer. Fig. 2.12 illustrates the reactant and product concentration profiles as they evolve with time [22]. It is observed that at  $t = 0$ , the reactant and product concentration is constant. However, at  $t \neq 0$  reactants begin to diffuse towards the catalyst layer and products diffuse away from the catalyst layer, leading to depletion of reactants and accumulation of products. Eventually, the reactant and product profiles drop linearly across the electrode, when a steady-state situation is reached. At steady-state, the flux of reactants will exactly match the depletion rate at the catalyst layer, in other words, the rate of consumption must equal the rate of supply, described by [22]

$$j = nFJ_{\text{diff}} \quad (43)$$

Where  $j$  is the operating current density of the fuel cell,  $J_{\text{diff}}$  is the diffusion flux of reactants to the catalyst layer and  $nF$  is required to convert the molar diffusion flux into the units of current density.

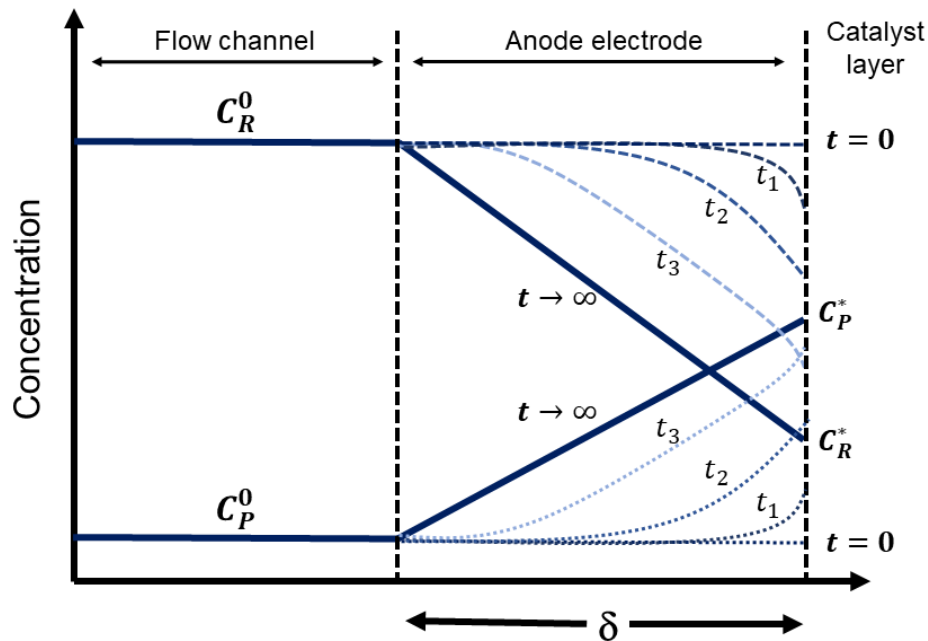


Figure 2.12 Time dependence of reactant and product concentration profiles at fuel cell electrode (Adapted from [22]).

$J_{diff}$  can be calculated by Fick's first law [22]

$$J_{diff} = -D \frac{dc}{dx} \quad (44)$$

For the steady-state situation, eq. 44 becomes [22]

$$J_{diff} = -D^{eff} \frac{C_R^* - C_R^0}{\delta} \quad (45)$$

where  $C_R^*$  is the reactant concentration at the catalyst layer,  $C_R^0$  is the reactant concentration at the flow channel,  $\delta$  is the diffusion layer thickness and  $D^{eff}$  is the effective reactant diffusivity in the catalyst layer. The effective diffusivity describes the diffusion in porous structures and, taking into account the blockage caused for the porosity and tortuosity of the material, and it is determined by [22]

$$D^{eff} = \varepsilon^\tau D \quad (46)$$

where  $\varepsilon$  and  $\tau$  are the porosity and tortuosity of the porous structure, respectively, and  $D$  is the diffusion coefficient of a species in a determined medium. By combining equations 43 and 45, and solving for the reactant concentration at the catalyst layer:

$$j = nFD^{eff} \frac{C_R^* - C_R^0}{\delta} \quad (47)$$

$$C_R^* = C_R^0 - \frac{j\delta}{nFD^{eff}} \quad (48)$$

The limiting case for mass transport is reached when the reactant concentration at the catalyst drops to zero, therefore the fuel cell cannot sustain higher current density than that which causes the concentration fall to zero. This is called limiting current density of a fuel cell, and it can be calculated from Equation (47) by setting  $C_R^* = 0$

$$j_L = nFD^{eff} \frac{C_R^0}{\delta} \quad (49)$$

Some strategies can be implemented in order to increase the limiting current density: Ensuring a high  $C_R^0$ , or ensuring that  $D^{eff}$  is large (about  $10^{-2} \text{ cm}^2 \text{ s}^{-1}$ ) and  $\delta$  is small (100 – 300  $\mu\text{m}$ ). A fuel cell will not be able to produce a higher current density than its calculated limiting current density,

however, due to other fuel cell losses, such as activation and ohmic losses, the fuel cell voltage may be reduced to zero before reaching the limiting current density.

The effect of the  $\eta_{conc}$  on the  $j$ - $V$  curves of fuel cells is illustrated in Fig. 2.13. As observed in the curves, the concentration loss only significantly affects fuel cell performance at high current density, this is, when  $j$  approaches  $j_L$ . However, since the effect is abrupt and severe, the onset of concentration loss practically marks the limit of the operating range of a fuel cell.

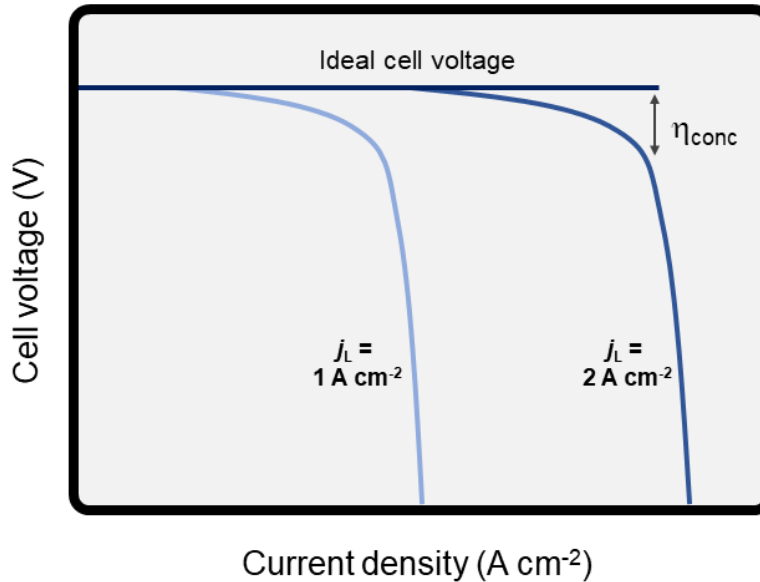


Figure 2.13 Effect of concentration loss on fuel cell performance.

## 2.2 Types of fuel cells

As mentioned in chapter 1, fuel cells are greatly versatile, capable of operating with a variety of fuel, electrolytes and within different ranges of temperature. The specific features of each type of fuel cell are dependent on their target application, for example, in transportation, where volume is not the main constraint, fuel cells feed with hydrogen are employed. Similarly, for stationary applications, where high power is required and temperature operation is not very restrictive, solid oxide fuel cells (SOFC) are preferred. On the other hand, for portable applications, where volume is very limited and room temperature operation is necessary, fuel cells using hydrogen-rich liquid fuels are more promising. For this reason, this section focuses only on discussing those types of fuel cells that are able to operate with liquid fuels at room temperature.

### 2.2.1 Proton-exchange membrane fuel cell (PEM-FC)

As mentioned in chapter 1, the most studied type of fuel cells is the denominated PEM-FC, since its operation is based on a proton-exchange membrane to separate the two half-reactions, anodic and cathodic. The hydrogen-fed PEM-FC is considered to be the pioneer of this type of fuel cells, however, they can also operate with liquid fuels without major changes in the main components. Fig. 2.14 shows the most important parts of a PEM-FC and their functions [95].

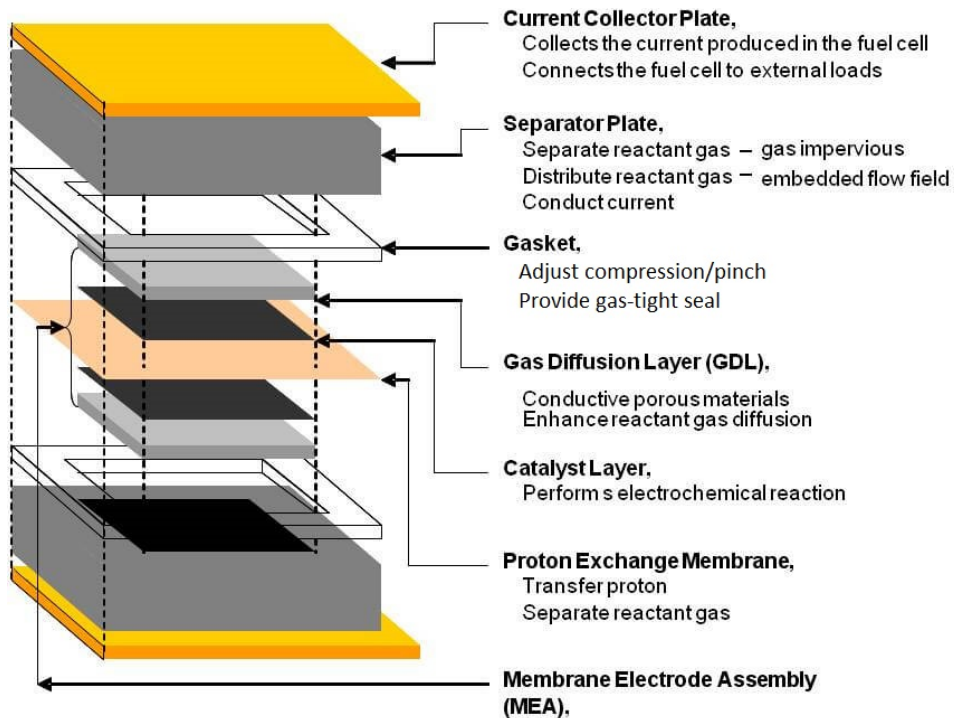


Figure 2.14 Schematic of PEM-FC main components [95].

The membrane is in charge of separating the anodic and cathodic reactions and conducting only positively charged ions from the anode to the cathode while impeding the pass of electrons [22]. In a PEM-FC, the membrane is typically found in the form of a membrane-electrode assembly (MEA), which is composed of membrane and the catalysts. A catalyst layer, typically a nanoparticulate material, is dispersed on a high-surface-area carbon support and then added on both sides of the membrane, anode on one side and cathode on the other [96]. The function of the catalysts is to perform the electrochemical reactions. The gas diffusion layers (GDL) sit next to the catalyst layers and they are in charge of facilitating the transport of reactant into the catalyst layer, as well as product removal. There are two GDLs, one at the cathode and one at the anode, and they are typically composed of a sheet of carbon paper, 100–300  $\mu\text{m}$  thick. The carbon fibers

are partially coated with polytetrafluoroethylene in order to make the paper hydrophobic and to prevent excessive water buildup [96]. There are also two flow plates, one at the anode and one at the cathode, and their function is to deliver and distribute the reactants within the cell. Additionally, the flow plates serve as bipolar plates, necessary when multiple MEAs are connected in series, as the plates separate the unit fuel cells and provide electrical conduction between cells [96].

The greatest challenges that the industry of PEM-FC face are related to the cost and durability of the fuel cell components. The lifetime of a PEM-FC is generally limited by the membrane degradation due to the physical and chemical damage sustained during operation. Besides, the membrane needs adequate hydration in order to provide good ionic conductivity. On the other hand, water excess prevent the reactants to reach the catalytic active sites [43]. This requires intricate water management systems that ultimately add complexity to the overall fuel cell operation. For these reasons, researchers have tried to develop fuel cells systems without membrane in order to simplify the operation and increase the durability of such systems.

### 2.2.2 Membraneless microfluidic fuel cell (ML- $\mu$ FFC)

The concept of membraneless microfluidic fuel cell (ML- $\mu$ FFC) was developed as a response to the numerous challenges related to the operation and miniaturization of PEM-FCs. Microfluidic fuel cells, also known as laminar flow fuel cells grant the opportunity to overcome the issues related to the membrane in PEM-FCs, since, as the name itself suggest, these devices lack a membrane in their constitution. Microfluidic fuel cell technology eliminates the need for a membrane by employing laminar flow of reactants at the microscale level. The configuration of laminar flow in a ML- $\mu$ FFC can be [5]:

- 1) **A single stream of electrolyte:** in this configuration, the membrane is replaced by an electrolyte stream in a microchannel. This configuration is suitable for cells using gas reactants, such as hydrogen and oxygen.
- 2) **Two parallel streams of fuel and oxidant:** This configuration is the most employed in fuel cells with liquid fuels and oxidants. The reactants in separate electrolytes streams flow parallel due to low Reynolds number, preventing them from mixing.
- 3) **Three parallel streams fuel, oxidant and electrolyte:** Similar to number 2, the liquid fuel, oxidant and electrolyte run down a microchannel in co-laminar flow.

This section focuses on the second configuration, as it is the most commonly used with liquid fuel and oxidant in aqueous electrolytes and the most developed type of ML- $\mu$ FCC. Each stream contains an electrolyte that facilitates the ionic transport between the electrodes, while the fuel and oxidant are transported separately by convective forces [57]. Fig. 2.15 shows the schematic of the ML- $\mu$ FCC presented by Choban et al. in 2004, one of the first works on the subject. It consists of a Y-shape microchannel with the electrodes on the walls [33]:

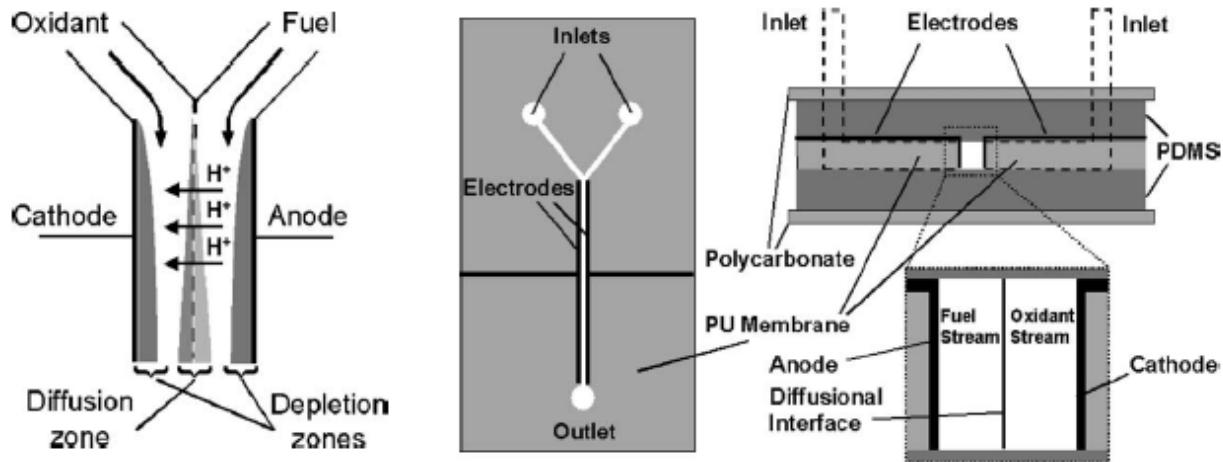


Figure 2.15 Schematic of the co-laminar flow based fuel cell presented by Choban et al. [33].

Microfluidics is the subject of fluid flow in microscale, formally defined as the study and application of fluid flow in microstructures with at least 1 dimension (X, Y or Z) in the range of 1–1000  $\mu\text{m}$  [5]. Fluid flow in microscale conduits is generally laminar, which is characterized by low Reynold's number  $Re$  [5]:

$$Re = \frac{\rho \bar{u} L}{\mu} \quad (50)$$

where  $\bar{u}$  is the fluid velocity,  $\rho$  is the density of the fluid,  $L$  is the hydraulic diameter and  $\mu$  is the fluid dynamic viscosity. As mentioned in chapter 1, ML- $\mu$ FCC rely on the fuel-oxidant interface instead of a membrane to separate the two half-reactions. At low  $Re$  (under 1000), the fuel and oxidant streams will run parallel down a single microfluidic channel without mixing (co-laminar flow). Exceeding the laminar flow threshold will result in turbulent flow, destabilizing the co-laminar interface and leading to mixing and loss of cell voltage.

Microfluidic laminar flow allows a great extent of control over the fluid interfaces and provides unique functionality, such as allowing the study of chemical reactions and transport phenomena

in real time [5]. In a ML- $\mu$ FFC, species transport can occur through convection, diffusion and electromigration, however, in absence of electromigration, the mixing between streams occurs by crosswise diffusion alone [5]. Microscale devices generally experience high Péclet numbers [5]

$$Pe = \frac{UD_h}{D} \quad (51)$$

where  $D$  is the diffusion coefficient. High  $Pe$  indicates that the rate of mass transfer due to crosswise diffusion is much lower than the streamwise convective velocity. In a ML- $\mu$ FFC, diffusive mixing is restricted to a thin region at the center of the microchannel. This region is depicted in Fig. 2.15 and it has an hourglass shape with maximum width at the walls of the channel. For this reason, the length of the microchannel and the position of the electrodes are constrained by the width of the co-laminar interdiffusion zone. This means that the electrodes must be sufficiently separated from the interface in order to prevent mixed potentials and reactant crossover. Additionally, the position and orientation of the electrodes influence the fuel utilization and overall performance of the fuel cell [5,22].

As to the evolution of the ML- $\mu$ FFCs, it was mentioned that one of the first proof-of-concept designs was the one reported in 2004 by Choban et al. (Fig. 2.15) [33]. This device was tested at room temperature using 2.1 M HCOOH as fuel and oxygen-saturated 0.5 M H<sub>2</sub>SO<sub>4</sub> oxidant at different flow rates, reaching an OCV of 0.4 V and 0.17 mW cm<sup>-2</sup> of maximum power density. Several variations of the original concept, mainly on the microchannel layout and position of electrodes have been introduced over the last 15 years. Fig. 2.16 shows the primary membraneless fuel cells developments. Although all of them employ co-laminar flow of 2 streams, they differ in architecture, materials employed and fabrication methods. Fuel cell designs shown in Figures 2.16a and 2.16b are monolithic cells with electrodes placed on the floor and on the walls of the microchannel, respectively. On the other hand, the design shown in Fig. 2.16c introduces an air-breathing cathode, which is in essence a porous, hydrophobic material as support for the cathode. The introduction of air-breathing cathodes facilitated the oxygen constant supply from the atmosphere to the cathode. In 2008, Kjeang et al. demonstrated that reactant streams passing through porous electrode materials are able to maintain laminar flow. They introduced flow-through electrodes in fuel cells (Fig. 2.16d) resulting in a significant increase of fuel utilization [97]. Most recent fuel cells developments include the use of flow-through electrodes combined with air-breathing cathodes.

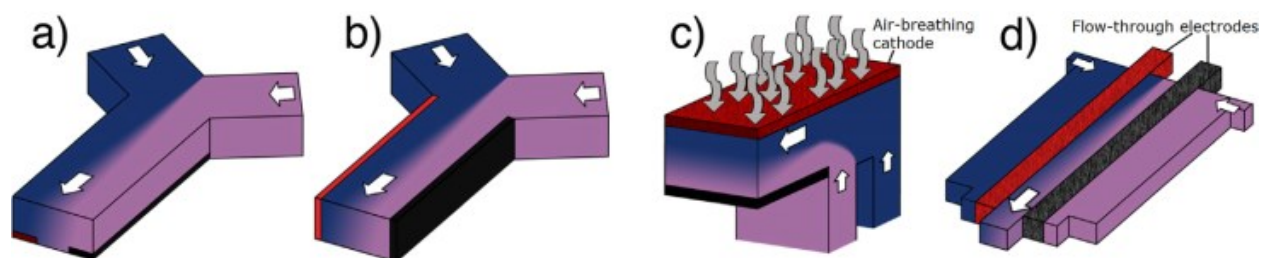


**Figure 2.16 Primary co-laminar flow fuel cells developments: a) monolithic with electrodes on floor, b) monolithic with electrodes on walls, c) F-channel with air-breathing cathode and d) monolithic with flow-through electrodes [97].**

Moreno-Zuria et al. reported the fuel cell performance evolution based on the different architectures developed over the years. Using formic acid as fuel, they evaluated a first generation ML- $\mu$ FFC, similar to that reported by Choban in 2004, and they subsequently developed new generation of fuel cells employing porous electrodes and a variety of microchannel architectures. Their results showed that with the use of porous electrodes and an air-breathing cathode it was possible to increase the power up to 900% in comparison with the first generation ML- $\mu$ FFC, while reducing the device dimensions by approximately 50% [98].

Numerous co-laminar fuel cells architectures have been reported over the last decade, typically as proof-of concept for different electrode materials and microchannel structures, however, single cells have insufficient voltage and power output for real applications. For practical applications, the fabrication of microfluidic stacks is necessary, nevertheless, the development of co-laminar stacks is challenging due to the need for efficient flow structures and manifolding in spatial-efficient cells arrays. One of the biggest limitations lays on the pre-requisite of maintaining a co-laminar reactant flow, which renders the use of passive ML- $\mu$ FFC impossible. It is at this point where a different fuel cell concept, such as mixed-reactant fuel cell, plays an interesting role.

### **2.2.3 Mixed-Reactant fuel cell (MRFC)**

Conventional fuel cells require a separator, either a membrane or a liquid-liquid interface to separate the anodic and cathodic reactions. In that sense, mixed-reactant fuel cells are unconventional fuel cells, since they break from the conventional paradigm by combining the fuel and oxidant in a single mixed stream [99]. The modern concept of a MRFC derives from the original notion from around half a century old. In essence, a single compartment vessel containing the reactants in an electrolyte with selective electrodes submerged in it, is a mixed-reactant fuel cell [64], however, such system is not practical. Modern MRFCs devices, also known as compact

mixed reactant, single chamber or separator-free fuel cells, are similar in external structure to the fuel cells devices previously discussed, however, they exhibit some particular features that make of MRFCs a potential solution to the challenge of fuel cell stack development for portable devices. Since the reactants are mixed in a single stream, MRFCs rely on the use of selective catalysts to perform the electrochemical reactions, while the fuel and oxidant are allowed to flow through a fully porous anode-cathode structure [61,64]. In theory, this structure may be planar, tubular or other geometry with the possibility of stacking cells in series or parallel configurations. MRFCs are extremely versatile and flexible in operation, since, in principle, they may be based on acidic, alkaline, molten carbonate, solid oxide or other type of fuel cell chemistry [64]. However, in all cases, the main requirements are for the anode to be selective to the fuel oxidation and for the cathode to be selective to the oxidant reduction.

The key advantages of MRFCs over conventional fuel cells for the development of stacks are [64]:

- 1) Simplified manifolding that results in more compact designs.
- 2) Surface strip geometry enables series cells connections and reactant exposure only on one side of the structure.
- 3) Possibility of employing thin-film fuel cell structure.
- 4) Closing stacking of thin-film cell and strip-cell geometries, resulting in higher volumetric power density.
- 5) Reduced amount of components that translate into lower fabrication costs.
- 6) Simple operation and more reliable systems due to reduced sealing requirements.

In comparison with PEM-FCs, a stack made of MRFCs may present a volume reduction as high as 80-90% and a reduction in cost of about 30-60% [64].

Among the most representative MRFCs developed in recent times, we find the device reported by Calabrese-Barton et al. which consists of a strip-cell architecture [61] that allows a straightforward stacking strategy, as shown in Fig. 2.17. This fuel cell had an active area of 32 cm<sup>2</sup> and it was continuously fed by aqueous methanol containing a constant supply of oxygen. The device performed decently in terms of OCV when compared with a typical 2-streams cell, however it was found a high ohmic resistance between neighboring cells.

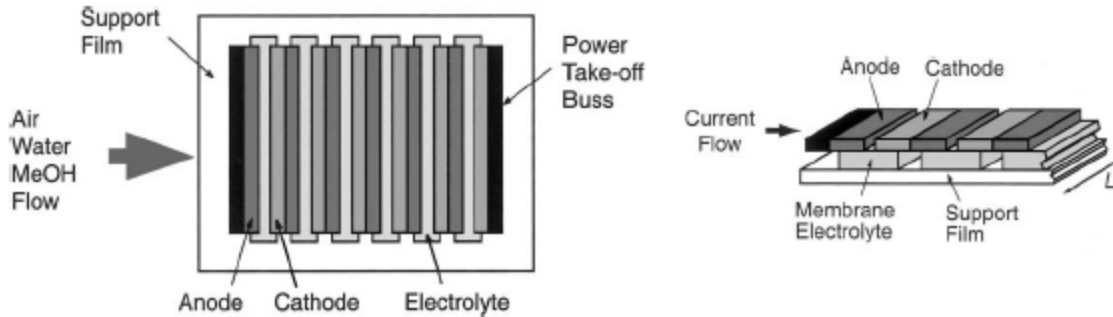


Figure 2.17 Mixed-reactant strip cell concept [61].

Another representative MRFC is the Swiss-roll liquid-gas mixed-reactant fuel cell, reported by Aziznia et al. [65], which consists of two fuel cells stacked in a cylindrical fashion made with flexible materials (Fig. 2.18). This device had an active area of 40 cm<sup>2</sup> and it operated with a liquid-gas mixture of borohydride-oxygen at 50 °C, achieving a maximum power density of 100 mW cm<sup>-2</sup>.

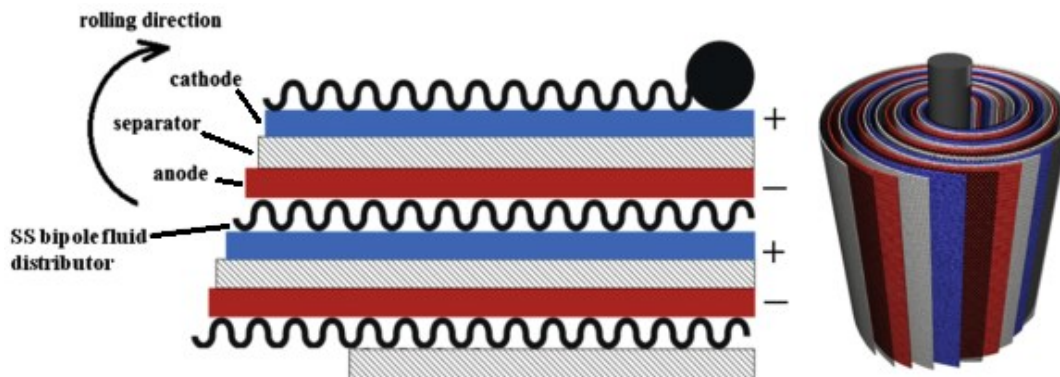


Figure 2.18 Cross-section of construction of the 2-cell Swiss-roll MRFC [65].

More recently, in 2019, researchers from Mantra Energy Alternatives Ltd, developed a 19-cell MRFC stack fueled by 2-phase mixture of alkaline potassium formate at 60 °C [99]. The device had a total active area of 665 cm<sup>2</sup> and it achieved a maximum power output of 120 W. They further connected three 19-cell stacks to a 250 W electric motor and were able to power an electric scooter for 15 min at 10 km h<sup>-1</sup>, being the first time that MRFCs are used for powering a vehicle.

Despite the aforementioned advantages, the development of MRFCs has not been as prolific as other type of fuel cell devices, especially when it comes to portable applications. To date, most of the fuel cell research for portable devices focuses on co-laminar fuel cells, however, as mentioned

before, those devices require a constant flow of reactant to maintain the co-laminar flow. This is achieved by the use of external pumps, which is ultimately an energy loss to the general balance, besides increasing considerably the overall volume of the system. Nevertheless, MRFCs are not affected by this restriction, as they don't require co-laminar flow and therefore, can operate in passive mode. For this reasons, we believe that MRFCs are a true alternative for developing a miniaturized new power source for portable applications.

#### **2.2.4 Direct methanol fuel cell (DMFC)**

The direct methanol fuel cells surged originally as a subcategory of PEM-FCs, in which methanol is used as fuel. In contrast with indirect methanol fuel cells, where methanol is reformed before being fed to the FC, DMFCs use aqueous solutions of methanol, typically around 1 M fed directly to the FC, while oxygen, either pure or from the air is used as oxidant. In comparison with hydrogen PEM-FCs, the efficiency of DMFCs is lower (around 20%), so they are targeted mainly to portable applications, where safety and ease of operation are more important than efficiency. Their main advantage over hydrogen FCs is the high energy density, relatively high stability and ease of transport of methanol [32,88,100].

The electrochemical reactions that occur in a DMFC in acidic and alkaline media are established in Chapter 1, Equations (1) to (5), having a thermodynamic cell voltage of a DMFC is 1.21 V [32]. In practice, this value is lower due to several irreversible losses, as in all fuel cells, however, there exists a significant loss that is exclusive of DMFCs, called the methanol crossover effect [41]. DMFCs employ typically PtRu anodes to perform the methanol oxidation reaction, while Pt catalysts are employed as cathode for performing the oxygen reduction reaction. In order to obtain a cell voltage as close as possible to the thermodynamic value, the two reactions must be performed separately, which is achieved by using a membrane in PEM-FCs or a liquid-liquid interface in membraneless fuel cells, however, methanol molecules tend to diffuse from the anode to the cathode through the membrane or through the co-laminar interface. Since the cathode is active to methanol, it will also oxidize the methanol that crosses over from the anode, resulting in mixed potentials at the cathode due to competition with the ORR. The methanol crossover is one of the greatest contribution on the inefficiency of DMFCs [70,101]. Consequently, researchers are actively working on finding ways to diminish the harmful effects of methanol crossover.

### 2.2.5 MR- $\mu$ DMFC

So far in the present thesis, it has been established that microfluidic fuel cells are strong candidates for developing an alternative compact power source for portable applications due to their miniaturized dimensions. Additionally, the advantages of using methanol as fuel for portable devices are well known. Therefore, after learning about the advantages of MRFCs over the ML- $\mu$ FFCs, the possibility of developing a miniaturized MRFC fueled by methanol turns out very attractive. By merging the concept of MRFC with microfluidics and the use of direct methanol, the result is naturally a MR- $\mu$ DMFC. Interestingly, this idea has not been exploited by the scientific community. The main limitation for developing a MR- $\mu$ DMFC lies in finding an efficient cathode material that is not active to methanol oxidation. Pt is generally used as cathode in DMFCs, however, pure Pt catalysts are not suitable for use in a MR- $\mu$ DMFC as Pt is active to both MOR and ORR, and the first requirement for MRFC is to have selective catalysts. Therefore, if a new cathode material with high catalytic activity towards the ORR and no activity towards the MOR is synthesized, it would be possible to apply microfluidics and develop a MR- $\mu$ DMFC. Moreover, given the advantages of MRFCs in terms of simplicity, it would be also possible to design and fabricate a MR- $\mu$ DMFC stack that has simple design and operation.

## 2.3 Oxygen Reduction Reaction (ORR)

Oxygen electrocatalysis has been extensively studied in the fields of electrochemistry due to its importance for energy conversion and storage and to the increasing demand for renewable technologies, such as metal-air batteries and fuel cells [102]. In fuel cell devices based on oxygen electrochemistry, such as hydrogen PEM-FC and DMFC, the oxygen reduction reaction (ORR) is the reaction occurring at the cathode, and it is recognized as the kinetically limiting component for said devices. To accomplish high energy conversion efficiency, the use of electrocatalysts is necessary in order to perform the ORR with an overpotential as close as zero as possible with a satisfactory reaction rate, yet, the ORR exhibits sluggish kinetics at practically all catalysts materials [36].

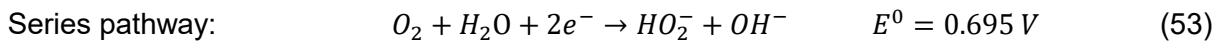
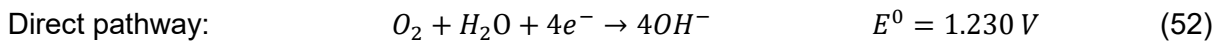
To date, Pt is the most used catalyst material for ORR due to its high catalytic activity and relatively low overpotential, but the inconvenient is the high cost and low abundance of the precious metal [103]. Despite, most of the fundamental studies for understanding the ORR has been done on Pt electrocatalysts, as is the most viable cathode material for hydrogen PEM-FCs and DMFCs. Due to the cost of Pt, the efficiency of a Pt catalyst for ORR is evaluated through the current obtained per Pt mass at a fixed potential. This ratio is called the mass activity [104].

Therefore, intense research has been undertaken with the objective of improving the intrinsic activity of Pt towards the ORR. This will allow to reduce the Pt loading at the electrodes without compromising fuel cell performance [37].

The ORR is a multi-electron process, highly irreversible in aqueous solution and it consists of multiple elementary reaction steps involving adsorption/desorption of oxygen-containing species, such as  $O$ ,  $OH$ ,  $O_2^-$ ,  $HO_2^-$  and  $H_2O_2$ . The ORR on Pt-based catalysts in aqueous solutions proceeds mainly by two pathways: direct reduction from  $O_2$  to  $H_2O$  by a 4-electron transfer or a 2-electron reduction from  $O_2$  to  $H_2O_2$ , which can be followed by a further reduction of  $H_2O_2$  to  $H_2O$  by another 2-electron transfer [36,105].

### 2.3.1 ORR in Alkaline media

Studying the ORR mechanism and kinetics is complicated not only because of the multiple reaction steps, but also because of the great influences from the pH value [106], solvation and polarity of water [107]. There exists some advantages of using alkaline media over acidic media for performing the ORR, for example, ORR kinetics is more rapid in alkaline media than in acidic media [36]. Alkaline media confers reduced adsorption energies of anions, which enables surface-independent outer-sphere electron transfer processes during the first stage of ORR [36,108]. Moreover, alkaline media provides a less corrosive environment to the catalysts. Similar to acidic media, the ORR on Pt catalysts in alkaline media has been identified to occur via direct and series pathways mechanisms [105]:



In order to study the ORR mechanism and the difference between acidic and alkaline media, it is important to understand the double layer structure of the electrode-electrolyte interface during ORR. In alkaline media, water molecules serve as solvent and as the source of protons required for ORR. In alkaline media, inner Helmholtz plane (IHP) is populated by adsorbed hydroxyl species, solvent water dipoles and chemisorbed  $O_2$ , whereas alkali metal ions are solvated and are expected to be found at the outer Helmholtz plane (OHP), as illustrated in Fig. 2.19 [109].

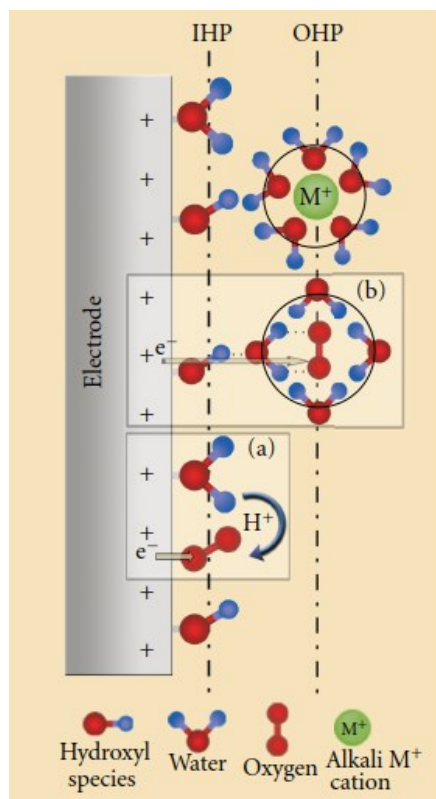
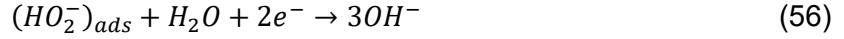
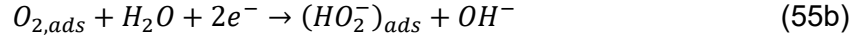
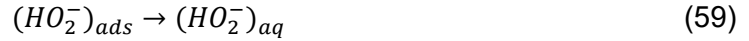
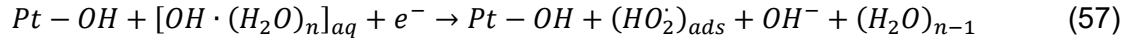


**Figure 2.19** Illustration of double-layer structure during ORR in alkaline media. Insets (a, b) illustrate the inner and outer sphere electro transfer processes [109].

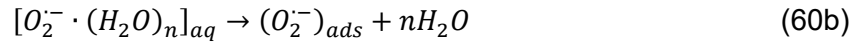
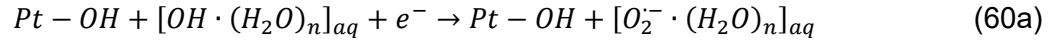
In the case of inner-sphere electron transfer mechanism (inset (a) of Fig. 2.19) during ORR, the mechanism involves strong chemisorption of molecular  $O_2$  on Pt active sites, followed by a  $4e^-/4H^+$  transfer. This stage of the mechanism is common to both acidic and alkaline media, however, the outer-sphere mechanism (inset (b)) appears to be unique to the alkaline conditions [109]. The solvated molecular  $O_2$  interacts with the adsorbed hydroxyl species via a hydrogen bond between the hydrogen atom in the hydroxyl and oxygen in the solvent. Such hydrogen bond stabilizes the solvated  $O_2$  in the OHP and promotes outer-sphere electron transfer to form superoxide species. Based on the evidence of the outer-sphere involvement, two ORR mechanisms in alkaline media have been proposed in the literature. The first one is the well-known inner-sphere mechanism, where  $O_2$  undergoes chemisorption at Pt sites, resulting in a direct  $4e^-$  path without desorption of intermediates like peroxide [109]:



The second proposed mechanism is the outer-sphere electron transfer, where solvated  $O_2$  weakly interacts with adsorbed hydroxyl species and a  $2e^-$  transfer is promoted, resulting in  $HO_2^-$  anion as a product that desorbs from the surface [109]:



Equation (57) involves other elementary steps:



$O_{2,aq}$  forms  $(O_2^{\cdot-})_{aq}$  through an electron transfer, followed by desolvation and adsorption on the oxide substructure of Pt to form  $(O_2^{\cdot-})_{ads}$ , where adsorbed hydroperoxyl radical is formed  $(HO_2^-)_{ads}$ . A second electron transfer to  $(HO_2^-)_{ads}$  forms  $(HO_2^-)_{ads}$ , which has a low binding energy on the oxide substructure of Pt. This leads to facile desorption of  $(HO_2^-)_{aq}$  anion. The interaction between  $OH \cdot (H_2O)_n$  and hydroxyl species at the surface causes certain nonspecificity with respect to the underlying catalyst metal. This nonspecificity results in the possibility of using a wide range of non-noble metals and metal oxides to perform the ORR in alkaline media [109].

## 2.4 Methanol Oxidation Reaction (MOR)

As mentioned in chapter 1, DMFCs are a potential alternative to hydrogen fed fuel cells due to the methanol high energy density and ease of storage and transportation of the liquid fuel. However, in practice, the true potential of DMFCs has not been exploited due in part to the kinetic limitations related to the MOR [110].

### 2.4.1 MOR in acidic and alkaline media

The electrooxidation of methanol on Pt and Pt-based materials has been exhaustively studied over the last 3 decades [111,112], and it can be represented by the general reaction mechanism displayed in Fig. 2.20 [113].

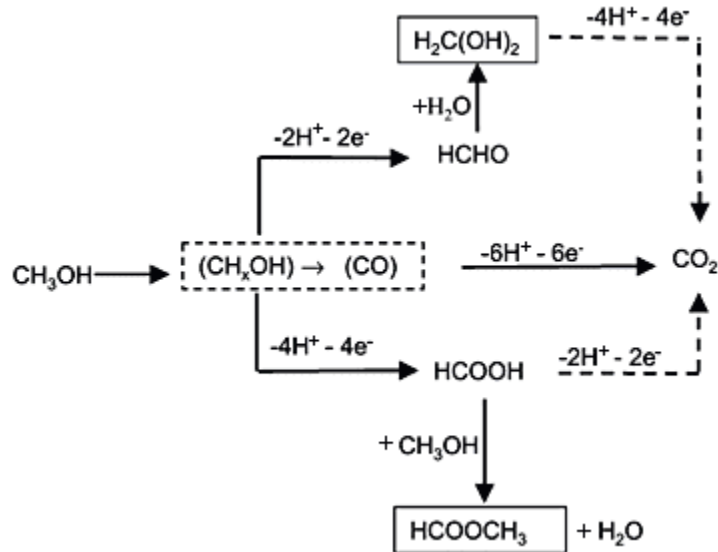
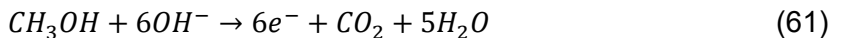


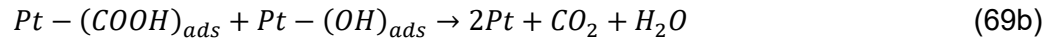
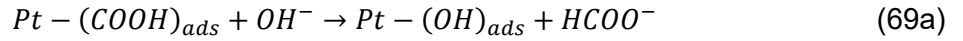
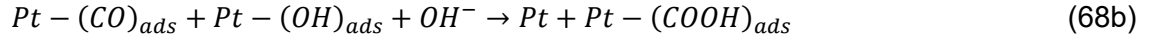
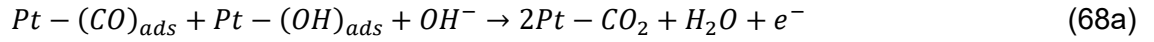
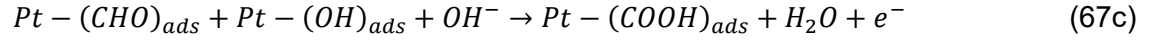
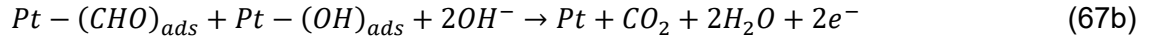
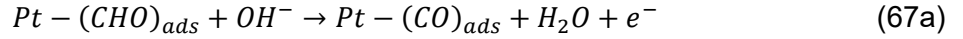
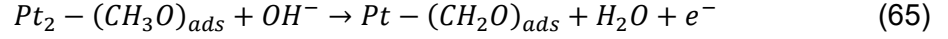
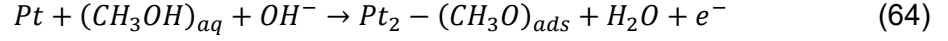
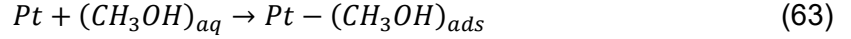
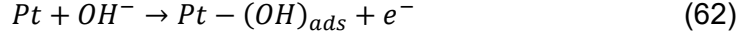
Figure 2.20 Simplified pathway for methanol oxidation [113].

The intermediate species shown in the MOR mechanism diagram bond strongly to Pt in acidic media, which results in poisoning of the catalyst and subsequent kinetic limitations. On the other hand, it has been proposed that in alkaline media, those intermediate species bond weakly to Pt, therefore poisoning effects are diminished, favoring a more efficient MOR [110].

The MOR in alkaline media can be written as [114]:



and the proposed mechanism for MOR on Pt in alkaline media can be described by the following series of steps [114]:



It has been identified that the rate determining step is the oxidation of the  $-CHO$  species (Eq. 67) [114].

A good catalyst for methanol oxidation must be able to break the C–H bond and facilitate the conversion of the resulting species into  $CO_2$ . The oxidative removal of  $(CO)_{ads}$  by adsorbed oxygen-containing species plays an important role on the catalytic activity to the MOR. On Pt, methanol is readily adsorbed and dehydrogenated at potentials close to 0.2 V (vs. RHE), however, there is no strong interaction of water with Pt to provide  $Pt - (OH)_{ads}$  species, necessary for the oxidation of  $(CO)_{ads}$  to  $CO_2$ , which results in catalyst poisoning [115]. On the other hand, PtRu alloys with Ru content between 10–40% is recognized as the best catalyst for MOR. The effect of Ru has been explained by the bi-functional mechanism, which describes the ability of Ru sites to dissociate water at lower potentials in comparison with Pt, thus generating the  $(OH)_{ads}$  species necessary for conversion of  $(CO)_{ads}$  sites to  $CO_2$  [115,116].

## 2.5 Methanol-tolerant catalysts for ORR

As mentioned before, Pt is the best catalysts for ORR in both acid and alkaline media, due to its high electrocatalytic activity. Nonetheless, Pt is also a good methanol dehydrogenation/oxidation catalyst [76]. Pt exhibits high electrocatalytic activities towards both ORR and MOR, and it is well known to be highly sensitive to the presence of even trace amount of liquid fuel or reactive intermediates [117,118]. This implies that if methanol and oxygen are present at a Pt cathode, the catalytic activity will tend towards the MOR. Such is the case of the methanol crossover effect, which occurs when methanol fuel molecules diffuse from the anode to the cathode through the polymer electrolyte in PEM-FCs or through the liquid-liquid interface in ML- $\mu$ DMFCs. In this case, methanol reacts directly at the cathode catalyst, causing mixed potentials on the cathode, besides lowering the efficiency of methanol utilization and reducing the ORR performance. Additionally, Pt catalyst is easily poisoned by strong CO adsorption, product of methanol oxidation, resulting in rapid deactivation of the cathode [41,118]. For these reasons, researchers have proposed the use of non-Pt metal catalysts, such as Pd-based nanomaterials (Pd-Ag, Pd-Ni, Pd-Fe, Pd-Co) [72,75,119-121], transition metal alloys (Ru-Se, Co-Se) [122-124], transition metal oxides ( $\text{MnO}_2$ ,  $\text{Mn}_2\text{O}_3$ ,  $\text{TiO}_2$ ,  $\text{WO}_3$ ,  $\text{MoO}_2$ ) [125,126], transition metal sulfides [127] and macrocyclic complexes [128] as potential alternatives to Pt-based catalysts for ORR in DMFCs. The aforementioned materials have the advantage of lower cost in comparison with Pt and they exhibit little to none activity towards the MOR. Particularly, metal oxides have attracted the attention of several research groups, since metal oxides have abundant sources, low cost, high chemical stability and abundant hydroxyl groups on their sources [126]. Although these electrocatalysts have high methanol tolerance, they exhibit a significant lower activity towards the ORR in comparison with Pt, due to higher reaction overpotential, slower kinetic reaction rates and low mass specific activity [120]. Moreover, as discussed in section 2.3.2, the outer-sphere electron transfer mechanism suggests that a 2-electron transfer is favoured on Pt-free catalysts.

More recently, M–N–C catalysts (M = Fe or Co), another type of platinum group metal (PGM)-free cathode catalyst have been the subject of thorough study due to their low cost and to an extraordinarily high selectivity towards the ORR [76,77]. The selectivity properties have been investigated through DFT computational calculations and it was demonstrated that, while Pt experiences a competition of oxygen and alcohols for active sites, Fe-N-C sites exhibit stronger adsorption of oxygen in comparison with alcohols and intermediates like acetic acid and acetaldehyde. The preferred adsorption of oxygen has been proposed as the cause of selectivity towards ORR [77]. However, the degree of ORR catalytic activity of M–N–C materials depends

heavily on many factors, such as iron/cobalt and nitrogen precursors and content, the nitrogen functionalities on the surface and the microporous structure, as well as the heat and leaching treatment conditions [129]. Therefore, a careful selection of all these parameters is crucial for obtaining highly efficient ORR catalysts. Moreover, the mass specific activity of this type of catalysts is significantly low in comparison with Pt. This makes it often necessary to employ thick layers of catalyst to achieve currents comparable to Pt, however this also increases the resistance of the catalyst layer. For these reasons, although promising, most of these M–N–C catalysts can hardly compete with the overall performance of Pt catalysts [129].

All of the aforementioned cathode materials are focused on reducing the cost of catalyst material and the methanol crossover effect in typical PEM-DMFCs, however, with a sufficiently high methanol tolerant and ORR selective cathode, there is the possibility of employing it in mixed-reactant DMFCs. Such is the case of a CBS (cage-bell structured) Pt-Ru nanoparticles cathode reported by Feng et al [80]. Said material exhibited Pt-like ORR performance and a fair degree of selectivity to the ORR due to the differential diffusion of methanol and oxygen in the porous Ru shell of the cage-bell nanostructures. As illustrated in Fig. 2.21, the catalytically active metal (Pt) was located at the core, shielded by a Ru shell, which is inactive to the MOR. Methanol and oxygen must diffuse to the interior of the nanoparticle, however, a methanol molecule is larger than an oxygen molecule, therefore, the diffusion of  $O_2$  is faster than that of methanol. As a result,  $O_2$  molecules reach the Pt core where the reduction reaction occurs, rendering the MOR a non-competitive event.

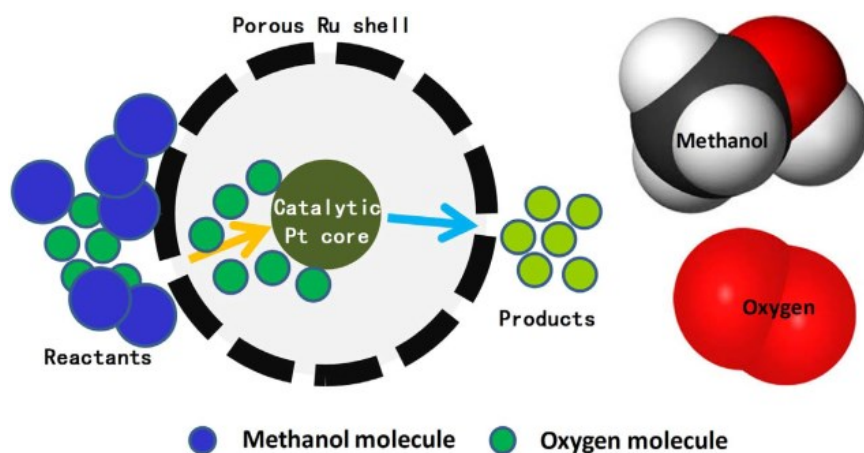


**Figure 2.21** Illustration of differential diffusion of oxygen and methanol in cage-bell structure Pt-Ru nanoparticles [80].

The CBS Ru-Pt nanoparticles were then used as cathode in a DMFC prototype that consisted of a single compartment vessel containing oxygen saturated electrolyte and methanol. The authors did not classified it as a microfluidic fuel cell nor a mixed-reactant fuel cell due probably to the nature of the testing settings. This fuel cell produced an OCV of 0.38 V and a maximum power of 15  $\mu$ W with the CBS cathode and an Au@Ag<sub>2</sub>S-Pt anode. For comparison, the same prototype was evaluated with Pt/C as both anode and cathode, resulting in an OCV of 0 V. This tests showed that the CBS Pt-Ru cathode exhibited only certain degree of selectivity, as the OCV was far from the thermodynamic value, however, the viability of using a selective cathode in a mixed-reactant DMFC was demonstrated. More significant, this study proved that, alternatively to the classical approach of alloying transition metals for methanol tolerance, good selectivity towards ORR can be achieved by creating a catalysts with an adequate structural design.

## 2.6 Synthesis methods

A catalyst material must comply with certain requirements in order to achieve high energy conversion efficiency while maintaining good durability. The design of efficient catalysts is one of the biggest challenges that researchers face when developing fuel cells systems and other energy conversion devices. The main factors to take into account when developing new catalysts materials are: (1) material electrode. (2), geometry of the catalytic centers, (3) particle size, (4) nature of the supporting material and (5) cost [130].

Nanoparticles exhibit several advantages over bulk materials, such as a higher catalytic activity and much larger surface areas with significantly less amount of material used [130]. For these reasons a number of nanoparticulate catalysts materials of different metals have been synthesized over the last couple of decades. The most common methods for synthesis of nanoparticles are chemical methods, such as impregnation, ionic exchange, colloidal and vapor phase synthesis [131,132]. However, other type of nanostructured catalysts such as thin layers can be developed using physical methods such as sputtering and pulsed laser deposition. Physical methods allow to rapidly grow of a number of materials, including metals and metal oxides on a variety of substrates. Other advantages of physical methods include the possibility of controlling the amount of material deposited and the thickness and morphology of the catalysts layers [82].

### 2.6.1 Pulsed Laser Deposition (PLD)

Pulsed laser deposition (PLD) is a physical vapor deposition (PVD) process that has emerged in the last two decades as a viable means of producing high quality thin films of a wide variety of materials, including insulators, semiconductors, high temperature superconductors, metals, and metal oxides [81]. It is a rapid, simple, and contaminant-free alternative synthesis method that allows good control on the deposition parameters [82]. In conventional PLD, a high power pulsed laser strikes a target of the material to be deposited. With sufficiently high energy density, each laser pulse vaporizes or ablates a small amount of the material creating a forward directed plasma plume. The ablation plume expands and propagates towards the substrate, providing the material flux for film growth. This process can be carried out in ultra-high vacuum or in the presence of a background gas, such as oxygen, helium or argon. The PLD has a number of practical advantages for laboratory development of new materials, and it delivers a much higher deposition rate than sputtering. Furthermore, the size, morphology and composition of deposited materials could be well controlled by modifying deposition conditions (pressure, background atmosphere, target-to-substrate distance and incident energy) [81,82].

Fig. 2.22, left panel shows the typical setup of single-beam PLD and the right panel describes the PLD process. The entire process is generally divided into three main stages [82]:

1. Laser-material interaction and plasma plume formation

When the laser strikes the target, the energy is absorbed by the material and the electromagnetic energy is converted into electronic excitation in form of plasmons, unbound electrons or excitons, and then to thermal, chemical and mechanical energy, which lead to the evaporation and ablation of the target. As a result, a plasma plume is developed on the surface of the target. The plasma plume consists of energetic species such as neutral atoms, molecules, ions, electrons, clusters, etc. The number of ablated atoms per square centimeter per second, known as the ablation rate, is determined by several factors such as the nature of the target, laser wavelength, duration of the pulse, and laser fluence  $F$  ( $F = \text{laser energy per pulse} / \text{focal spot area}$ , in  $\text{J cm}^{-2}$ ). The chosen laser fluence needs to provide a desired ablation rate to ensure a homogeneous plasma plume and to avoid generating micron-sized particulates or damaging the target. KrF excimer laser ( $\lambda = 248 \text{ nm}$ , pulse duration = 10–30 ns) and Nd:YAG laser ( $\lambda = 266 \text{ nm}$ , pulse duration = 7 ns) are the most often lasers for PLD, while the on-target fluence is typically set between 2 and 8  $\text{J cm}^{-2}$  for most materials.

## 2. Plasma expansion

When the plasma plume is developed on the target, the ejected species expand and propagate along the direction perpendicular to the target surface. If the ablation is performed under high vacuum, the resulting plume is very narrow and forward directed. On the other hand, in presence of a gas with high pressure in the chamber, a shock wave front arises from collisions between the expanding plasma and the surrounding gas molecules. The plasma plume then propagates with gradually decreasing velocity towards the substrate. The spatial distribution of the laser-induced plume is non-uniform due to its highly-directed nature, for this reason the target must be rotated in order to ensure homogeneity of the deposited film. In addition, the background gas pressure significantly influences the microstructure, chemistry and properties of the deposited films. One way the gas participates during the deposition process is as a reactive species (e.g.  $O_2$ ) during the collisions between the plasma plume and the background gas. For example,  $O_2$  is typically employed to compensate for the loss of oxygen and to ensure stoichiometric transfer from target to substrate in the case of metal oxides deposits. Another way the background gas participates is when a non-reactive gas (e.g. He, Ar) is introduced to tune the kinetic energy (KE) of the ablated species in the plume. With sufficiently high pressure, the gas molecules confine the plasma in a smaller volume, which increases the number of collisions between the plasma and the gas. As a result, the KE of the propagating species decreases to an extent determined by gas pressure/mass, affecting the nucleation rate and growth kinetics of the film.

## 3. Nucleation and growth of the film on the substrate surface

In this stage, the plasma plume reaches the surface of the substrate and the nucleation and growth take place. Film nucleation and growth kinetics are dependent on the kinetic energy, density of the species in the plasma plume and nature of substrate (temperature, roughness, crystallographic orientation). Movchan and Demchishin [133] proposed a model, further enhanced by Infortuna et al. [134] that describes the effect of the temperature and the background gas pressure on the film microstructure. In this thesis, we only focused on the effect of the background gas pressure, which, as mentioned in the plasma expansion section, affects the KE of the species. In the absence of gas, the flux of highly energetic species are able to reorder at the substrate surface, yielding a dense and highly oriented film made of large nanocrystallites. On the other hand, for deposition occurring at high gas pressure, collisions between the plume and gas molecules cause cluster deposition-diffusion-aggregation, cluster melting and coalescence, and cluster implantation, resulting in an uneven, rough film microstructure. Additionally, the incident angles of the ejected species get widen with increasing gas pressure, thus enhancing the oblique

flux of species and forming voids due to shadowing effect. Moreover, the substrate rotation enhances the shadowing effects due to the continuous changes of the deposition angle at different points on the substrate [135,136].

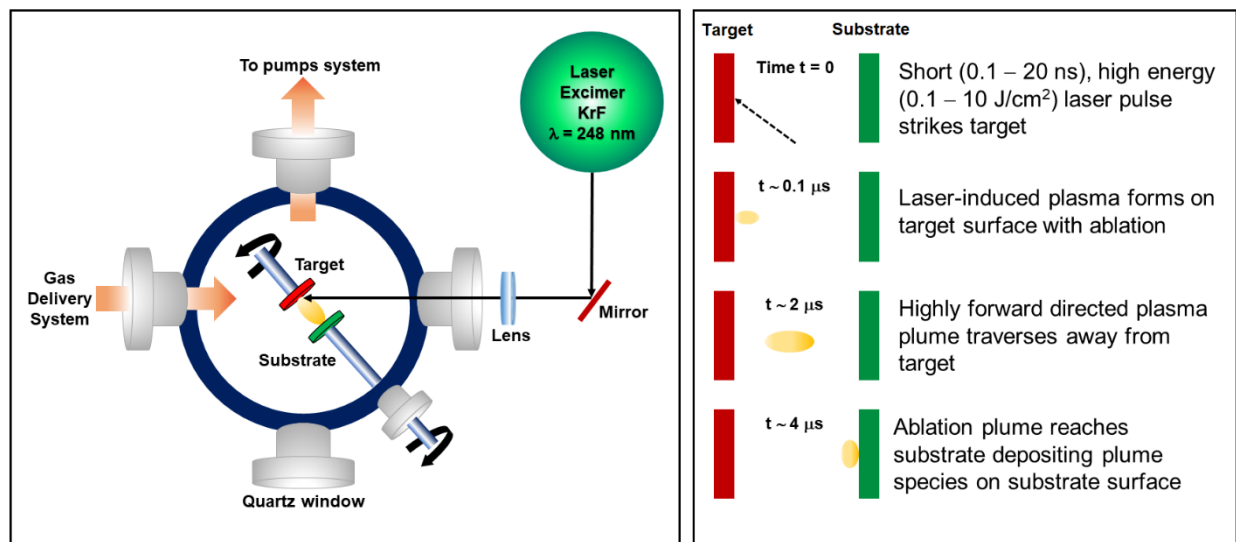


**Figure 2.22** Left panel: Schematic illustration of single beam PLD setup. Right panel: Description of the PLD process.

## 2.7 Material characterization: Physicochemical techniques

In this section, the different physicochemical characterization techniques used in this project are described. The different methods include scanning electron microscopy (SEM) for the study of the morphology of the films, X-Ray Diffraction (XRD) for determining the crystalline structure of the materials and X-Ray Photoelectron Spectroscopy (XPS) for the analysis of the chemical composition at the surface of the samples. Additionally, Neutron Activation Analysis (NAA) was employed for measuring the mass loading ( $\mu\text{g cm}^{-2}$ ) of Pt on the deposits.

### 2.7.1 Scanning Electron Microscopy (SEM)

The scanning electron microscope is a very versatile instrument for examination and analysis of the microstructure morphology of a variety of samples. Unlike an optical microscope, where the image magnification is achieved through visible light and a system of lenses, the image formation in SEM is product of the interaction between a scanning focused beam of electrons and a sample. The use of electrons allows to obtain images with higher resolution and greater depth of field, in comparison with optical microscopes. The electrons interact with atoms in the sample, resulting in two major types of interactions: elastic interactions and inelastic interactions. The former results

from the deflection of the incident electron by the specimen atomic nucleus or by outer shell electrons of similar energy, while the latter is caused by a variety of interactions between the incident electrons and the electrons and atoms of the sample. Elastic scattering is characterized by negligible energy loss during the collision and by a wide-angle directional change of the scattered electron. Backscattered electrons (scatter angle  $> 90^\circ$ ) are useful for developing images of samples. On the other hand, in inelastic scattering, the primary beam electron transfers substantial energy to the sample, resulting in ionization of the specimen atoms and in the generation of secondary electrons (SE), which typically possess energies of less than 50 eV and that can be used to image or analyze the sample. Additionally, some other signals are produced from the collisions between electrons and the sample, including emission of characteristic X-Rays and Auger electrons (Fig. 2.23). The secondary electron emission is the most widely used signal for image generation. Secondary electrons are typically used for the visualization of surface texture and roughness. Due to their low energy, secondary electrons are readily attracted to a detector carrying some applied bias. The energy of the electrons is then converted into photons (visible light) by a scintillator. Afterwards, the photons travel down a quartz light pipe into a photomultiplier tube (PTM), where the quantum energy of the photons is converted back into electrons. The output voltage from the PTM is then amplified to being output as brightness modulation on the SEM screen [137].

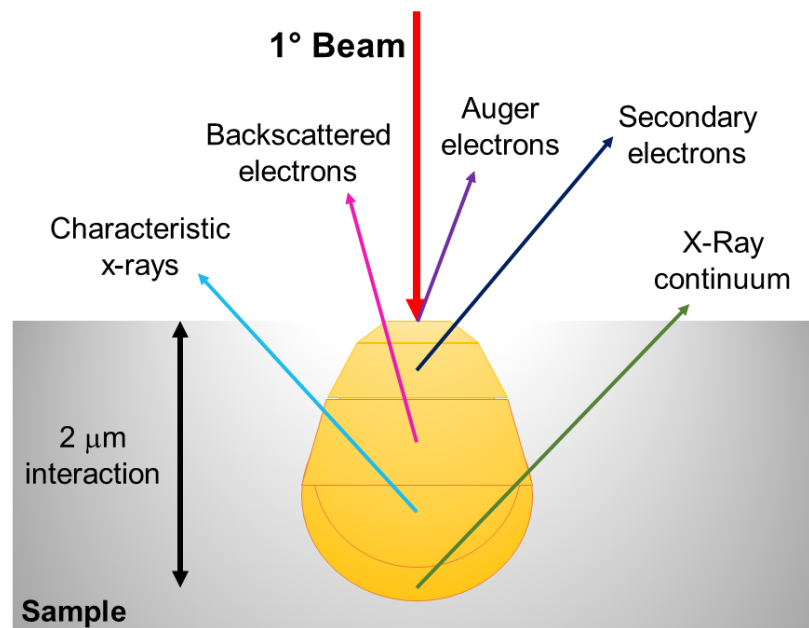


**Figure 2.23** Signals generated form the interaction between electron beam and specimen under study in SEM.

### 2.7.2 X-Ray Diffraction (XRD)

X-ray diffraction is a rapid and non-destructive analysis technique in material science, mostly used for phase identification and characterization of crystalline materials, as well as to determining the crystallinity of a sample and the lattice parameters. Such analysis is done in a diffractometer through the constructive interference of X-rays and a crystalline sample. X-rays generated by a cathode ray tube are filtered to produce monochromatic radiation and then collimated to a single direction towards the sample. As, shown in Fig. 2.24, the constructive interference results from the interaction of the incident X-rays with a set of lattice planes with an equal interplanar distance when conditions satisfy Bragg's law [138]:

$$n\lambda = 2d \sin \theta \quad (70)$$

where  $\lambda$  is the wavelength of the incident X-rays,  $n$  is a positive integer,  $d$  is the spacing between adjacent planes in the lattice and  $\theta$  is the angle of incidence/reflection to the plane.

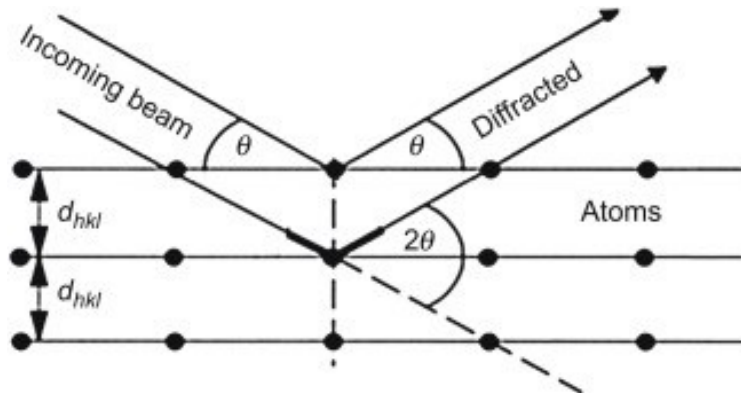


Figure 2.24 Diffraction of X-ray by parallel planes of atoms in a crystalline material [139].

The diffraction pattern, acquired by scanning the sample through a  $2\theta$  range, is plotted as intensity vs.  $2\theta$ . A diffractogram shows a series of peaks that occur where the X-ray are diffracted by different crystal planes. A diffraction pattern is characteristic of a particular sample, therefore, by comparison with a standard reference, it can be used to identify the crystalline structure of the material under study. In order to positively match the diffractogram with a standard, both peak positions and relative intensities must fit for a particular phase. Additionally, the crystallite size can be calculated using the Scherrer equation [138],

$$L = \frac{0.89\lambda}{B(2\theta)\times\cos\theta} \quad (71)$$

where  $L$  is the mean size of the crystalline domain,  $B(2\theta)$  is the full width at half maximum (FWHM) in radians of the peak under study,  $\lambda$  is the wavelength of the X-ray in meters and  $\theta$  is the Bragg angle in radians.

The lattice constant, which refers to the physical dimension of unit cells in a crystal lattice, can also be calculated from the diffractogram and the derived Bragg's equation in terms of the miller indexes ( $[h, k, l]$  for a face-centered cubic) [138].

$$a = \frac{\lambda \times \sqrt{h^2 + k^2 + l^2}}{2 \sin \theta} \quad (72)$$

### 2.7.3 X-Ray Photoelectron Spectroscopy (XPS)

X-Ray Photoelectron Spectroscopy is a surface analysis technique that is used for determining the elemental composition, empirical formula, chemical state and electronic state of a material's surface, as its analysis depth is about 5–10 nm.

The working principle of XPS is based on the photoelectric effect (Fig. 2.25). During the analysis, the surface of the sample is illuminated by an X-ray of known energy, generally Al ( $K\alpha$ ) at 1486.7 eV, and a photoelectron is emitted via the photoelectric effect and it reaches the electron energy analyzer. The kinetic energy of the emitted photoelectron is measured and the atomic core level binding energy of the sample is determined by [140]

$$E_B = h\nu - E_K - \Phi \quad (73)$$

where  $E_B$  is the binding energy of the core electron,  $h\nu$  is the energy of the incident X-ray,  $E_K$  is the kinetic energy of the photoelectron as measured by the instrument and  $\Phi$  is the work function dependent on both the material and spectrometer.

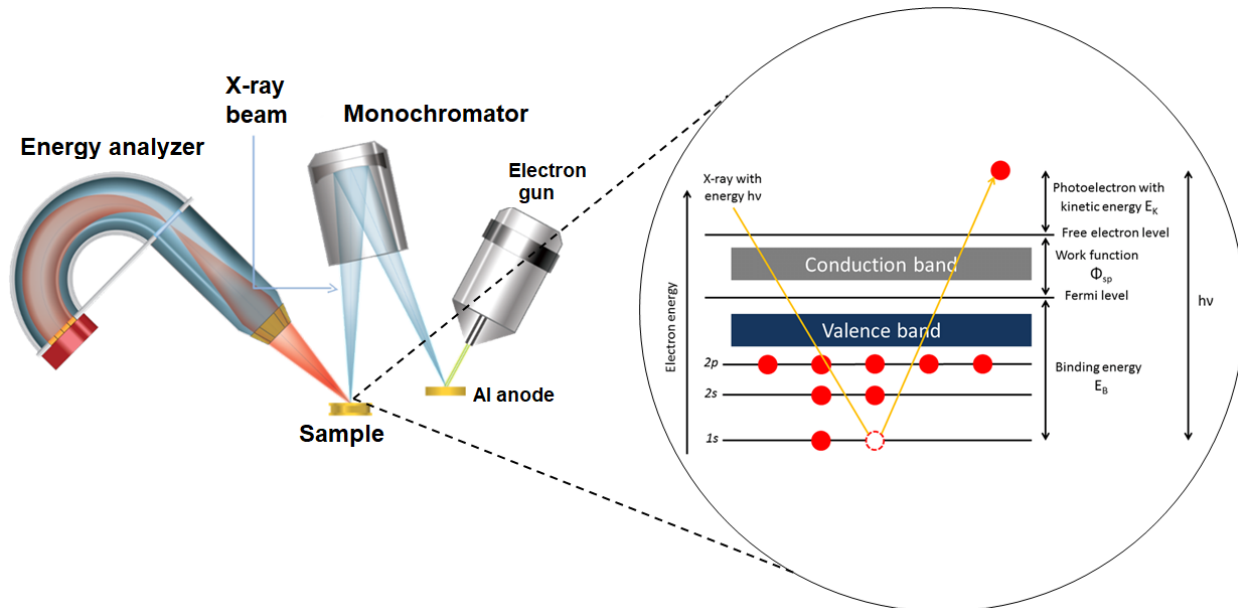


Figure 2.25 Schematic diagram of the working principle of XPS [141,142].

In an XPS spectrum, intensity of photoelectrons is plotted as a function of binding energy (in eV). The intensity of the photoelectrons is proportional to the amount of the element analyzed within the XPS sample. On the other hand, the binding energy is related to several factors: (1) the element analyzed, (2) the orbital from which the electron is ejected, and (3) the chemical environment of the analyzed atom. Experimentally, two types of XPS spectra are acquired during analysis, a survey spectrum is first obtained to overview all the elements present in the sample, while high-resolution spectra are acquired for specific elements. Each element has a characteristic set of signals at determined BE values. These characteristic values allow qualitative analysis, such as elemental composition and determination of chemical states on a material surface [143].

#### 2.7.4 Neutron Activation Analysis (NAA)

Neutron activation analysis is a non-destructive technique for determining the concentration of elements in samples, either solid, liquid or gas. This method focuses only on the nucleus of samples and it requires a source of neutrons. The sample is bombarded with neutrons, causing the element to form radioactive isotopes and to emit detectable gamma-rays. The radioactive emissions and radioactive decay paths are unique and well known for each element, therefore it

is possible to determine the concentration and mass of the elements in the sample by studying the emission spectra (Fig. 2.26) [144].

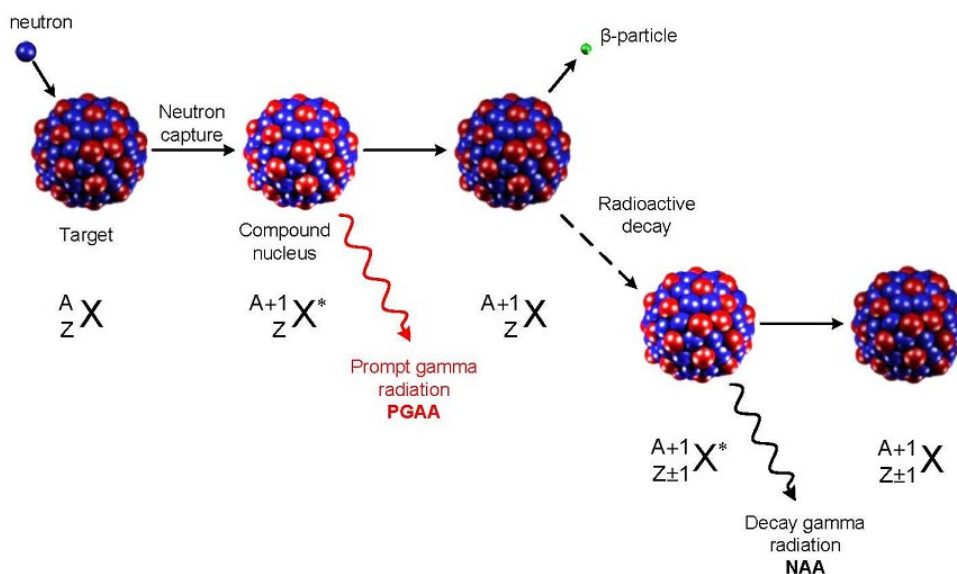


**Figure 2.26** Schematic diagram of the process of neutron capture, followed by radioactive decay and gamma radiation [144].

## 2.8 Material characterization: Electrochemical techniques

Electrochemical characterization techniques are powerful and convenient tools for the search for new catalytic materials for fuel cells. This section presents the different electrochemical techniques used to study the properties and evaluate the catalytic performance of the materials synthesized in this project.

### 2.8.1 Cyclic Voltammetry (CV)

Cyclic voltammetry is one of the most important tools for the analysis of electrochemical phenomena. Through CV, it is possible to study reaction mechanisms as well as oxidation and reduction rates of electrochemical reactions occurring at the interface between an electrode and an electrolyte solution. CV is often initially conducted to survey the electrochemical properties of electroactive species and catalytic activity of new materials.

In CV, the potential of the working electrode is linearly swept back and forth at a constant rate between 2 potential limits, and the current flow between the working electrode and the counter electrode is recorded accordingly. The current vs. potential is then plotted to obtain a cyclic voltammogram. The shape of the voltammogram is defined by several parameters, including the

scan rate and potential range. Fig. 2.27a shows a typical potential-time wave applied for CV, while the current-potential response is shown in Fig. 2.27b. During a CV, the initial potential is that where no electrochemical process occur (A). Towards the positive scan, at a critical potential (B), the electroactive species starts to being oxidized and an anodic current starts to flow. As the potential value increases, so does the current, however, a peak (C) appears at a certain potential, due to a characteristic diffusion-controlled process. At this point, the diffusion layer of the electroactive species has grown sufficiently so that the flux of reactant from the solution to the electrode is not fast enough to satisfy that required by the Nernst equation. As the potential increases beyond this point, the current starts to decay until the potential scan is reversed (D). In the reverse scan, current generated by a reduction reaction will start to flow at a critical point and form a cathodic current peak (E).

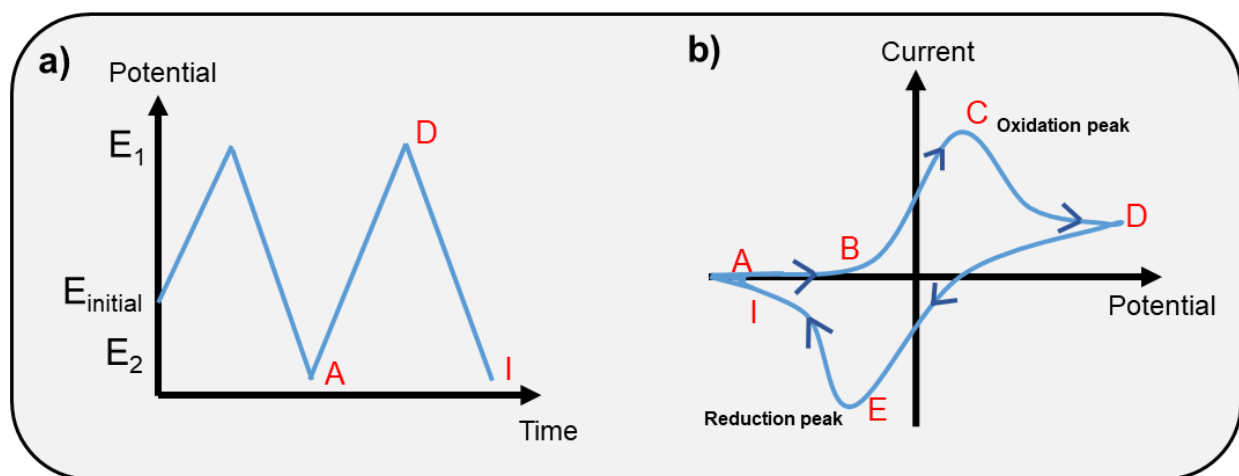


Figure 2.27 a) Potential-time wave applied for CV, and b) resulting current-potential curve (cyclic voltammogram).

If the reaction is thermodynamically reversible or kinetically fast enough, the peak in a cyclic voltammogram is governed by the Randles-Sevcik equation [91]:

$$i_p = (2.69 \times 10^5) n^{3/2} D^{1/2} v^{1/2} A C \quad (74)$$

where  $i_p$  is the peak current (in A),  $n$  is the number of electrons,  $D$  is the diffusion coefficient (in  $\text{cm}^2 \text{s}^{-1}$ ),  $v$  is the scan rate (in  $\text{V s}^{-1}$ ),  $A$  is the area of the working electrode (in  $\text{cm}^2$ ) and  $C$  is the concentration of the electroactive species (in  $\text{mol cm}^{-3}$ ).

### 2.8.2 Linear Scan Voltammetry (LSV)

LSV is another type of voltammetry technique that operates in a similar manner to CV and it can be viewed as half of a cyclic voltammogram. In LSV, the potential is linearly swept from an initial potential to a final potential instead of being cycled between these two potentials. LSV is employed to study systems where the reaction of interest is irreversible, such as the oxygen reduction on Pt.

### 2.8.3 Chronoamperometry (CA)

In the chronoamperometry technique, the potential of the working electrode is instantaneously stepped (Fig. 2.28a) from a potential where no faradaic reaction occurs (e.g. OCP) to a potential where the reaction is limited by mass transfer. The resulting current is measured as function of time, as shown in Fig. 2.28b.

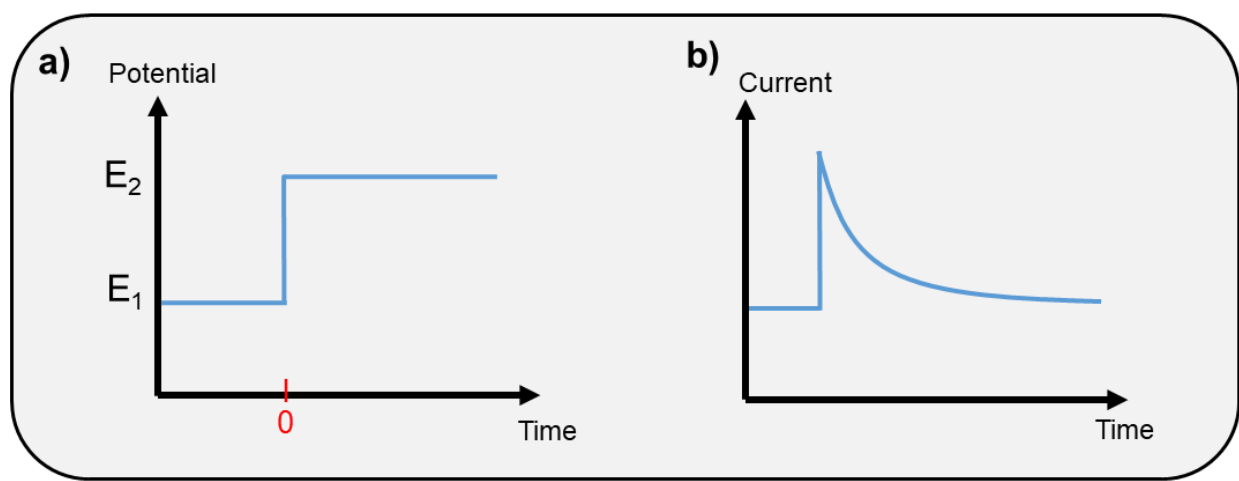


Figure 2.28 a) Typical waveform of CA, and b) current-time response.

Experimentally, an instant current rise is observed when the voltage changes, and then it begins to decay with time. This initial current is typically very large, in part because current is consumed for discharging the electrochemical double layer established adjacent to the WE. The reactants in the vicinity of the electrode are rapidly consumed due to the high overvoltage applied. As time progresses, the diffusion layer grows due to the depletion of reactant, resulting in a decrease of concentration gradient and the observed decay in the current. The diffusion-limited time-current dependence at a planar electrode is governed by the Cottrell equation [91]:

$$i = \frac{nFAC\sqrt{D}}{\sqrt{t\pi}} \quad (75)$$

where  $n$  is the number of electrons involved in the reaction,  $F$  is the Faraday's constant,  $A$  is the area of the electrode,  $C$  is the concentration of the electroactive species,  $D$  is the diffusion coefficient of the electroactive species and  $t$  is time.

### 2.8.4 Rotating Ring Disk Electrode (RRDE)

RRDE is a hydrodynamic technique, similar to the rotating disk electrode (RDE) technique, where convection of the electroactive species from the solution to the electrode is forced by means of a rotating working electrode. This technique is mostly employed to gather information about electrode reaction kinetics. In RRDE, the electrode rotation rate is held constant (usually between 100 and 2400 rpm) while the electrode potential is swept from one potential to another at a constant rate (Fig. 2.29a) [145]. A voltammogram under RRDE will show a current increment (anodic or cathodic) as the potential moves past the standard electrode potential for certain electrochemical reaction. In contrast to typical CV, at sufficiently negative potential, the current eventually reaches a maximum current (limiting current) as shown in Fig. 2.29b, where any electroactive species that reaches the surface of the electrode is immediately converted to product (with their respective electron flow). At this point, the rate of electron flow is only limited by the mass transport rate, which is related to the rotation rate of the electrode. Faster rotation rates result in faster mass transport rates. Thus, the limiting current increases with rotation rate [145].

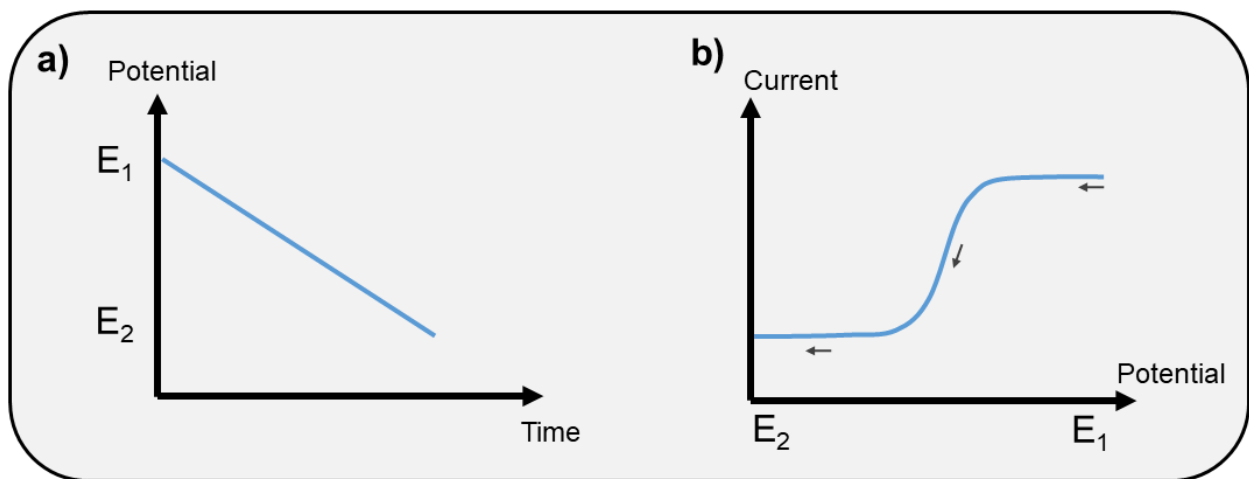


Figure 2.29 a) Typical waveform of a voltammogram in RRDE, and b) resulting current-potential curve.

In a RRDE configuration, a concentric ring is placed around a disk electrode, as shown in Fig. 2.30a. During operation, the overall flow pattern at the RRDE initially brings the molecules and ions to the disk surface, where an electrochemical reaction occurs (typically reduction, at sufficiently negative potential). Subsequently, the outward radial flow carries a fraction of the products generated at the disk past the surface of the ring electrode, as depicted in Fig. 2.30b. This flow pattern allows products generated at the disk to be detected (typically oxidized) as they are swept past the ring electrode, which holds a sufficiently positive potential throughout the experiment.

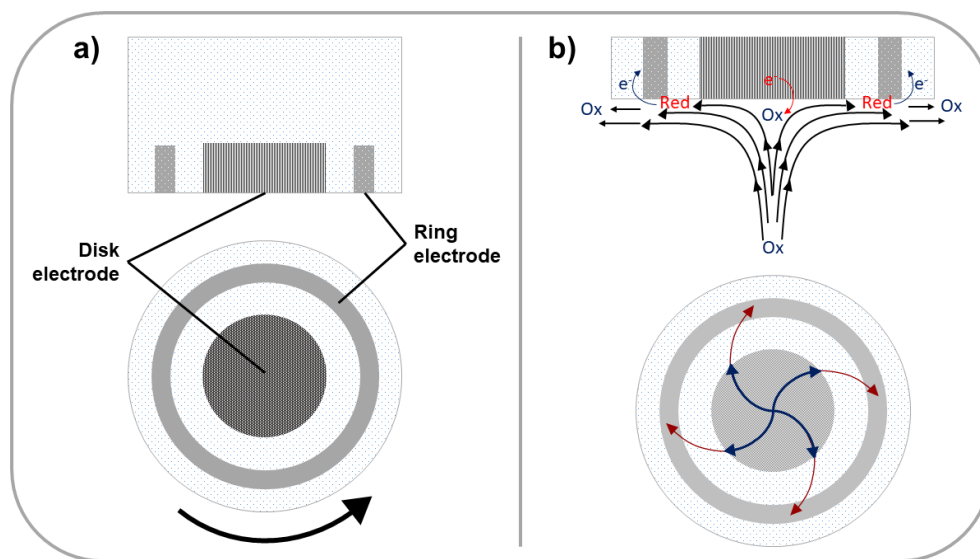
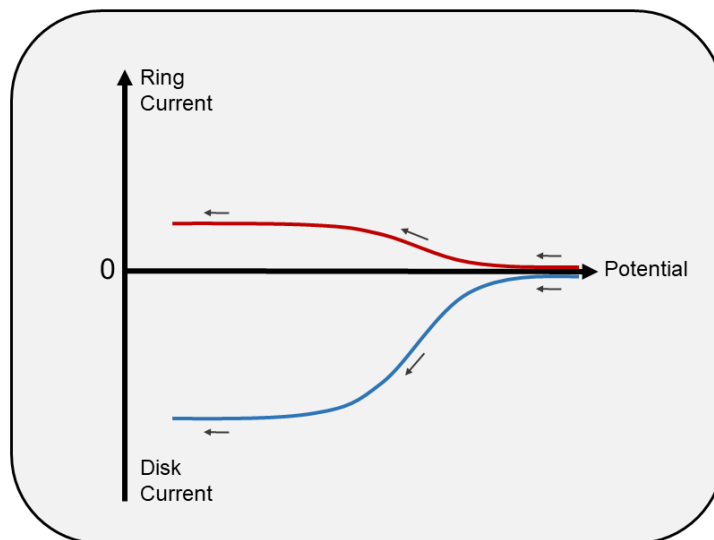


Figure 2.30 a) RRDE cross-section and top view, and b) streamlines during operation.

A key parameter of the ring-disk geometry is the collection efficiency, which is the fraction of the material from the disk than subsequently flows past the ring, and it can be expressed as a fraction between 0.1 and 1.0 or as percentage [36,145]. The collection efficiency is commonly measured empirically by using a well-known redox system, typically the ferrocyanide/ferricyanide system. Experimentally, the ferricyanide is reduced to ferrocyanide at the disk electrode. As this occurs, the generated ferrocyanide is swept away from the disk toward the ring electrode, where some of the product is oxidized back to ferricyanide [145]. The resulting curves are shown in Fig. 2.31. The measured ratio between the ring (anodic) limiting current and the disk (cathodic) limiting current is the empirical collection efficiency.



**Figure 2.31** Typical curves obtained from the ferricyanide/ferrocyanide system at a RRDE.

The RRDE technique is commonly used for the determination of a certain reaction pathway when there are two known competing pathways. As long as one of these two proceeds through an electrochemical species that can be detected at the ring, it is possible to determine the favored pathway. The most commonly studied reaction at RRDE is undoubtedly the oxygen reduction reaction, which can proceed either through a 2-electron transfer or a 4-electron transfer [36,145].



## CHAPTER 3 METHODOLOGY

### 3.1 Synthesis

Nanostructured binderless cathode electrodes were synthesized by single beam pulsed laser deposition on a carbon substrate. These catalytic materials were prepared in 2 steps. First, a Pt layer was deposited on the substrate and this was further coated with a metal or metal oxide (Ag,  $\text{Fe}_2\text{O}_3$  or  $\text{Mn}_2\text{O}_3$ ) layer, thus having a layer-onto-layer architecture, as illustrated in Fig. 3.1. The objective is to obtain an electrode material with high catalytic activity towards the ORR and that exhibits no activity towards the MOR, i.e., a cathode selective to the oxygen reduction for using in mixed-reactant direct methanol fuel cells.

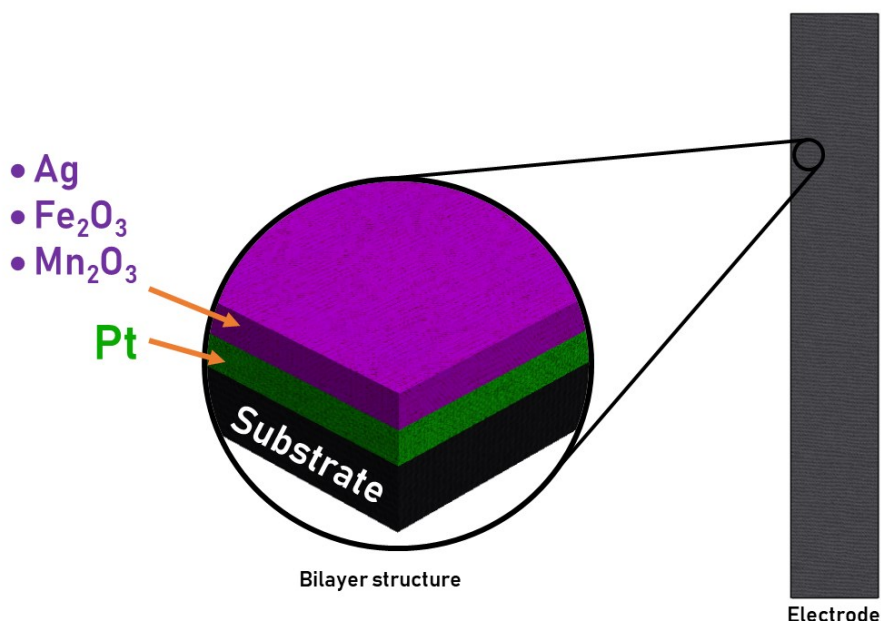
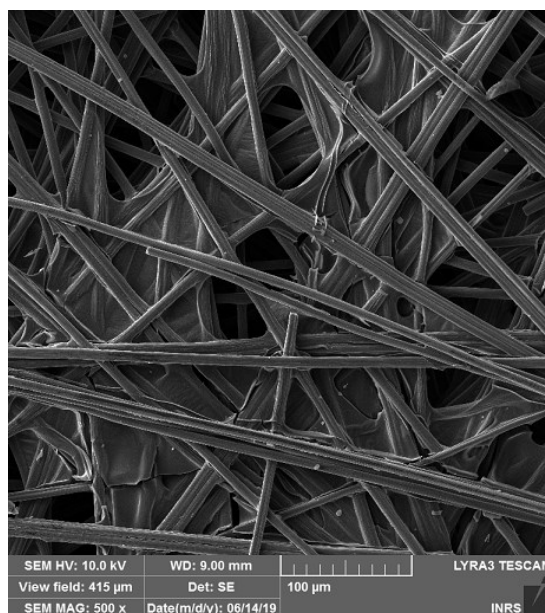


Figure 3.1 Illustration of the bilayer structure of the catalyst synthesized on this work.

#### 3.1.1 Substrate

Untreated carbon paper (CP, Toray Paper TGP-H-060) was used as substrate/current collector of the catalysts materials. This low-cost carbon fiber composite substrate consists of a dense array of carbon microfibers (Fig. 3.2), suitable for catalyst backing layer and it is often used as gas diffusion layer in fuel cells [146].



**Figure 3.2** SEM image of the carbon paper substrate.

### **3.1.2 Catalytic materials**

Three different bilayer cathode materials were synthesized and studied in this work. In all cases the first layer was a porous Pt film, whereas for the second layer, three different alternatives, Ag, Fe<sub>2</sub>O<sub>3</sub> and Mn<sub>2</sub>O<sub>3</sub> were evaluated.

### **3.1.5 Experimental conditions**

In order to obtain the desired ORR performance and methanol tolerance, several deposits were made varying some key deposition parameters. Three values of background pressure were employed for the synthesis: under vacuum (UV), 0.5 Torr of He and 2 Torr of He. By changing the pressure it is possible to obtain different surface morphologies, which affect the surface area of the films. The amount of material deposited and thus the thickness of the film is dependent on the number of laser pulses, for this reason deposits with different number of pulses were made for each catalyst with different morphology. The objective was to study the effect of the thickness on the diffusion of oxygen and methanol through porous layers.

In table 3.1 are reported the different deposition conditions of the materials synthesized by PLD. As screening method for detecting the most promising bilayer cathode, first all the deposits shown in this table were studied individually through electrochemical techniques. The tests focused mainly on identifying the morphology with higher electroactive area and the catalyst behavior towards ORR in absence and presence of methanol. Subsequently, the best candidate materials

were combined in a bilayer fashion, in such way that the best performing Pt deposit was coated with the better suited Ag, Fe<sub>2</sub>O<sub>3</sub> and Mn<sub>2</sub>O<sub>3</sub> layers. Thus, in the results section of this thesis, only the catalysts with optimum performance are reported. Nevertheless, as a mean to better understand the selection of optimum catalysts and to demonstrate the effect of morphology and layer thickness, the results regarding the rest of combinations are presented in Appendix I.

**Table 3.1 Materials synthesized by PLD**

Material	Fluence (J cm <sup>-2</sup> )	Background pressure (Torr He)	Number of Pulses
Pt	4	UV	10,000
			20,000
			30,000
		0.5	10,000
			20,000
			30,000
		2	10,000
			20,000
			30,000
Ag	4	UV	10,000
			20,000
			30,000
		0.5	10,000
			20,000
			30,000
		2	10,000
			20,000
			30,000
Fe <sub>2</sub> O <sub>3</sub>	2.5	0.5	10,000
			20,000
			30,000
		2	10,000
			20,000
			30,000
Mn <sub>2</sub> O <sub>3</sub>	2.5	0.5	10,000
			20,000
			30,000
		2	10,000
			20,000
			30,000

**UV: under vacuum.**

In table 3.2 are reported the optimal experimental conditions for the synthesis of the two best performing cathodes developed in this work: Ag/Pt/CP and Mn<sub>2</sub>O<sub>3</sub>/Pt/CP. Pt, Ag and Mn<sub>2</sub>O<sub>3</sub> deposits were carried out by single beam PLD using CP as substrate. The Pt (99.99%), Ag

(99.99%) and Mn<sub>2</sub>O<sub>3</sub> (99.90%) targets used for the deposition were purchased from Kurt J. Lesker Co. All the deposits were made at room temperature using a KrF excimer laser ( $\lambda = 258$  nm), pulse width = 17 ns, and repetition rate = 40 Hz. The laser fluence for Pt and Ag was fixed to 4 J cm<sup>-2</sup>, and for Mn<sub>2</sub>O<sub>3</sub> it was set to 2.5 J cm<sup>-2</sup>. In all cases, the target-substrate distance was set to 5 cm. Prior to each deposition, the chamber was evacuated using a turbo pump ( $4 \times 10^{-5}$  Torr). In order to obtain a uniform ablation, the targets were continuously rotated and translated during the deposition.

**Table 3.2** Optimum synthesis conditions of the bilayer cathodes developed in this work.

Substrate	First catalyst layer				Second catalyst layer			
	Material	Fluence (J cm <sup>-2</sup> )	Pulses	Background pressure	Material	Fluence (J cm <sup>-2</sup> )	Pulses	Background pressure
CP	Pt	4	20,000	2 Torr He	Ag	4	20,000	0.5 Torr He
					Mn <sub>2</sub> O <sub>3</sub>	2.5	20,000	0.5 Torr He

CP: carbon paper, UV: under vacuum.

### 3.2 Physicochemical characterization

The surface morphology of the synthesized materials was studied by SEM (TESCAN, LYRA3) operated at 15 and 20 kV.

The crystalline structure of all the deposits was determined by XRD using a Bruker D8 Advance diffractometer equipped with a Cu K $\alpha$  source. The diffractometer was operated at 40 kV and 40 mA. All diffractograms were acquired in the Grazing Incidence Diffraction (GID) scan mode with an incident angle of 2°, 2 $\theta$  angular step size of 0.05° and acquisition time of 5 s per step.

XPS measurements were performed in order to determine the chemical composition of the surface elements on the samples and their oxidation states. The study was carried out in a VG Escalab 220i-XL equipped with an Al K $\alpha$  source (1486.6 eV). The anode was operated at 10 kV and 20 mA and the pass energy of the analyzer was fixed at 20 eV. The samples were analyzed with a spot size of 150 × 800  $\mu$ m located approximately in the center of the sample. First, survey spectra in the 0 – 1350 eV range were acquired, followed by higher resolution multiplex scan spectra (Ag 3d, Mn 3s, Mn 2p, Pt 4f, O 1s and C 1s core levels). The analysis of the elements was carried out with CasaXPS software (Casa Software Ltd.) by fitting the core level spectra after

a Shirley background removal. The C 1s core level peak at 284.6 eV, resulting from hydrocarbon contaminants at the surface was used as an internal reference. All spectra were recalibrated with respect to the C 1s core level peak of adventitious carbon contamination.

### 3.3 Electrochemical characterization

The electrochemical properties of the samples were studied in alkaline medium (0.5 M KOH, Fisher chemical, 85.8%) in a three-compartment electrochemical cell at room temperature, using an Autolab PGSTAT302N potentiostat/galvanostat. The working electrodes have a geometric area of 0.370 cm<sup>2</sup>. A Pt coil was used as counter electrode and an Ag/AgCl, 4 M KCl, as reference electrode. All reported potentials in the present work are referred to reversible hydrogen electrode (RHE).

The electrochemical profiles were obtained using cyclic voltammetry (CV) in an oxygen-free solution (Ar bubbled for 30 min prior to each CV). The potential window was cycled until obtaining a stable and reproducible response.

Linear sweep voltammetry (LSV) and Rotating ring-disk electrode (RRDE) techniques were used to study the catalytic activity towards the ORR in oxygen saturated 0.5 M KOH solution (O<sub>2</sub> bubbled for 30 min before each test). RRDE measurements were carried out with a bipotentiostat (Pine, Model AFCBP1) and an AFMSRCE electrode rotator (Pine Research Instrumentation), using a RRDE with GC disk (5.5 mm diameter) and a Pt ring (6.5 and 8.5 mm inner and outer diameter, respectively). The as-prepared samples, with 0.19 cm<sup>2</sup> geometric area, were attached to the glassy carbon disk using carbon conductive tape. The collection efficiency (*N*) was determined experimentally following the methodology described in the literature [103,147]. Due to the slight geometry change, *N* was found to be 0.36, different from 0.38 supplied by the manufacturer. For the detection of H<sub>2</sub>O<sub>2</sub> generated at the disk, the potential for the Pt ring was set to 1.3 V vs RHE. The peroxide yield and the electron transfer number (*n*) were calculated according to Eq. 76 and Eq. 77 [148], respectively:

$$H_2O_2\% = 200(I_r/N)/I_d + I_r/N \quad (76)$$

$$n = 4I_d/(I_d + I_r/N) \quad (77)$$

Where *I<sub>d</sub>* and *I<sub>r</sub>* are the disk and ring current, respectively.

Methanol tolerance was evaluated by LSV under oxygen atmosphere in presence of different concentrations (1 to 5 M) of MeOH (ACS Reagent,  $\geq 99.8\%$ ).

### 3.4 Fuel cell testing

A microfluidic fuel cell device was fabricated in order to evaluate the catalysts. The design of the fuel cell used in this stage of the study derives from an air-breathing fuel cell with flow-through electrodes, reported by Ortiz-Ortega et al. [149]. Some modifications were made in the dimensions of the components in order to further miniaturize the device. This device is denominated Cell G1 throughout this work. The fuel cell consists of porous electrodes in a channel with a V-shape geometry (Fig. 3.3). The implementation of porous electrodes maximizes the reactants utilization, which translates into improved performance, compared to non-porous electrodes [5,150,151]. The electrodes are placed in a channel made of Silastic™, which also works as sealing layer. A cutter plotter was used to obtain the shape of the channel. The electrodes-channel set was sandwiched between two PMMA plates fabricated by a Computer Numerical Control (CNC) micro milling system and the ensemble was tightened by M1.6 machine screws, having total dimensions of 38 x 38 x 8.4 mm (L x W x H) with a volume of the microchannel of 25  $\mu\text{L}$ . A 0.1  $\text{cm}^2$  window was made on both bottom and top plates as air-intakes for the air-breathing cathode. Pogo pins were used as current collectors, which allowed to significantly reduce the device dimensions. As usual with flow-through electrodes fuel cells, the current and power density values here reported are normalized to the electrode cross-sectional area (0.015  $\text{cm}^2$ ) to the flow of reactants. In all cases, the anode was a composite PtRu catalyst (50:50, 4  $\text{mg cm}^{-2}$  mass loading) purchased from Fuel Cell Store.

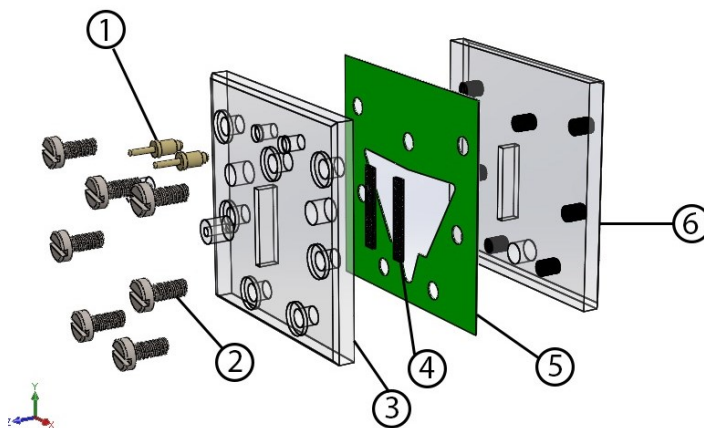


**Figure 3.3** Schematic representation of the components and assembly of the microfluidic fuel cell G1 (1-Pogo pin, 2-Screw, 3-Top PMMA plate, 4-Porous electrodes, 5-Microchannel and 6-Bottom PMMA plate).

This fuel cell design was originally intended for operating with a typical 2-stream flow [149], as shown in Figure 3.4, where that the fuel and oxidant are injected separately to the microfluidic fuel cell. The two streams subsequently come into contact forming a liquid-liquid interface due to co-laminar flow in the channel that acts as a separator between flows avoiding convective mixing. However, for evaluating the methanol tolerant cathodes under mixed-reactant conditions, a modification on the operation of the fuel cell was made.

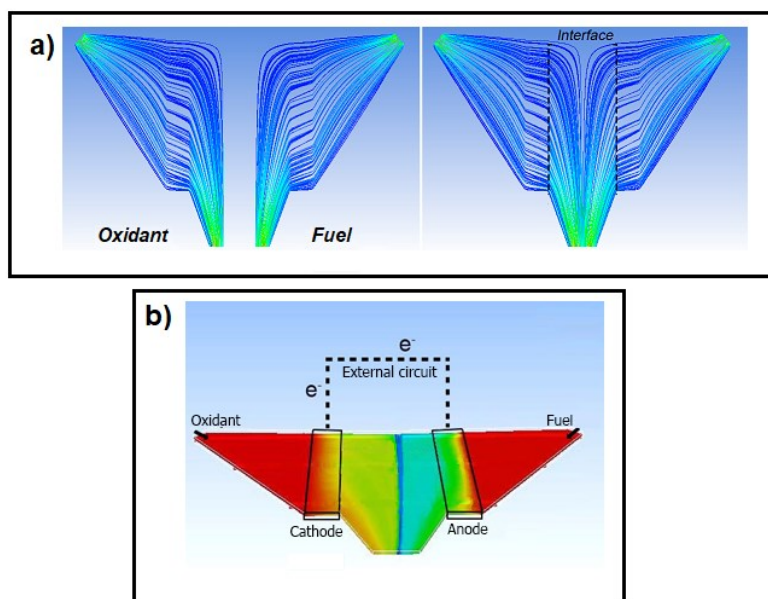


**Figure 3.4** a) Flow simulation of cell G1 in a typical 2 stream configuration and b) reactant profiles.

Fig. 3.5 illustrates the experimental conditions for evaluating the bilayer catalysts in the Cell G1. As a benchmark, first the cathodes were evaluated under a 2-stream configuration (Fig. 3.5a), i.e. a methanol solution was injected to the anode while the cathode was fed with 0.5 M KOH solution. Afterwards, for the mixed-reactant operation, the fuel cell was fed with a single solution containing MeOH in KOH as electrolyte, supplied simultaneously to both the anode and the cathode, as depicted in Fig. 3.5b. Five different concentrations of methanol (1 – 5 M) were employed. Stability measurements under mixed-reactant conditions were performed using chronoamperometry technique by applying 0.35 V during 2 h.

All fuel cell performance measurements were conducted at room temperature ( $22 \pm 2$  °C) under totally passive mode, and the data was recorded using a Scribner Fuel Cell Test System (Scribner Associates model 890CL load system), controlled by Fuel cell Test Software version 3.8.

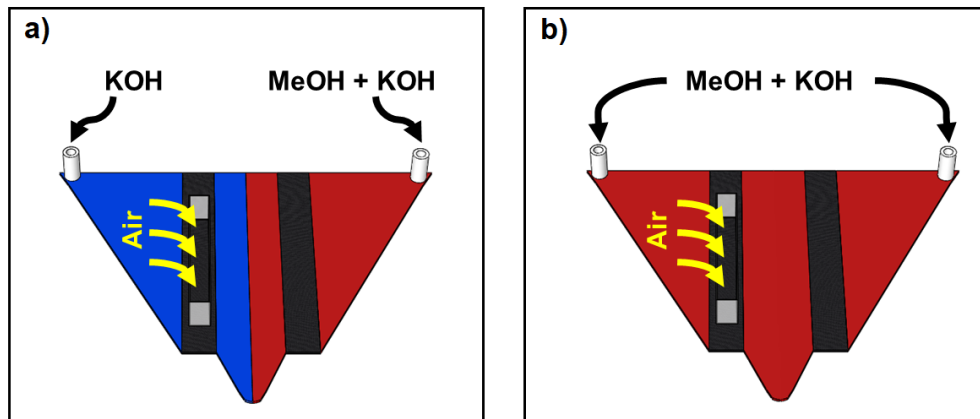


Figure 3.5 Cell G1 in a) 2 stream configuration and b) mixed-reactant configuration

### 3.5 Development of a new MR- $\mu$ DMFC

As stated previously in this thesis, one of the main objective is to exploit the features of the methanol tolerant catalysts developed in this work for using them in mixed-reactant  $\mu$ DMFCs. Since cell G1 is in essence a 2-stream FC, it is thus necessary to develop a true MR- $\mu$ DMFC, which can be eventually turned into a passive MR- $\mu$ DMFC stack with the capability to supply enough energy for low power applications.

As mentioned in Chapter 1, numerical simulation is a powerful tool for the analysis of electrochemical phenomena, distribution of chemical species, and a convenient method for optimizing certain fuel cell components, therefore, it can be used for the design and study of new fuel cells systems. For these reasons, in this work we employ numerical simulation in order to develop a more fuel-efficient and better performing MR- $\mu$ DMFC.

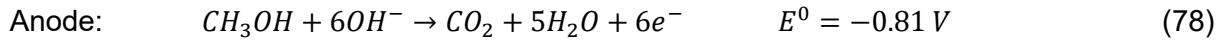
#### 3.5.1 Numerical methodology and model definition

The construction of the mathematical model for studying new fuel cell designs requires certain experimental data in order to best predict the behavior of future experimental systems. For this reason, testing of an existing  $\mu$ DMFC was used as base for the development of the numerical simulation. The fuel cell used in this stage was the cell G1 under mixed-reactant conditions. The objective is to obtain theory that allows the designing and feature optimization of a new microfluidic fuel cell system. For the model to accurately predict experimental data, some elements of the original device, such as the catalytic materials, catalyst loading and electrodes dimensions are kept unchanged. We then focus the theory on studying different electrode

arrangements and their impact on the fuel utilization, as well as the effect of the electrodes separation on the ohmic resistance of the fuel cell.

In order to obtain the model, each component of the cell G1 was constructed through computer-aided design (CAD) software. COMSOL Multiphysics ® was employed for solving the coupled electrochemical reactions and transport phenomena in the microchannel of the  $\mu$ FFC. The model definition included porous electrodes and an air-breathing cathode. The properties of every component, such as electrode features, fluid density and viscosity and electrochemical parameters, provided in tables 3.3 and 3.4 were annexed to the database in the software.

The occurring reactions in a DMFC in alkaline media are [39]:



A complete MOR to carbon dioxide is assumed to occur at the PtRu anode [115], while the ORR on the  $Mn_2O_3/Pt$  cathode proceeds through a 4-electron transfer, as determined experimentally [152]. The reaction intermediates are not considered in this model. Room temperature ( $T=298K$ ) was established for the  $\mu$ FFC operation. An isothermal condition inside the microchannel was established since the liquid velocities through the channel are  $\bar{u} < 1 \text{ cm s}^{-1}$ . Fluid flow in microscale devices is typically laminar and governed by low Reynolds numbers [153],

$$Re = \frac{\rho \bar{u} L}{\mu} \quad (81)$$

where  $\bar{u}$  is the fluid velocity,  $\rho$  the density of the fluid,  $L$  is the hydraulic diameter and  $\mu$  is the fluid dynamic viscosity. Viscous effects dominate over inertial effects and surface forces are more relevant than body forces, therefore the body forces and the viscous dissipation are assumed as negligible (Equations 82, 83 and 84) [153]. Due to the laminar nature of microfluidics,  $\bar{u}$  for incompressible Newtonian fluids can be deduced by solving the Navier–Stokes equations for momentum conservation in 3D (Eq. 5), provided that the continuum assumption is appropriate (as in most microscale liquid flows) [154],

$$\rho \left( \frac{\partial \bar{u}}{\partial t} + \bar{u} \cdot \nabla \bar{u} \right) = -\nabla p + u \nabla^2 \bar{u} + \bar{f} \quad (82)$$

where  $p$  represents pressure,  $\rho$  is the fluid density and  $\bar{f}$  summarizes the body forces per unit volume. At very low Reynolds numbers, the non-linear convective terms can be neglected, resulting in linear and predictable Stokes flow [5].

$$\rho \frac{\partial \bar{u}}{\partial t} = -\nabla p + u \nabla^2 \bar{u} + \bar{f} \quad (83)$$

Furthermore, mass conservation for fluid flow obeys the continuity equation [155].

$$\frac{\partial \rho}{\partial t} + \nabla(\rho \bar{u}) = 0 \quad (84)$$

To solve the flow distribution in the porous media, Darcy's law was employed [155],

$$\bar{u} = -\frac{k}{\mu} \nabla p \quad (85)$$

where  $k$  is the intrinsic permeability of the porous media. Intrinsic permeability, known as the permeability for the single phase flow, is independent of the nature of the fluid but dependent on the geometry of the medium [156]. Since the fuel and the electrolyte are dilute solutions, their density input value is that of water.

Based on preliminary experimental results described in section 5.5, an open circuit voltage of 0.77 V was established for the simulation. According to the studies on the selectivity of the cathode, methanol crossover does not affect the performance of the fuel cell [152], for this reason the model does not consider any methanol crossover effect.

The theoretical equilibrium potential of the  $\mu$ FFC is mainly affected by anodic and cathodic activation losses ( $\eta_{a,a}, \eta_{a,c}$ ), ohmic losses ( $\eta_r$ ), losses of mass transport at the electrodes ( $\eta_{m,a}, \eta_{m,c}$ ) and fuel-oxidant crossover or internal short circuits ( $\eta_x$ ) [22].

$$E_{cell} = E^0(T, p) - \eta_{a,a} - |\eta_{a,c}| - \eta_r - \eta_{m,a} - |\eta_{m,c}| - \eta_x \quad (86)$$

The contribution of mass transfer losses to the voltage profile is minimized in the model due to the use of high concentration of methanol and to the constant supply of oxygen from the atmosphere and the higher diffusion coefficient in air, in comparison with water. For this reason there is no sharp drop of voltage at high current densities. This way, the activation and ohmic

losses contributed in greater proportion. Ohmic losses are attributed to the ionic resistance of the electrolyte ( $R_{electrolyte}$ ) and to the resistance of the electrodes and electrical connections ( $R_{external}$ ) [22].

$$\eta_r = I(R_{electrolyte} + R_{external}) \quad (87)$$

Electrochemical reactions are assumed to occur in the porous electrodes covered by a thin layer of catalyst particles [90,157,158]. The catalyst layer is treated as a boundary. The species concentration distribution over the electrodes is governed by diffusion-convection transport, and can be calculated by solving mass conservation equation [54].

$$\nabla(-D_i \nabla C_i + C_i \vec{u}) = S_i \quad (88)$$

where  $D_i$  is the diffusion coefficient of species “ $i$ ” and  $S_i$  is the net rate of change of species “ $i$ ” by electrochemical reactions over the anode and cathode, and represents the rate of consumed species per cubic meter [158].

$$S_i = \left[ \frac{mol}{m^3} \right] \quad (89)$$

While the electrochemical reactions occur, fuel and oxidant are consumed over the corresponding electrodes to generate the current. Current density distribution is estimated by Butler-Volmer equation as a function of volumetric exchange current of a given electrode ( $i_0$ ) at reference concentration ( $C_{i,ref}$ ) [22].

$$j_0 = a i_0 \left( \frac{C_i}{C_{i,ref}} \right)^{\beta_i} \left[ \exp\left(\frac{\alpha_a F \eta}{RT}\right) - \exp\left(-\frac{\alpha_c F \eta}{RT}\right) \right] \quad (90)$$

where  $a$  is the active specific surface area,  $C_i$  is concentration of the species “ $i$ ” (fuel or oxidant),  $\beta_i$  is the reaction order of the species for the elementary charge transfer step,  $\alpha_a$  and  $\alpha_c$  are the anodic and cathodic charge transfer coefficients,  $R$  is the universal gas constant,  $T$  is the operation temperature,  $F$  is the Faraday’s constant and  $\eta$  is the surface overpotential, as expressed by [159]

$$\eta = \Phi_s - \Phi_e - E^0(T, P) \quad (91)$$

where  $\Phi_s$  and  $\Phi_e$  are the electric potential of electrode and electrolyte, respectively. The transportation of charged species toward the cathode and the electric field inside the electrolyte was modeled by using the electric potential equation for both the anode and cathode [160].

$$\sigma_i \Delta \Phi_i = i_i \quad (92)$$

where  $i_i$  is the current source term ( $\text{A m}^{-3}$ ),  $\Phi_i$  is the electrical potential, and  $\sigma_i$  is the electrical conductivity [161].

Both the oxidant and fuel are in KOH solution, thus  $\text{OH}^-$  ions are considered to be uniformly distributed inside the microchannel [160]. The total ohmic resistance of the cell was determined to be  $19 \Omega$  (Fig. 3.6), as measured by Electrochemical Impedance Spectroscopy (EIS) recorded in the frequency range from 1 Hz-10 kHz with applied AC amplitude of 10 mV. Besides the ohmic losses, the Nyquist plot shows that the cathode activation losses are much greater than the anode activation losses, as observed in the relative size of the semicircles.

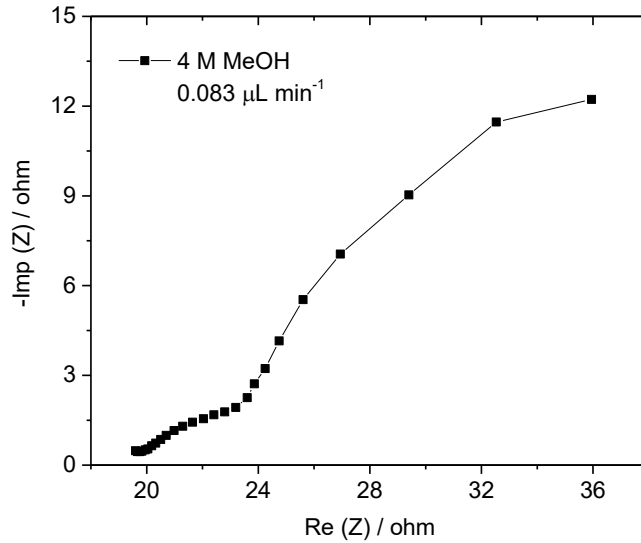


**Figure 3.6** Impedance spectra recorded for cell G1 at OCV.

The initial concentration of the fuel was set to 4 M at the anode and zero at the cathode. For the simulation of the air-breathing cathode, a section of the electrode is exposed to the ambient with an inlet concentration equal to the oxygen concentration in the atmosphere ( $9.35 \text{ mol m}^{-3}$ ) [155]. Due to the porous structure of the cathode and anode, the binary diffusion coefficients utilized in the porous media are corrected with the porosity ( $\varepsilon$ ) and tortuosity ( $\tau$ ) of the media [146,155].

$$D_{ij}^{eff} = D_{ij} \frac{\varepsilon}{\tau} \quad (93)$$

In order to facilitate the numerical simulation, a steady-flow operation with a single inlet velocity of  $0.083 \mu\text{L min}^{-1}$  was established instead of using a transient behavior.

Table 3.3 Input values for the generation of the model.

Parameter	Description	Value	Units	Reference
$C_{i,MeOH}$	Reference concentration of methanol	4000	mol m <sup>-3</sup>	
$C_{i,O_2}$	Reference concentration of oxygen	9.35	mol m <sup>-3</sup>	[87]
$D_{O_2(H_2O)}$	Diffusivity of oxygen in water	$2.1 \times 10^{-9}$	m <sup>2</sup> s <sup>-1</sup>	[87]
$D_{O_2(Air)}$	Diffusivity of oxygen in air	$2.1 \times 10^{-5}$	m <sup>2</sup> s <sup>-1</sup>	[87]
$D_{CH_3OH}$	Diffusivity of methanol as anolyte	$5 \times 10^{-10}$	m <sup>2</sup> s <sup>-1</sup>	[87]
$n_a$	Number of electrons transferred at the anode	6	–	[87]
$n_c$	Number of electrons transferred at the cathode	4	–	[87]
$F$	Faraday's constant	96485	C mol <sup>-1</sup>	[87]
$J_{o,a}$	Exchange current density at the anode	10	A m <sup>-2</sup>	Fitted
$J_{o,c}$	Exchange current density at the cathode	$0.5 \times 10^{-7}$	A m <sup>-2</sup>	Fitted
$k$	Permeability of electrodes	$6.15 \times 10^{-12}$	m <sup>2</sup>	[146]
$K$	Electrical conductivity of electrodes	15000	( $\Omega$ m) <sup>-1</sup>	[162]
$R$	Universal gas constant	8.1314	J mol <sup>-1</sup> K <sup>-1</sup>	[87]
$T$	Temperature	298	K	
$\alpha_a$	Anodic charge transfer coefficient	0.5	–	[87]
$\alpha_c$	Cathodic charge transfer coefficient	0.5	–	[87]
$\varepsilon_a$	Porosity of the anode	0.78	–	[146]
$\varepsilon_c$	Porosity of the cathode	0.65	–	[146]
$\mu$	Viscosity	0.001003	–	*
$\rho$	Density of anolyte and electrolyte stream	998.2	kg m <sup>-3</sup>	*
$\tau_a$	Tortuosity of the anode	2.55	–	[146]
$\tau_c$	Tortuosity of the cathode	1.95	–	[146]
$\sigma$	Electrolyte ionic conductivity	60	S m <sup>-1</sup>	[163]
$v$	Flow inlet	0.083	$\mu$ L min <sup>-1</sup>	

\*From the software database.

**Table 3.4**      **Boundary conditions.**

---

$[\text{CH}_3\text{OH}] = 4 \text{ M}$
$E_0 = 0.77 \text{ V}$ as initial reversible potential
$C = C_0$ at the inlet
$\bar{u} = (0, \bar{u}_0)$ , $\bar{u}_0 = \text{inlet velocity}$
$\bar{u}_0 = 0.083 \mu\text{L min}^{-1}$
$\bar{u} = (0, 0)$ at the walls
$p = 0$ at the outlet

---

### 3.5.2 Fabrication of Cell G2

Two different electrodes-microchannel configurations were studied in this work through the obtained model. The electrode arrangements are shown in Fig. 3.7 and detailed described in section 6.2. Subsequently, a new MR- $\mu\text{DMFC}$  was developed with the optimal features according to the numerical simulation. The resulting microfluidic device is denominated cell G2 throughout this work. The single stream inlet is positioned at the left of the anode and the channel opens in a V-shape until meeting the length of the electrodes (10 mm). The resulting volume of the microchannel is 56  $\mu\text{L}$  and the total device dimensions are indicated in Fig. 3.8.

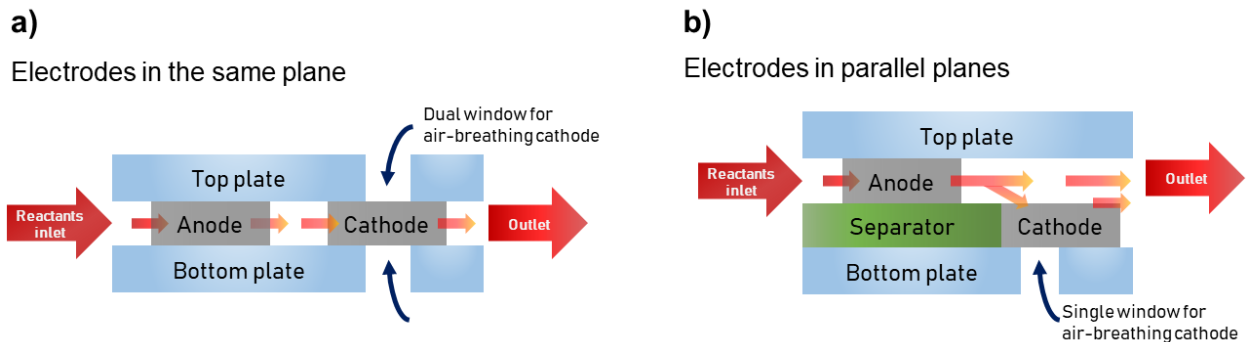


**Figure 3.7**      **Representation of the two different electrode arrangements. The components are not to scale.**

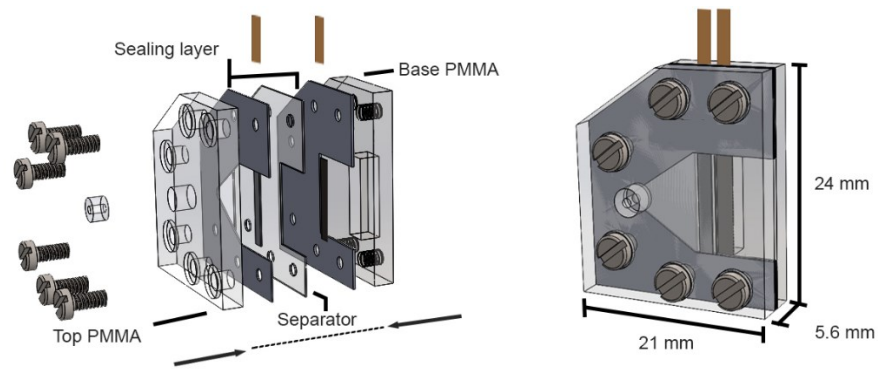


**Figure 3.8 Representation of components and assembly of cell G2, developed after numerical simulation.**

For the fabrication of cell G2, all the components were modeled in SolidWorks®. The top and bottom plates parts were then machined on 2.5 mm Poly(methyl methacrylate) (PMMA) by Computer Numerical Control (CNC) micromachining (Fig. 3.9, Nomad 883, Carbide 3D). A 10 mm × 1.5 mm cut was machined on the bottom plate as window for the air-breathing cathode. A separator (Polyethylene Terephthalate sheet, 200 µm thick) was used between the anode and the bottom plate, while the top sealing layer shapes the profile of the microchannel. The sealing components were made of Silastic™ layers, 200 µm thickness. A cutter plotter was used to obtain the profile of the microchannel, separator and gaskets. The electrodes dimensions are 10 mm × 1.5 mm × 0.15 mm. The electrical contacts were made with strips of copper tape (SPI Supplies®). The electrodes-microchannel set was sandwiched between the two PMMA plates and the ensemble was tightened by M1.6 machine screws.

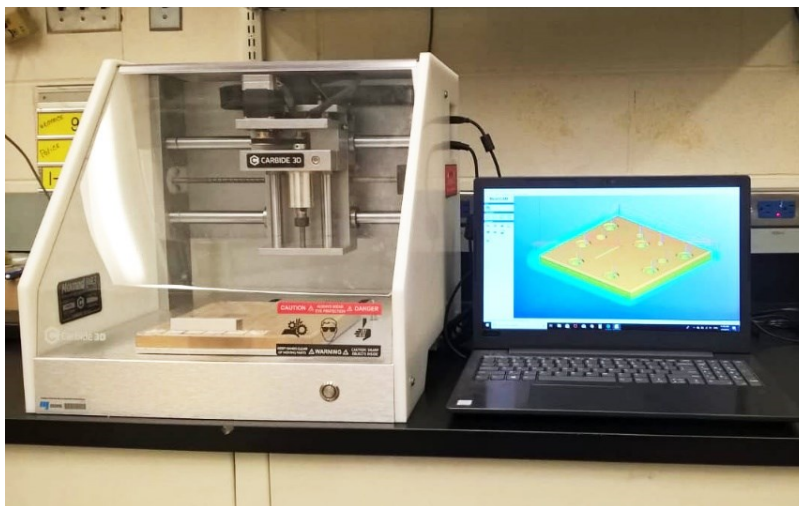


**Figure 3.9 CNC machine used for the fabrication of the devices.**

### 3.5.3 Test of the single cell

Prior to the fabrication and evaluation of the G2 cell, performance tests were run on the G1 cell in order to find the optimum fuel concentration for maximum performance with the electrodes employed. Methanol concentrations from 1 to 5 M in 0.5 M KOH were considered. The microfluidic device was operated at room temperature ( $22 \pm 2$  °C) and under totally passive mode.  $\text{Mn}_2\text{O}_3/\text{Pt}/\text{CP}$  material was used as cathode while the anode was commercial PtRu/C. After identifying the optimum concentration, the cell G2 having the same electrodes was tested using 56  $\mu\text{L}$  of 4 M MeOH in 0.5 M KOH solution at room temperature and under passive operation. When filling the microchannel, the reactant stream flows through the anode and then runs on the surface of the cathode where the thin layer of catalyst is deposited, while the opposite face (gas diffusion layer) is exposed to the air. Typically, the performance of fuel cells employing flow-through electrodes is normalized using the cross-sectional area of the electrodes [149,150], thus, the current and power output of cell G1 and G2 are normalized by  $0.015 \text{ cm}^2$ . Although in the G2 design, only the anode is, in strict terms, a flow-through electrode, its performance is normalized with the cross-sectional area in order to make it directly comparable with its earlier iteration, since the electrodes remain unchanged. The durability and stability of the cell G2 was tested using chronoamperometry technique by applying 0.3 V during 6 h. The fuel cell performance and stability measurements were performed on a Scribner Fuel Cell Test System (Scribner Associates model 890CL load system), controlled by Fuel Cell Test Software version 3.8.

## 3.6 Development of a 4-cell MR- $\mu\text{DMFC}$ stack

A new 4-cell MR- $\mu\text{DFMC}$  stack was developed from the single cell G2. The device consists basically of 4 G2 cells unified in a single block. The detailed description of the stack is presented in section 6.4. The materials and fabrication methods for the fuel cell stack are the same as described in section 3.5.2.

### 3.6.1 Test of the stack

In a first testing stage, 4 M MeOH in 0.5 M KOH solution was supplied to the stack and each cell was evaluated individually using the same conditions described for the cell G2 in section 3.5.3. Then, the four cells were connected in series and in parallel arrangements and the performance of the device was tested. The stability of the four cells connected in series was evaluated by applying 1.2 V during 120 min.

The second part of the tests consisted in using the fuel cell stack as a power supply. For this, the four cells in series arrangement were directly connected to a green LED (0603 SMD LED, Kingbright) and the system was kept in operation under passive mode during 4 h.



## CHAPTER 4 RESULTS: Ag/Pt/CP CATHODE

### 4.1 Physicochemical characterization

Figure 4.1 presents the SEM images of the Pt, Ag and Ag/Pt films synthesized by PLD onto CP substrate. Top views SEM images reveal that Pt film (Figure 4.1a) is very porous, and micro-cracks can be seen at the surface (Figure 4.1a'). On the other hand, the surface of the Ag film looks smoother (Figure 4.1b and 4.1b'). A similar surface morphology is seen for Ag deposited onto Pt (Figure 4.1c and 4.1c'). The thickness of the films was estimated by cross-section SEM images to be 25 nm (Figure 4.1a''), 25 nm (Figure 4.1b''), and 50 nm (Figure 4.1c'') for Pt, Ag and Ag/Pt respectively.

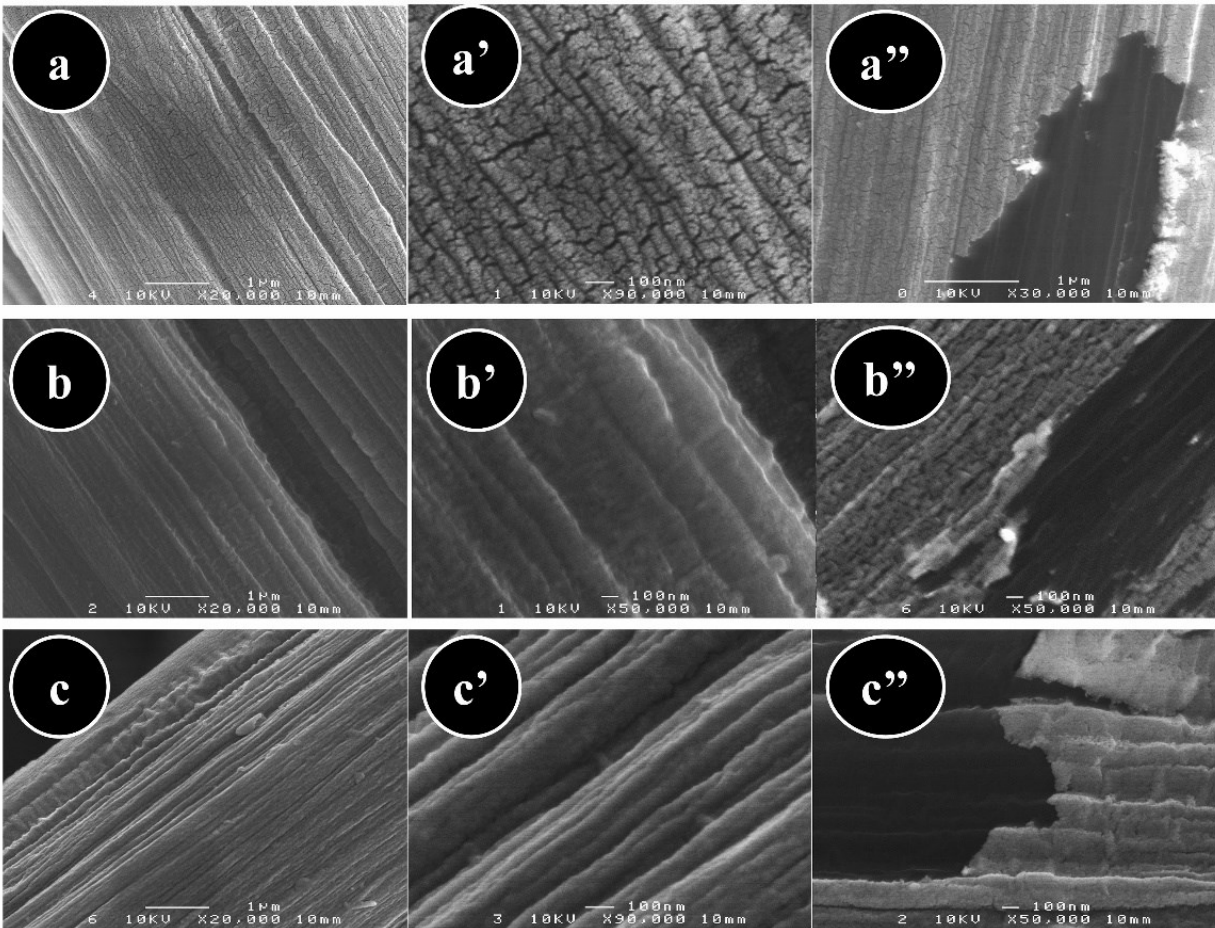


Figure 4.1 SEM images of a) Pt/CP, b) Ag/CP and c) Ag/Pt/CP. (a' b', c') corresponding higher magnifications, and (a'', b'', c'') corresponding cross-section images.

The XRD profiles of the synthesized films are presented in Figure 4.2. The profile of the Pt shows the diffraction peaks Pt(111), Pt(200), Pt(220), and Pt(311) and strong peaks of the CP substrate. The lattice parameter estimated from the Pt(111) peak was found to be 3.91 Å, which is consistent with that of bulk Pt (JCDs 04-0802), whereas the mean crystallite size was found to be 11.9 nm. As for Ag, the Ag(111), Ag(200), Ag(220), Ag(311) and Ag(222) could be identified. The lattice parameter calculated using the strongest peak Ag(111) was found to be 4.09 Å in agreement with Ag (JCDs 04-0783) and the mean crystallite size equal to 31 nm. After coating the Pt/CP with silver, peaks originating from the platinum metal were still detected. No significant shift in the peak position was observed for both Pt and Ag. However, the Scherrer analysis of the primary (111) peaks for both Pt and Ag revealed that the mean crystalline size of Pt decreased to 8.2 nm, whereas that of Ag decreased to 16.2 nm.

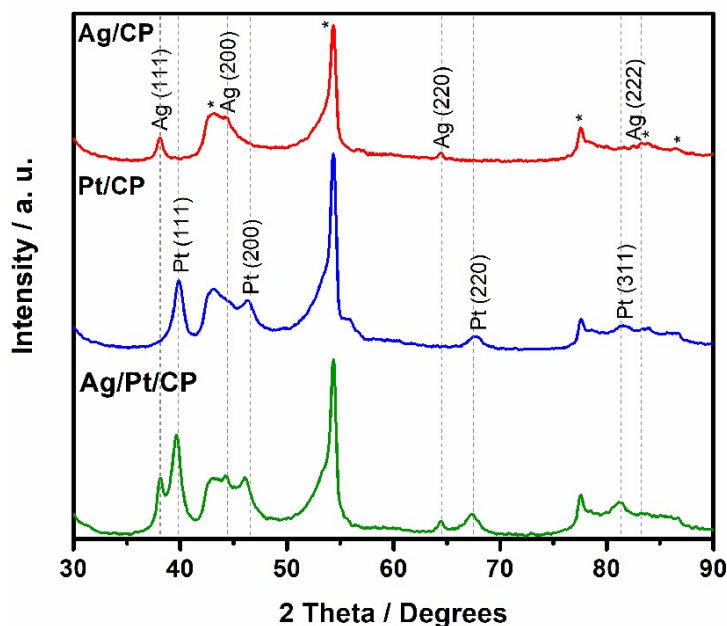


Figure 4.2 XRD patterns of Pt/CP, Ag/CP and Ag/Pt/CP. (\*) Carbon.

XPS measurements were performed to determine the chemical composition of surface elements and their oxidation states. The surveys scan spectra revealed that (Pt, O, C) and (Ag, O, C) are the only elements existing on the surface of Pt/CP and Ag/CP, respectively (Figure 4.3). The XPS survey scan of the Ag/Pt/CP sample showed peaks just for Ag, C and O and no peak related to Pt was detected on the surface, indicating that the Ag film fully coated the surface of the beneath Pt layer. The small amount of oxygen detected on the surface comes from the ambient atmosphere during samples manipulation

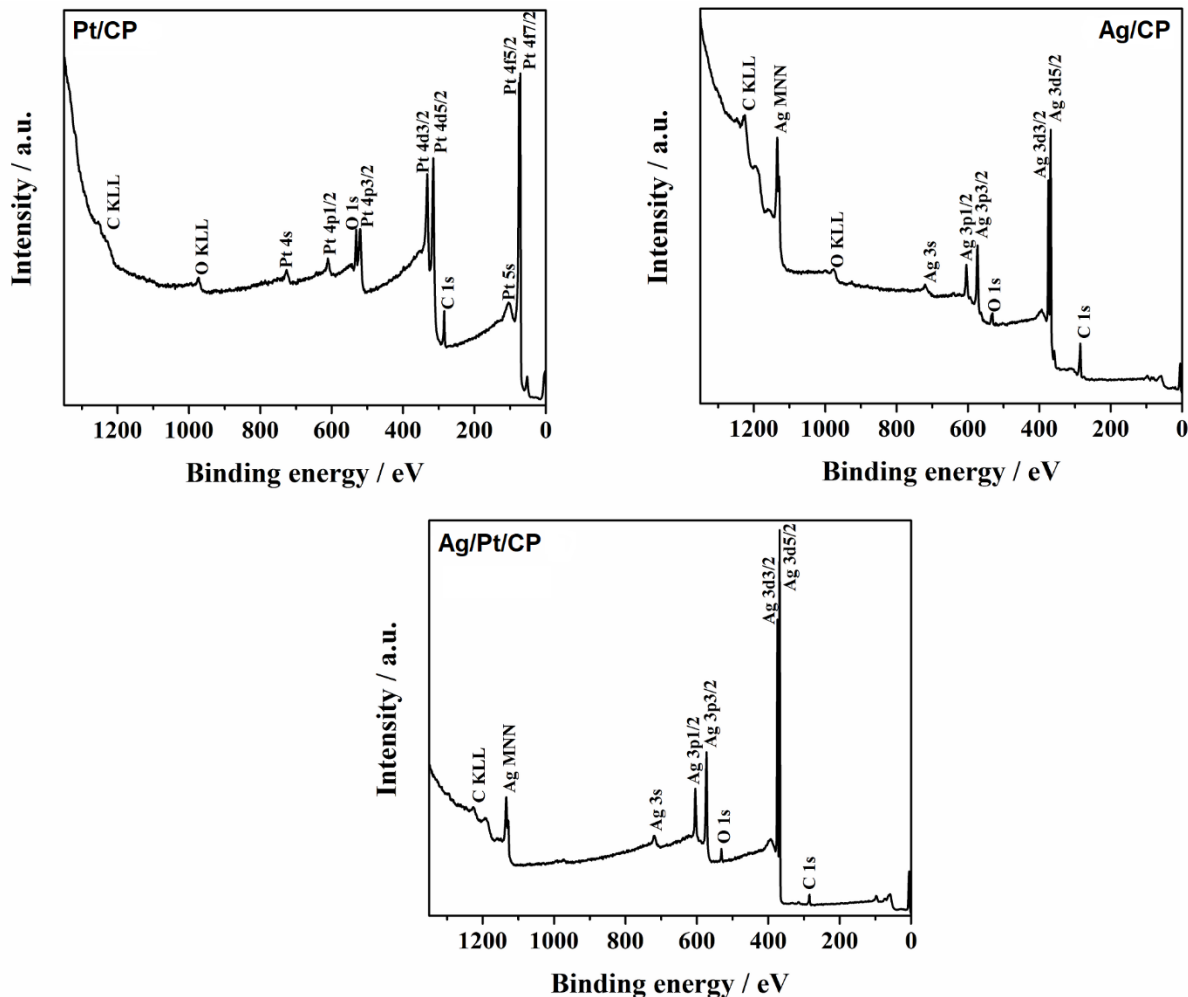


Figure 4.3 XPS survey scans of Pt/CP, Ag/CP and Ag/Pt/CP.

Figure 4.4 displays the collected high-resolution core level XPS spectra of the Pt 4f and Ag 3d regions. Satisfactory fitting of each core level peak was obtained using only one component with an asymmetric profile. The Pt 4f<sub>7/2</sub> and Pt 4f<sub>5/2</sub> peaks were located at 71.3 eV and 74.6 eV, respectively. The 3.3 eV binding energy difference between the two Pt 4f peaks is consistent with Pt being in a metallic state [164]. The Ag 3d<sub>5/2</sub> and Ag 3d<sub>3/2</sub> for both Ag/CP and Ag/Pt/CP are positioned 368.4 eV and 374.4 eV, respectively. The binding energy difference of 6 eV indicates that Ag is in metallic state [165]. These observations further indicate that in the Ag/Pt/CP, the underlying Pt layer did not affect the valence states of Ag. However, the Ag 3d peaks in the Ag/Pt/CP are narrower than those in the Ag/CP, indicating smaller particles size for the former, which is in agreement with the XRD findings [164].

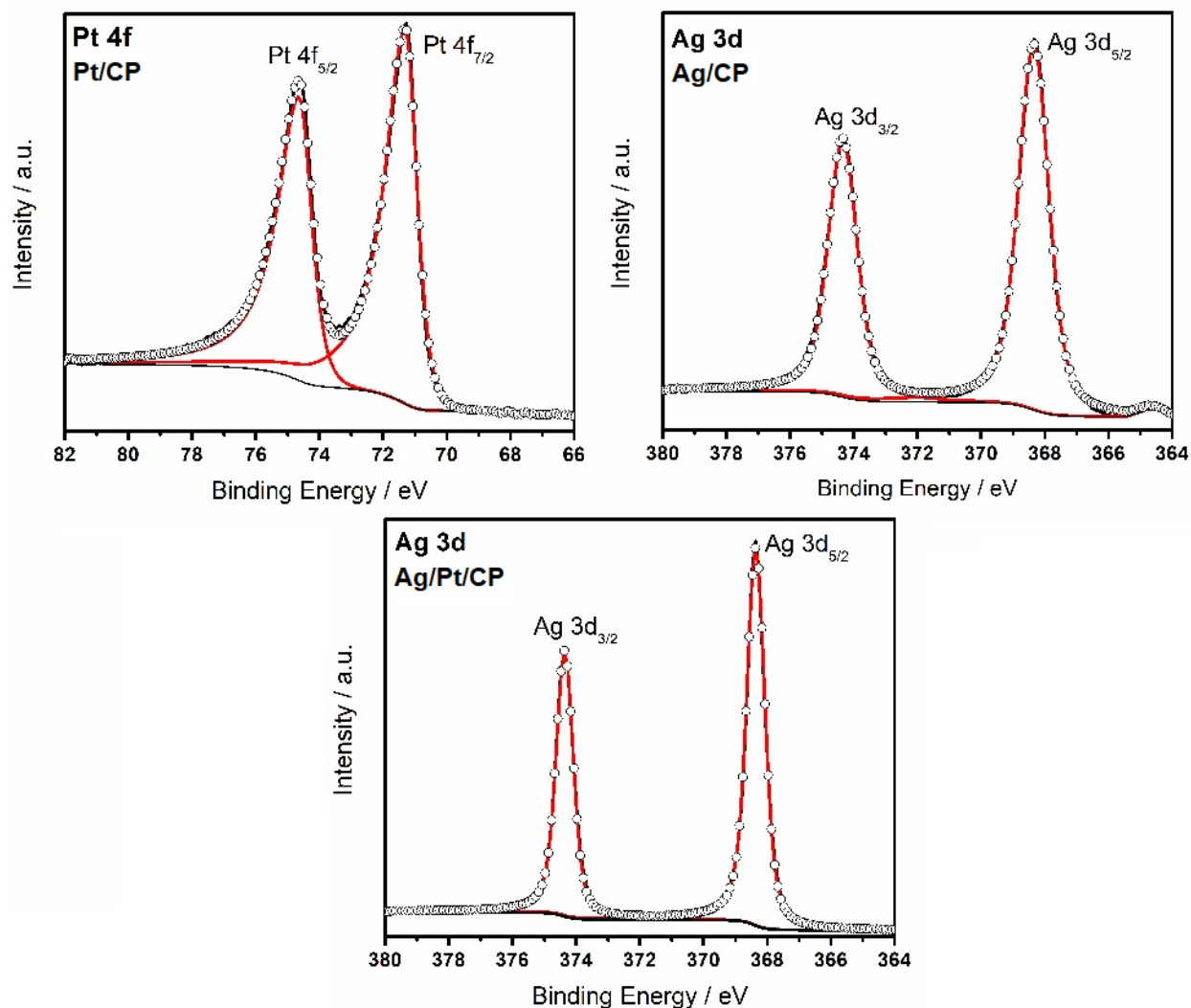


Figure 4.4 High-resolution XPS core-level spectra of Pt 4f in Pt/CP, Ag 3d in Ag/CP and Ag 3d in Ag/Pt/CP.

## 4.2 Electrochemical characterization

Figures 4.5a, 4.5b and 4.5c show CVs recorded at  $20 \text{ mV s}^{-1}$  scan rate in  $0.5 \text{ M KOH}$  oxygen free solution at the Pt/CP, Ag/CP and Ag/Pt/CP catalysts, respectively. The CV of Pt/CP (Figure 4.5a) shows well-defined features of Pt including hydrogen adsorption/desorption below  $\sim 0.5 \text{ V}$  versus RHE, Pt oxide formation/reduction above  $\sim 0.6 \text{ V}$  and a double layer (dl) region in between [166,167]. The CV of the Ag/CP catalyst displays anodic current peaks (two major ones (AII and AIII) and a small anodic shoulder (AI). The reverse potential scan exhibits two cathodic contributions (one cathodic shoulder CI and one major peak CII) (figure 4.5b). According to the literature, the anodic shoulder AI is ascribed the electroformation of soluble  $[\text{Ag}(\text{OH})_2]^-$  complex

species, All to the electroformation of  $\text{Ag}_2\text{O}$ , and AllI to nucleation and three dimensional growth of the  $\text{Ag}_2\text{O}$  layer, while the cathodic contributions Cl and CII could be related to processes involved in electroreduction of  $\text{Ag(I)}$  oxygen species [168]. The CV of  $\text{Ag/Pt/CP}$  catalyst (figure 4.5c) presents similar voltammetric features with broadly identical peak positions and shapes but with significantly higher current densities. Note that the CV features of the Pt, (Pt-oxide formation/reduction and hydrogen region) are present with smaller current density, suggesting that Pt is coated by a thin layer. These observations are in agreement with the XRD and XPS results. The superior electrocatalytic activity performance of the  $\text{Ag/Pt/CP}$  results from depositing Ag onto the Pt layer, which has a high surface area due to the high background pressure employed during the deposition [83,169].

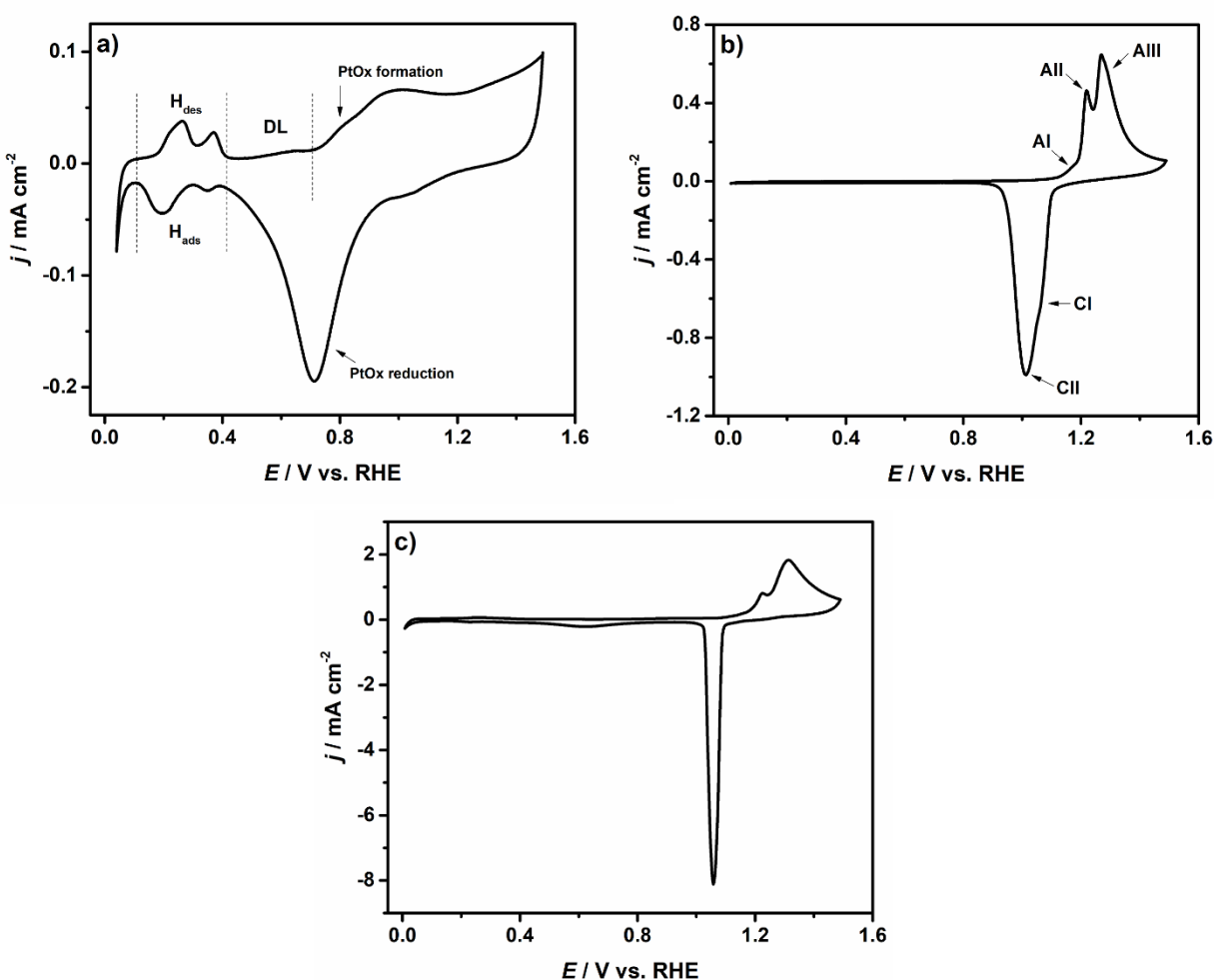


Figure 4.5 Electrochemical profiles of a) Pt/CP, b) Ag/CP and c) Ag/Pt/CP catalysts recorded by CV at 20  $\text{mV s}^{-1}$  scan rate in 0.5 M KOH oxygen free solution.

### 4.3 ORR performance

The catalytic behavior of the synthesized materials in an oxygen-saturated environment was studied. During the ORR, oxygen molecules can accept either a two or four electron transfer. The number of electrons involved during this process is an important parameter for the evaluation of the catalytic performance, as it provides insight into the reaction mechanism. For this reason, rotating ring disk electrode (RRDE) measurements were performed using the three different catalysts.

Fig. 4.6a displays the typical RRDE voltammograms obtained at 400 rpm in O<sub>2</sub>-saturated 0.5 M KOH solution at a scan rate of 10 mV s<sup>-1</sup>. It can be seen that the current density at 0.9 V for Ag/Pt is -0.2 mA cm<sup>-2</sup>, while for Ag, the ORR has not started at said potential. The current density on the former is markedly similar to that of Pt/CP, nevertheless, the reaction seems slightly more sluggish on the bilayer material in comparison with Pt. In addition, the ORR limiting current observed for Ag/Pt/CP and Pt/CP are fairly similar (~2.8 mA cm<sup>-2</sup>) and considerably higher than the one observed on Ag/CP (~2.1 mA cm<sup>-2</sup>). The amount of hydrogen peroxide produced at the Pt/CP and the Ag/Pt/CP catalysts is below 5% at any point, in contrast to Ag/CP, where it increases from 4 to 11% as the potential is swept to the cathodic direction, as shown in Fig. 4.6b. These observations indicate that the ORR on Pt and on the bilayer cathode proceeds almost entirely through the four electron pathway. This was confirmed by means of the calculation of *n* for the three catalysts. As depicted in Fig. 4.6c, the average *n* value in the potential range from 0.8 to 0.45 V is 3.91 and 3.84 for Pt/CP and Ag/Pt/CP, respectively, while on Ag/CP, the value of *n* decreases to 3.45 at 0.6 V. These results reveal that the Ag coating does not significantly affect the catalytic activity of the beneath Pt layer, as the number of electrons transferred is very similar and close to the theoretical value of 4 electrons. The aforementioned suggests that the ORR on the bilayer catalyst is actually carried out on the inner Pt layer, whereas the external Ag layer does not participate or has a negligible effect on the ORR performance of Pt under these conditions. A possible explanation is that oxygen molecules are able to diffuse through the porous Ag layer and reacting at the Pt, a phenomenon previously studied in a porous Ru shell with a Pt core [80]. Though the two components of the cathode are active to the ORR, it is clear that the overpotential required for the reaction to proceed on Pt is less than on Ag. Fig. 4.6d shows the Tafel plots of the three catalysts. It is observed that the Tafel slope in the low overpotential region for Ag/Pt/CP is 72 mV dec<sup>-1</sup>, while for Ag/CP, the slope is 84 mV dec<sup>-1</sup>, which is considerably higher than the slope on Pt (61 mV dec<sup>-1</sup>).

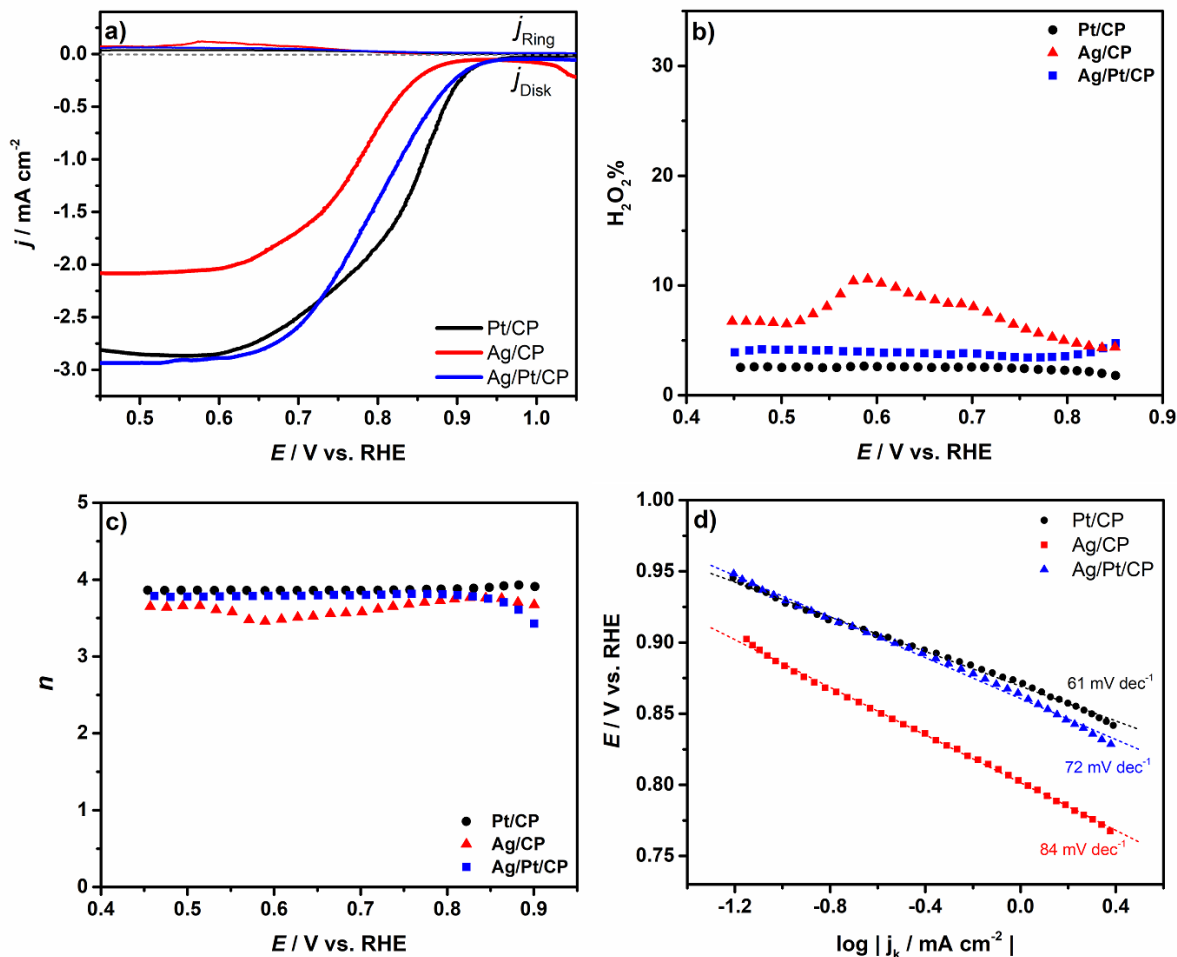


Figure 4.6 RRDE voltammograms of Pt/CP, Ag/CP and Ag/Pt/CP acquired in  $O_2$  saturated 0.5 M KOH solution at 400 rpm, b)  $H_2O_2$  yield, c) electron transfer number ( $n$ ) and d) Tafel plots.

#### 4.4 Selectivity of the Ag/Pt/CP cathode towards the ORR and methanol tolerance

First, the electroactivity of the three catalysts towards the Methanol Oxidation Reaction (MOR) was studied. Figure 4.7a shows the CVs of the Pt/CP, Ag/CP and Ag/Pt/CP catalysts recorded in 0.5 M KOH + 1 M MeOH at a scan rate  $20 \text{ mV s}^{-1}$ . In the case of Pt/CP catalyst, a prominent oxidation peak of methanol can be observed. On the other hand, the Ag/CP and Ag/Pt/CP catalysts exhibited a very weak activity with regard to MOR (as shown in the inset in Fig. 4.7a), i.e., the peak currents for methanol oxidation with Ag/CP and Ag/Pt/CP were about 1/512 and 1/474 of that displayed by the Pt/CP catalyst. This results indicate that after coating Pt with Ag, the methanol adsorption was blocked. Thus, the lower catalytic activity of Ag/Pt/CP towards the MOR could only be attributed to the presence of Ag, which has significant inhibition for this reaction on the surface. Methanol or oxygen must diffuse through the porous layer of the Ag

nanoparticles to access the active Pt core for electrocatalysis to occur. In this case, the larger molecular size of methanol would obstruct its diffusion, rendering the oxidation of methanol on Ag/Pt/CP a non-competitive event. The isolation of the electrocatalyst from the methanol is highly important for preparing a methanol-tolerant electrocatalyst. Meanwhile, the Ag showed almost no effect on the O<sub>2</sub> diffusion due to the smaller size of the oxygen molecule and easy diffusion through the porous layer of Ag.

Afterwards, the ORR performance of the three catalysts in the absence of methanol was tested. Figure 4.7b compares slow LSVs (5 mV s<sup>-1</sup>) in oxygen-saturated 0.5 M KOH solution. As can be observed, the Ag/CP and Ag/Pt/CP catalysts displayed very well defined mass transfer and kinetic regions similar to Pt/CP catalyst. The onset potential of the ORR is 0.96 V, 0.88 V and 0.92 V vs RHE for Pt/CP, Ag/CP and Ag/Pt/CP, respectively. At higher overpotentials, the kinetics of ORR at Ag/Pt/CP are slightly slower than those at the Pt/CP catalyst, while they are very sluggish at the Ag/CP catalyst. Subsequently, the ORR performance of the catalysts in the presence of methanol was tested. Figure 4.7c compares voltammograms in oxygen-saturated 0.5 M KOH solution containing 1 M of methanol concentration. The ORR on Pt/CP is completely inhibited in the presence of methanol due to the occurrence of MOR on Pt. On the other hand, at the Ag/CP and Ag/Pt/CP catalysts, it is rather the MOR that is prohibited. Notwithstanding, it is the Ag/Pt/CP catalyst that showed the best methanol tolerance. Remarkably, even at much higher concentrations of methanol up to 5 M, the bilayer catalyst remained highly tolerant to methanol oxidation, i.e., the current density decreased by only 8% compared to the one recorded with 0 M of methanol (Figure 4.7d). This result is significant, since it means that more fuel (methanol) can be fed at the anode, while the poisoning effect at the cathode can be disregarded, making the Ag/Pt/CP a promising cathode catalyst for practical DMFCs applications. Thus, it can be suggested that the upper Ag layer impedes methanol molecules to reach the surface of the beneath Pt layer and enables only oxygen molecules to attain the Pt surface and being reduced.

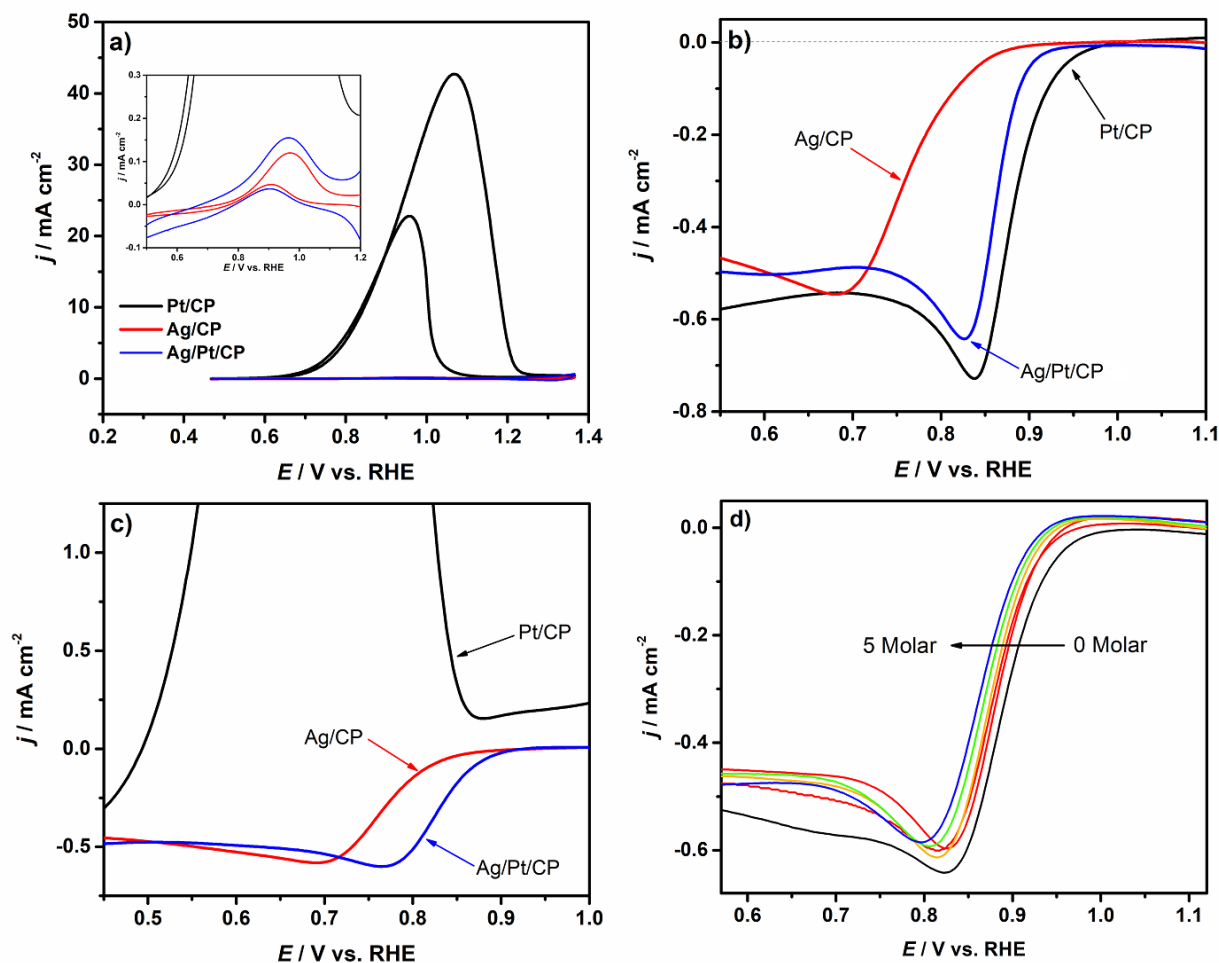
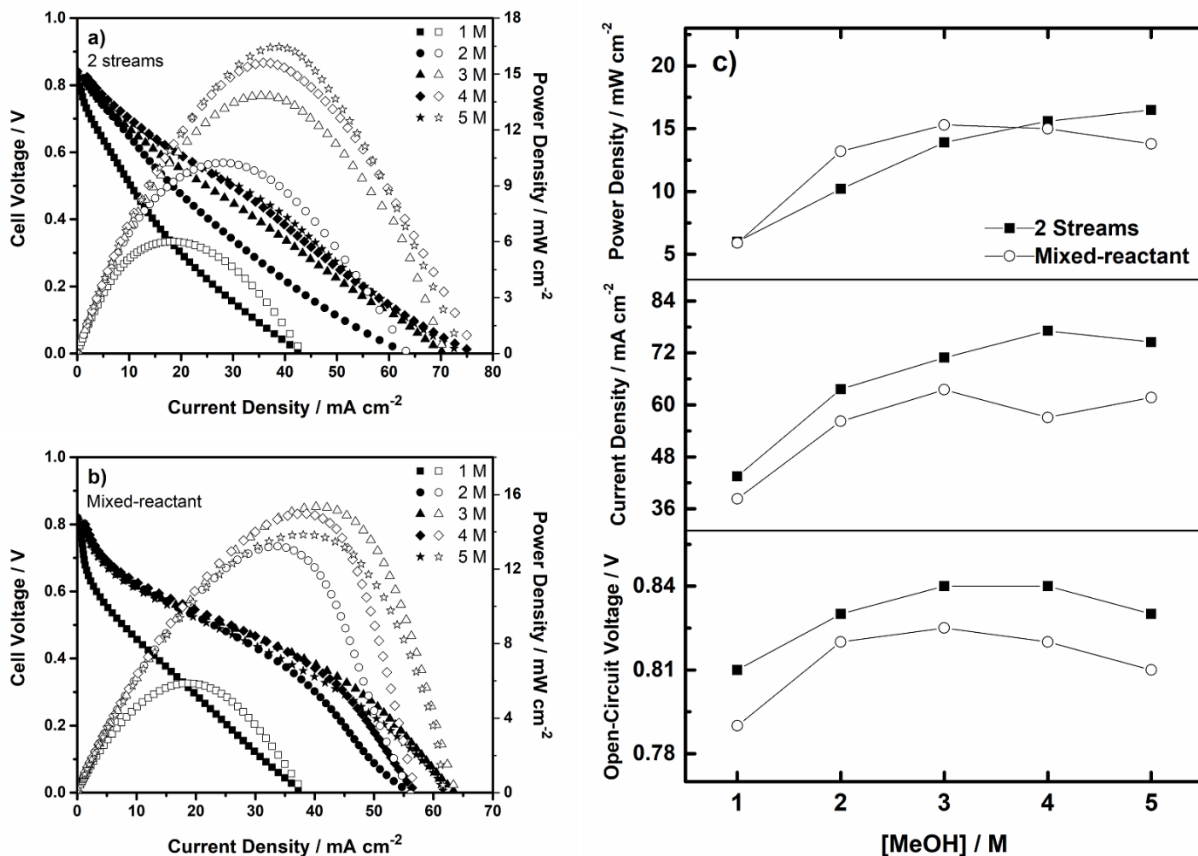


Figure 4.7 Electroactivity towards a) MOR in oxygen-free 1 M MeOH in 0.5 M KOH solution, b) ORR in oxygen-saturated 0.5 M KOH solution, c) ORR in oxygen-saturated 0.5 M KOH + 1 M MeOH, and d) ORR at Ag/Pt/CP cathode in oxygen-saturated 0.5 M KOH containing 0–5 M MeOH.

## 4.5 Fuel cell performance

Figures 4.8a and 4.8b display the performance of the ML- $\mu$ DMFC obtained with under typical 2-stream operation and under mixed-reactant conditions, respectively. In both cases, the cathode was Ag/Pt/CP and the anode was PtRu/C. For clarity, the performance parameters (OCV, maximum current density and peak power density) obtained with each concentration of methanol are presented in Fig. 4.8c. It is observed that in all cases, the fuel cells operating with 2 streams (separated reactants) exhibited slightly higher OCV, 20 mV in average for each MeOH concentration, with respect to the mixed-reactant operation. Similarly, the maximum current density reached by the fuel cell with separated reactants is slightly higher ( $\sim 7$  mA cm<sup>-2</sup>) at all methanol concentrations with respect to the mixed-reactant operation. Nevertheless, the peak

power density obtained with the fuel cell under mixed-reactant conditions is comparable to that generated by the fuel cell with 2 streams, even reaching higher values at low fuel concentrations (1–3 M MeOH). From the fuel cell polarization curve, it is possible to deduce that this behavior is clearly due to the ohmic region of the curve. In all cases, it is observed that the mixed-reactant fuel cell exhibits lower ohmic losses than the fuel cell operating with 2-streams. The difference is possibly due to the lack of anolyte–catholyte interface in the mixed-reactant fuel cell, which contributes to overall lower electrolyte resistance, resulting in a better performing fuel cell at low methanol concentrations, whereas at 4 and 5 M MeOH, the methanol crossover effect overrides the ohmic gain. The stability of the fuel cell under mixed-reactant conditions was evaluated through chronoamperometry at 0.35 V during 2 h using 3 MeOH solution in 0.5 M KOH. The  $i-t$  curve is shown in Fig. 4.9, where a stable behavior is observed. In average, the fuel cell produced  $7 \text{ mA cm}^{-2}$ , demonstrating short-term stability under mixed-reactant conditions.



**Figure 4.8** Polarization curves (full symbols) and power density curves (open symbols) obtained during the operation of the passive ML- $\mu$ DMFC in a) typical 2-stream configuration and b) under mixed-reactant operation using different concentrations of MeOH, c) OCV, max. current density and max. power density values extracted from Fig. 4.8 a and b.

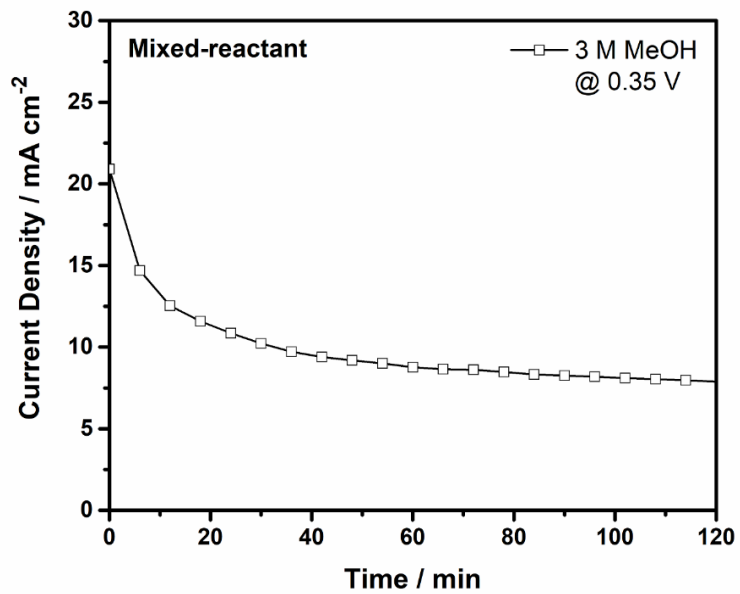


Figure 4.9 Chronoamperometric curve obtained at 0.35 V for the study of the stability of the ML- $\mu$ DMFC using 3 M MeOH.



## CHAPTER 5 RESULTS: $\text{Mn}_2\text{O}_3/\text{Pt}/\text{CP}$ CATHODE

### 5.1 Physicochemical characterization

Fig. 5.1 shows the top view SEM images of Pt,  $\text{Mn}_2\text{O}_3$  and  $\text{Mn}_2\text{O}_3/\text{Pt}$  materials synthesized by PLD onto carbon paper. The image of Pt/CP (Fig. 5.1a) shows the features of the Pt layer deposited on the substrate. This film exhibits a rough surface and porous morphology, typical of materials synthesized at high background pressure due to the interaction between the energetic species in the plasma plume and the inert gas [81,170]. These observations are consistent with Pt films previously reported [171]. On the other hand, the  $\text{Mn}_2\text{O}_3$  film (Fig. 5.1b) exhibits a rough, yet less porous surface due to the lower background pressure set during the deposition. A quite similar morphology is observed for the  $\text{Mn}_2\text{O}_3/\text{Pt}/\text{CP}$  material (Fig. 5.1c), meaning that the  $\text{Mn}_2\text{O}_3$  film coats homogeneously the Pt layer underneath it. A cross-section SEM image of the bilayer material (Fig. 5.1d) clearly shows the two layers deposited on a CP fiber, with an estimated thickness of 25 nm for each layer. In addition, the elemental distribution in the  $\text{Mn}_2\text{O}_3/\text{Pt}/\text{CP}$  sample obtained through EDS mapping (Fig. 5.2) reveals the presence of C, Mn and Pt elements due to the depth penetration of the X-Ray and further show that both Mn and Pt are found evenly distributed.

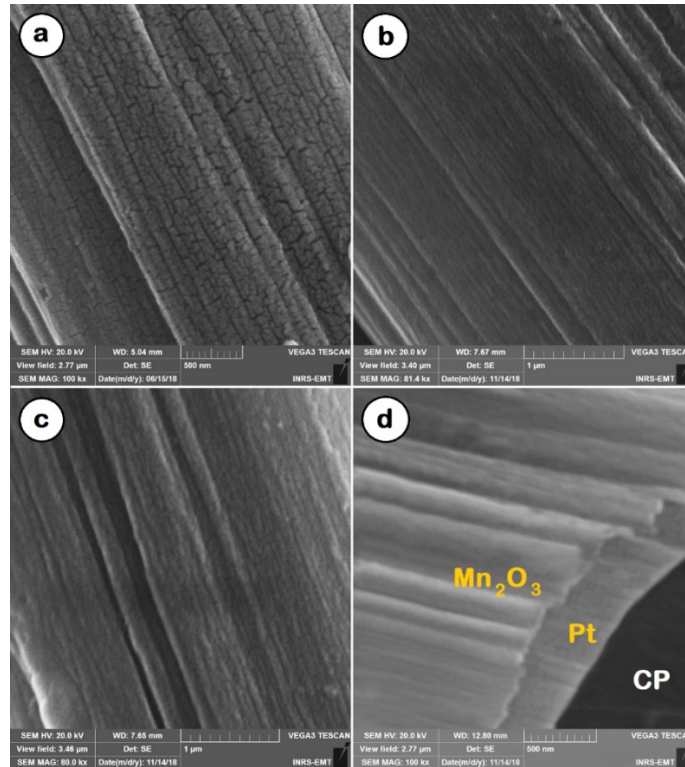
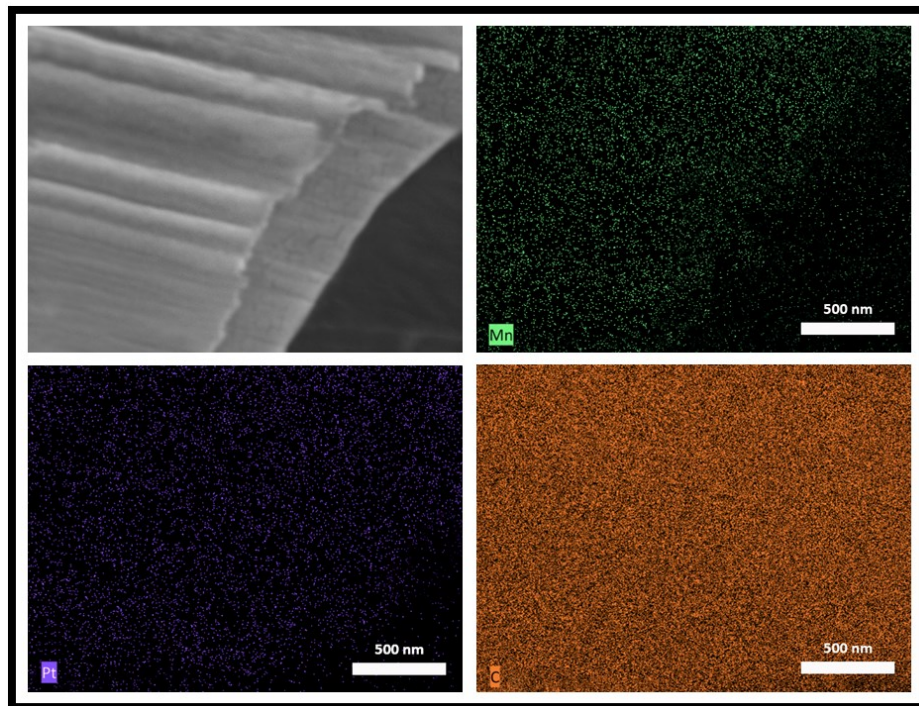


Figure 5.1 SEM images of a) Pt/CP, b)  $\text{Mn}_2\text{O}_3/\text{CP}$ , c)  $\text{Mn}_2\text{O}_3/\text{Pt}/\text{CP}$  and d) Cross-section of  $\text{Mn}_2\text{O}_3/\text{Pt}/\text{CP}$ .



**Figure 5.2** EDS elemental mapping of  $\text{Mn}_2\text{O}_3/\text{Pt}/\text{CP}$ .

The XRD patterns of the Pt/CP,  $\text{Mn}_2\text{O}_3/\text{CP}$  and  $\text{Mn}_2\text{O}_3/\text{Pt}/\text{CP}$  deposits are presented in Fig. 5.3. The profile of the Pt sample exhibits a typical face-centered cubic structure. The crystallographic planes (111), (200), (220) and (311) are observed at  $39.76^\circ$ ,  $46.16^\circ$ ,  $67.32^\circ$  and  $81.12^\circ$ , respectively. The average crystallite size was calculated through the Scherrer's equation. The resulting value was 19 nm, and the lattice parameter estimated from the Pt (111) peak was 3.92 Å, which is consistent with the Pt (JCPDS 04-0208) standard. Signals from the carbon support (marked with (\*)) were also detected. On the other hand, in the diffractogram of the  $\text{Mn}_2\text{O}_3$  sample, only the peaks from the C support were observed, which suggests that the PLD-synthesized  $\text{Mn}_2\text{O}_3$  is most likely amorphous. As to the binary  $\text{Mn}_2\text{O}_3/\text{Pt}$  material, the crystallographic planes (111), (200), (220) and (311) from Pt were observed but with considerably less intensity than in the Pt sample, due probably to the  $\text{Mn}_2\text{O}_3$  layer on the Pt. All the peaks are located in the same positions previously described for Pt/CP, suggesting that there is no interaction between the Pt and the  $\text{Mn}_2\text{O}_3$  layers.

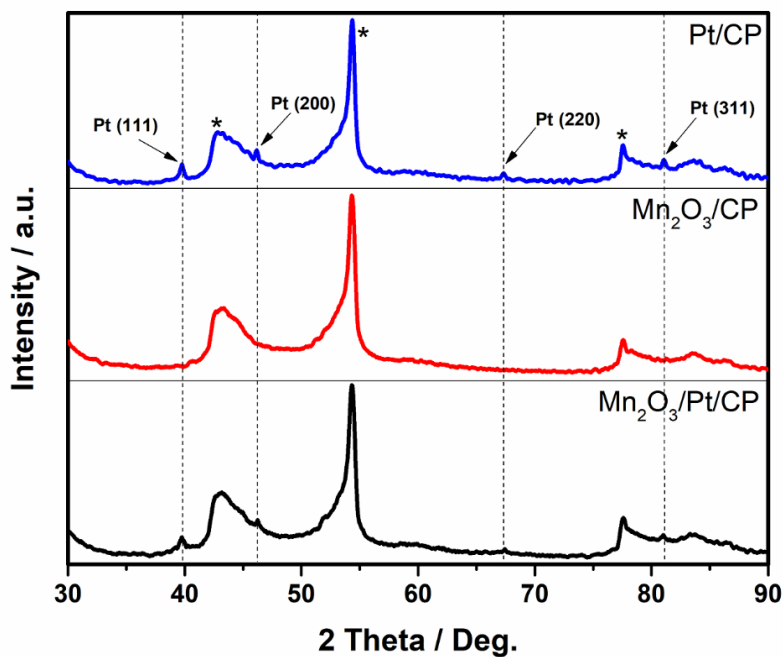


Figure 5.3 XRD patterns of Pt/CP, Mn<sub>2</sub>O<sub>3</sub>/CP and Mn<sub>2</sub>O<sub>3</sub>/Pt/CP.

The XPS survey scan spectra, reported in Fig. 5.4, revealed that [Pt, C, O] and [Mn, C, O] are the only elements existing in the surface of the Pt/CP and Mn<sub>2</sub>O<sub>3</sub>/CP materials, respectively. However, in the survey scan of the binary Mn<sub>2</sub>O<sub>3</sub>/Pt/CP sample, only Mn, C and O elements were readily identified, while the signals from Pt were barely observed, indicating that the Pt film is homogeneously coated by the Mn<sub>2</sub>O<sub>3</sub> layer.

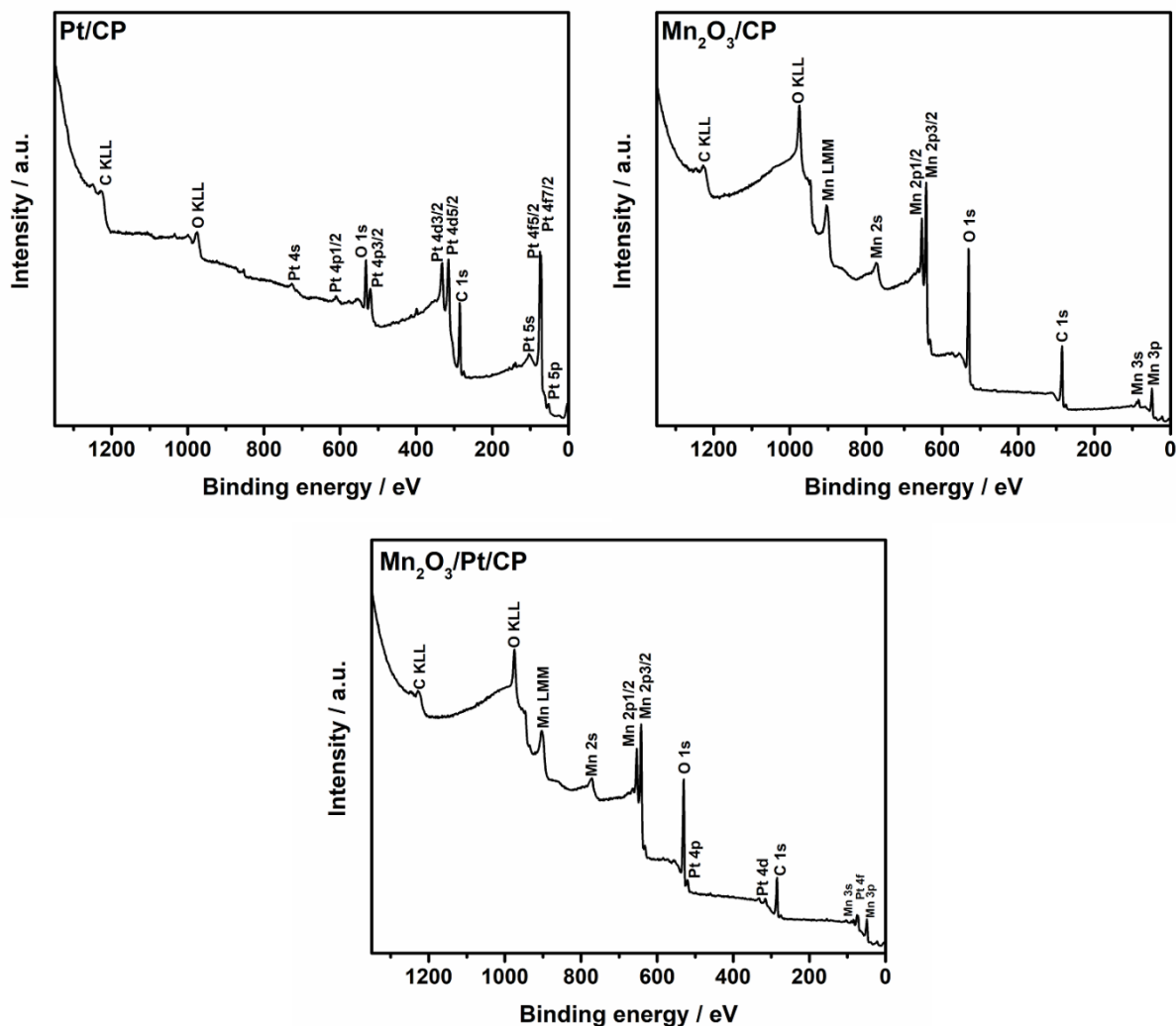


Figure 5.4 XPS survey scans of Pt/CP, Mn<sub>2</sub>O<sub>3</sub>/CP and Mn<sub>2</sub>O<sub>3</sub>/Pt/CP.

The high-resolution Pt 4f core level XPS spectrum from Pt/CP is displayed in Fig. 5.5a. The spectrum exhibits a doublet that consists of a low energy band (Pt 4f<sub>7/2</sub>) and a high energy band (Pt 4f<sub>5/2</sub>) located at 70.92 and 74.25, respectively. Satisfactory fitting was obtained using a single component with an asymmetric profile. The position of the Pt 4f<sub>7/2</sub> and Pt 4f<sub>5/2</sub> peaks and the binding energy (BE) difference of 3.33 eV between them are consistent with platinum in metallic state [164]. In Fig. 5.5b, the high-resolution Mn 3s core level XPS spectrum obtained from the Mn<sub>2</sub>O<sub>3</sub>/CP sample is shown, since it has been reported that the analysis of the multiplet splitting of the Mn 3s peak is a useful and reliable method to determine the oxidation state of Mn [172, 173]. The multiplet split of the Mn 3s peak consists of a lower binding energy peak and a higher binding energy peak, located at 83.40 and 88.90 eV, respectively. The 5.50 eV BE difference between

the 2 peaks is consistent with Mn(III) in  $\text{Mn}_2\text{O}_3$  [173,174]. This finding was further corroborated with the analysis of the Mn 2p core level XPS spectrum, shown in Fig. 5.6. The spectrum exhibits a spin orbit splitting, corresponding to the Mn 2p<sub>3/2</sub> and Mn 2p<sub>1/2</sub> peaks. Satisfactory fitting of the Mn 2p<sub>3/2</sub> peak was obtained using 5 components and the fitting parameters are consistent with  $\text{Mn}_2\text{O}_3$  compound [175]. Similar results were obtained for the binary  $\text{Mn}_2\text{O}_3/\text{Pt}/\text{CP}$  material. The analysis of the Mn 3s peak, displayed in Fig. 5.5c, revealed that Mn is found as  $\text{Mn}_2\text{O}_3$ , as the BE difference of the multiplet split is 5.5 eV. After multiple high-resolution scans of the Pt 4f region, the doublet was clearly enough recorded to be studied (Fig. 5.5d). The Pt 4f<sub>7/2</sub> and Pt 4f<sub>5/2</sub> peaks were located at 70.95 and 74.28 eV respectively, and the fitting was obtained with a single asymmetric component. The 3.33 eV BE difference between the peaks indicates that Pt is found in metallic state. This study confirmed that the Pt and  $\text{Mn}_2\text{O}_3$  films do not interact each other, as the valence state of both Pt and Mn remains unaltered in the bilayer material.

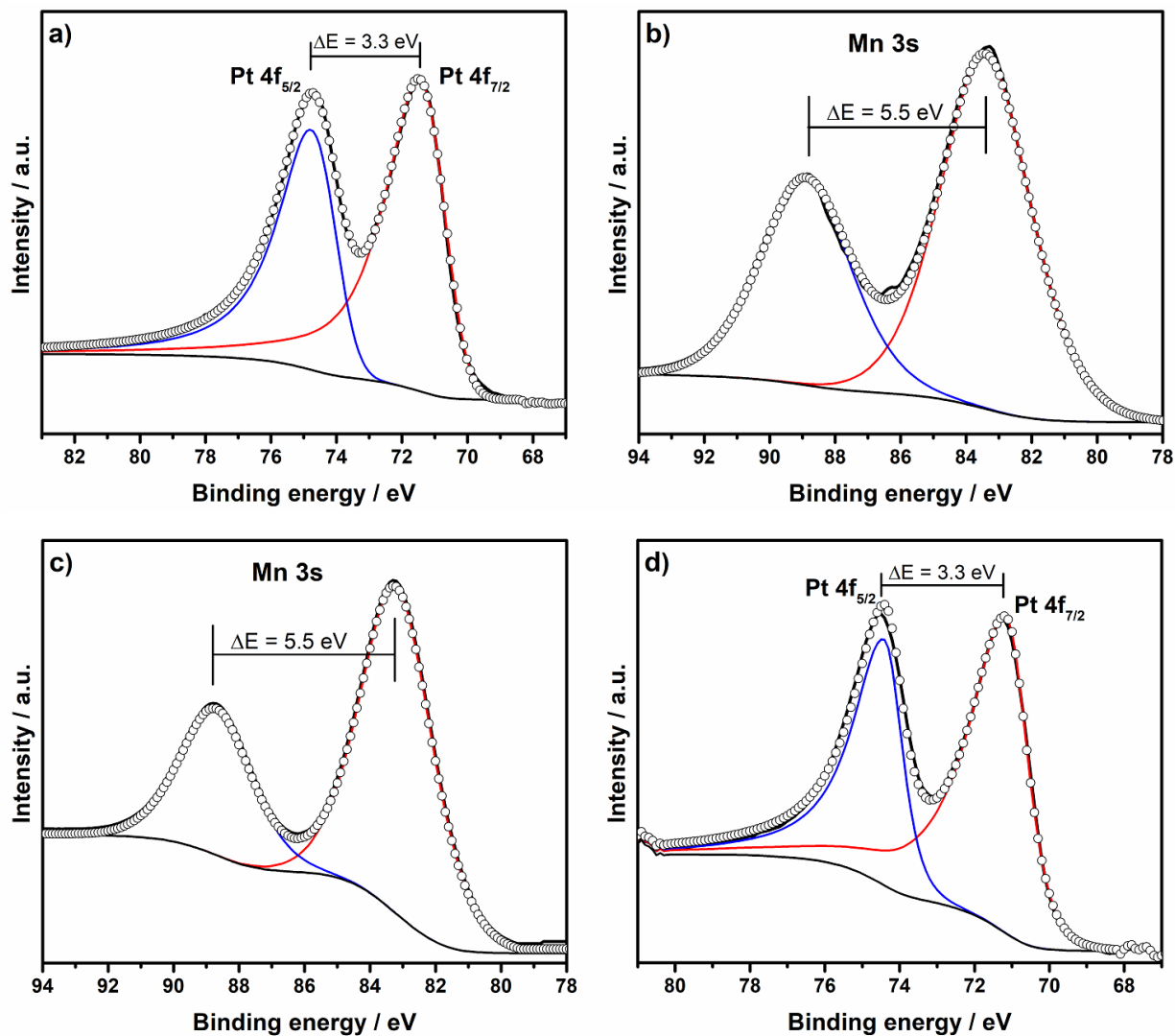


Figure 5.5 High-resolution XPS core-level spectra of a) Pt 4f in Pt/CP, b) Mn 3s in Mn<sub>2</sub>O<sub>3</sub>/CP, c) Mn 3s in Mn<sub>2</sub>O<sub>3</sub>/Pt/CP and d) Pt 4f in Mn<sub>2</sub>O<sub>3</sub>/Pt/CP.

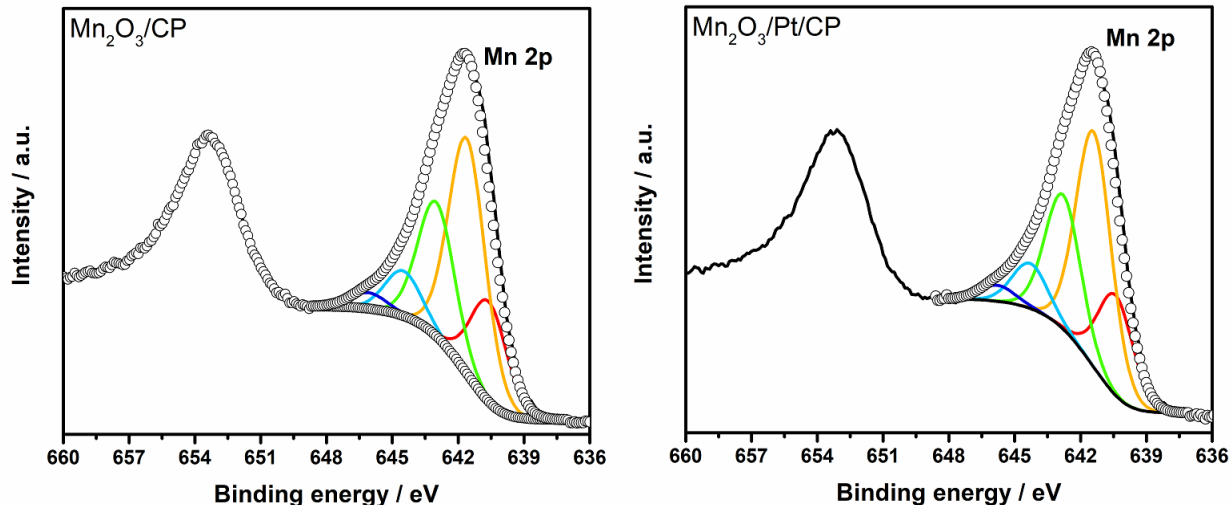


Figure 5.6 High-resolution XPS core-level spectra of Mn 2p in Mn<sub>2</sub>O<sub>3</sub>/CP(left) and Mn 2p in Mn<sub>2</sub>O<sub>3</sub>/Pt/CP (right).

## 5.2 Electrochemical characterization

Figures 5.7a, b and c show the electrochemical profiles of the Pt/CP, Mn<sub>2</sub>O<sub>3</sub>/CP and Mn<sub>2</sub>O<sub>3</sub>/Pt/CP catalysts, respectively, recorded at 20 mV s<sup>-1</sup> scan rate in an oxygen-free 0.5 M KOH solution. The cyclic voltammogram obtained from Pt/CP (Fig. 5.7a) exhibits well defined features of a typical Pt electrode, i.e. the hydrogen adsorption/desorption region at potentials below 0.4 V, the Pt oxide formation/reduction above 0.7 V, and the double layer (DL) zone located in between [176]. Fig. 5.7b displays the electrochemical profile of Mn<sub>2</sub>O<sub>3</sub>/CP, which, under these conditions is characterized by the appearance of several voltammetric peaks that are associated to different redox processes occurring during the electrochemical formation of various manganese oxides [177,178]. In this CV, different regions have been identified according to similar reports in the literature [177-180]. In the cathodic direction scan, manganese dioxide is reduced to manganese oxyhydroxide (MnOOH) between 1.5 and 0.76 V. Then, the peaks located between 0.76 and 0.57 V are associated to the formation of Mn<sub>2</sub>O<sub>3</sub> and Mn<sub>3</sub>O<sub>4</sub>, and the region located at potentials below 0.57 V corresponds to the domain of Mn(OH)<sub>2</sub>. Afterwards, in the anodic direction scan, the zone between 0.56 and 0.8 V is associated to the formation of Mn<sub>2</sub>O<sub>3</sub>. The peak located at 0.88 V is generated by the oxidation of Mn<sub>2</sub>O<sub>3</sub> to form MnOOH, and the region above 0.98 V corresponds to the formation of MnO<sub>2</sub> [177-180]. The same features are observed in the electrochemical profile of the Mn<sub>2</sub>O<sub>3</sub>/Pt/CP catalyst (Fig. 5.7c) but with overall higher current density for all the redox processes. Note that the features of Pt are masked by those of the Mn<sub>2</sub>O<sub>3</sub>. The PtOx reduction peak appears at a potential very close to the formation of Mn<sub>2</sub>O<sub>3</sub> and Mn<sub>3</sub>O<sub>4</sub>, therefore the wider

features in the region between 0.8 and 0.7 V. The hydrogen region is slightly observed as well in the voltammogram of the bilayer electrode between 0.2 and 0.4 V in both cathodic and anodic scans. These results indicate that the Pt layer is coated by the  $\text{Mn}_2\text{O}_3$  layer, which is in agreement with XRD and XPS analyses.

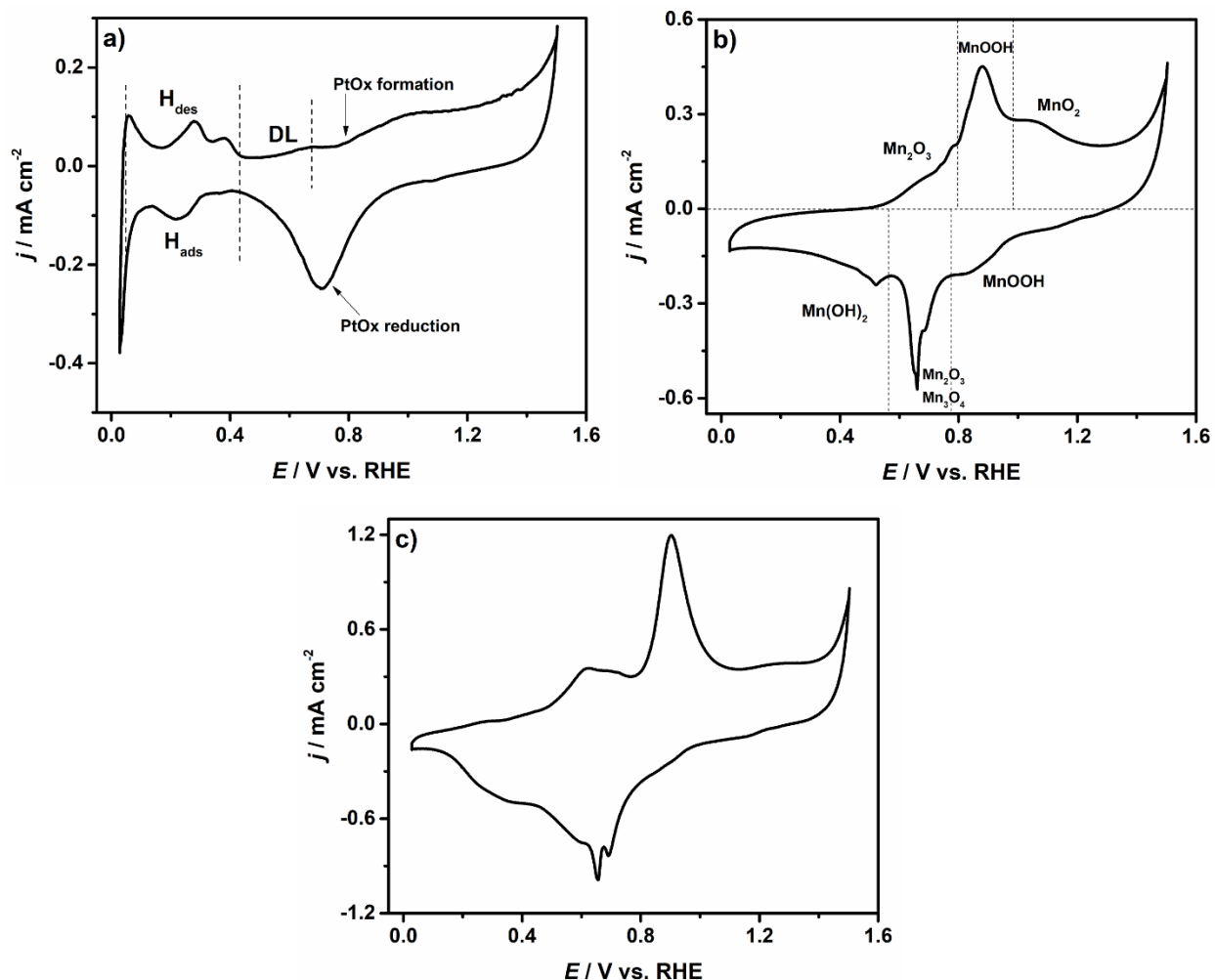


Figure 5.7 Electrochemical profiles of a) Pt/CP, b)  $\text{Mn}_2\text{O}_3/\text{CP}$  and c)  $\text{Mn}_2\text{O}_3/\text{Pt/CP}$ , obtained in 0.5 KOH oxygen-free solution at  $20 \text{ mV s}^{-1}$  scan rate.

### 5.3 ORR performance

The catalytic behavior of the synthesized materials in an oxygen-saturated environment was studied through rotating ring disk electrode (RRDE). Figure 5.8a displays the typical RRDE voltammograms obtained at 400 rpm in  $\text{O}_2$ -saturated 0.5 M KOH solution at a scan rate of  $10 \text{ mV s}^{-1}$ . It can be seen that the current density at 0.9 V for  $\text{Mn}_2\text{O}_3$  is  $-0.17 \text{ mA cm}^{-2}$ , while for  $\text{Mn}_2\text{O}_3/\text{Pt/CP}$  it is  $-1.11 \text{ mA cm}^{-2}$ . The latter is markedly similar to the current density for Pt/CP,

which is  $-1.15 \text{ cm}^{-2}$ . The amount of hydrogen peroxide produced at the Pt/CP and the  $\text{Mn}_2\text{O}_3/\text{Pt}/\text{CP}$  catalysts is below 4% at any point, in contrast to  $\text{Mn}_2\text{O}_3/\text{CP}$ , where it increases from 22 to 28% as the potential is swept to the cathodic direction, as shown in Figure 5.8b. These observations indicate that the ORR on Pt and the bilayer cathodes proceeds almost entirely through the four electron pathway. This was confirmed by means of the calculation of  $n$  for the three catalysts. As depicted in Figure 5.8c, the average  $n$  value in the potential range from 0.9 to 0.45 V is 3.94 and 3.91 for Pt/CP and  $\text{Mn}_2\text{O}_3/\text{Pt}/\text{CP}$ , respectively. There is a slight decrease of  $n$  at less positive potentials, due to  $\text{O}_2$  reduction on carbon, which occurs at higher overpotentials. These results reveal that the  $\text{Mn}_2\text{O}_3$  coating does not affect the catalytic activity of the beneath Pt layer, as the number of electrons transferred is practically the same than the obtained for the Pt catalyst ( $3.9 e^-$ ), which is close to the theoretical value of 4 electrons. The aforementioned suggests that the ORR on the bilayer catalyst is actually carried out on the inner Pt layer, whereas the external  $\text{Mn}_2\text{O}_3$  layer does not participate or has a negligible effect on the ORR performance of Pt under these conditions. A possible explanation is that oxygen molecules are able to diffuse through the porous  $\text{Mn}_2\text{O}_3$  layer and reacting at the Pt, a phenomenon previously studied in a porous Ru shell with a Pt core [80]. Additionally, this results is consistent with the observations from the Ag/Pt/CP material presented in section 4.3. Though the two components of the cathode are active to the ORR, it is clear that the overpotential required for the reaction to proceed on Pt is less than on  $\text{Mn}_2\text{O}_3$ . Fig. 5.8d shows the Tafel plots of the three catalysts. It is observed that the Tafel slope in the low overpotential region for  $\text{Mn}_2\text{O}_3/\text{Pt}/\text{CP}$  is fairly similar than that of Pt/CP (70 and 69  $\text{mV dec}^{-1}$ , respectively), while for  $\text{Mn}_2\text{O}_3/\text{CP}$ , the slope is 122  $\text{mV dec}^{-1}$ , significantly different from that of Pt/CP.

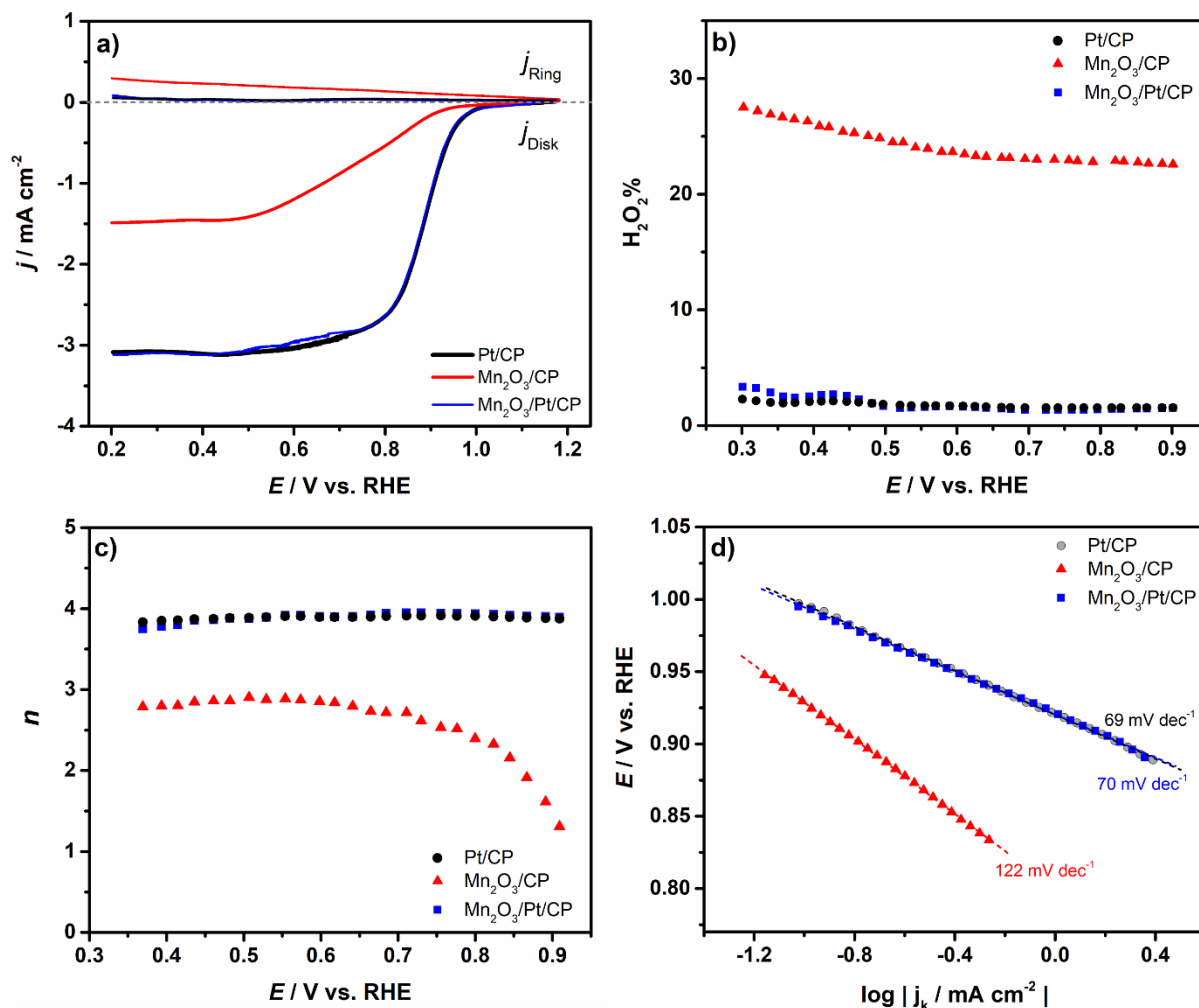


Figure 5.8 RRDE voltammograms of Pt/CP, Mn<sub>2</sub>O<sub>3</sub>/CP and Mn<sub>2</sub>O<sub>3</sub>/Pt/CP acquired in O<sub>2</sub> saturated 0.5 M KOH solution at 400 rpm, b) H<sub>2</sub>O<sub>2</sub> yield, c) electron transfer number ( $n$ ) and d) Tafel plots.

#### 5.4 Selectivity of the Mn<sub>2</sub>O<sub>3</sub>/Pt/CP cathode towards the ORR and methanol tolerance

Similarly to section 4.4, first, the catalytic activity of Pt/CP, Mn<sub>2</sub>O<sub>3</sub>/CP and Mn<sub>2</sub>O<sub>3</sub>/Pt/CP electrodes towards the MOR was studied. Fig. 5.9a shows the CVs recorded in oxygen-free 1 M MeOH + 0.5 M KOH solution. In the case of Pt, the typical peak of the methanol oxidation [181], starting at 0.44 V is observed, confirming the activity of Pt/CP towards the MOR. However, for the Mn<sub>2</sub>O<sub>3</sub>/CP and Mn<sub>2</sub>O<sub>3</sub>/Pt/CP electrodes (see inset), the obtained CV profiles are practically the same than those acquired in a methanol-free solution (see Fig. 5.7b and 5.7c). This outcome demonstrates that Mn<sub>2</sub>O<sub>3</sub> is not active towards the MOR, and further indicates that after coating Pt with the Mn<sub>2</sub>O<sub>3</sub> layer, the methanol adsorption on Pt is blocked.

Next, the electroactivity of the three catalysts towards the ORR in absence and presence of MeOH was studied by LSV at  $5 \text{ mV s}^{-1}$ . The linear voltammograms shown in Fig. 5.9b were obtained in oxygen-saturated 0.5 M KOH solution, and they display well defined mass transfer and kinetic regions for the three materials. From the curves, it is observed that the onset potential of the ORR on Pt/CP is located at  $\approx 0.97 \text{ V}$ . On the other hand, a less positive ORR onset potential ( $\approx 0.89 \text{ V}$ ) as well as lower peak current density was observed for the  $\text{Mn}_2\text{O}_3/\text{CP}$  electrode due to higher overpotential, in comparison with Pt/CP. The catalytic performance of  $\text{Mn}_2\text{O}_3/\text{CP}$  is consistent with other reports in the literature [182,183]. In agreement with Fig. 5.8, the  $\text{Mn}_2\text{O}_3/\text{Pt}/\text{CP}$  bilayer catalyst exhibits very similar activity than Pt/CP, as the curves practically overlap. It is observed that the onset potential of the ORR is identical in both systems and, in addition, the reaction rate is apparently the same. In order to contrast these results with the ORR activity in presence of MeOH, Fig. 5.9c shows the linear voltammograms obtained in an oxygen-saturated 0.5 M KOH solution containing 1 M MeOH. From the curves it is evident that the ORR on Pt/CP is completely inhibited due to the occurrence of MOR in a competitive event, which is the expected behavior of a Pt electrode. On the other hand, the  $\text{Mn}_2\text{O}_3/\text{CP}$  and  $\text{Mn}_2\text{O}_3/\text{Pt}/\text{CP}$  catalysts clearly perform the ORR, and the features of the curves indicate similar activity than the systems without methanol, i.e. practically the same ORR onset potential and current density than the shown in Fig. 5.9b.

A hypothesis that explains these observations could be proposed with basis on the molecular volume of oxygen and methanol molecules. The volume of  $\text{O}_2$  is  $26.8 \text{ \AA}^3$  while for MeOH is  $41.6 \text{ \AA}^3$ . Thus, the oxygen molecules would more easily diffuse through the porous  $\text{Mn}_2\text{O}_3$  layer and react at the Pt surface, since as displayed, the ORR is more favorable on Pt than on  $\text{Mn}_2\text{O}_3$ . On the other hand, methanol molecules having a larger molecular size, are impeded on the superficial  $\text{Mn}_2\text{O}_3$  layer, being this the reason why the methanol oxidation is not carried out at the bilayer catalyst. Therefore, the inhibition of the MOR on  $\text{Mn}_2\text{O}_3/\text{Pt}/\text{CP}$  is attributed to  $\text{Mn}_2\text{O}_3$  and as a consequence, the process between the MOR and ORR becomes a non-competitive event.

Remarkably, even at methanol concentration as high as 5 M, the  $\text{Mn}_2\text{O}_3/\text{Pt}/\text{CP}$  cathode remained tolerant to methanol oxidation, as the negative shift on the ORR onset potential was only of 19 mV, while the current density decreased by only 15% in comparison with 0 M MeOH, as shown in Fig. 5.9d.

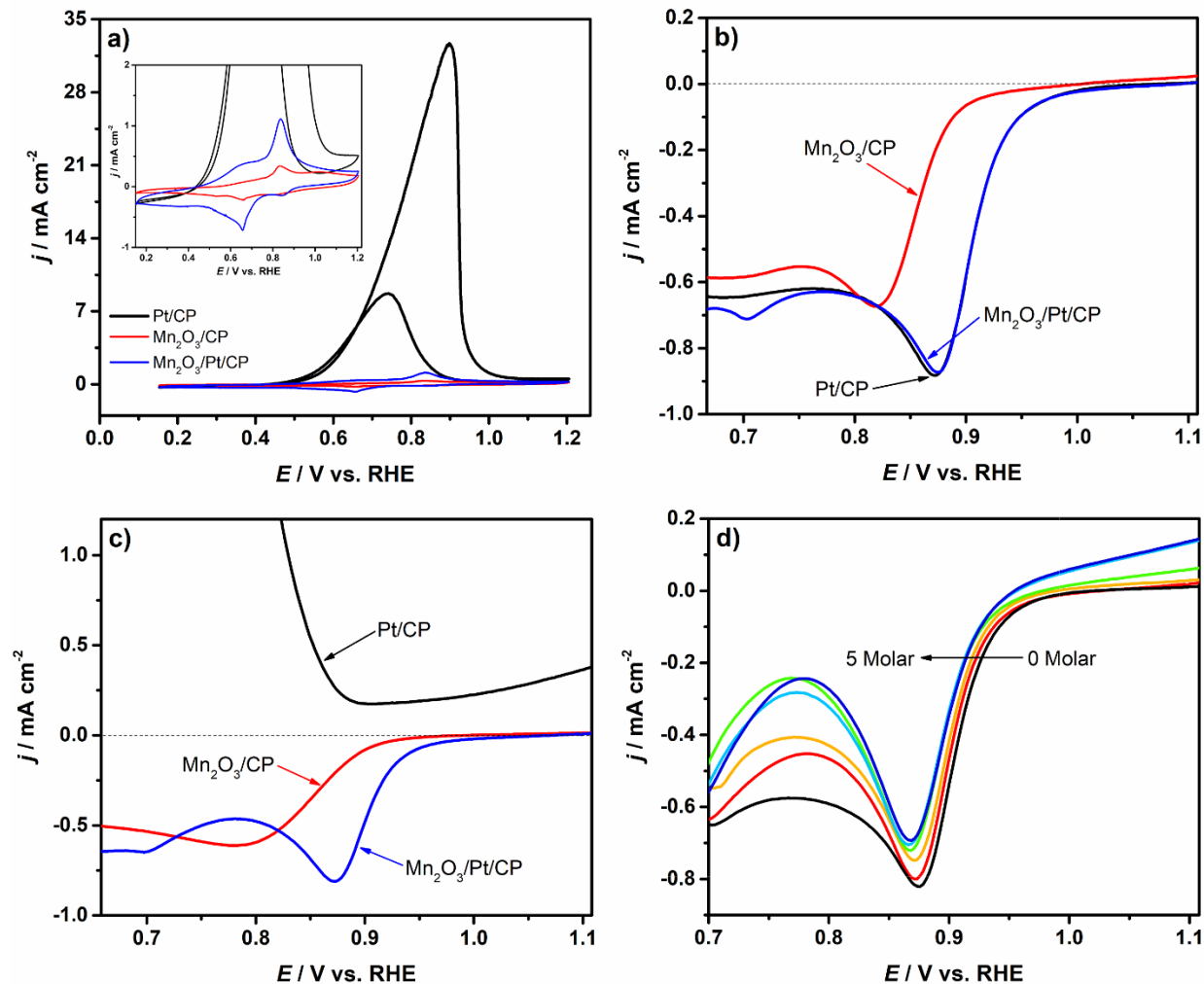
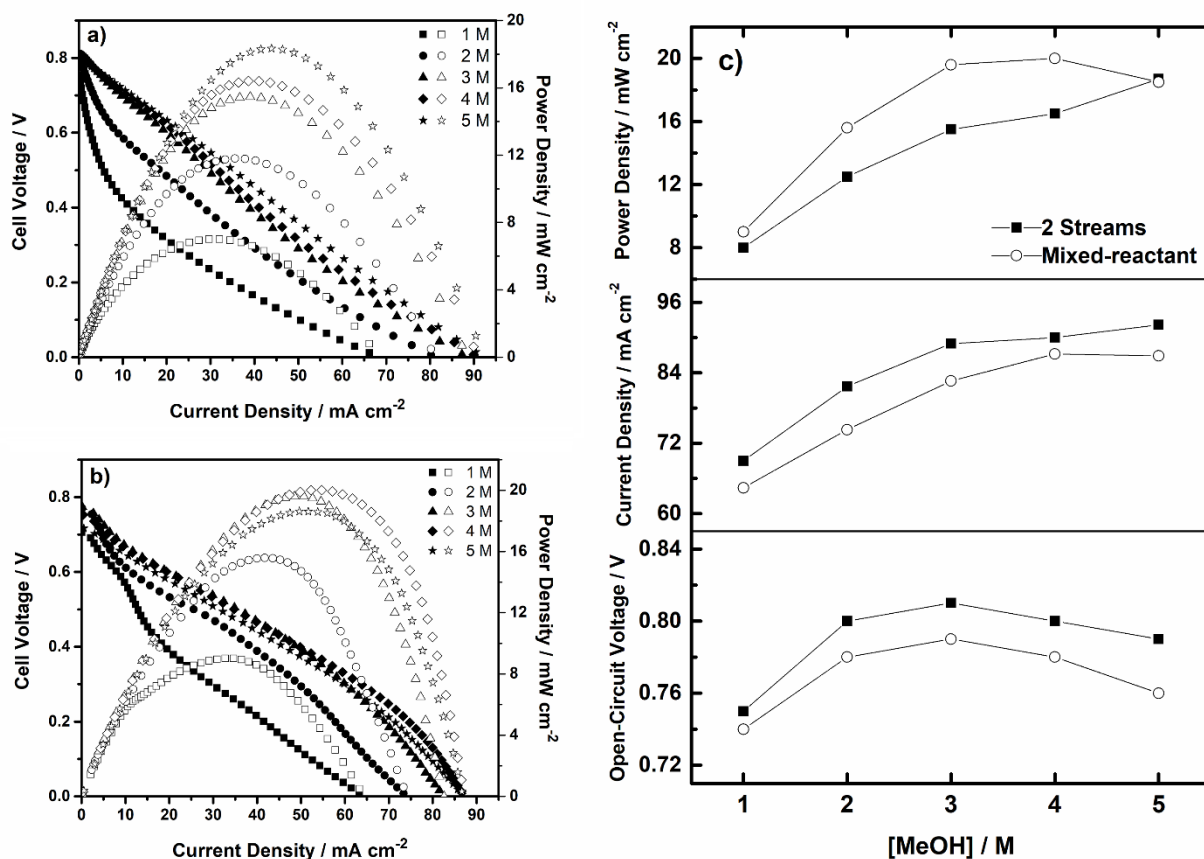


Figure 5.9 Electroactivity towards a) MOR in oxygen-free 1 M MeOH in 0.5 M KOH solution, b) ORR in oxygen-saturated 0.5 M KOH solution, c) ORR in oxygen-saturated 0.5 M KOH + 1 M MeOH, and d) ORR at  $\text{Mn}_2\text{O}_3/\text{Pt/CP}$  cathode in oxygen-saturated 0.5 M KOH containing 0–5 M MeOH.

## 5.5 Fuel cell performance

Figures 5.10a and 5.10b display the performance of the ML- $\mu$ DMFC obtained with under typical 2-stream operation and under mixed-reactant conditions, respectively. In both cases, the cathode was  $\text{Mn}_2\text{O}_3/\text{Pt/CP}$  and the anode was PtRu/C. For clarity, the performance parameters (OCV, maximum current density and peak power density) obtained with each concentration of methanol are presented in Fig. 5.10c. It is observed that in all cases, the fuel cells operating with 2 streams (separated reactants) exhibited slightly higher OCV, 20 mV in average for each concentration, with respect to the mixed-reactant operation. Similarly, the maximum current density reached by the fuel cell with separated reactants is slightly higher ( $\sim 6 \text{ mA cm}^{-2}$ ) at all methanol concentrations

with respect to the mixed-reactant operation. Interestingly, the peak power density obtained with the fuel cell under mixed-reactant conditions was higher than that generated by the fuel cell with 2 streams. This was observed for methanol concentrations in the range of 1 to 4 M, while with 5 M, the peak power density value is quite similar in both cases. From the fuel cell polarization curve, it is possible to deduce that this behavior is clearly due to the ohmic region of the curve. In all cases, it is observed that the mixed-reactant fuel cell exhibits lower ohmic losses than the fuel cell operating with 2-streams. The difference is possibly due to the lack of anolyte–catholyte interface in the mixed-reactant fuel cell, which contributes to overall lower electrolyte resistance, resulting in a better performing fuel cell. Therefore, the MR- $\mu$ DMFC concept is a viable alternative to the typical microfluidic fuel cell. The stability of the fuel cell under mixed-reactant conditions was evaluated through chronoamperometry at 0.35 V during 2 h using 4 MeOH solution in 0.5 M KOH. The  $i-t$  curve is shown in Fig. 5.11, where a stable behavior is observed. In average, the fuel cell produced 15 mA cm<sup>-2</sup>, demonstrating short-term stability under mixed-reactant conditions.



**Figure 5.10** Polarization curves (full symbols) and power density curves (open symbols) obtained during the operation of the passive ML- $\mu$ DMFC in a) typical 2-stream configuration and b) under mixed-reactant operation using different concentrations of MeOH, c) OCV, current density and power density values extracted from Fig. 5.10 a and b.

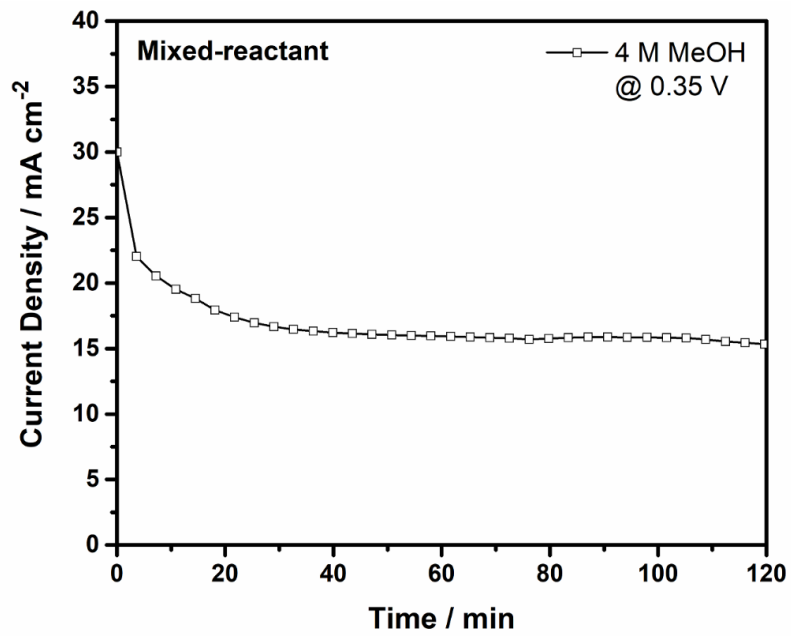


Figure 5.11 Chronoamperometric curve obtained at 0.35 V for the study of the stability of the ML- $\mu$ DMFC using 4 M MeOH.

## CHAPTER 6 RESULTS: DEVELOPMENT OF A MIXED-REACTANT MICROFLUIDIC FUEL CELL STACK

---

### 6.1 Validation of the model

In order to determine the optimum fuel concentration input value for the simulation, experimental polarization curves were obtained with the cell G1 using 1 to 5 M MeOH under mixed-reactant conditions and passive operation. (Fig. 5.10b). The curves show that the highest OCV was obtained with 3 M MeOH (0.77 V), however, the best performance was obtained with 4 M MeOH. Although the OCV was slightly lower at 0.75 V with 4 M, the cell delivered the highest current and power density output (87 mA cm<sup>-2</sup> and 19.5 mW cm<sup>-2</sup>, respectively).

For the numerical simulation, a steady-flow condition with an inlet velocity approaching zero was established instead of using a transient behavior. The latter would emulate the passive operation of the real fuel cell, however, the aforementioned concession was made in order to facilitate the resolution of the model. The flowrate value used in simulation, 0.083 μL min<sup>-1</sup>, is the minimum flow rate supplied experimentally by the pump (Cole-Parmer Dual-Syringe Infusion Pump). In order to ascertain the validity of the model prior to its construction under this particular condition, experiments were made using the cell G1 under passive operation and at 0.083 μL min<sup>-1</sup> flowrate. Fig. 6.1 shows the comparison of polarization curves obtained at zero flow and at 0.083 μL min<sup>-1</sup> flowrate. There is no noticeable difference between the two polarization curves, as they both have the same OCV, current and power density output, indicating that the effect of the flowrate is negligible at this value. Therefore, the use of this particular condition for the development of the model is substantiated.

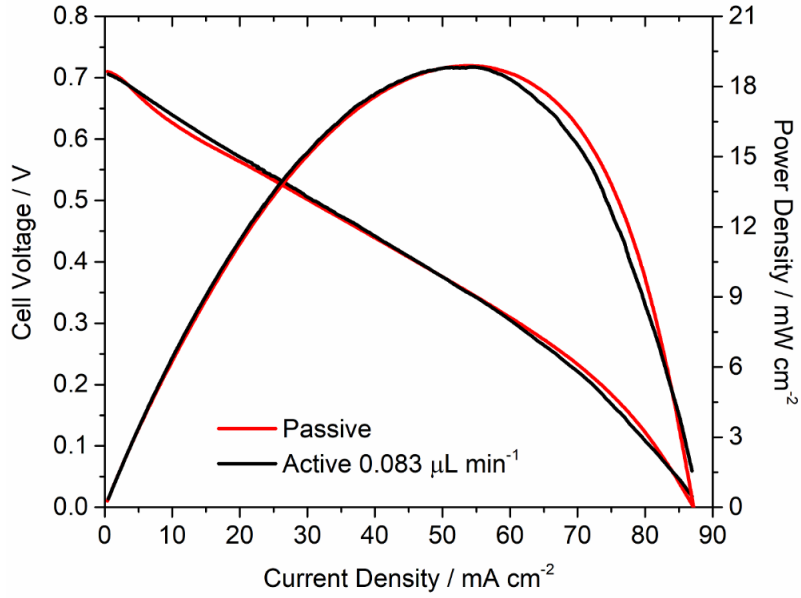


**Figure 6.1 Comparison of polarization curves obtained at  $0.083 \mu\text{L min}^{-1}$  flowrate and at passive operation.**

After obtaining the mathematical model, the data was validated by comparing a simulated polarization curve with an experimental one. Fig. 6.2 displays the polarization and power curves obtained with the cell G1 and from the numerical simulation, in both cases using 4 M MeOH. It is clear that the model is in agreement with the experiment, since the performance observed in both cases is practically the same. The difference in peak power density between the two curves is only  $0.57 \text{ mW cm}^{-2}$ . This indicates that the model is accurate and it can be used to investigate new fuel cell systems with similar characteristics, such as electrode dimensions and catalysts load. Therefore the model was applied for developing the evolution of cell G1, systematically denominated cell G2.

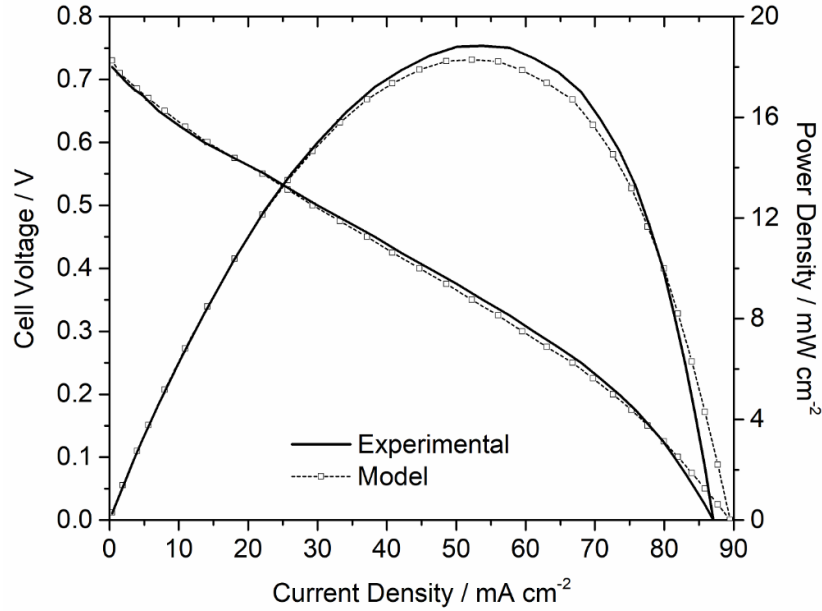


**Figure 6.2** Comparison of experimental and simulated polarization curves for validation of the model obtained with cell G1 using 4 M MeOH.

## 6.2 Development of Cell G2

Two different electrodes-microchannel configurations were studied in this work (Shown in Fig. 3.7 and again in Fig. 6.3), where the main difference between them is noticeably the position of the electrodes. In the first configuration (Fig. 6.3a), the electrodes are in the same plane, comparable to a strip-cell geometry [61] in a similar fashion than cell G1 and other works in the literature [149,184,185]. On the other hand, the second configuration introduces a new architecture with a separator that allows to place the cathode in a parallel plane below the anode plane (Fig. 6.3b), thus modifying the microchannel layout.

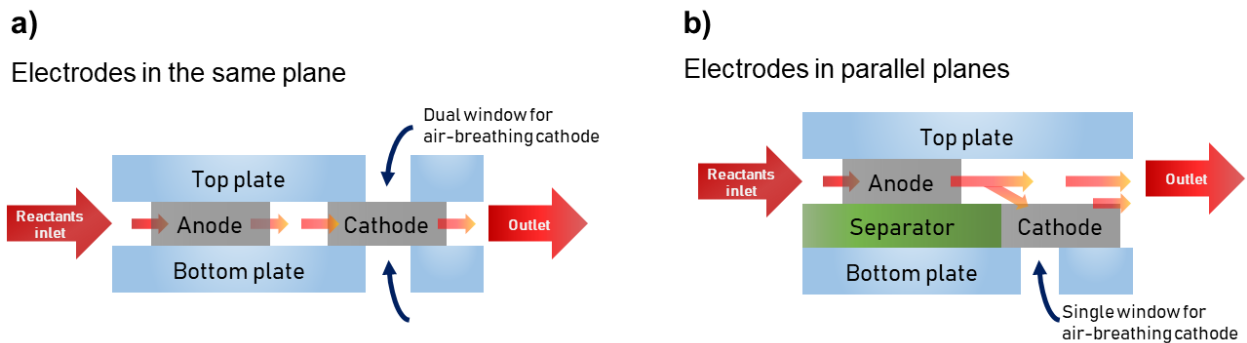


**Figure 6.3** Representation of the two different electrode arrangements studied with the mathematical model. The components are not to scale.

The two different electrode-microchannel arrangements were analysed through the newly obtained model. Simulated polarization and power curves for the two systems are shown in Fig. 6.4a. It is observed that the fuel cell design with electrodes in parallel planes exhibits a theoretical superior performance. According to the simulation, with this configuration it is possible to obtain 45% more current density and 20% higher power density, with respect to the configuration with electrodes in the same plane. It is important pointing out that the electrodes are identical and the anode-cathode distance in both cases is set constant to 3 mm. Moreover, the fuel utilization was calculated for the two designs at different values of cell voltage. The curve constructed with the resulting values (Fig. 6.4b), indicates that a considerably higher fuel utilization can be achieved with the fuel cell with electrodes in parallel planes, reaching up to 61%, in contrast with the cell with electrodes in the same plane, where the fuel utilization does not surpass 43%. It has been identified that under these conditions, oxygen is the limiting reactant in DMFCs [22,35,186], therefore a greater supply of oxygen results in more reacting fuel, and this is likely to be the cause of such performance improvement.

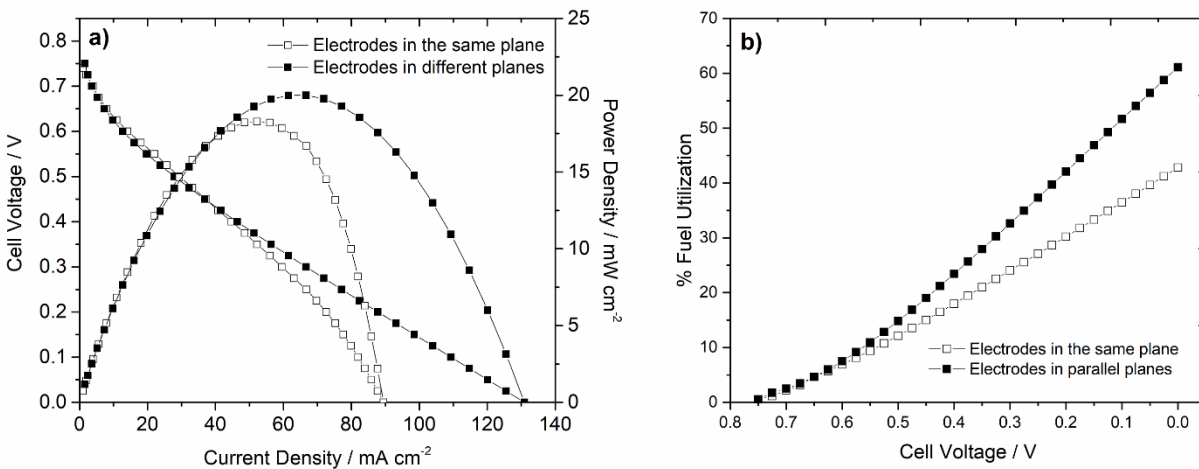


**Figure 6.4** Comparison of a) polarization and power density curves and b) fuel utilization, calculated for the 2 different electrode configurations. The distance between electrodes in both cases is 3 mm.

The explanation for the performance difference can be found through flow simulation. Fig. 6.5 shows the fuel and electrolyte stream inside the microchannel of the two fuel cell designs. The simulation revealed that, in the case of the cell with electrodes in the same plane (Fig. 6.5, top), a turbulent region is generated around the cathode, due to the porosity of the electrode in conjunction with the windows for air-breathing. It is observed that after wetting the cathode, the fluid tends to exit the microchannel through the windows creating a flood zone that hinders the air

flow from the atmosphere to the cathode. On the other hand, the design with electrodes in parallel planes (Fig. 6.5, bottom) does not present this problem. Since the stream is allowed to flow turbulence-free over the cathode, the single window for air-breathing at the bottom remains unobstructed and the air can freely flow and react at the cathode.

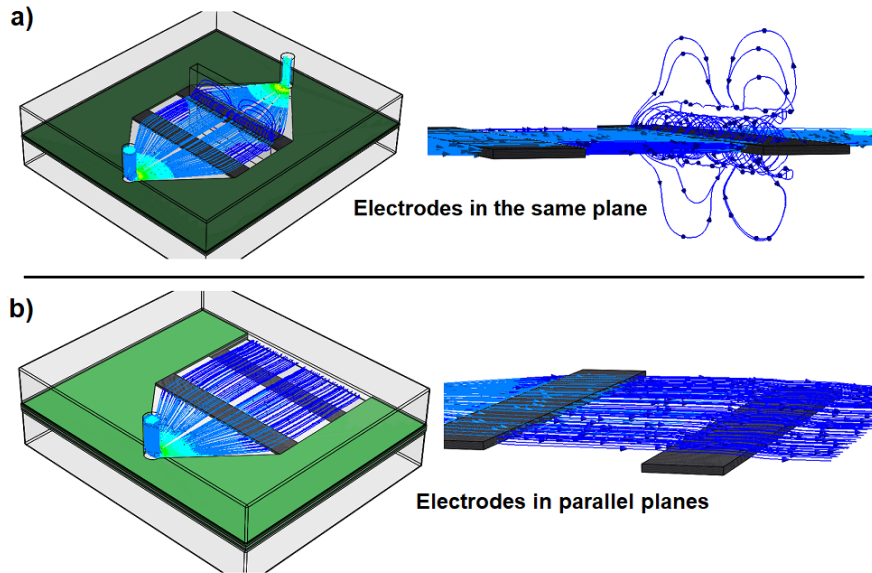


**Figure 6.5** Flow simulation study of the 2 different electrode configuration.

Based on these results, the proposal with electrodes in different planes is the obvious choice towards the development of a more efficient mixed-reactant microfluidic fuel cell. Through the recently created model, it is possible to optimize some parameters for improving the theoretical performance of this particular fuel cell design. A way of increasing the current and power density of a fuel cell, is by reducing the ohmic resistance for ionic transport caused by the electrolyte in the microchannel [22]. For this reason, the effect of the anode-cathode separation on the performance was analysed. Three distance values were considered (3 mm, 1.5 mm and 0.3 mm). The ohmic resistance for ionic transport on the electrolyte depends on the average charge-transfer distance between the electrodes ( $d_{ct}$ ), the cross-sectional area for charge transfer ( $A_{ct}$ ), and the ionic conductivity ( $\sigma$ ) [22].

$$R_{electrolyte} = \frac{d_{ct}}{A_{ct}\sigma} \quad (94)$$

In this case the cross-sectional area for charge transfer and the ionic conductivity are constant. The calculated resistance for each separation value is reported in Table 6.1.

**Table 6.1**      **Calculated resistance for different values of distance between electrodes.**

<b>d<sub>ct</sub> (cm)</b>	<b>Resistance (Ω)</b>
0.3	33.33
0.15	16.67
0.03	3.33

**(A<sub>ct</sub> = 0.015 cm<sup>2</sup>, σ = 0.6 S cm<sup>-1</sup>).**

Fig. 6.6a shows the CAD-created models used for the computational study of ohmic resistance caused by the electrolyte. In Fig. 6.6b are displayed the simulated polarization and power density curves, showing the difference of the energy delivery in function of the electrode separation. A consistent increasing performance is observed as the distance between the electrodes shortens. At 3 mm, the maximum current density is 130 mA cm<sup>-2</sup>. This increases to 142 mA cm<sup>-2</sup> at 1.5 mm and it rises up to 154 mA cm<sup>-2</sup> at 0.3 mm, which is experimentally the lower limit for electrode separation. Similarly, the peak power density increases from 20 mW cm<sup>-2</sup> to 24 mW cm<sup>-2</sup> for 3 mm and 0.3 mm, respectively. According to Equation (94), the electrolyte resistance decreased with shorter electrode separation, thus, if the cell resistance is decreased, fuel cell performance will improve. Additionally, the fuel utilization was calculated as a function of the applied cell voltage. Fig. 6.6c shows that the maximum fuel utilization is achieved on the fuel cell with the shortest distance between electrodes. According to the simulation, the highest possible fuel utilization for the initial arrangement is 61%, and it increases up to 71% at 0.3 mm electrode separation. For fuel cells operating at constant-flow-rate condition, the fuel consumption rate is dependent on the local current [22], thus, higher current draw, favored by lower resistance, increases the use of fuel. In order to better understand the fuel utilization in this fuel cell, it is necessary to study fuel profiles at the anode, since the passive operation reduces the convective transport in the microchannel [156,187,188]. Fig. 6.5d shows the fuel profiles at the anode calculated as function of the applied potential, obtained for a cell with distance between electrodes of 0.3 mm. As we can observe in the profiles, the fuel is not replenished by the stream, due to its very low flowrate (passive operation in a real fuel cell). Consequently, higher fuel consumption is promoted at the porous electrode, being more noticeable at the left of the anode where the concentration drop is more pronounced at lower potential values. The results reported in Fig. 6.6 were taken into account for the optimization of cell G2 and thus the electrode-separation in the final design is 0.3 mm. The resulting device is shown in Fig. 6.7a.

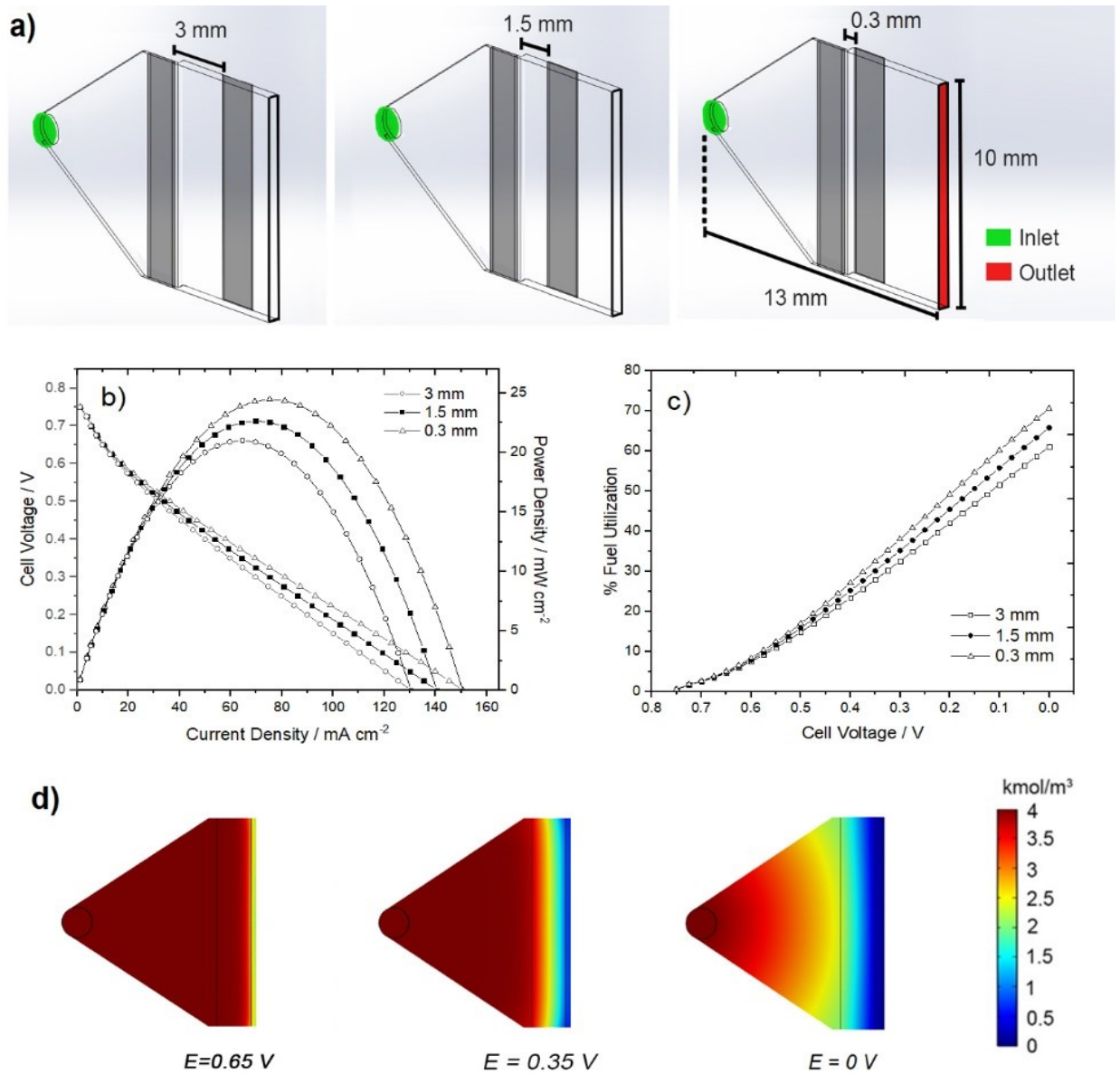


**Figure 6.6** a) CAD-created models used for the computational study, b) effect of electrode separation on fuel cell voltage profile c) fuel utilization for the three distances between electrodes, and d) fuel profiles at the anode under different potentials operation (0.3 mm electrode separation).

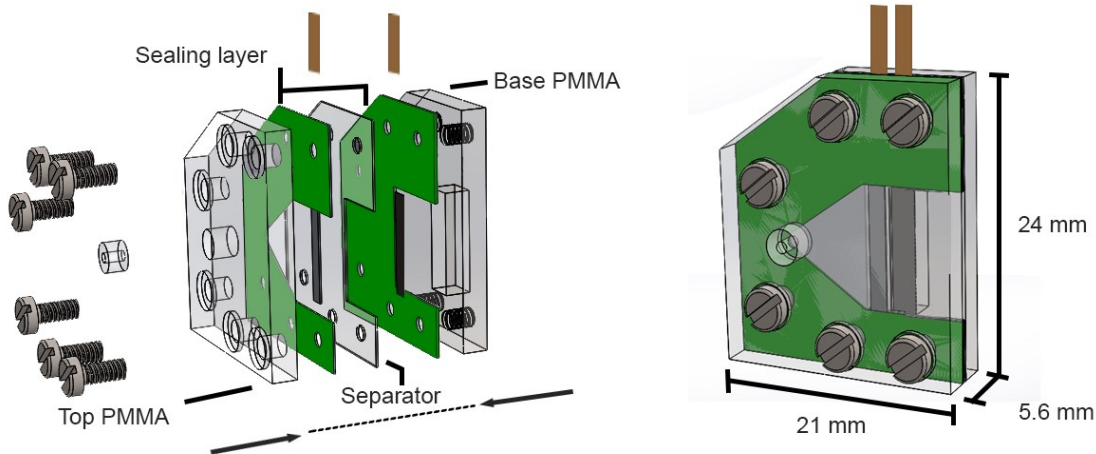


**Figure 6.7 Representation of components and assembly of cell G2 developed after numerical simulation.**

### 6.3 Performance of cell G2

Fig. 6.8a shows the experimental polarization curve obtained from the newly developed cell G2 and the performance comparison with cell G1, both employing 4 M MeOH in 0.5 M KOH under passive operation. In both cases, the cathode was  $\text{Mn}_2\text{O}_3/\text{Pt}/\text{CP}$  and the anode was  $\text{PtRu}/\text{C}$ . Despite the catalyst layer at the cathode is absolutely exposed to the fuel in the electrolyte, the cell G2 generates an OCV of 0.8 V, which is a value representative of DMFCs [100,189,190]. This indicates that the methanol crossover does not affect the performance of the electrodes and the MOR and the ORR occur only at the anode and at the cathode, respectively. This system reached a maximum current density of  $150 \text{ mA cm}^{-2}$ , and a peak power density of  $28 \text{ mW cm}^{-2}$ . The cell voltage profile exhibits an abrupt voltage drop at the beginning of the curve, due to the anode and cathode activation loss, typical of DMFCs [22,191]. Focusing on the ohmic region of the polarization curve, it is worth pointing out that the ohmic loss is substantially smaller in comparison with cell G1. Since the ionic resistance tends to dominate over the electronic resistance, the marked improvement results from reducing the distance between electrodes, thus decreasing the fuel cell overall resistance. In comparison with the theoretical polarization curve of cell G2 (Fig 6.8b), the experiment yielded a slightly higher performance, with a peak power density of  $28 \text{ mW cm}^{-2}$  vs.  $24 \text{ mW cm}^{-2}$  for the simulation. The OCV and maximum current density are practically the same in both cases, therefore the model can be considered to be accurate. The power density difference is clearly due to the ohmic contribution. Let us remember that the numerical simulation was created using some experimental parameters from cell G1, such as the total ohmic resistance. In order to obtain a more accurate mathematical model for cell G2, it would be

necessary to take into account the resistance of each component into a more complex simulation. However, this is a challenging operation and furthermore, the sum of resistances would not reflect the true total resistance of the fuel cell due to variations in contacts, assembly and operating conditions [22]. As to the mass transfer region, no significant losses were observed due to the use of a high MeOH concentration and to the constant replenishment of  $O_2$  from air at the cathode [149]. The fuel cell stability test is displayed in Fig. 6.8c. A chronoamperometric measurement was performed at 300 mV during 6 h. The average value of the current density obtained from the device was  $39 \text{ mA cm}^{-2}$ , thus confirming the stability of the cell G2 in this time window. A performance comparison of different microfluidic DMFCs is reported in table 6.2. From this comparison, it can be observed that under similar conditions (electrolyte, fuel concentration, temperature), the cell G2 exhibits the strongest performance.

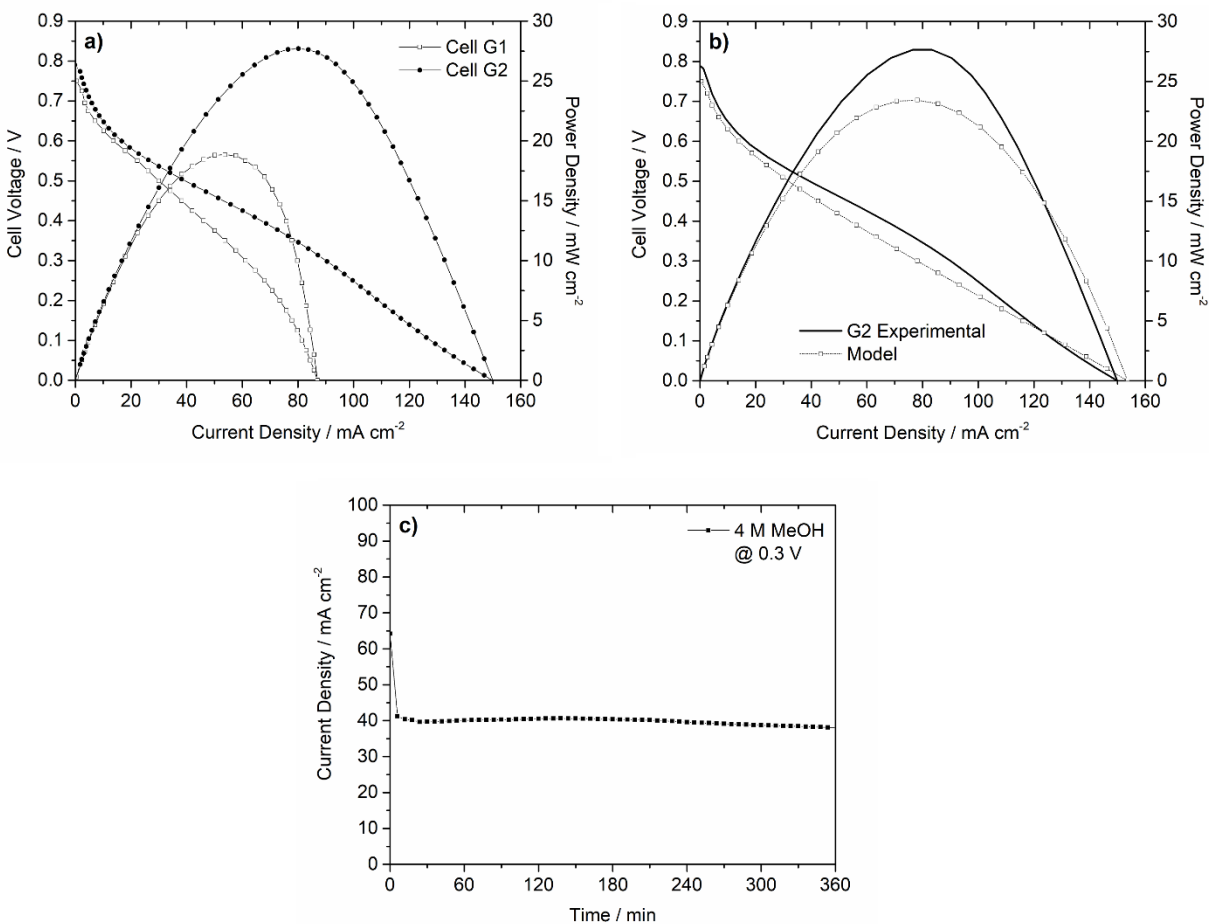


**Figure 6.8** a) Performance comparison between cells G1 and G2, b) comparison between model and cell G2 and c) chronoamperometry of cell G2 obtained with 4 M MeOH at 0.3 V.

**Table 6.2 Literature survey of recent microfluidic DMFCs.**

Reference	Flowrate ( $\mu\text{L min}^{-1}$ )	Electrolyte	[MeOH]	OCV (V)	Max current ( $\mu\text{A}$ )	Max current density ( $\text{mA cm}^{-2}$ )	Peak power ( $\mu\text{W}$ )	Peak power density ( $\text{mW cm}^{-2}$ )	Features
[192]	Passive	0.5 M $\text{H}_2\text{SO}_4$	2 M	0.50	14	-	1.4	-	On-chip FC, fabricated by MEMS
[51]	Passive	0.5 M $\text{H}_2\text{SO}_4$	2 M	0.45	15	-	2	-	On-chip FC, fabricated by MEMS
[52]	80	0.5 M $\text{H}_2\text{SO}_4$	2 M	0.45	86	-	12	-	On-chip FC, fabricated by MEMS
[87]	Passive	0.5 M $\text{H}_2\text{SO}_4$	2 M	0.45	35	-	2.8	-	On-chip FC, fabricated by MEMS
[193]	Driven by capillary forces	0.5 M KOH	4 M	0.55	-	22	-	2	FC on paper strip
[71]	100	0.5 M $\text{H}_2\text{SO}_4$	2 M	0.84	-	25	-	6.9	Ladder-shaped microchannel, fabricated by MEMS
[194]	400	Nafion™ 117	2 M	0.55	-	100	-	10	PEM-FC fabricated by MEMS
[195]	Passive	Nafion™ 117	2 M	0.50	-	2.5	-	0.28	PEM-FC fabricated by MEMS
[42]	Passive	1 M KOH	3 M	0.42	-	11	-	1.1	AEM.-FC fabricated by MEMS
[196]	Passive	1 M KOH	7 M	0.70	-	9	-	1.2	AEM.-FC fabricated by MEMS
[189]	100	1 M KOH	1 M	0.75	-	160	-	21.1	Orthogonal flow, fabricated by laser cutting
[197]	500	0.5 M $\text{H}_2\text{SO}_4$	2 M	0.69	-	34	-	7.4	Polymer separator-FC, machined on polyethylene.
[198]	160	0.5 M $\text{H}_2\text{SO}_4$	1 M	0.50	-	7.3	-	1.4	Monolithic FC, fabricated by MEMS
[199]	400	1 M KOH anolyte/0.5 M $\text{H}_2\text{SO}_4$ catholyte	3 M	1.24	-	73.4	-	30	V-shape microchannel, fabricated by soft lithography
[200]	50	1 M KOH	10 M	0.90	-	120	-	25	Vapor feed FC, fabricated by laser cutting <sup>6</sup>
[201]	3400	0.5 M $\text{H}_2\text{SO}_4$	5 M	0.35	-	40.9	-	3	MRFC, machined on PEEK.
This work (single cell)	Passive	0.5 KOH	4 M	0.8	-	150	-	28	MRFC, machined on PMMA

**FC: Fuel cell, MEMS: Microelectromechanical systems, PEM: Proton exchange membrane, AEM: Alkaline exchange membrane, MRFC: Mixed-reactant fuel cell, PEEK: Polyether ether ketone, PMMA: Poly(methyl methacrylate).**

#### **6.4 Development and performance of a 4-cell MR- $\mu$ DMFC stack**

A microfluidic fuel cell stack was developed from the G2 mixed-reactant fuel cell. All the components, assembly and a photograph of the fabricated device are shown in Fig. 6.9. The stack consists of 4-G2 cells incorporated in a single integrated device. The fuel cells are arranged in a serial path fashion, i.e. there is a single inlet at the beginning of the path for cell 1. The outlet of cell 1 then becomes the inlet of cell 2, which in turn leads to cell 3 until subsequently reaching cell 4. This design simplifies the reactant delivery to the individual cells and the electrical connections between them. Furthermore, it allows to optimize the dimensions of the device by reducing the amount of components typically needed in a fuel cell stack. The total volume of the microchannel in the 4-cell stack is 234  $\mu$ L. Since no pumps system is needed, the resulting device has a footprint of 22.5 cm<sup>2</sup> and it occupies a total volume is 12.6 cm<sup>3</sup>. Being a very compact fuel cell stack, it is theoretically possible to obtain higher power per unit of total volume [65,66], which is desirable for any type of energy conversion system. In order to balance the pressure between cells and minimize the bypass current, a serpentine flow field (20.75 mm length  $\times$  500  $\mu$ m width) was designed. The serpentine, placed between the outlet and inlet of adjacent cells, generates high-enough ionic resistance and prevents a short circuit within the device caused by the conductivity of the electrolyte [202].

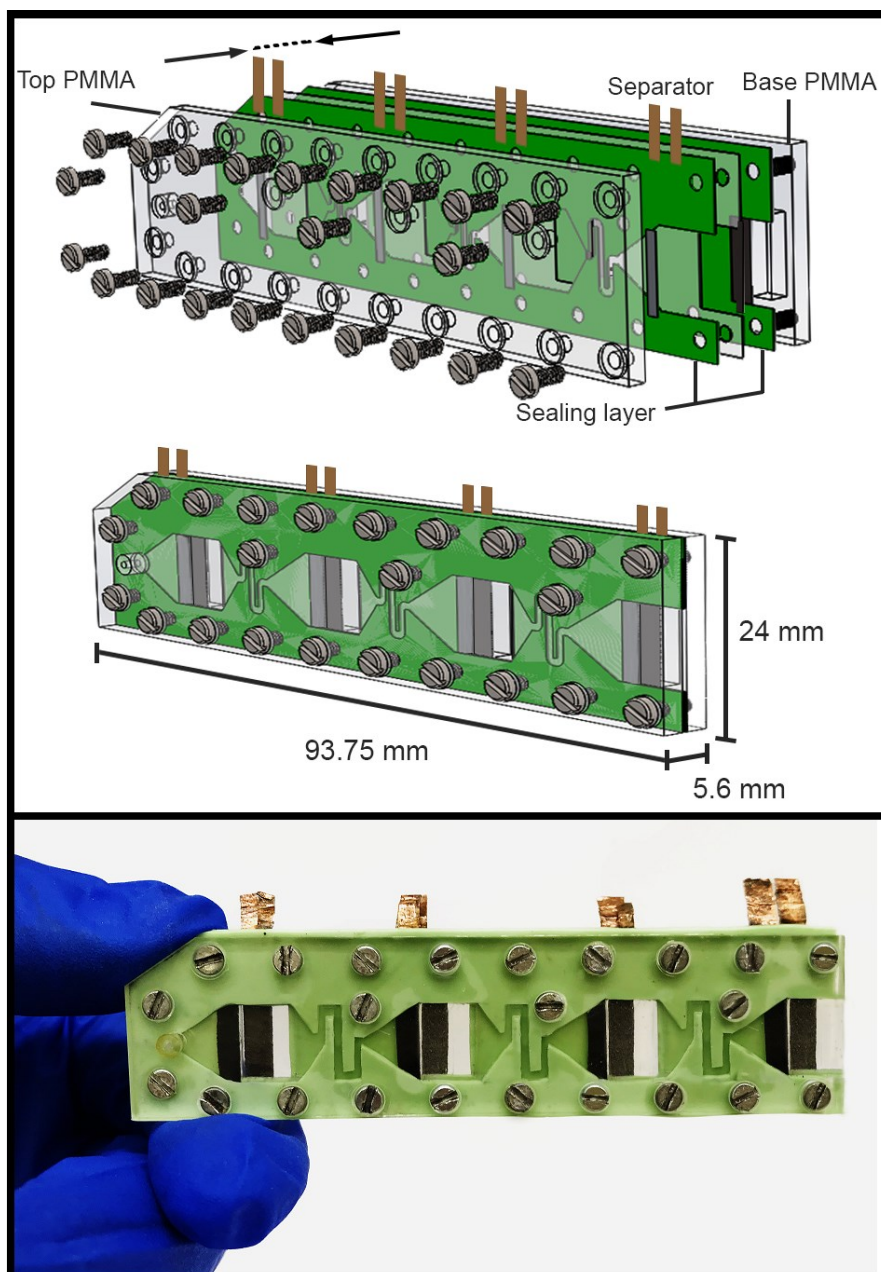
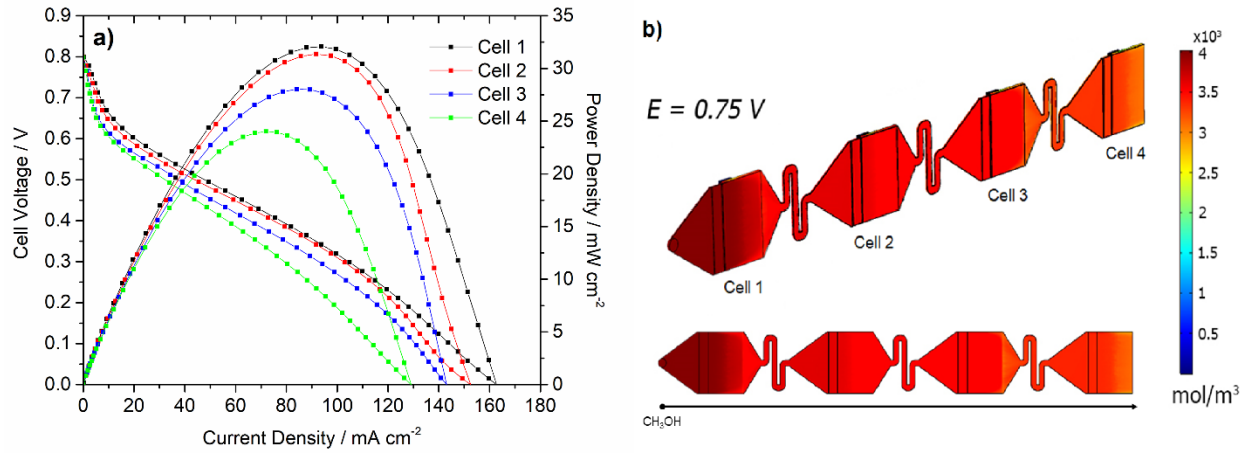


Figure 6.9 Representation of components, assembly and photograph of the 4-cell MR- $\mu$ DMFC stack.

For studying the performance of the MR- $\mu$ DMFC stack, first the four cells were individually tested. Fig. 6.10a shows the polarization and power curves obtained from each cell using 4 M MeOH in 0.5 M KOH (Cathode:  $\text{Mn}_2\text{O}_3/\text{Pt}/\text{CP}$ , Anode:  $\text{PtRu}/\text{C}$ ). In all cases, the OCV is between 0.77 and 0.80 V, which is within the values observed in the single G2 cell. However, a trend emerges when looking at the maximum current density and peak power density of each cell. These two values decrease as we move from cell 1 to 4. In order to explain this phenomenon, the fuel profiles for

all the cells in the stack were studied at a cell voltage close to the OCV. The simulation revealed a dependent relationship between the fuel concentration and the length of the fuel path. In Fig. 6.10b can be observed that a slight amount, less than 1 M of fuel is consumed as it flows from cell 1 to 4. Therefore, each cell has less reacting fuel than the preceding cell, resulting in lower current and power density. Based on this result, it is possible to infer that although it seems intuitive to add more cells in the serial path, this would be a counterproductive measure for achieving a stable stack performance.

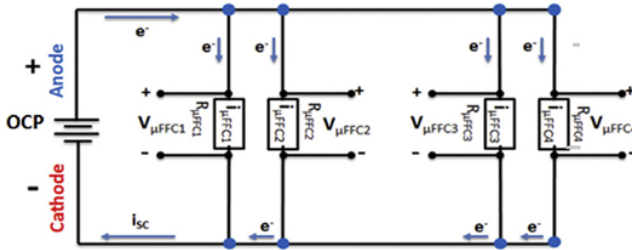


**Figure 6.10** a) Polarization and power density curves and b) fuel profiles of individual cells in the MR- $\mu$ DMFC stack.

Next, we evaluated the stack with the four cells electrically connected in series and parallel arrangements (circuit diagram in Fig. 6.11) and the connection efficiency was calculated according to Equation (95) [203].

$$\eta = \frac{V|_{Pmax} \times I|_{Pmax}}{\sum_{i=0}^n V_i|_{Pmax} \times I_i|_{Pmax}} \quad (95)$$

## Parallel Connection



## Series Connection

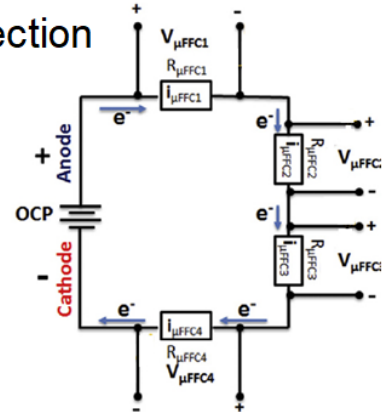
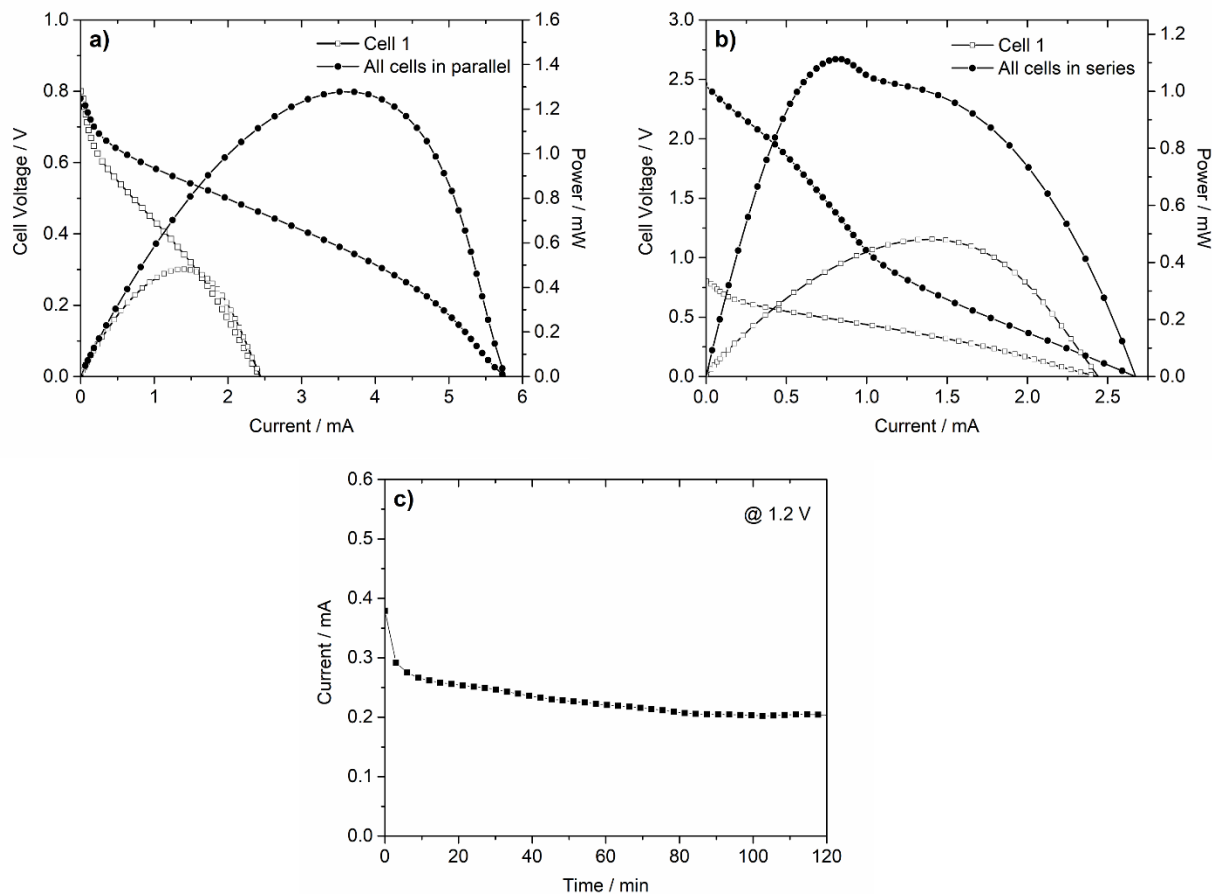


Figure 6.11 Circuit diagram of connections performed for the study of the 4-cell MR- $\mu$ DMFC stack

It is well known that in series connection, the resulting voltage will be the sum of the individual cells voltage, and similarly in parallel connection, the current output will be the sum of the current produced by individual cells. However, this is true only if all the cells in the circuit are equal in voltage and current, since a weaker cell will cause an imbalance. The performance of the stack without current and power normalization is displayed in Fig. 6.12, along with the performance of cell 1 for comparison purposes. Fig. 6.12a shows the polarization curve obtained in parallel connection, which exhibits an OCV of 0.78 V and maximum current output of 5.8 mA, while a peak power of 1.3 mW was reached. This values represent efficiency of 73.80%. The efficiency losses are, in greater extent, consequence of the differences in cell performances [22]. Moreover, the microfluidic interconnections likely provide undesired electrical connections among unit cells, resulting in parasitic currents. The serpentine between cells is meant to diminish this effect, however, the inter-cell potential gradients generated by electrode processes are capable of driving the ionic currents through the fluid, causing energy losses [163,203,204]. The same applies for the polarization curve obtained in series connection, displayed in Fig. 6.12b, which exhibits an OCV of 2.46 V and maximum current output of 2.7 mA, while a peak power of 1.1 mW was obtained with an efficiency connection of 64.23%. In addition to the aforementioned causes for performance loss, greater ohmic losses are observed in this configuration due to the sum of the individual resistances of components, such as electrodes, flow structures and interconnections. The stability of the MR- $\mu$ DMFC stack was evaluated in series connection at 1.2 V during 2 h. The chronoamperometric curve, shown in Fig. 6.12c exhibits a stable behavior during this time window with an average current density of 0.23 mA.



**Figure 6.12** Polarization and power density curves of the 4-cell stack in a) parallel connection, b) series connection, and d) chronoamperometric curve of the stack in series connection. In all cases 4 M MeOH in 0.5 M KOH was used.

Finally, in order to demonstrate the potential capabilities of this MR- $\mu$ DMFC stack towards practical applications, the device was used as power supply for an LED (Fig. 6.13). The four cells in the stack were connected in series to meet the voltage requirement and the assembly was directly connected to the LED. As can be observed in the photograph, the device is able to operate in conditions close to real application, that is, room temperature and passive mode in a compact packaging. This test demonstrated that the MR- $\mu$ DMFC stack is capable not only of powering the LED, but it also keeps a constant operation during at least 4 h (Fig. 6.14) with a single charge of 234  $\mu$ L of reactant solution. It is noteworthy that the use of a selective cathode and the concept of mixed-reactant fuel cell allowed to develop a very compact and well performing system with less components and simpler operation than most fuel cell stacks. The aforementioned is a remarkable feat and a step forward towards the development of more efficient fuel cells. We acknowledge that the performance of the device could be further improved by making a more

effective separation between unit cells to minimize the losses due to parasitic currents. It might be also necessary to implement an assembly method that ensures that all the cells in the stack behave equivalently. Moreover, numerical simulation can be employed for optimizing the window for air-breathing, a crucial component of this kind of fuel cell, as the air flow structure plays a key role in the cathode efficiency [88,205,206] and thus in the overall fuel cell performance.

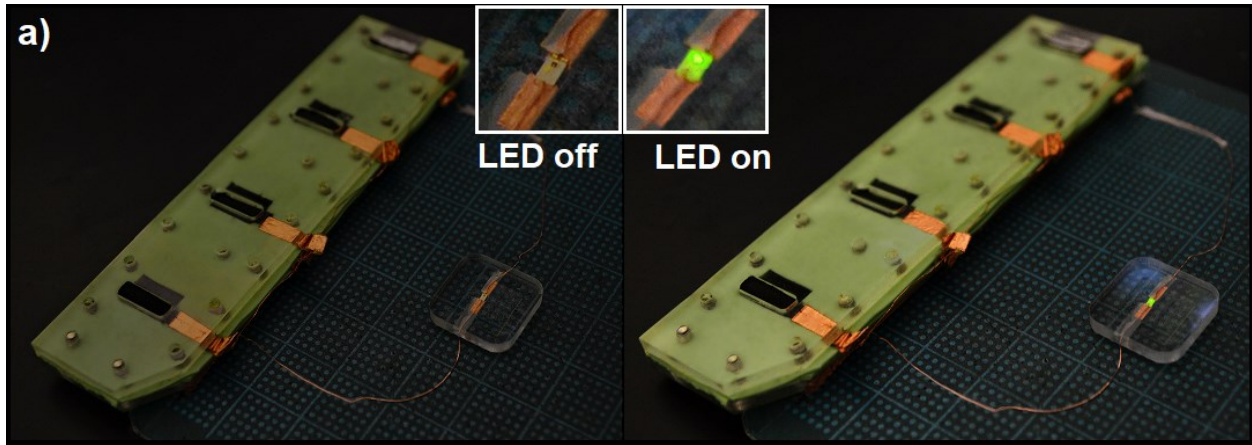


Figure 6.13 Photograph of fuel cell powering a green LED.

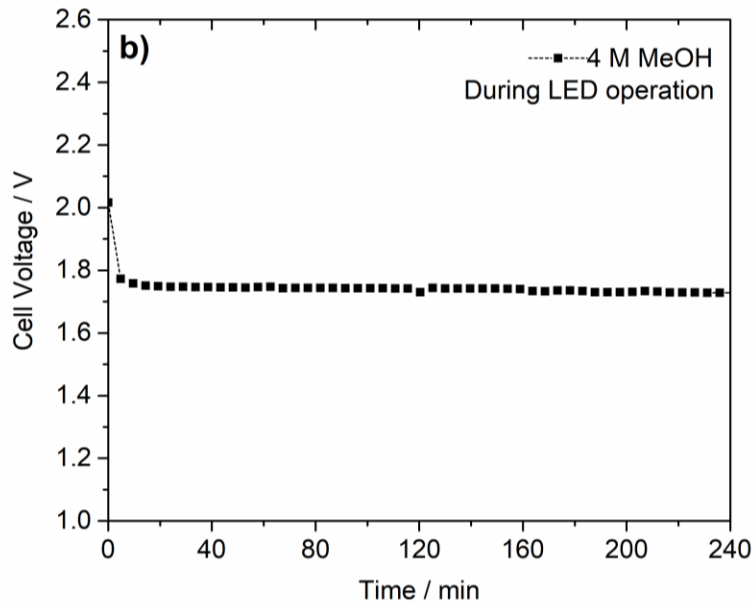


Figure 6.14 Voltage profile of the MR- $\mu$ DMFC stack during operation of the green LED.

## CONCLUSIONS

---

### Methanol-tolerant catalysts

In the present work, Ag/Pt and Mn<sub>2</sub>O<sub>3</sub>/Pt bilayer catalyst were successfully grown on CP using the pulsed laser deposition technique. For both materials, the physicochemical characterization confirmed the presence of a second layer (Ag for Ag/Pt and Mn<sub>2</sub>O<sub>3</sub> for Mn<sub>2</sub>O<sub>3</sub>/Pt) coating the surface of the Pt layer. Both bilayer materials exhibited catalytic activity towards the ORR, however, in the case of the Mn<sub>2</sub>O<sub>3</sub>/Pt catalyst, the activity is practically identical to Pt in KOH solution. Additionally, the catalysts showed high tolerance to the MOR, although the performance exhibited by the Mn<sub>2</sub>O<sub>3</sub>/Pt material in presence of methanol was superior in comparison with Ag/Pt. In both cases, such behavior results from the contribution of the two components in the material, i.e. the ORR occurs through a 4-electron transfer at the Pt layer while the tolerance property is attributed to the secondary layer (Ag or Mn<sub>2</sub>O<sub>3</sub>). These observations suggest that the binary materials are capable of discriminating between oxygen and methanol molecules, likely due to their different molecular size, and therefore, they selectively perform the ORR in presence of MeOH. The electrochemical studies performed to evaluate the activity towards the MOR, revealed that Ag is slightly active to the methanol oxidation, while the catalytic activity of Mn<sub>2</sub>O<sub>3</sub> towards the same reaction is considerably less. For this reason the Mn<sub>2</sub>O<sub>3</sub>/Pt catalyst showed better tolerance to methanol while maintaining its activity towards the ORR. Afterwards, the cathodes were evaluated in a membraneless  $\mu$ DMFC under mixed-reactant conditions and passive mode. The fuel cell performance parameters demonstrated that even at methanol concentration as high as 5 M, the oxidation and reduction reactions are carried out at their respective electrodes. By comparing the performance obtained with the two different cathodes, it is evident that the fuel cell yielded a better performance (higher OCV, maximum current density and peak power density) when employing the Mn<sub>2</sub>O<sub>3</sub>/Pt cathode. For this reason, the Mn<sub>2</sub>O<sub>3</sub>/Pt/CP cathode was used in the development of a new MR- $\mu$ DMFC stack.

### **Microfluidic mixed-reactant fuel cell stack.**

The numerical simulation developed in this work accurately predicts the behavior of experimental fuel cell systems. Through the model and flow simulation, it was possible to study different electrode arrangements and the effect of the disposition of electrodes on the fuel cell performance. The efficiency of previous designs was restricted by deficient air-flow due to turbulence and flooding at the cathode, as occurred in the G1 design. This problem was solved with the new electrodes disposition, where the anode and the cathode are in parallel planes. In addition, this arrangement allowed to significantly shorten the distance between electrodes, which reduced the resistance of the fuel cell, thus improving the performance, ultimately reaching 81% fuel utilization. A new MR- $\mu$ DMFC was fabricated according to the simulation and the experimental results showed good correlation with the theory. From this single cell, a passive 4-cell MR- $\mu$ DMFC stack was developed. Due to the feature optimization through computer simulation and to the use of a selective cathode, it was possible to incorporate four mixed-reactant fuel cells into a very compact body. The resulting device exhibits a straightforward design with a small number of components and simpler operation than most fuel cells stacks. The new stack was capable of powering a green LED during 4 h with a single charge of 234  $\mu$ L, thus demonstrating the good performance and capabilities of mixed-reactant fuel cells for potential practical applications. On the basis of additional simulation results, the performance of the device could be further improved by creating a more effective separation between cells, minimizing the losses due to parasitic currents and optimizing the air flow structure. If successful, such performance boosts would position the mixed-reactants microfluidic fuel cells as a viable, cost-effective candidate for the next generation of portable devices.

## PERSPECTIVES

---

In order to unquestionably be considered as a contender or replacement of Li-ion batteries, the power and durability of current microfluidic fuel cells must be substantially improved. It is clear that there is still room to further improve the performance of MR- $\mu$ DMFCs.

Regarding the selective cathode, the ORR performance of our bilayer cathode approach seems to be exceptionally close to that of Pt, which remains as the best catalyst for ORR. However, the cathode performance in terms of current density can be enhanced by increasing the Pt active area or by increasing the catalysts loading. Additionally, the electronic conductivity of the electrode can be enhanced by growing the selective catalyst onto carbon nanotubes or graphene substrates.

For a single cell, more numerical studies can be carried out studying different electrodes–microchannel arrangements in order to further increase the fuel utilization and the conversion efficiency. Moreover, the air-flow structure on the cathode plate can be optimized through flow simulation studies.

As to a microfluidic stack device, there are multitude of possibilities for arranging the cells. The mixed-reactant and passive operation opens the door to a virtually endless variety of new designs, which is not feasible with co-laminar based fuel cells. Numerical simulation can be also employed for studying promising stack designs.

Finally, regarding the fabrication of MR- $\mu$ DMFCs, the PMMA substrate employed in this work can be replaced by thinner, flexible polymeric substrates in order to decrease the total volume of the device, resulting in higher volumetric power density.



## REFERENCES

---

- [1] Zhao T. Micro fuel cells: principles and applications. Massachusetts: Academic Press; 2009.
- [2] Dyer CK. Fuel cells for portable applications. J Power Sources 2002;106:31-4.
- [3] Achmad F, Kamarudin SK, Daud WRW, Majlan E. Passive direct methanol fuel cells for portable electronic devices. Appl Energy 2011;88:1681-9.
- [4] Wilberforce T, Alaswad A, Palumbo A, Dassisti M, Olabi A-G. Advances in stationary and portable fuel cell applications. Int J Hydrogen Energy 2016;41:16509-22.
- [5] Kjeang E. Microfluidic fuel cells and batteries. New York: Springer; 2014.
- [6] Digikey. KXTJ3-1057 (2019) <https://www.digikey.ca/product-detail/en/kionix-inc/KXTJ3-1057/KXTJ3-1057CT-ND/6573089>. (Accessed December 11, 2019).
- [7] Digikey. SEN-14666 (2019) <https://www.digikey.com/products/en?mpart=SEN-14666&v=1568>. (Accessed December 11, 2019).
- [8] Digikey. MIKROE-55 (2019) <https://www.digikey.ca/product-detail/en/mikroelektronika/MIKROE-55/1471-1236-ND/4495600>. (Accessed December 11, 2019).
- [9] Digikey. LG L29K-G2J1-24-Z (2019) <https://www.digikey.ca/product-detail/en/osram-opto-semiconductors-inc/LG-L29K-G2J1-24-Z/475-2709-1-ND/1938876>. (Accessed December 11, 2019).
- [10] Digikey. SLR-56VR3F (2019) <https://www.digikey.ca/product-detail/en/rohms-semiconductor/SLR-56VR3F/511-1264-ND/636992>. (Accessed December 11, 2019).
- [11] Sala-Deco. N20 DC 1.5V 0.02A 1600RPM Output Speed Electric Mini Motor (2019) <https://www.amazon.ca/Sala-Deco-0-02A-1600RPM-Output-Electric/dp/B07L958NHP>. (Accessed December 11, 2019).
- [12] Arduino. Arduino Micro (2019) <https://store.arduino.cc/usa/arduino-micro>. (Accessed December 11, 2019).
- [13] Digikey. PiTFT 3.5" Touch Screen for Raspberry Pi (2019) <https://www.digikey.ca/products/en?mpart=2441&v=1528>. (Accessed December 11, 2019).

- [14] Digikey. CMOS Camera Module SEN-11745 (2019) <https://www.digikey.com/products/en?mpart=SEN-11745&v=1568>. (Accessed December 11, 2019).
- [15] Malik MY. Power consumption analysis of a modern smartphone. arXiv preprint arXiv:12121896 2012.
- [16] Mahesri A, Vardhan V. Power consumption breakdown on a modern laptop. International Workshop on Power-Aware Computer Systems 2004:165-80.
- [17] Apple. 12-inch MacBook Environmental Report (2017) [https://www.apple.com/th/environment/pdf/products/notebooks/12-inch\\_MacBook\\_PER\\_June2017.pdf](https://www.apple.com/th/environment/pdf/products/notebooks/12-inch_MacBook_PER_June2017.pdf). (Accessed December 11, 2019).
- [18] Lu L, Han X, Li J, Hua J, Ouyang M. A review on the key issues for lithium-ion battery management in electric vehicles. J Power Sources 2013;226:272-88.
- [19] Nitta N, Wu F, Lee JT, Yushin G. Li-ion battery materials: present and future. Mater Today 2015;18:252-64.
- [20] Meesala Y, Jena A, Chang H, Liu R-S. Recent advancements in Li-ion conductors for all-solid-state Li-ion batteries. ACS Energy Lett 2017;2:2734-51.
- [21] Larminie J, Dicks A, McDonald MS. Fuel cell systems explained: J. Wiley Chichester, UK; 2003.
- [22] O'hayre R, Cha S-W, Prinz FB, Colella W. Fuel cell fundamentals. New Jersey: John Wiley & Sons; 2016.
- [23] Gröger O, Gasteiger HA, Suchsland J-P. Electromobility: Batteries or fuel cells? J Electrochem Soc 2015;162:A2605-A22.
- [24] Hall PJ, Bain EJ. Energy-storage technologies and electricity generation. Energy policy 2008;36:4352-5.
- [25] Das HS, Tan CW, Yatim A. Fuel cell hybrid electric vehicles: A review on power conditioning units and topologies. Renew Sust Energ Rev 2017;76:268-91.
- [26] Wang Y, Chen KS, Mishler J, Cho SC, Adroher XC. A review of polymer electrolyte membrane fuel cells: technology, applications, and needs on fundamental research. Appl Energy 2011;88:981-1007.
- [27] Wang S, Jiang SP. Prospects of fuel cell technologies. Natl Sci Rev 2017;4:163-6.

- [28] Elmer T, Worall M, Wu S, Riffat SB. Fuel cell technology for domestic built environment applications: State-of-the-art review. *Renew Sust Energ Rev* 2015;42:913-31.
- [29] Franceschini EA, Corti HR. Applications and Durability of Direct Methanol Fuel Cells. Dordrecht: Springer; 2014.
- [30] Peighambaroust S, Rowshanzamir S, Amjadi M. Review of the proton exchange membranes for fuel cell applications. *Int J Hydrogen Energy* 2010;35:9349-84.
- [31] Rosli R, Sulong A, Daud W, Zulkifley M, Husaini T, Rosli M, et al. A review of high-temperature proton exchange membrane fuel cell (HT-PEMFC) system. *Int J Hydrogen Energy* 2017;42:9293-314.
- [32] Ong B, Kamarudin S, Basri S. Direct liquid fuel cells: A review. *Int J Hydrogen Energy* 2017;42:10142-57.
- [33] Choban ER, Markoski LJ, Wieckowski A, Kenis PJ. Microfluidic fuel cell based on laminar flow. *J Power Sources* 2004;128:54-60.
- [34] Chen X, Zhang Z, Shen J, Hu Z. Micro direct methanol fuel cell: functional components, supplies management, packaging technology and application. *Int J Enegy Res* 2016.
- [35] Seo SH, Lee CS. Effect of operating parameters on the direct methanol fuel cell using air or oxygen as an oxidant gas. *Energy Fuels* 2008;22:1212-9.
- [36] Ge X, Sumboja A, Wu D, An T, Li B, Goh FT, et al. Oxygen reduction in alkaline media: from mechanisms to recent advances of catalysts. *ACS Catal* 2015;5:4643-67.
- [37] Wang Y-J, Zhao N, Fang B, Li H, Bi XT, Wang H. Carbon-supported Pt-based alloy electrocatalysts for the oxygen reduction reaction in polymer electrolyte membrane fuel cells: particle size, shape, and composition manipulation and their impact to activity. *Chem Rev* 2015;115:3433-67.
- [38] Corti HR, Gonzalez ER. Introduction to direct alcohol fuel cells: Springer; 2014.
- [39] Choban ER, Spendelow J, Gancs L, Wieckowski A, Kenis P. Membraneless laminar flow-based micro fuel cells operating in alkaline, acidic, and acidic/alkaline media. *Electrochim Acta* 2005;50:5390-8.
- [40] Yang JH, Bae YC. Methanol crossover effect for direct methanol fuel cells: applicability of methanol activity in polymer electrolyte membrane. *J Electrochem Soc* 2008;155:B194-B9.

- [41] Mondal S, Soam S, Kundu PP. Reduction of methanol crossover and improved electrical efficiency in direct methanol fuel cell by the formation of a thin layer on Nafion 117 membrane: Effect of dip-coating of a blend of sulphonated PVdF-co-HFP and PBI. *J Membr Sci* 2015;474:140-7.
- [42] Verjullo RW, Santander J, Sabaté N, Esquivel JP, Torres-Herrero N, Habrioux A, et al. Fabrication and evaluation of a passive alkaline membrane micro direct methanol fuel cell. *Int J Hydrogen Energy* 2014;39:5406-13.
- [43] Radenahmad N, Afif A, Petra PI, Rahman SM, Eriksson S-G, Azad AK. Proton-conducting electrolytes for direct methanol and direct urea fuel cells—A state-of-the-art review. *Renew Sust Energ Rev* 2016;57:1347-58.
- [44] Jung E, Jung U, Yang T, Peak D, Jung D, Kim S. Methanol crossover through PtRu/Nafion composite membrane for a direct methanol fuel cell. *Int J Hydrogen Energy* 2007;32:903-7.
- [45] Li X, Faghri A. Review and advances of direct methanol fuel cells (DMFCs) part I: design, fabrication, and testing with high concentration methanol solutions. *J Power Sources* 2013;226:223-40.
- [46] Chae KJ, Choi M, Ajayi FF, Park W, Chang IS, Kim IS. Mass transport through a proton exchange membrane (Nafion) in microbial fuel cells. *Energy Fuels* 2007;22:169-76.
- [47] Ansari Y, Tucker T, Huang W, Klein I, Lee S-Y, Yarger J, et al. A flexible all-inorganic fuel cell membrane with conductivity above Nafion, and durable operation at 150 C. *J Power Sources* 2016;303:142-9.
- [48] Sgroi MF, Zedde F, Barbera O, Stassi A, Sebastián D, Lufrano F, et al. Cost Analysis of Direct Methanol Fuel Cell Stacks for Mass Production. *Energies* 2016;9:1008.
- [49] Cao J, Xu J, Chen Z, Wang W, Huang Q, Zou Z. A silicon-based micro direct methanol fuel cell stack with a serial flow path design. *Int J Energy Res* 2013;37:370-6.
- [50] Yu Y, Wang Y, Zhang S, Zhang P, Xue S, Xie Y, et al. The construction of integrated Si-based micro proton exchange membrane fuel cells with improved performances. *Nano Energy* 2019;61:604-10.
- [51] Tominaka S, Nishizeko H, Ohta S, Osaka T. On-chip fuel cells for safe and high-power operation: investigation of alcohol fuel solutions. *Energy Environ Sci* 2009;2:849-52.

- [52] Tominaka S, Obata H, Osaka T. On-chip direct methanol fuel cells of a monolithic design: consideration on validity of active-type system. *Energy Environ Sci* 2009;2:845-8.
- [53] Ferrigno R, Stroock AD, Clark TD, Mayer M, Whitesides GM. Membraneless vanadium redox fuel cell using laminar flow. *J Am Chem Soc* 2002;124:12930-1.
- [54] Shaegh SAM, Nguyen N-T, Chan SH. A review on membraneless laminar flow-based fuel cells. *Int J Hydrogen Energy* 2011;36:5675-94.
- [55] Masdar MS, Zainoodin AM, Rosli MI, Kamarudin SK, Daud WRW. Performance and stability of single and 6-cell stack passive direct methanol fuel cell (DMFC) for long-term operation. *Int J Hydrogen Energy* 2017;42:9230-42.
- [56] Cohen JL, Westly DA, Pechenik A, Abruña HD. Fabrication and preliminary testing of a planar membraneless microchannel fuel cell. *J Power Sources* 2005;139:96-105.
- [57] Ho B, Kjeang E. Planar multiplexing of microfluidic fuel cells. *J Fluids Eng* 2013;135:021304.
- [58] Salloum KS, Posner JD. A membraneless microfluidic fuel cell stack. *J Power Sources* 2011;196:1229-34.
- [59] Kjeang E, McKechnie J, Sinton D, Djilali N. Planar and three-dimensional microfluidic fuel cell architectures based on graphite rod electrodes. *J Power Sources* 2007;168:379-90.
- [60] Wang Y, Leung DY. A circular stacking strategy for microfluidic fuel cells with volatile methanol fuel. *Appl Energy* 2016;184:659-69.
- [61] Barton SC, Patterson T, Wang E, Fuller T, West A. Mixed-reactant, strip-cell direct methanol fuel cells. *J Power Sources* 2001;96:329-36.
- [62] Shukla A, Raman R, Scott K. Advances in Mixed-Reactant Fuel Cells. *Fuel cells* 2005;5:436-47.
- [63] Barton SC, Deng W, Gallaway JW, Levendovsky S, Olson T, Atanassov P, et al. Mixed-feed direct methanol fuel cell: Materials and design solutions. *ECS Trans* 2006;1:315-22.
- [64] Priestnall MA, Kotzeva VP, Fish DJ, Nilsson EM. Compact mixed-reactant fuel cells. *J Power Sources* 2002;106:21-30.
- [65] Aziznia A, Oloman CW, Gyenge EL. A Swiss-roll liquid-gas mixed-reactant fuel cell. *J Power Sources* 2012;212:154-60.

- [66] Kothandaraman R, Deng W, Sorkin M, Kaufman A, Gibbard HF, Barton SC. Methanol anode modified by semipermeable membrane for mixed-feed direct methanol fuel cells. *J Electrochem Soc* 2008;155:B865-B8.
- [67] Aziznia A, Oloman CW, Gyenge EL. Platinum-and Membrane-Free Swiss-Roll Mixed-Reactant Alkaline Fuel Cell. *ChemSusChem* 2013;6:847-55.
- [68] Aziznia A, Oloman CW, Gyenge EL. Experimental advances and preliminary mathematical modeling of the Swiss-roll mixed-reactant direct borohydride fuel cell. *J Power Sources* 2014;265:201-13.
- [69] Tu H-C, Wang Y-Y, Wan C-C, Hsueh K-L. Semi-empirical model to elucidate the effect of methanol crossover on direct methanol fuel cell. *J Power Sources* 2006;159:1105-14.
- [70] Ahmed M, Dincer I. A review on methanol crossover in direct methanol fuel cells: challenges and achievements. *Int J Energy Res* 2011;35:1213-28.
- [71] Huo W, Zhou Y, Zhang H, Zou Z, Yang H. Microfluidic direct methanol fuel cell with ladder-shaped microchannel for decreased methanol crossover. *Int J Electrochem Sci* 2013;8:4827-38.
- [72] Liu M, Lu Y, Chen W. PdAg nanorings supported on graphene nanosheets: highly methanol-tolerant cathode electrocatalyst for alkaline fuel cells. *Adv Funct Mater* 2013;23:1289-96.
- [73] Choi J-H, Johnston CM, Cao D, Babu PK, Zelenay P. Se-modified Ru nanoparticles as ORR catalysts: Part 2: Evaluation for use as DMFC cathodes. *J Electroanal Chem* 2011;662:267-73.
- [74] Singh R. Palladium selenides as active methanol tolerant cathode materials for direct methanol fuel cell. *Int J Hydrogen Energy* 2011;36:10006-12.
- [75] Li X, Huang Q, Zou Z, Xia B, Yang H. Low temperature preparation of carbon-supported PdCo alloy electrocatalysts for methanol-tolerant oxygen reduction reaction. *Electrochim Acta* 2008;53:6662-7.
- [76] Sebastián D, Serov A, Artyushkova K, Gordon J, Atanassov P, Aricò AS, et al. High Performance and Cost-Effective Direct Methanol Fuel Cells: Fe-N-C Methanol-Tolerant Oxygen Reduction Reaction Catalysts. *ChemSusChem* 2016;9:1986-95.
- [77] Sebastian D, Serov A, Matanovic I, Artyushkova K, Atanassov P, Arico A, et al. Insights on the extraordinary tolerance to alcohols of Fe-NC cathode catalysts in highly performing direct alcohol fuel cells. *Nano Energy* 2017;34:195-204.

- [78] Gago AS, Gochi-Ponce Y, Feng YJ, Esquivel JP, Sabaté N, Santander J, et al. Tolerant chalcogenide cathodes of membraneless micro fuel cells. *ChemSusChem* 2012;5:1488-94.
- [79] Scott K, Shukla AK, Jackson CL, Meuleman WRA. A mixed-reactants solid-polymer-electrolyte direct methanol fuel cell. *J Power Sources* 2004;126:67-75.
- [80] Feng Y, Yang J, Liu H, Ye F, Yang J. Selective electrocatalysts toward a prototype of the membraneless direct methanol fuel cell. *Sci Rep* 2014;4.
- [81] Ashfold MN, Claeysens F, Fuge GM, Henley SJ. Pulsed laser ablation and deposition of thin films. *Chem Soc Rev* 2004;33:23-31.
- [82] Eason R. Pulsed laser deposition of thin films: applications-led growth of functional materials. New Jersey: John Wiley & Sons; 2007.
- [83] Wang Y, Mohamedi M. Synthesis, Characterization, and Electrochemical Activity of Laser Co-deposited Pt–MnO<sub>2</sub>-Decorated Carbon Nanotube Nanocomposites. *ChemElectroChem* 2016;3:1787-93.
- [84] Gougis M, Tabet-Aoul A, Ma D, Mohamedi M. Laser synthesis and tailor-design of nanosized gold onto carbon nanotubes for non-enzymatic electrochemical glucose sensor. *Sens Actuators B Chem* 2014;193:363-9.
- [85] Spohr E. Computer simulation of the structure of the electrochemical double layer. *J Electroanal Chem* 1998;450:327-34.
- [86] Kaffash A, Rostami K, Zare HR. Modeling of an electrochemical nanobiosensor in COMSOL Multiphysics to determine phenol in the presence of horseradish peroxidase enzyme. *Enzyme Microb Technol* 2019;121:23-8.
- [87] Tominaka S, Ohta S, Osaka T, Alkire R. Prospects of on-chip fuel cell performance: improvement based on numerical simulation. *Energy Environ Sci* 2011;4:162-71.
- [88] Wu H-W. A review of recent development: Transport and performance modeling of PEM fuel cells. *Appl Energy* 2016;165:81-106.
- [89] Khazaei I, Rava A. Numerical simulation of the performance of solid oxide fuel cell with different flow channel geometries. *Energy* 2017;119:235-44.
- [90] Bazylak A, Sinton D, Djilali N. Improved fuel utilization in microfluidic fuel cells: A computational study. *J Power Sources* 2005;143:57-66.

- [91] Bard AJ, Faulkner LR, Leddy J, Zoski CG. Electrochemical methods: fundamentals and applications. New York: Wiley; 1980.
- [92] Gomes MTS, Oliveira MMO, Fonseca MA, Oliveira JA. An expeditious experiment to determine the Faraday constant. J Chem Educ 2004;81:116.
- [93] Spiegel C. Designing and building fuel cells. New York: McGraw Hill Professional; 2007.
- [94] Noiying P, Hinaje M, Thounthong P, Raël S, Davat B. Using electrical analogy to describe mass and charge transport in PEM fuel cell. Renew Energy 2012;44:128-40.
- [95] Store FC. Direct Methanol Fuel Cell Hardware (2019) <https://www.fuelcellstore.com/direct-methanol-fuel-cell-hardware-test-cell>. (Accessed February 8, 2020).
- [96] Energy OoEER. Parts of a Fuel Cell (2019) <https://www.energy.gov/eere/fuelcells/parts-fuel-cell>. (Accessed February 8, 2020).
- [97] Goulet M-A, Kjeang E. Co-laminar flow cells for electrochemical energy conversion. J Power Sources 2014;260:186-96.
- [98] Moreno-Zuria A, Dector A, Cuevas-Muñiz F, Esquivel J, Sabaté N, Ledesma-García J, et al. Direct formic acid microfluidic fuel cell design and performance evolution. J Power Sources 2014;269:783-8.
- [99] Forsyński P, Oloman C, Kazemi S, Nickchi T, Usgaocar A. Development and use of a mixed-reactant fuel cell. J Power Sources 2019;414:366-76.
- [100] Munjewar SS, Thombre SB, Mallick RK. Approaches to overcome the barrier issues of passive direct methanol fuel cell—Review. Renew Sust Energ Rev 2017;67:1087-104.
- [101] Kamarudin SK, Achmad F, Daud WRW. Overview on the application of direct methanol fuel cell (DMFC) for portable electronic devices. Int J Hydrogen Energy 2009;34:6902-16.
- [102] Higgins D, Zamani P, Yu A, Chen Z. The application of graphene and its composites in oxygen reduction electrocatalysis: a perspective and review of recent progress. Energy Environ Sci 2016;9:357-90.
- [103] Hancock CA, Ong AL, Slater PR, Varcoe JR. Development of  $\text{CaMn}_{1-x}\text{Ru}_x\text{O}_{3-y}$  ( $x=0$  and  $0.15$ ) oxygen reduction catalysts for use in low temperature electrochemical devices containing alkaline electrolytes: ex situ testing using the rotating ring-disk electrode voltammetry method. Journal of Materials Chemistry A 2014;2:3047-56.

- [104] Jaouen F, Herranz J, Lefevre M, Dodelet J-P, Kramm UI, Herrmann I, et al. Cross-laboratory experimental study of non-noble-metal electrocatalysts for the oxygen reduction reaction. *Appl Mater Interfaces* 2009;1:1623-39.
- [105] Song C, Zhang J. PEM fuel cell electrocatalysts and catalyst layers. London: Springer; 2008.
- [106] Tarasevich M, Korchagin O. Rapid diagnostics of characteristics and stability of fuel cells with proton-conducting electrolyte. *Russ J Electrochem* 2014;50:737-50.
- [107] Bockris J, Reddy A, Gamboa-Aldeco M.: *Modern Electrochemistry 1, Ionics*. Kluwer Academic/Plenum Publishers, New York; 1998.
- [108] Ramaswamy N, Tylus U, Jia Q, Mukerjee S. Activity descriptor identification for oxygen reduction on nonprecious electrocatalysts: linking surface science to coordination chemistry. *J Am Chem Soc* 2013;135:15443-9.
- [109] Ramaswamy N, Mukerjee S. Fundamental mechanistic understanding of electrocatalysis of oxygen reduction on Pt and non-Pt surfaces: acid versus alkaline media. *Adv Phys Chem* 2012;2012.
- [110] Yu EH, Scott K, Reeve RW. A study of the anodic oxidation of methanol on Pt in alkaline solutions. *J Electroanal Chem* 2003;547:17-24.
- [111] Zhou Y, Neyerlin K, Olson TS, Pylypenko S, Bult J, Dinh HN, et al. Enhancement of Pt and Pt-alloy fuel cell catalyst activity and durability via nitrogen-modified carbon supports. *Energy Environ Sci* 2010;3:1437-46.
- [112] Léger J-M. Mechanistic aspects of methanol oxidation on platinum-based electrocatalysts. *J Appl Electrochem* 2001;31:767-71.
- [113] Vielstich W. Electrochemical energy conversion: methanol fuel cell as example. *J Brazil Chem Soc* 2003;14:503-9.
- [114] Beden B, Léger J-M, Lamy C. *Modern aspects of electrochemistry*. New York: Springer; 1992.
- [115] Tripković AV, Štrbac S, Popović KD. Effect of temperature on the methanol oxidation at supported Pt and PtRu catalysts in alkaline solution. *Electrochem Commun* 2003;5:484-90.
- [116] Lović J. The kinetics and mechanism of methanol oxidation on Pt and PtRu catalysts in alkaline and acid media. *J Serb Chem Soc* 2007;72:709-12.

- [117] Fang Y, Yang X, Wang L, Liu Y. An alkaline direct methanol fuel cell with a polymer fiber membrane and MnO<sub>2</sub>-catalyzed cathode. *Electrochim Acta* 2013;90:421-5.
- [118] Wang B. Recent development of non-platinum catalysts for oxygen reduction reaction. *J Power Sources* 2005;152:1-15.
- [119] Yang H, Vogel W, Lamy C, Alonso-Vante N. Structure and electrocatalytic activity of carbon-supported Pt–Ni alloy nanoparticles toward the oxygen reduction reaction. *J Phys Chem B* 2004;108:11024-34.
- [120] Neergat M, Gunasekar V, Rahul R. Carbon-supported Pd–Fe electrocatalysts for oxygen reduction reaction (ORR) and their methanol tolerance. *J Electroanal Chem* 2011;658:25-32.
- [121] Zhao J, Sarkar A, Manthiram A. Synthesis and characterization of Pd-Ni nanoalloy electrocatalysts for oxygen reduction reaction in fuel cells. *Electrochim Acta* 2010;55:1756-65.
- [122] Sanabria-Chinchilla J, Asazawa K, Sakamoto T, Yamada K, Tanaka H, Strasser P. Noble metal-free hydrazine fuel cell catalysts: EPOC effect in competing chemical and electrochemical reaction pathways. *J Am Chem Soc* 2011;133:5425-31.
- [123] Nekooi P, Akbari M, Amini MK. CoSe nanoparticles prepared by the microwave-assisted polyol method as an alcohol and formic acid tolerant oxygen reduction catalyst. *Int J Hydrogen Energy* 2010;35:6392-8.
- [124] Liu G, Zhang H, Hu J. Novel synthesis of a highly active carbon-supported Ru<sub>85</sub>Se<sub>15</sub> chalcogenide catalyst for the oxygen reduction reaction. *Electrochem Commun* 2007;9:2643-8.
- [125] Liu Y, Ishihara A, Mitsushima S, Kamiya N, Ota K-i. Transition metal oxides as DMFC cathodes without platinum. *J Electrochem Soc* 2007;154:B664-B9.
- [126] Zhang Z, Liu J, Gu J, Su L, Cheng L. An overview of metal oxide materials as electrocatalysts and supports for polymer electrolyte fuel cells. *Energy Environ Sci* 2014;7:2535-58.
- [127] Eijsbouts S, Mayo S, Fujita K. Unsupported transition metal sulfide catalysts: From fundamentals to industrial application. *Appl Catal A-Gen* 2007;322:58-66.
- [128] Zhang L, Zhang J, Wilkinson DP, Wang H. Progress in preparation of non-noble electrocatalysts for PEM fuel cell reactions. *J Power Sources* 2006;156:171-82.

- [129] Wei Q, Zhang G, Yang X, Chenitz Rg, Banham D, Yang L, et al. 3D porous Fe/N/C spherical nanostructures as high-performance electrocatalysts for oxygen reduction in both alkaline and acidic media. *Appl Mater Interfaces* 2017;9:36944-54.
- [130] Hoogers G. *Fuel cell technology handbook*. Florida: CRC press; 2003.
- [131] Sharma S, Ganguly A, Papakonstantinou P, Miao X, Li M, Hutchison JL, et al. Rapid microwave synthesis of CO tolerant reduced graphene oxide-supported platinum electrocatalysts for oxidation of methanol. *J Phys Chem C* 2010;114:19459-66.
- [132] Cheng F, Shen J, Peng B, Pan Y, Tao Z, Chen J. Rapid room-temperature synthesis of nanocrystalline spinels as oxygen reduction and evolution electrocatalysts. *Nature chemistry* 2011;3:79.
- [133] Movchan B, Demchishin A. Obtaining depositions during vacuum condensation of metals and alloys. *Fiz Met Metalloved* 1969;28:653-60.
- [134] Infortuna A, Harvey AS, Gauckler LJ. Microstructures of CGO and YSZ thin films by pulsed laser deposition. *Adv Funct Mater* 2008;18:127-35.
- [135] Passoni L, Ghods F, Docampo P, Abrusci A, Martí-Rujas J, Ghidelli M, et al. Hyperbranched quasi-1D nanostructures for solid-state dye-sensitized solar cells. *ACS nano* 2013;7:10023-31.
- [136] Mukherjee S, Gall D. Structure zone model for extreme shadowing conditions. *Thin Solid Films* 2013;527:158-63.
- [137] Zhou W, Apkarian R, Wang ZL, Joy D. *Fundamentals of scanning electron microscopy (SEM)*. New York: Springer; 2006.
- [138] Stanjek H, Häusler W. Basics of X-ray Diffraction. *Hyperfine Interact* 2004;154:107-19.
- [139] Hübschen G, Altpeter I, Tschuncky R, Herrmann H-G. *Materials characterization using Nondestructive Evaluation (NDE) methods*: Woodhead publishing; 2016.
- [140] Biesinger M. X-ray Photoelectron Spectroscopy (XPS) Reference Pages (2009) <http://www.xpsfitting.com/2008/09/xps-fundamentals.html>. (Accessed December 11, 2019).
- [141] University of Virginia School of Engineering and Applied Science. Scanning X-ray Photoelectron Spectrometer (XPS) (2019) <https://engineering.virginia.edu/research/facilities/nanoscale-materials-characterization-facility/instrumentation/x-ray-3>. (Accessed December 11, 2019).

- [142] Vandenbroucke A. Abatement of volatile organic compounds by combined use of non-thermal plasma and heterogeneous catalysis: Ghent University; 2015.
- [143] Sharma J, Beard B. Fundamentals of X-ray photoelectron spectroscopy (XPS) and its applications to explosives and propellants. New Jersey: Springer; 1990.
- [144] Hamidatou L, Slamene H, Akhal T, Zouranen B. Concepts, instrumentation and techniques of neutron activation analysis. Imaging and Radioanalytical Techniques in Interdisciplinary Research—Fundamentals and Cutting Edge Applications, InTech, Rijeka 2013:141-78.
- [145] Peroff A. Rotating Ring Disk Electrode Fundamentals (2019) <https://pineresearch.com/shop/kb/theory/hydrodynamic-electrochemistry/rotating-electrode-theory/>. (Accessed February 8, 2020).
- [146] El-Kharouf A, Mason TJ, Brett DJ, Pollet BG. Ex-situ characterisation of gas diffusion layers for proton exchange membrane fuel cells. J Power Sources 2012;218:393-404.
- [147] Antoine O, Durand R. RRDE study of oxygen reduction on Pt nanoparticles inside Nafion®: H<sub>2</sub>O<sub>2</sub> production in PEMFC cathode conditions. J Appl Electrochem 2000;30:839-44.
- [148] Sunarso J, Torriero AA, Zhou W, Howlett PC, Forsyth M. Oxygen reduction reaction activity of La-based perovskite oxides in alkaline medium: a thin-film rotating ring-disk electrode study. J Phys Chem C 2012;116:5827-34.
- [149] Ortiz-Ortega E, Goulet M-A, Lee JW, Guerra-Balcázar M, Arjona N, Kjeang E, et al. A nanofluidic direct formic acid fuel cell with a combined flow-through and air-breathing electrode for high performance. Lab Chip 2014;14:4596-8.
- [150] Goulet M-A, Kjeang E. Reactant recirculation in electrochemical co-laminar flow cells. Electrochim Acta 2014;140:217-24.
- [151] Shaegh SAM, Nguyen N-T, Chan SH, Zhou W. Air-breathing membraneless laminar flow-based fuel cell with flow-through anode. Int J Hydrogen Energy 2012;37:3466-76.
- [152] Abrego-Martínez J, Wang Y, Moreno-Zuria A, Wei Q, Cuevas-Muniz F, Arriaga L, et al. Nanostructured Mn<sub>2</sub>O<sub>3</sub>/Pt/CNTs selective electrode for oxygen reduction reaction and methanol tolerance in mixed-reactant membraneless micro-DMFC. Electrochim Acta 2019;297:230-9.
- [153] Yu Y, Zuo Y, Zuo C, Liu X, Liu Z. A hierarchical multiscale model for microfluidic fuel cells with porous electrodes. Electrochim Acta 2014;116:237-43.

- [154] Kjeang E, Djilali N, Sinton D. Microfluidic fuel cells: A review. *J Power Sources* 2009;186:353-69.
- [155] Shaegh SAM, Nguyen N-T, Chan SH. An air-breathing microfluidic formic acid fuel cell with a porous planar anode: experimental and numerical investigations. *J Micromech Microeng* 2010;20:105008.
- [156] Nield DA, Bejan A. *Convection in porous media*. New York: Springer; 2006.
- [157] Xu H, Zhang H, Wang H, Leung DY, Zhang L, Cao J, et al. Counter-flow formic acid microfluidic fuel cell with high fuel utilization exceeding 90%. *Appl Energy* 2015;160:930-6.
- [158] Chang M-H, Chen F, Fang N-S. Analysis of membraneless fuel cell using laminar flow in a Y-shaped microchannel. *J Power Sources* 2006;159:810-6.
- [159] Wang H-N, Zhu X, Zhang B, Ye D-D, Chen R, Liao Q, et al. Two-phase computational modelling of a membraneless microfluidic fuel cell with a flow-through porous anode. *J Power Sources* 2019;420:88-98.
- [160] Tanveer M, Kim K-Y. Effects of geometric configuration of the channel and electrodes on the performance of a membraneless micro-fuel cell. *Energy Convers Manage* 2017;136:372-81.
- [161] Ubong E, Shi Z, Wang X. Three-dimensional modeling and experimental study of a high temperature PBI-based PEM fuel cell. *J Electrochem Soc* 2009;156:B1276-B82.
- [162] Ghouse M, Al-Boeiz A, Abaoud H, Al-Garni M. Preparation and evaluation of PTFE-bonded porous gas diffusion carbon electrodes used in phosphoric acid fuel cell applications. *Int J Hydrogen Energy* 1995;20:727-36.
- [163] Gilliam R, Graydon J, Kirk D, Thorpe S. A review of specific conductivities of potassium hydroxide solutions for various concentrations and temperatures. *Int J Hydrogen Energy* 2007;32:359-64.
- [164] Wagner CD. *Handbook of X-ray photoelectron spectroscopy*. Minnesota: Perkin-Elmer; 1979.
- [165] Asami K. A precisely consistent energy calibration method for X-ray photoelectron spectroscopy. *J Electron Spectrosc Relat Phenom* 1976;9:469-78.
- [166] Markovic N, Gasteiger H, Ross PN. Kinetics of oxygen reduction on Pt (hkl) electrodes: implications for the crystallite size effect with supported Pt electrocatalysts. *J Electrochem Soc* 1997;144:1591-7.

- [167] Gisbert R, García G, Koper MT. Adsorption of phosphate species on poly-oriented Pt and Pt (1 1 1) electrodes over a wide range of pH. *Electrochim Acta* 2010;55:7961-8.
- [168] El Rehim SSA, Hassan HH, Ibrahim MA, Amin MA. Electrochemical behaviour of a silver electrode in NaOH solutions. *Monatsh Chem* 1998;129:1103-17.
- [169] Estrada-Solís M, Abrego-Martínez J, Moreno-Zuria A, Arriaga L, Sun S, Cuevas-Muñiz F, et al. Use of a bilayer platinum-silver cathode to selectively perform the oxygen reduction reaction in a high concentration mixed-reactant microfluidic direct ethanol fuel cell. *Int J Hydrogen Energy* 2019;44:18372-81.
- [170] Wang Y, Tabet-Aoul A, Mohamedi M. Laser synthesis of hierarchically organized nanostructured TiO<sub>2</sub> films on microfibrinous carbon paper substrate: Characterization and electrocatalyst supporting properties. *J Power Sources* 2015;299:149-55.
- [171] Abrego-Martínez J, Wang Y, Ledesma-García J, Cuevas-Muñiz F, Arriaga L, Mohamedi M. A pulsed laser synthesis of nanostructured bi-layer platinum-silver catalyst for methanol-tolerant oxygen reduction reaction. *Int J Hydrogen Energy* 2017;42:28056-62.
- [172] Chigane M, Ishikawa M. Manganese oxide thin film preparation by potentiostatic electrolyses and electrochromism. *J Electrochem Soc* 2000;147:2246-51.
- [173] Cerrato JM, Hochella Jr MF, Knocke WR, Dietrich AM, Cromer TF. Use of XPS to identify the oxidation state of Mn in solid surfaces of filtration media oxide samples from drinking water treatment plants. *Environ Sci Technol* 2010;44:5881-6.
- [174] Junta JL, Hochella MF. Manganese (II) oxidation at mineral surfaces: A microscopic and spectroscopic study. *Geochim Cosmochim Acta* 1994;58:4985-99.
- [175] Biesinger MC, Payne BP, Grosvenor AP, Lau LW, Gerson AR, Smart RSC. Resolving surface chemical states in XPS analysis of first row transition metals, oxides and hydroxides: Cr, Mn, Fe, Co and Ni. *Appl Surf Sci* 2011;257:2717-30.
- [176] Daubinger P, Kieninger J, Unmüssig T, Urban G. Electrochemical characteristics of nanostructured platinum electrodes—a cyclic voltammetry study. *Phys Chem Chem Phys* 2014;16:8392-9.
- [177] Yano M, Suzuki S, Miyayama M, Ohgaki M. Effects of microstructure on electrode properties of nanosheet-derived Hx (Ni<sub>1/3</sub>Co<sub>1/3</sub>Mn<sub>1/3</sub>) O<sub>2</sub> for electrochemical capacitors. *Nanomaterials* 2013;3:204-20.

- [178] Fiedler DA. Rapid evaluation of the rechargeability of  $\gamma$ -MnO<sub>2</sub> in alkaline media by abrasive stripping voltammetry. *J Solid State Electrochem* 1998;2:315-20.
- [179] Valim R, Santos M, Lanza MRdV, Machado SAS, Lima FHBd, Calegaro ML. Oxygen reduction reaction catalyzed by  $\epsilon$ -MnO<sub>2</sub>: influence of the crystalline structure on the reaction mechanism. *Electrochim Acta* 2012;85:423-31.
- [180] Calegaro M, Lima F, Ticianelli E. Oxygen reduction reaction on nanosized manganese oxide particles dispersed on carbon in alkaline solutions. *J Power Sources* 2006;158:735-9.
- [181] Matsuoka K, Iriyama Y, Abe T, Matsuoka M, Ogumi Z. Electro-oxidation of methanol and ethylene glycol on platinum in alkaline solution: Poisoning effects and product analysis. *Electrochim Acta* 2005;51:1085-90.
- [182] Cheng F, Su Y, Liang J, Tao Z, Chen J. MnO<sub>2</sub>-based nanostructures as catalysts for electrochemical oxygen reduction in alkaline media. *Chem Mater* 2009;22:898-905.
- [183] Lima FH, Calegaro ML, Ticianelli EA. Investigations of the catalytic properties of manganese oxides for the oxygen reduction reaction in alkaline media. *J Electroanal Chem* 2006;590:152-60.
- [184] Gurrola M, Ortiz-Ortega E, Farias-Zuñiga C, Chávez-Ramírez A, Ledesma-García J, Arriaga L. Evaluation and coupling of a membraneless nanofluidic device for low-power applications. *J Power Sources* 2016;307:244-50.
- [185] Galindo-de-la-Rosa J, Arjona N, Moreno-Zuria A, Ortiz-Ortega E, Guerra-Balcázar M, Ledesma-García J, et al. Evaluation of single and stack membraneless enzymatic fuel cells based on ethanol in simulated body fluids. *Biosens Bioelectron* 2017;92:117-24.
- [186] Finkelstein DA, Kirtland JD, Mota ND, Stroock AD, Abruña HD. Alternative Oxidants for High-Power Fuel Cells Studied by Rotating Disk Electrode (RDE) Voltammetry at Pt, Au, and Glassy Carbon Electrodes. *J Phys Chem C* 2011;115:6073-84.
- [187] Ebrahimi Khabbazi A. Comprehensive numerical study of microfluidic fuel cells: University of British Columbia; 2010.
- [188] Chen R, Zhao T. Mathematical modeling of a passive-feed DMFC with heat transfer effect. *J Power Sources* 2005;152:122-30.
- [189] Kwok Y, Wang Y, Tsang AC, Leung DY. Graphene-carbon nanotube composite aerogel with Ru@Pt nanoparticle as a porous electrode for direct methanol microfluidic fuel cell. *Appl Energy* 2018;217:258-65.

- [190] Mehmood A, Scibioh MA, Prabhuram J, An M-G, Ha HY. A review on durability issues and restoration techniques in long-term operations of direct methanol fuel cells. *J Power Sources* 2015;297:224-41.
- [191] Knorr F, Sanchez DG, Schirmer J, Gazdzicki P, Friedrich K. Methanol as antifreeze agent for cold start of automotive polymer electrolyte membrane fuel cells. *Appl Energy* 2019;238:1-10.
- [192] Tominaka S, Ohta S, Obata H, Momma T, Osaka T. On-chip fuel cell: micro direct methanol fuel cell of an air-breathing, membraneless, and monolithic design. *J Am Chem Soc* 2008;130:10456-7.
- [193] Esquivel J, Del Campo F, De La Fuente JG, Rojas S, Sabate N. Microfluidic fuel cells on paper: meeting the power needs of next generation lateral flow devices. *Energy Environ Sci* 2014;7:1744-9.
- [194] Zhou Ya, Wang X, Guo X, Qiu X, Liu L. A water collecting and recycling structure for silicon-based micro direct methanol fuel cells. *Int J Hydrogen Energy* 2012;37:967-76.
- [195] Sabaté N, Esquivel JP, Santander J, Hauer JG, Verjullo RW, Gràcia I, et al. New approach for batch microfabrication of silicon-based micro fuel cells. *Microsystem Technologies* 2013;20:341-8.
- [196] Verjullo R, Santander J, Ma J, Alonso-Vante N. Selective CoSe 2/C cathode catalyst for passive air-breathing alkaline anion exchange membrane  $\mu$ -direct methanol fuel cell (AEM- $\mu$ DMFC). *Int J Hydrogen Energy* 2016;41:19595-600.
- [197] Sun F, He H, Huo W. Polymer separator and low fuel concentration to minimize crossover in microfluidic direct methanol fuel cells. *Int J Energy Res* 2015;39:643-7.
- [198] Shen M, Walter S, Gijs M. Monolithic micro-direct methanol fuel cell in polydimethylsiloxane with microfluidic channel-integrated Nafion strip. *J Power Sources* 2009;193:761-5.
- [199] Martins CA, Ibrahim OA, Pei P, Kjeang E. Towards a fuel-flexible direct alcohol microfluidic fuel cell with flow-through porous electrodes: Assessment of methanol, ethylene glycol and glycerol fuels. *Electrochim Acta* 2018;271:537-43.
- [200] Wang Y, Leung DY, Xuan J, Wang H. A vapor feed methanol microfluidic fuel cell with high fuel and energy efficiency. *Appl Energy* 2015;147:456-65.

- [201] Ma J, Habrioux A, Morais C, Alonso-Vante N. Electronic modification of Pt via Ti and Se as tolerant cathodes in air-breathing methanol microfluidic fuel cells. *Phys Chem Chem Phys* 2014;16:13820-6.
- [202] Winkelmann J. *Diffusion in gases, liquids and electrolytes*. Berlin: Springer-Verlag Berlin Heidelberg; 2017.
- [203] Wang H, Gu S, Leung DY, Xu H, Leung MK, Zhang L, et al. Development and characteristics of a membraneless microfluidic fuel cell array. *Electrochim Acta* 2014;135:467-77.
- [204] Moreno-Zuria A, Ortiz-Ortega E, Gurrola M, Chávez-Ramírez A, Ledesma-García J, Arriaga L. Evolution of microfluidic fuel stack design as an innovative alternative to energy production. *Int J Hydrogen Energy* 2017:27929-39.
- [205] Hwang J, Wu S, Lai L, Chen Co-K, Lai D. Effect of breathing-hole size on the electrochemical species in a free-breathing cathode of a DMFC. *J Power Sources* 2006;161:240-9.
- [206] Henriques T, César B, Branco PC. Increasing the efficiency of a portable PEM fuel cell by altering the cathode channel geometry: a numerical and experimental study. *Appl Energy* 2010;87:1400-9.



## APPENDIX I

This section shows the electrochemical characterization of the most representative samples synthesized for this thesis. The following results are helpful to understand the selection process of the optimum catalysts reported in chapters 4 and 5.

The results regarding the  $\text{Fe}_2\text{O}_3/\text{Pt}/\text{CP}$  material, not presented in the results section of this thesis are also shown in this appendix.

### Ag/Pt/CP catalysts

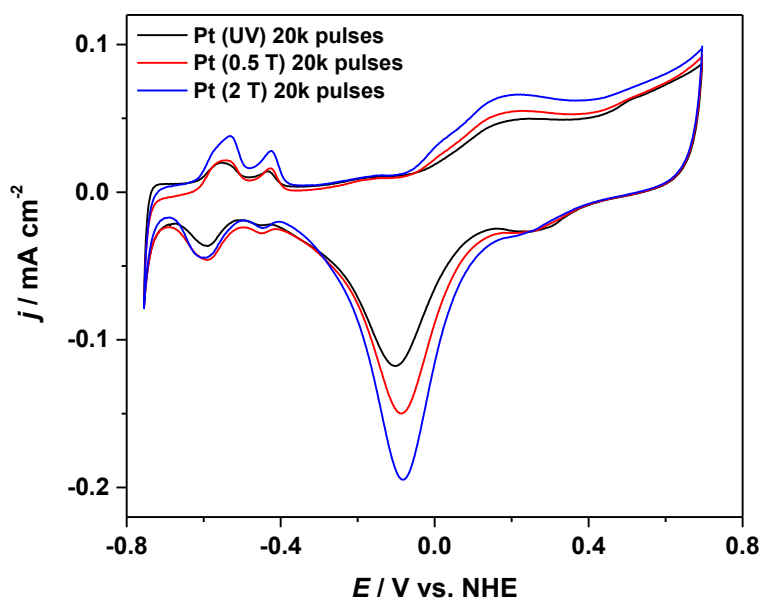


Figure AI 1 Effect of background gas pressure on the active area of the Pt film. Voltammograms recorded in oxygen-free 0.5 M KOH.

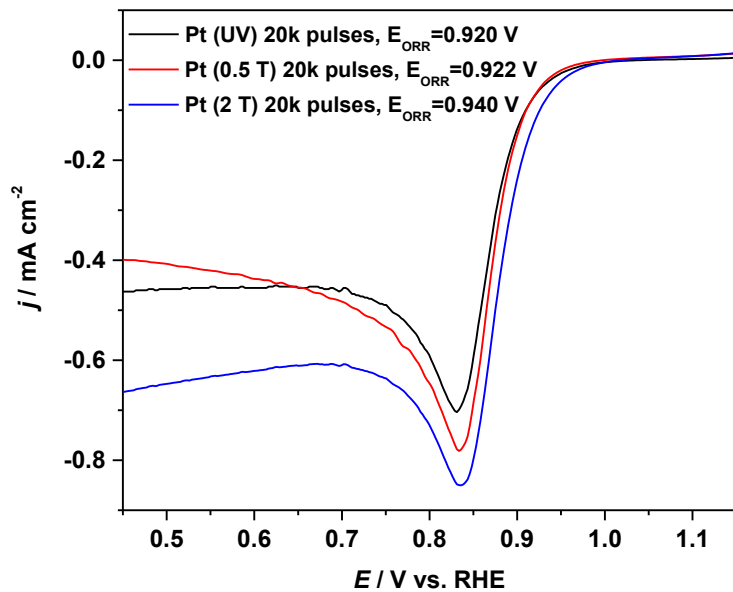


Figure Al 2 Effect of background gas pressure on the onset potential of ORR for the Pt films. Voltammograms obtained in oxygen-saturated 0.5 M KOH.

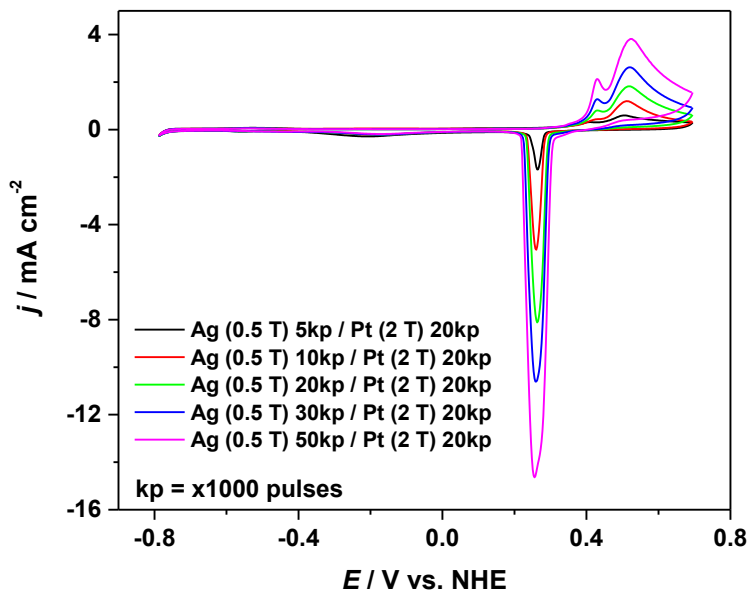


Figure Al 3 Effect of the Ag layer thickness on the electrochemical profile of the sample. With the thinnest Ag layer, the Pt layer is greatly exposed to the solution, however as the Ag layer thickens, the sample behavior approaches that of Ag bulk material, losing the Pt features. CVs obtained in oxygen-free 0.5 M KOH.

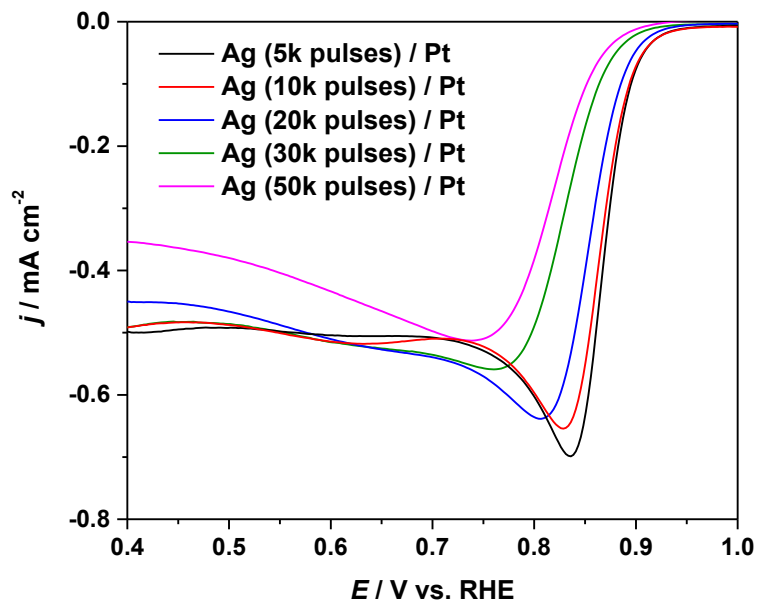


Figure Al 4 Effect of the Ag layer thickness on the ORR activity. The best performance is obtained with the thinnest Ag layer. As the Ag layer thickens, the onset potential becomes less positive, approaching that of Ag. LSVs obtained in oxygen-saturated 0.5 M KOH.

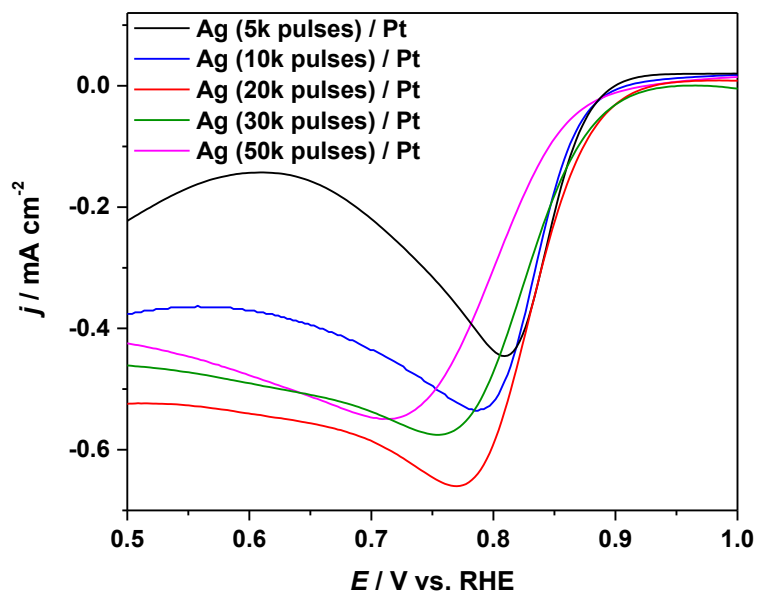


Figure Al 5 Effect of the Ag layer thickness on the activity towards ORR in the presence of MeOH. With the thinnest Ag layer, the material exhibits the poorest methanol tolerance, as the Pt layer is greatly exposed to the solution. On the other hand, with the thickest Ag layer, the material exhibits higher tolerance to MeOH but the ORR onset potential is the least positive, similar to bulk Ag. The best performance (compromise between onset potential and methanol tolerance) was obtained with the Pt material coated with an Ag layer of 20kp. Voltammograms recorded in oxygen-saturated 0.5 M KOH + 1 M MeOH.

## Mn<sub>2</sub>O<sub>3</sub>/Pt/CP catalysts

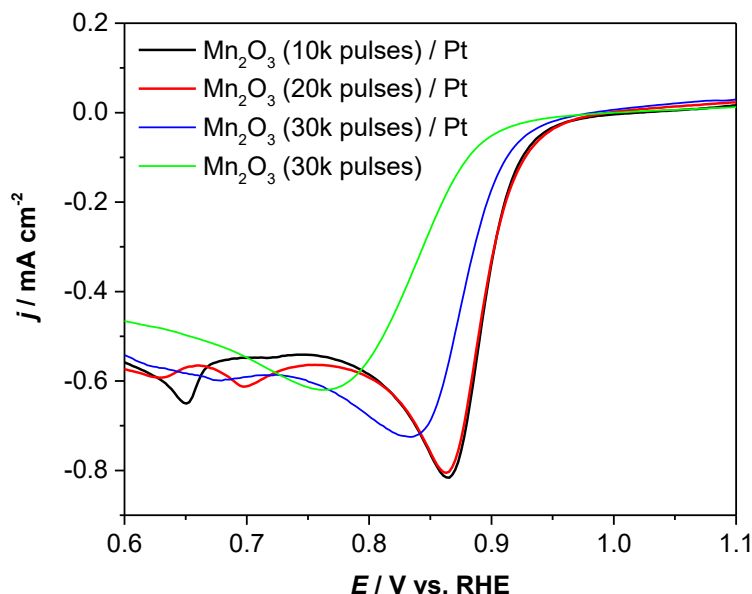


Figure AI 6 Effect of the Mn<sub>2</sub>O<sub>3</sub> layer thickness on the ORR activity. The best performance is obtained with the thinnest Mn<sub>2</sub>O<sub>3</sub> layers (10 and 20kp). However, with thicker Mn<sub>2</sub>O<sub>3</sub> layer (30kp), the material starts to behave like Mn<sub>2</sub>O<sub>3</sub> alone. LSVs obtained in oxygen-saturated 0.5 M KOH.

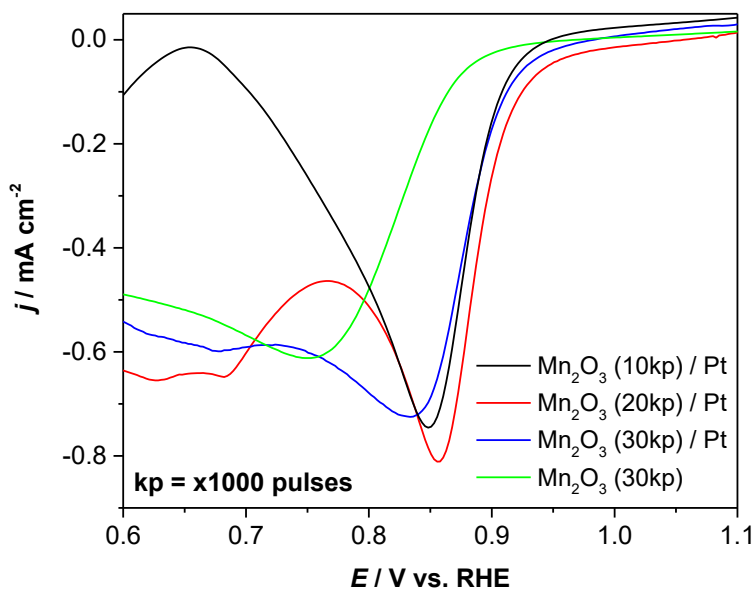


Figure AI 7 Effect of the Mn<sub>2</sub>O<sub>3</sub> layer thickness on the activity towards ORR in the presence of MeOH. With the thinnest Mn<sub>2</sub>O<sub>3</sub> layer, the material exhibits the poorest methanol tolerance. On the other hand, with the thickest Ag layer, the material exhibits high tolerance to MeOH but the ORR onset potential is the least positive. The best performance (compromise between onset potential and methanol tolerance) was obtained with the Pt material coated with a Mn<sub>2</sub>O<sub>3</sub> layer of 20 kp. LSVs recorded in oxygen-saturated 0.5 M KOH + 1 M MeOH.

## Fe<sub>2</sub>O<sub>3</sub>/Pt/CP catalysts

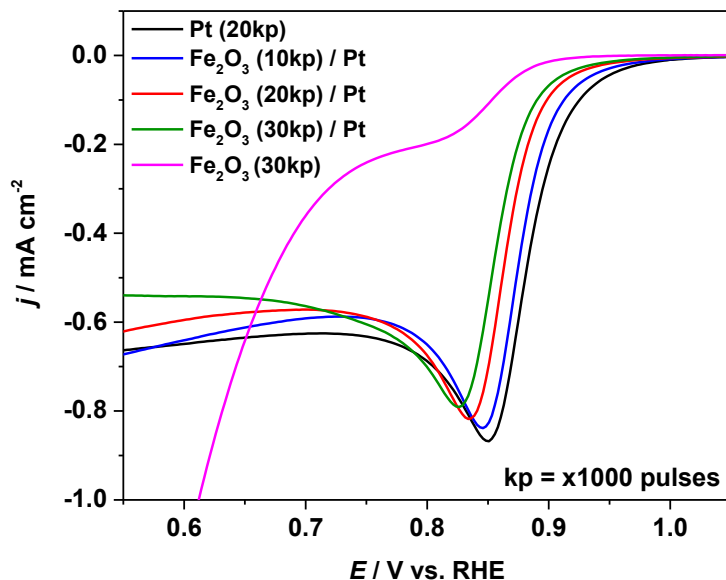


Figure Al 8 Effect of the Fe<sub>2</sub>O<sub>3</sub> layer thickness on the activity towards the ORR. The thinner the Fe<sub>2</sub>O<sub>3</sub> layer, the more similar activity to Pt. Conversely, with thicker Fe<sub>2</sub>O<sub>3</sub> layer, the activity approaches that of the pure Fe<sub>2</sub>O<sub>3</sub> material.

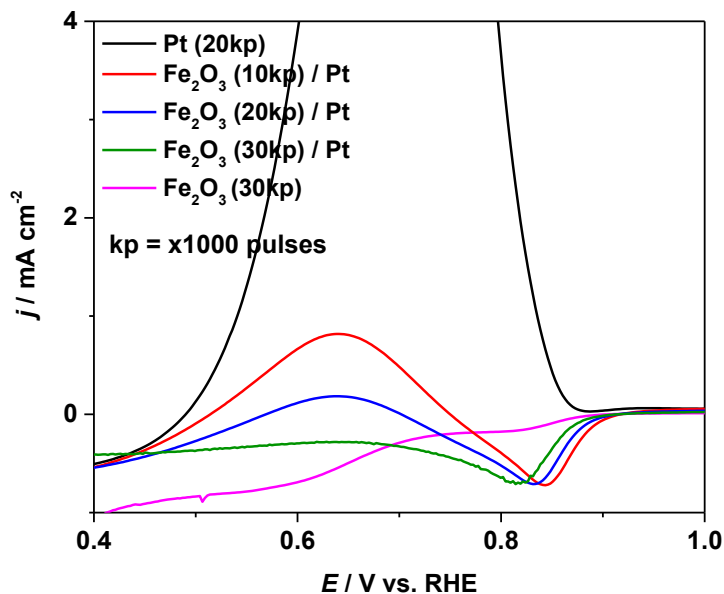


Figure Al 9 Effect of Fe<sub>2</sub>O<sub>3</sub> layer thickness on the activity towards ORR in presence of MeOH. The pure Pt film shows activity towards the MOR. As the Fe<sub>2</sub>O<sub>3</sub> layer thickness increases, the bilayer material becomes more tolerant to MeOH, but at the same time it loses performance in terms of ORR onset potential, ultimately approaching that of the pure Fe<sub>2</sub>O<sub>3</sub> material.

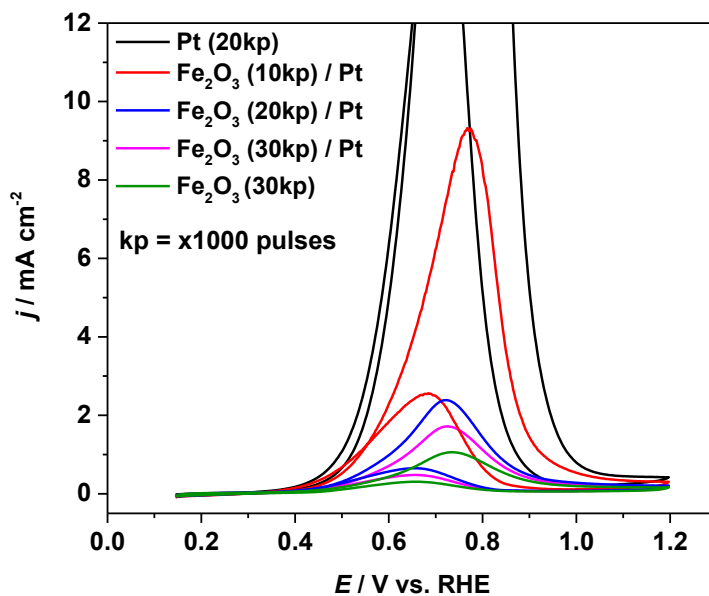


Figure Al 10 Coating the Pt layer with  $\text{Fe}_2\text{O}_3$  layer decreases the catalytic activity towards the MOR, however, high methanol tolerance cannot be achieved since  $\text{Fe}_2\text{O}_3$  is slightly active to the MOR.

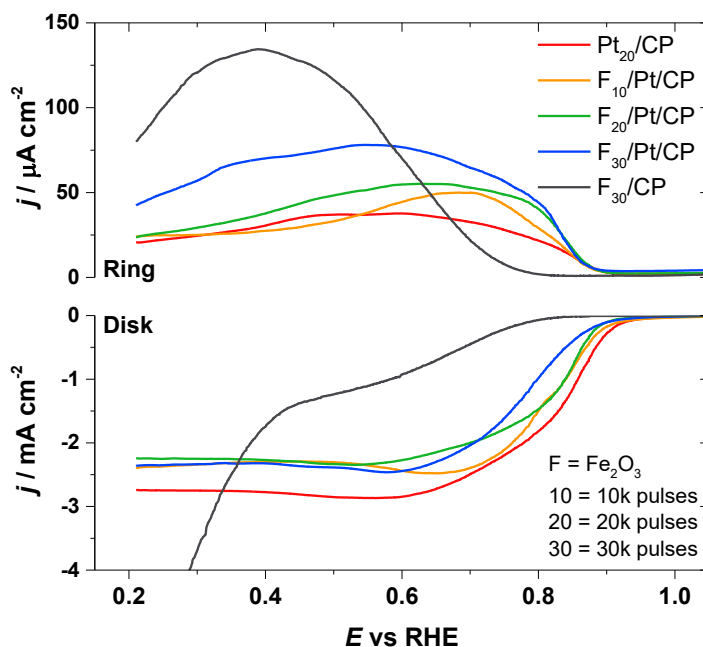


Figure Al 11 ORR performance of the different materials studied by RRDE. The ring current and therefore the amount of hydrogen peroxide increases with the thickness of the  $\text{Fe}_2\text{O}_3$  layer.

Since the overall catalytic activity of the  $\text{Fe}_2\text{O}_3/\text{Pt}/\text{CP}$  material was not in any case better than  $\text{Ag}/\text{Pt}/\text{CP}$  or  $\text{Mn}_2\text{O}_3/\text{Pt}/\text{CP}$ , it was not included in the results section of this thesis.

## APPENDIX II

---

### Scientific papers published during the thesis.

1. A. Moreno-Zuria, J. C. Abrego-Martínez, S. Sun, M. Mohamedi. "Prospects of membraneless mixed-reactant microfluidic fuel cells: evolution through numerical simulation" Submitted.
2. B. López-González, J. C. Abrego-Martínez, B. S. Hernández-Sarmiento, A. Moreno-Zuria, Youling Wang, Mohamed Mohamedi, L.G. Arriaga, F.M. Cuevas-Muñiz. "PLD Electrodes in a coupled microfluidic fuel cell to a lab on a chip system for energy generation" *Journal of Physics: Conference Series* 1407 (2019) 012011.
3. M. J. Estrada-Solís, J. C. Abrego-Martínez, A. Moreno-Zuria, L. G. Arriaga, Shuhui Sun, F. M. Cuevas-Muñiz, Mohamed Mohamedi. "Use of a bilayer platinum-silver cathode to selectively perform the oxygen reduction reaction in a high concentration mixed-reactant microfluidic direct ethanol fuel cell" *International Journal of Hydrogen Energy*, 44 (2019) 18372-18381.
4. J. C. Abrego-Martínez, Y. Wang, A. Moreno-Zuria, F. M. Cuevas-Muñiz, L. G. Arriaga, S. Sun, M. Mohamedi, "Nanostructured  $\text{Mn}_2\text{O}_3/\text{Pt}/\text{CNTs}$  selective electrode for oxygen reduction reaction and methanol tolerance in mixed-reactant membraneless micro-DMFC" *Electrochimica Acta*, 297 (2019) 230-239.
5. J. C. Abrego-Martínez, A. Moreno-Zuria, F. M. Cuevas-Muñiz, L. G. Arriaga, S. Sun, M. Mohamedi, "Design, fabrication and performance of a mixed-reactant membraneless micro direct methanol fuel cell stack" *Journal of Power Sources*, 371 (2017) 10-17.
6. J. C. Abrego-Martínez, A. Moreno-Zuria, Youling Wang, F. M. Cuevas-Muñiz, L. G. Arriaga, S. Sun, M. Mohamedi, "Fabrication and evaluation of passive alkaline membraneless microfluidic DMFC" *International Journal of Hydrogen Energy*, 42 (2017) 21969-21975.
7. J. C. Abrego-Martínez, Youling Wang, J. Ledesma-Garcia, F. M. Cuevas-Muñiz, L. G. Arriaga, M. Mohamedi. "A pulsed laser synthesis of nanostructured bi-layer platinum-silver catalyst for methanol-tolerant oxygen reduction reaction" *International Journal of Hydrogen Energy*, 42 (2017) 28056-28062.

### **Conference presentations**

- November 2018: MRS Fall meeting (Oral), Boston, MA.
- October 2018: iCAMP 2018, (Oral), Montreal, Canada.
- June 2018: EMP18 (Poster), Montreal, Canada.
- October 2017: CQMF/QCAM 1er colloque annuel (Oral), Sherbrook, Canada.
- October 2016: 9e Colloque Annuel du CQMF (Oral), Montreal, Canada.

### **Awards and Honors**

- Internship scholarship (2015), provided by CONACYT (National Council of Science and Technology) to participate in the MATECSS (Materials and Technology for Energy Conversion, Saving and Storage) training program.
- Doctoral scholarship (2016–2020), provided by MATECSS (Materials and Technologies for Energy Conversion, Saving and Storage) Excellence Scholarship program.